INcreasing Safety in NPPs by **C**overing Gaps in **E**nvironmental **F**atigue **A**ssessment – focusing on gaps between laboratory data and component **SCALE**

INCEFA-SCALE Compendium: Advanced Research and Integrated Findings on Environmentally Assisted Fatigue

This project has received funding from the Euratom Research & Training Programme 2019-2020 under grant agreement n^{o} 945300.

INCEFA-SCALE: Increasing Safety in NPPs by Covering Gaps in Environmental Fatigue Assessment – focusing on gaps between laboratory data and component scale

The INCEFA-SCALE Compendium: Advanced Research and Integrated Findings on Environmentally Assisted Fatigue

DOI: 10.5281/zenodo.18799092

https://incefascale.unican.es/

Edited by INCEFA-SCALE Project.

Editors:

- Sergio Arrieta
- Sergio Cicero

This project has received funding from the Euratom Research & Training Programme 2019-2020 under grant agreement nº 945300.

Foreword

This Reference Book compiles the research and technical outcomes of the INCEFA-SCALE Project[1], providing a comprehensive record of the experimental and analytical work performed to advance nuclear structural integrity.

As a collaborative milestone, this document synthesizes contributions from our partners to offer a modernised framework for evaluating environmentally assisted fatigue. Lead contributors are acknowledged at the beginning of each section, reflecting the collective expertise driving this international effort.

Authors/Contributors (alphabetical order):

Arrieta, Sergio (University of Cantabria)
Austin, Tim (JRC)
Beswick, Jack (Amentum)
Casulli, Louise (Framatome)
Cicero, Román (Innomerics)
Cicero, Sergio (University of Cantabria)
Connolly, Brian (University of Manchester)
Courtin, Stéphan (EDF)
Currie, Chris (Rolls-Royce)
Cuvilliez, Sam (EDF)
Damiani, Thomas (EPRI)
Doremus, Luc (Framatome)
Dundulis, Gintautas (KTU)
Fernández-Viña Reinoso, Antonio (CIEMAT)
Gee, Petra (Innomerics)
Grimm, Michael (Framatome GmbH)
Huret, Joseph (ASNR)
Jacquemoud, Clementine (CEA)
Le Roux, Jean-Christophe (EDF)
Lee, Hyeong-yeon (KAERI)
Martin, Oliver (JRC)
McLennan, Alec (Amentum)
Novotny, Radek (JRC)
Que, Zaiqing (VTT)
Schnablova, Ivana (UJV)
Seppänen, Tommi (VTT)
Spätig, Philippe (PSI)

[1] CORDIS: https://cordis.europa.eu/project/id/945300.

Editor's note:

The analysis and conclusions contained in this document are based on the data available in February 2026. For the latest updates until the end of the INCEFA-SCALE Project (March 2026), please consult: https://incefascale.unican.es/

Manuscript completed in March 2026.

1st edition.

NCEFA-SCALE: Increasing Safety in NPPs by Covering Gaps in Environmental Fatigue Assessment – focusing on gaps between laboratory data and component scale

Index:

CHAPTER 1 INTRODUCTION TO THE INCEFA-SCALE PROJECT

This Chapter describes the strategic framework of the project, including the limitations of current ASME codified methods and the experimental aims designed to bridge laboratory data with industrial "feature" applications, by Alec McLennnan.

1.1 THE INCEFA-SCALE PROJECT

INCEFA-SCALE kicked off in September 2020 and is a five-year project supported by the European Commission Horizon 2020 programme. It is the successor to the INCEFA-PLUS programme (2015 to 2020) that was reported at ASME PVP2020 [1.1–1.4]. This Chapter will provide an overview of the project goals, structure, technical approaches, status, and a discuss the direction of the work.

The goals of INCEFA-SCALE are to improve predictions of fatigue lifetimes of Nuclear Power Plant (NPP) components when subjected to Environmentally Assisted Fatigue (EAF) loading and provide guidance on the transferability of laboratory-scale testing results to component-scale behaviour.

INCEFA-SCALE strategy:

1. The development of an improved mechanistic understanding of EAF, through characterisation of laboratory tested stainless steel EAF specimens coupled with datamining of the MatDB database (the JRC-administered database [1.5] in which INCEFA-PLUS and other data is already stored).
2. Testing focused on defining the effects of Variable Amplitude (VA) loading and surface finish on the fatigue life of 316L stainless steel. Features testing will investigate testing notched geometries across multiple laboratories, multi-axial loading, and complex loading in standard specimen designs.
3. Using the output from the two previous points, the project will analyse the results against codified and non-codified methods. This will produce guidance on the transferability of laboratory-scale data to component scale and plant relevant loading conditions.

The project consists of six Work Packages (WP) as illustrated in Figure 1.1 with the interdependencies between the WPs in Figure 1.2.

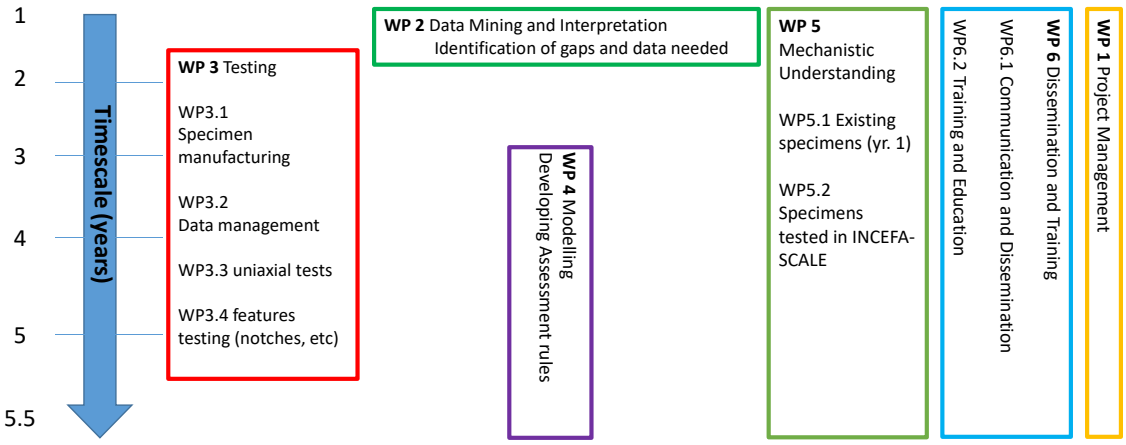

Figure 1.1. INCEFA-SCALE work package structure plus timescales for WP activities.

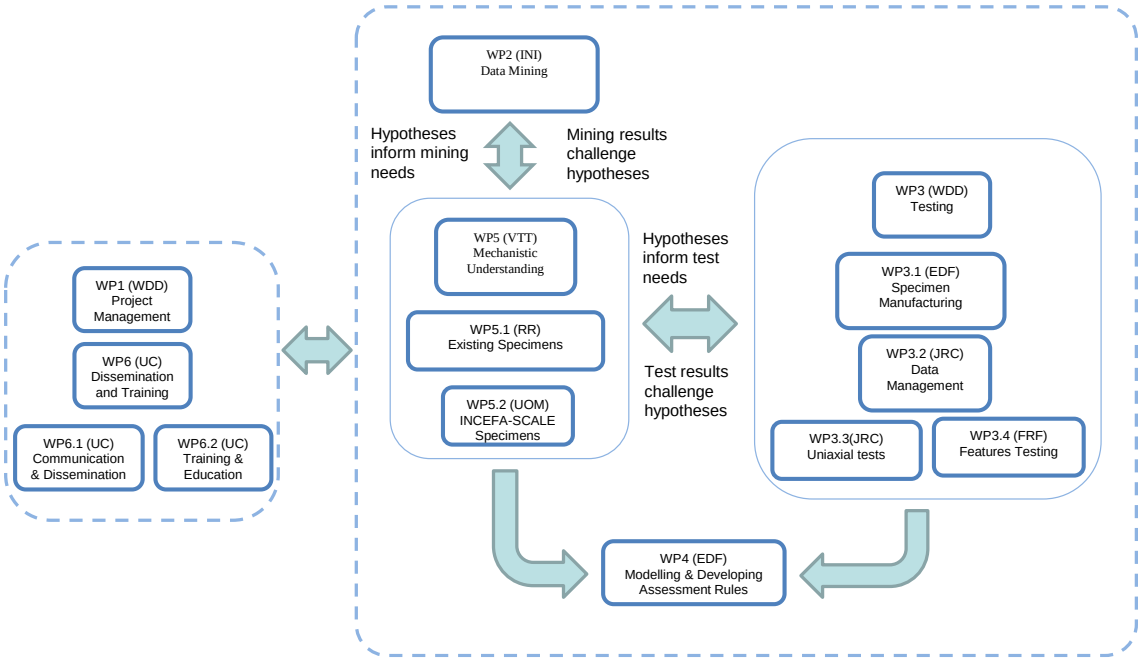

Figure 1.2. INCEFA-SCALE work package inter-dependencies.

The project team is comprised of seventeen organisations. Fourteen of these organisations have testing capabilities that cover air and simulated Pressurized Water Reactor (PWR) primary water environments, plus a range of specimen geometries and loading possibilities. The three organisations without testing capabilities focus on data analysis, fatigue assessment methodologies and/or material characterisation. This combination of capabilities provides the INCEFA-SCALE programme with a sufficient range and depth of skills and understanding to deliver the broad aims of the project.

The participating organisations are (fatigue testing laboratories are in bold):

- **Amentum**, project coordinator - UK.
- **Paul Scherrer Institute (PSI)** - Switzerland.
- **ÚJV-Řež, a.s. (UJV)** - Czech Republic.
- **Teknologian Tutkimuskeskus VTT Oy (VTT)** - Finland.
- **Centro de Investigaciones Energéticas, Medioambientales y Tecnológicas (CIEMAT)** - Spain.
- **Autorité de Sûreté Nucléaire et de Radioprotection (ASNR)** - France.
- **University of Cantabria (UC)** - Spain.
- **Comissariat a l´Energie Atomique et aux Energies Alternatives (CEA)** - France.
- **European Commission, Joint Research Centre (JRC)** - the Netherlands.
- **Framatome (FRF)** - France.
- **Electricité de France (EDF)** - France.
- Innomerics (INI) - Spain.
- Rolls-Royce (RR) - UK.
- **Framatome GmbH (FRG)** - Germany.
- **Kaunas University of Technology (KTU)** - Lithuania.
- **Korea Atomic Energy Research Institute (KAERI)** - South Korea.
- University of Manchester (UOM) - UK.

- Electric Power Research Institute (EPRI) - USA.
- The United States Nuclear Regulatory Commission (USNRC) - USA.
- Naval Nuclear Laboratory (NNL) - USA.

Good cooperation and communication are important for INCEFA-SCALE. Biannual project meetings, working groups, an Expert Panel, and an independent Advisory Board are actively providing advice and assessment of the direction of testing within the INCEFA-SCALE Project. They also had the task of guiding the selection of test conditions to maintain a reasonable balance between the parameters being investigated and the number of tests available to support conclusions.

A final feature of INCEFA-SCALE is the external relationships with EPRI, USNRC, NNL and JNRA. These relationships, established during INCEFA-PLUS, will ensure that the project's objectives (illustrated in Figure 1.3) are as relevant and useful as possible to the wider engineering community.

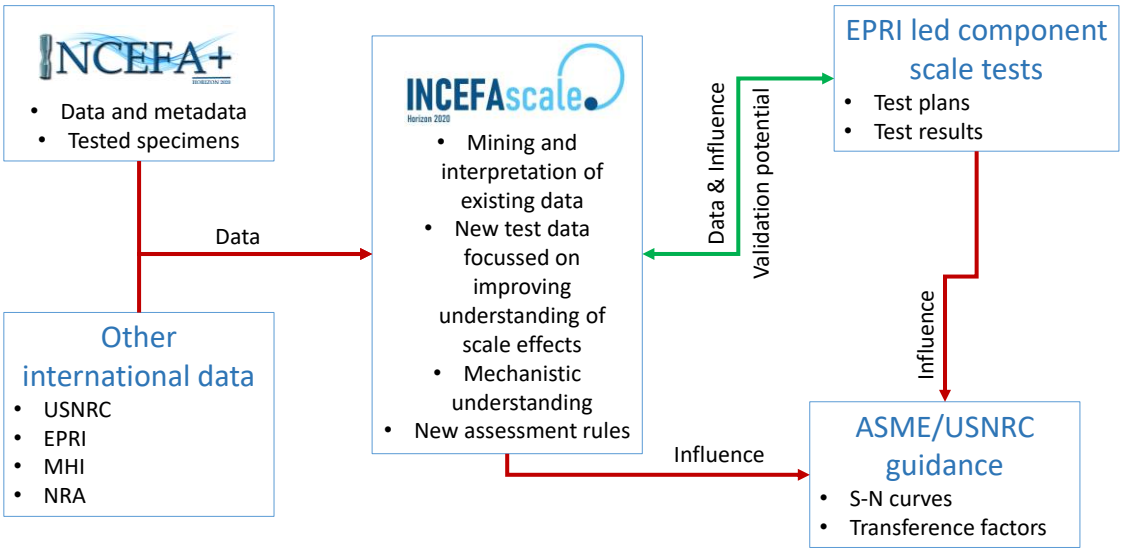

Figure 1.3. INCEFA-SCALE external relationships and high-level objectives.

The aim identified for the INCEFA-SCALE Project is to improve the transference of laboratory data to plant assessment methodologies. This aim is achieved by the combination of testing, characterisation, and analysis work packages.

1.2 OVERVIEW, CONCEPT AND OBJECTIVES

Safely accounting for EAF failure of components in nuclear plant is an important part of structural integrity assessments for the nuclear industry. However, there is a discrepancy between the good EAF Operating Experience (OPEX) for nuclear components and the difficulty in obtaining an acceptable result from a fatigue assessment.

A reason for this discrepancy is that the assessment procedures described in codes and standards are generally based on laboratory test results that simplify and idealise the real conditions that plant components are subjected to. The loading experienced by in-service components can produce alternating stresses from sources such as thermal transients or vibration. In addition to alternating stresses, mean stress can be produced from sources like

weld residual stress or variable amplitude loading. The sources of these stresses are not necessarily constant or simple and this creates complex stresses that can be very different from laboratory conditions. Further increasing the complexity, real components may be exposed to corrosive environments and have geometries that are different from standard test specimens. The combinations of these conditions can produce complex multi-dimensional fatigue loading combined with environmental effect that are not simple to quantify or assess.

To utilise some of the simplified fatigue methods, the multidimensional loading requires reduction to one-dimensional parameters. For example, conversion of a set of multi-axial strains or stresses into a single characterising parameter that is compatible with current analytical methods. The assumptions and methods used to simplify real conditions to create fatigue assessments and use them to assess plant life must be well understood to support confidence in their use and development. A substantial challenge in bridging the knowledge gap, is to generate data that can effectively be used to study these processes and support simplifications.

Addressing the knowledge gap that exists between fatigue behaviour represented by laboratory tests and the more complex behaviour experienced by plant components is a very challenging subject. Topics that either require or have been performed in the pursuit of this gap include variable parameters (like temperature, strain rate or loading) [1.6], multiaxial loading [1.7], loading order effects [1.8–1.10], size effects [1.11], welds, and geometrical features [1.12,1.13]. These experiments are broadly considered non-standard and need substantial development to enable integration with assessment methods or interpretation with other fatigue data. This gap requires continuous development of testing methods, new small-scale testing methods, and the creation of novel experimental facilities. Such testing frequently encounters unforeseen complications that need consideration when interpreting and using the data produced.

Type-300 austenitic stainless steel is a common material choice for primary circuit components and piping in a PWR nuclear power plant. In service, the primary circuit materials must withstand conditions including high temperatures, pressurised aqueous primary coolant water, and loading that may be dynamic and non-monotonic. The design fatigue curves, and related code cases defined in the ASME Boiler Pressure Vessel Code [1.14–1.16], and similar codes, are typically considered to be bounding of expected variations in material properties and in-service conditions. These fatigue methods use data from simplified laboratory testing to provide environmental cumulative fatigue usage factors that are equated to component lifetime predictions [1.11,1.17]. Benchmarking of these methods against a small number of component scale tests suggests that the codified methods may contain an undefined level of excess conservatism that is likely to originate from the translation of simple laboratory data to real component scale loading. Furthermore, the lack of publicly available real-world examples of EAF failure in plants also suggests an undue level of conservatism in these codes. The compromises involved in translating laboratory testing to plant conditions have resulted in a high-priority Knowledge Gap [1.18].

Aspects of the laboratory-to-plant scale Knowledge Gap have been the subject of a large amount of research over the past five years. This research has provided a greater understanding of the relationship between the environment and loading shape or surface finish. New methods now exist that are capable of better predicting the fatigue life of stainless steel specimens undergoing

plant-relevant loading and thermal transients [1.6], or defining the influence of plant realistic surface finishes [1.19]. These methods identify and remove undue conservatism from assessments by more accurately defining an effective environmental effect or a reduction in surface finish and size-effect transference factors. Despite these advancements, a level of undefined conservatism associated with the laboratory-to-plant Knowledge Gap remains. Therefore, increasing the understanding of the EAF behaviour of stainless steels is paramount for providing guidance and advances in the transferability of laboratory-scale testing results to component-scale behaviour. The INCEFA-SCALE Project will address this need.

In parallel to laboratory tests with more plant relevant conditions, EPRI (USA) have commissioned a series of component-scale EAF tests [1.20] to provide component data using known loading and environmental conditions. These tests will advance a poorly understood area of fatigue by increasing the availability of component-scale data. However, in isolation these component-scale tests will not fully address the Knowledge Gap and define the conservatism in fatigue assessments. The INCEFA-SCALE programme is complementary to the component-scale tests and necessary for advancing this area of fatigue.

Investigating EAF and its impact on fatigue assessments is an active area of research for the nuclear industry. To ensure that INCEFA-SCALE supported the aims of the nuclear industry and the goals of Horizon 2020 funding, the areas of study for INCEFA-SCALE were informed by a survey of the state-of-the-art in nuclear EAF R&D. Partners were asked to identify areas where current analytical design methodologies were expected to contain inadequacies in the form of either excessive conservatism or a lack of empirical/mechanistic understanding. To maximise the effectiveness of this activity and limit bias, these were first formed at the individual partner level before being collated and discussed in wider meetings. The full list of topics is provided in Table 1.1.

The range of areas that were identified represent a significant amount of engineering work that far exceeds the scope and available resources within INCEFA-SCALE. To maximise the effectiveness of the project and arrive at a consensus on which areas should be investigated, each topic was rated against the following criteria:

- Perceived benefit to plant life assessments.
- Difficulty to implement experimentally.
- Difficulty to formulate into revised guidance.
- Availability of existing data.

For example, providing meaningful benefits to engineering assessments by improving the understanding of the role of hydrogen on EAF is considered to be very difficult due to the lack of a well-developed scientific framework for describing the effects of hydrogen on these materials, difficulty in accurately measuring hydrogen and monitoring its transport throughout a test, and no clear basis for how any improvements could be incorporated into current design codes (e.g., ASME BPVC Section III). Conversely, for variable amplitude loading testing can be readily performed on the equipment already available to partners, improvements to current fatigue endurance methodologies are well understood (as modifications to the transference factors in the example of ASME BPVC Section III endurance curves), and the potential identified benefits of between a factor of 2-10 on fatigue endurance lifetime predictions are large.

Furthermore, loading history was identified as a critical topic to address in NUREG/CR-6909, Rev.1 [1.11], if a new benchmark for EAF assessment was to be proposed.

This approach enabled the project to focus on identifying the most effective and realistic areas of investigation to maximise the chances of successful outcomes within INCEFA-SCALE. The following items were identified as the intended focus of testing and used by WP3 to plan out the necessary test matrices:

- **Complex waveforms (variable amplitude loading, all Phases).**
- **Material performance (i.e., fatigue behaviour of 316L material).**
- **Multi-axial loading/notches (Phases II & III).**
- Surface roughness (to be included in Phases I & II).
- Solid versus hollow specimens (to be included in Phases I & II).

The described prioritisation of work was further reinforced as surface finish [1.3,1.19,1.21], material variability and data scatter [1.21,1.22], size effects [1.21] and variable strain rates [1.6] have been the subject of large amounts of work resulting in the development of multiple ongoing ASME code-cases. The substantial amount of work and progress in these areas and the code-cases limited the value of further work in these areas when compared to VA loading, notch effects and multi-axial loading.

1.3 DESIGN FATIGUE CURVES AND CODIFIED METHODS

1.3.1 ASME

The beneficiaries of the grant agreement identified the methods described in NUREG/CR-6909, Rev.1 [1.11] as the benchmark for environmentally assisted fatigue assessments. Therefore, this method and its intended application to the ASME code is used as the benchmark for the data generated by INCEFA-SCALE. Other standards and methods will be considered in WP4, but for the sake of simplicity and cooperation NUREG/CR-6909, Rev.1 is considered the “lingua franca” of EAF. The project considers both the NUREG/CR-6909, Rev.1 approach to environmental effects and the construction of the ASME BPVC Section III design curves contained therein. A description of historic and alternative methods can be found in [1.23].

The basis for the ASME BPVC Section III [1.24] fatigue design curves for carbon steel, low alloy steel, austenitic stainless steel, and nickel based alloy are the mean air fatigue curves (eq. 1.1 and Table 1.2), derived from laboratory tests on uniaxial specimens with standard fully reversed loading [1.11]. These curves are then modified for mean stress using the modified Goodman mean stress correction [1.25] and adjusted using factors on both stress (2) or cycles (12), with the worst case defining the design curve as shown in Figure 1.4. The construction of these two factors is different [1.11]. The factor of 12 of on cycles is intended to account for the combined effect on fatigue life of sub-factors such as material variability and data scatter, size effect, surface finish and other factors and loading history. The value of 12 being derived from a Monte Carlo analysis of the individual factors and selecting values that bounds 95% of the mean population with the result being rounded up for consistency with ASME methods.

Mechanism of Interest	What are the current gaps/conservatisms?	Routes towards improved understanding?
Role of hydrogen in environmentally assisted fatigue	Hydrogen is expected to be a key factor in contributing to increased fatigue damage for stainless steels undergoing cyclic loading in PWR water. Developing mechanistic understanding helps with data interpretation and informs improved assessment methods.	Development of assessment framework for understanding how to characterise hydrogen transport through material and inform potential mitigations. Examination of crack tip and fracture surface morphology under different conditions. Understanding of oxide rupture rates and effect on hydrogen ingress. Impact of hydrogen on strain localisation in near surface regions of damage and at crack tips.
Short Crack Growth – Early stages of cracking and transition to long crack growth	Understanding of full fatigue life in components requires better descriptions of each individual stage of fatigue (nominally nucleation of small defect, short crack growth, and long crack growth). Defining a realistic description of the depth at which cracks transition from short to long crack growth (i.e., at which long fatigue crack growth (FCG) methods can be safely applied) reduces conservatism in postulating the size of initial flaws and allows for more FCG lifetime to be claimed in assessments where this is relevant.	Dedicated short crack growth testing. Monitoring of early growth in endurance tests and/or striation counting to estimate short crack growth (SCG) rates. Direct current potential drop or like monitor early crack growth. Identification of differences in rates for different surface preparation conditions, grain sizes, residual stress, etc.
Temperature effects during plant-realistic (complex) loading	Current assessment methodologies are typically based on the maximum temperature during a loading cycle. Experimental evidence has shown that reduced fatigue damage can occur when the temperature varies during the cycle. Typical plant transients are often characterised by varying temperatures. Since temperature has a large effect on fatigue, demonstrating that damage is not always characterised by the maximum temperature can drastically alter fatigue life predictions.	SNW, WKR and WTKR methods developed to account for these effects analytically. Requires stronger mechanistic underpinning. Endurance/FCG testing using complex waveforms where temperature is cycled during the test. Characterisation of standard fatigue damage at different temperatures. Some low temperature (<100 °C) testing has shown much higher FCG than expected which is not clearly understood.
Development of fatigue damage in stress/strain gradients	Majority of fatigue testing is performed under membrane or constant ΔK loading. Thermal loading can establish stress/strain gradients where cracks may be growing into a diminishing stress/strain gradient. Cracks growing into decreasing stress/strain fields may experience differences in crack closure, oxide build up, crack direction etc. Taking advantage of gradients in analysis extends predicted lifetimes.	Testing using specimens that induce a stress/strain gradient or testing with thermal cycles. Characterisation of subsequent damage/crack development. A key question is 'when a stress/strain gradient is present, what combination of strain amplitude/depth is suitable for describing the damage?' (e.g., the surface stress may be very high but the fatigue life is longer. Comparing the results to standard membrane testing may show that the strains at a depth of X microns are the controlling factor since these affect the accumulation of damage in the near surface).
Enhancement and retardation of FCG cracks	A better mechanistic understanding of enhancement underpins improved FCG methods and helps to support their wider application. In some materials (typically high sulphur but not limited to these) retardation can occur. The mechanisms for this are not completely understood. Retardation may be a stochastic process and difficult to incorporate into plant assessments with confidence, but better understanding could yield benefits if behaviour can be confidently described. 316 type materials appear to have lower FCG rates and better understanding of the reasons for this could underpin less conservative FCG guidance.	FCG testing of materials with different sulphur levels/stacking fault energies under conditions that promote enhancement/retardation. Examination of crack tips with focus on near tip deformation and oxide build up. Comparison of 304 and 316 type materials.
Effects of multiaxial loading on development of fatigue damage	Current methods for combining multiaxial loads are overly conservative. Improved methods may result in lower effective predicted strains which result in longer lifetimes in assessments. Effects of other relevant parameters (surface roughness, environment etc) under multiaxial loading are not well understood.	Testing under multiaxial loading conditions (typically biaxial for thermal loading). General characterisation of fatigue damage in these materials to identify differences from membrane loading (crack direction, nucleation sites, oxide formation under multiaxial loading where rupture may differ etc). Understanding of loading under fully plastically deformed loading.

Effects of variable amplitude loading on development of fatigue damage	Variable amplitude loading introduces complexity into both endurance and FCG fatigue behaviour. Lifetimes are typically calculated using Miner's rule but this may not always be valid/optimal. ASME generally accounts for these effects in high cycle fatigue through a factor of 2 on stress in this region of the curve. Improved description of effects required for more complicated analysis models and possible reduction of ASME factor of 2.	Testing using variable amplitude loading targeting different types of VA (ending in tension compression, tests with underloads/overloads, random spectrum testing, high cycle fatigue). Characterisation of development of damage and cracking under VA testing (e.g., do cracks develop and get stuck at grain boundaries, do overloads enable those cracks to progress, is material resistance increased in presence of overloads?).
Effects of surface condition on fatigue initiation and SCG	Surface condition may influence fatigue endurance lifetimes and crack nucleation behaviour. Interaction between physical surface roughness (where roughness is classically expected to lead to surface stress concentrations that reduce effective fatigue life) and sub surface condition as a result of processing method (e.g., cold worked near surface layer that may alter fatigue life). This aspect has already removed a lot of conservatism through previous investigations and introduction of Fen integrated type methods. Further potential decrease in conservatisms could be possible if factors such as cold work can be shown to increase endurance resistance. Suggest more novel/important aspect of this is understanding the effects of surface condition in non-standard test conditions (i.e., not membrane loaded specimens but ones with gradients, notches, variable amplitude and multiaxial loading).	Testing with range of surface preparation techniques. Examination of surfaces and near surface deformation, characterisation of formation of short cracks. Focus on identifying potential phase transformations in near surface regions (e.g., martensite). Examination of formation and configuration of microcracking, including any dependence on environment, strain rate and strain amplitude. Interplay of surface roughness with multi-axial loading (including interaction of grinding orientation), variable amplitude and surface gradient.
Development of material properties during cyclic loading in environment	Previous testing has suggested possible differences in hardening behaviour between similarly loaded tests in air and PWR water environment (possibly linked to dynamic strain ageing in the presence of hydrogen). Accurate descriptions of hardening behaviour are required for more advanced fatigue models (e.g., variable amplitude).	Examination of previously collected hysteresis data to examine differences in air and water. Expected to be difficult to investigate through microscopy.
Development of fatigue damage in notches/features	Reduction in conservatism associated with current methods as a result of improved understanding of effect of notches on development of fatigue damage under different loading conditions. INCEFA-PLUS observed differences in results from hollow test specimens at EDF, Jacobs and PSI which remains unexplained.	Examination of development of fatigue damage in notched test specimens. SCG kinetics from a notch. Testing of specimens with range of different notch radii fabricated using different methods. Interactions of notches with other factors. Hollow specimens have potential to include multiaxial stress states depending on internal pressure with FE required to understand this.
Effects of static hot holds on recovery of fatigue damage	Previous testing has provided evidence for the existences of so-called 'hold time effects', where fatigue life extension has occurred when long periods of static hold time have been incorporated into a test. The underlying potential mechanisms for this effect are not well understood.	Perform additional hold time testing under conditions more favourable to the observation of these effects. Microstructural characterisation including TEM to understand how development of dislocation structures and point defects might affect material performance.

Table 1.1. Summary of technical/mechanistic areas of interest from INCEFA-SCALE Consortium.

$$ln(N) = A - Bln(\varepsilon_a - C)$$ eq. 1.1

where A, B, and C are coefficients, N is the number of cycles and ε_a is the strain amplitude.

Material	A	B	C
Carbon Steels	6.583	1.975	0.113
Low-Alloy Steels	6.339	1.808	0.151
Austenitic Stainless Steel	6.891	1.920	0.112
Nickel based Alloy			

Table 1.2. Parameters for eq. 1.1 from NUREG/CR-6909, Rev.1 [1.11].

The factor on stress or strain has a value of 2 and is made up of subfactors dealing with data scatter, size, surface finish, loading sequence, as well as effects such as secondary hardening and dynamic strain aging [1.11]. These effects are not cumulative over the high cycle region, and unlike the factor on cycles, only the most dominant of those subfactors controls the net adjustment factor. Furthermore, these parameters mainly influence the growth of microstructurally short cracks, and their effect depends on operating conditions, environment, materials properties, and fabrication processes. The method used to determine the value of this adjustment factor is much less documented and unclear.

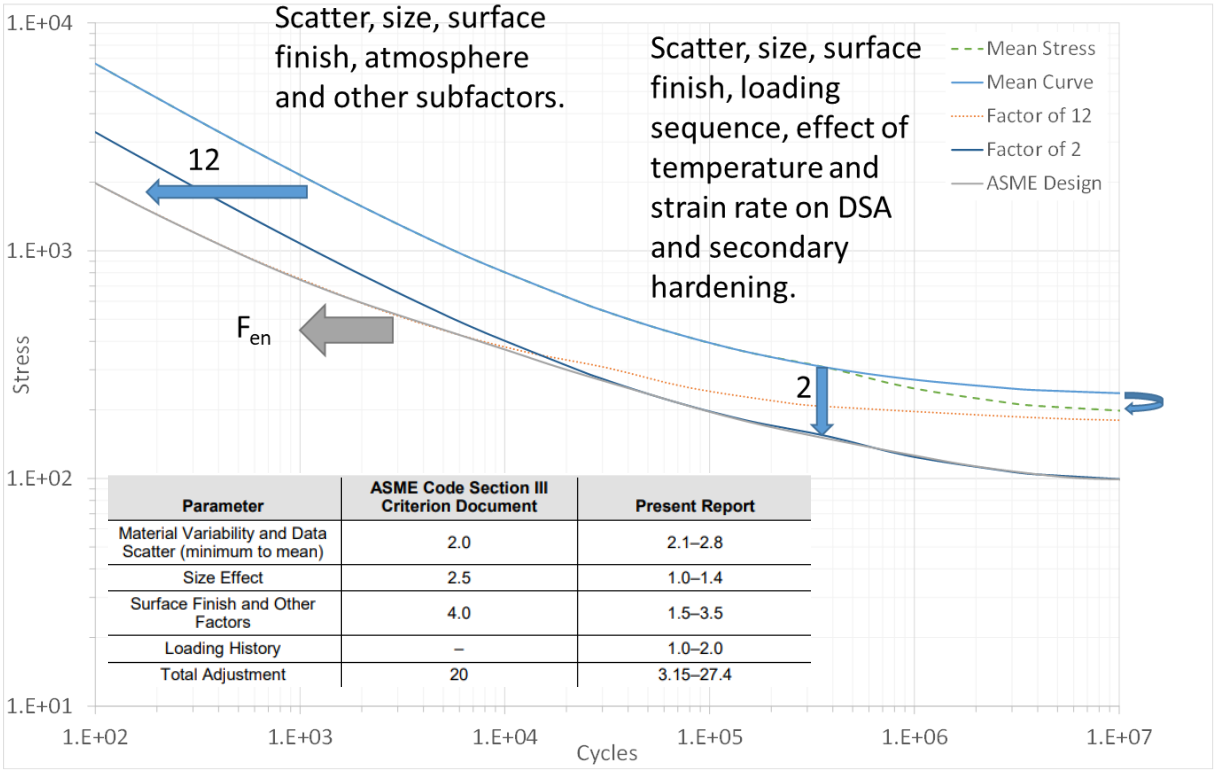

Figure 1.4. Annotated ASME BPVC [1.24] design curve including (inset table) the values of the subfactors that make up the adjustment factor applied to the number of cycles from NUREG/CR-6909, Rev.1 [1.11].

How the environmental factor is applied to the design curve to calculate allowable cycles has the potential to produce results that are more conservative than the previous ASME design curves that used adjustment factors of 2 and 12. NUREG/CR-6909, Rev.1 method produces values for F_{en} ranging from 1 to ≈142 for carbon/low alloy steel (eq. 1.2), 1 to ≈13 for stainless

steel (eq. 1.2), and 1 to ≈4 for nickel based alloys (eq. 1.2). As this threatened the extant position of nuclear plant, with respect to fatigue, the technical basis and application of these methods are the subject of significant research.

$$F_{en} = e^{((0.003-0.031\dot{\varepsilon}^*)S^*T^*O^*)} \quad \text{eq. 1.2}$$

$$F_{en} = e^{(-\dot{\varepsilon}^*T^*O^*)} \quad \text{eq. 1.3}$$

where $\dot{\varepsilon}^*$, S*, T*, and O* are transformed strain rate, sulphur content, temperature, and dissolved oxygen content respectively. The formulae for these values can be found in [1.11].

This research has resulted in new methods being proposed such as F_{en}-threshold [1.19,1.26] and the Weighted Strain Life (SNW) [1.6,1.27] approach which significantly improved the fatigue assessment methods available. In the case of F_{en}-threshold the magnitude of the environmental factor can be reduced by up to a factor of 3, based on observations that the surface finish effect in PWR conditions could be offset by environmental effects and therefore does not require inclusion in the overall transference factor of 12. Significant value was provided to industry from this benefit, achieved from relatively straight forward environmental testing targeted at specific aspects of the fatigue assessment procedure.

As described above, the advancements made over the past 20 years on fatigue assessment methods [1.6,1.19,1.23,1.26] have made significant progress on addressing several valuable but less complex EAF R&D hypotheses. This means that future progress requires more difficult research topics to be undertaken. Research studying the interactions between the adjustment factor of 2 on stress or strain and the application of environmental factors has the potential to have as much positive impact as the past research on surface finish for the nuclear industry, because transient loading in this regime accounts for an appreciable amount of many components' lives. A reduction in the factor of 2 would result in a larger proportion of these transients falling below the threshold for being included in an analysis. However, the testing is substantially more difficult to perform from a test execution, reliability, and fidelity point-of-view.

The industry has been using existing data to perform new analysis and interpretation to justify reductions in the subfactors making up the factor of 2 on stress or strain. These works include statistical analyses evaluating the subfactors for material variability and data scatter indicating a factor of 1.4-1.7 [1.28,1.29] would be sufficient to account for data scatter. However, to take advantage of a reduction in these sub-factors it is necessary to demonstrate that other subfactors such as loading history do not then become the dominant subfactor determining the overall factor on stress/strain. INCEFA-SCALE aims to support this international research by investigating the loading history and surface finish subfactors and to demonstrate whether they remain independent within the context of an EAF assessment. It is crucial to the successful creation of future methods that the environmental effects and how they interact with the subfactors be accounted for within research programmes that form the technical basis. This collaborative and cooperative approach with wider industry research was used to increase the impact of INCEFA-PLUS and is being used for the same reason within INCEFA-SCALE.

The success of the research programmes targeting reductions in the subfactors, for example surface finish for the adjustment factor on cycles required the test programmes to isolate the effects and study behaviour under nominally relevant loading conditions. Furthermore, adequate coverage of those relevant conditions was also essential to demonstrate that the conclusions were generally applicable under a reasonable range of parameters. These are important aspects that are needed for revisions to the subfactors that construct the factor on stress or strain.

1.3.2 DEVELOPMENT OF NEW METHODS

A parallel work stream has been run by the Japan Welding Engineering Society [1.30] to develop a new method for defining the design fatigue curves. These curves are based on best-fit equations of the form used by Langer [1.25] and in the NUREG/CR-6909, Rev.1 technical basis [1.11]. Furthermore, they use tensile strength as a variable which has the benefit of allowing the curves to be considered as material specific and account for the effect of temperature. The representation of the best-fit equation (eq. 1.4-eq. 1.6), along with a method for determining cyclic yield (eq. 1.7), and coefficients is taken from Currie et al. [1.10] and with the values themselves from Asada et al. [1.30]. The method uses the Smith-Watson-Topper (SWT) mean stress correction [1.31]. Substantial effort was made to produce a technical basis for the adjustment factors that are applied to the best-fit curve in the definition of the design curves. As such, these design curves take advantage of the advancements made in understanding the impact of EAF on the fatigue life of materials, providing methods with a detailed technical basis for accounting for fatigue behaviour and defining conservatism.

$$S_{apr} = AN_f^B + S_e \quad \text{eq. 1.4}$$

$$S_e = GS_u + J \quad \text{eq. 1.5}$$

$$A = H - LS_u \quad \text{eq. 1.6}$$

$$S'_y = \max(S_y, MS_u + P) \quad \text{eq. 1.7}$$

Type	H	L	B	J	G	M	P
Stainless Steel	5.09E4	0	-0.485	0	0.488	0.252	141
Ni-Cr-Fe	1.2E5	28	-0.580	36	0.450	0.726	0
Carbon and Low Alloy Steel							

Table 1.3. Fatigue life coefficients by Asada et al. [1].

The methods of producing the design fatigue curves and accounting for mean stress effects were refined by Currie et al. [1.10]. The refinements made to the method include a significant change to the way the correction for mean stress is applied, an improved surface finish adjustment factor calculation, a detailed design fatigue curve and a simplified design fatigue curve. These refinements are necessary because of an error in the mean stress correction approach derived by Langer [1.25]. The error has two aspects, first the magnitude of mean stress is underestimated due to the incorrect assumption of linear behaviour over all strain amplitudes. Second the mean stress correction is applied over an insufficient range of stress amplitude as

mean stress is assumed to shake down to zero at stress amplitudes above yield. The production of the simplified method, in addition to the detailed, is to accommodate situations were inverting a Ramberg-Osgood equation and accounting for complex material behaviour to support the correct evaluation of mean stress is impractical. This simplified solution offers similar results to the detailed method while handling the issues of mean stress.

1.4 REFERENCES

[1.1] K. Mottershead, M. Bruchhausen, S. Cicero, S. Cuvilliez, INCEFA-PLUS: Increasing Safety in NPPs by Covering Gaps in Environmental Fatigue Assessment, in: Vol. 1 Codes Stand., American Society of Mechanical Engineers, 2020: pp. 1–5. doi:10.1115/PVP2020-21220.

[1.2] S. Cuvilliez, A. Mclennan, K. Mottershead, J. Mann, M. Bruchhausen, INCEFA-PLUS Project: Lessons learned from the project data and impact on existing Fatigue Assessment Procedures; PVP2020-21106, Am. Soc. Mech. Eng. Press. Vessel. Pip. Div. PVP. (2020) 1–8.

[1.3] M. Bruchhausen, A. McLennan, R. Cicero, C. Huotilainen, K. Mottershead, J.-C. le Roux, M. Vankeerberghen, INCEFA-PLUS Project: Review of the Test Programme, in: Vol. 1 Codes Stand., American Society of Mechanical Engineers, 2020. doi:10.1115/PVP2020-21377.

[1.4] A. McLennan, P. Spätig, J.-C. Le Roux, J. Waters, P. Gill, J. Beswick, N. Platts, INCEFA-PLUS Project: The Impact of using Fatigue Data generated from Multiple Specimen Geometries on the Outcome of a Regression Analysis; PVP2020-21422, Am. Soc. Mech. Eng. Press. Vessel. Pip. Div. PVP. (2020).

[1.5] Joint Research Center - European Commission, ODIN Portal - MatDB, (2025). https://odin.jrc.ec.europa.eu/alcor/.

[1.6] C. Currie, A. Morley, D. Leary, N. Platts, M. Twite, K. Wright, Further Validation of the Strain-Life Weighted (SNW) Fen Method for Plant Realistic Strain and Temperature Waveforms, in: Vol. 1A Codes Stand., American Society of Mechanical Engineers, 2018. doi:10.1115/PVP2018-84879.

[1.7] H. Dhahri, C. Gourdin, G. Perez, S. Courtin, J.-C. Le Roux, H. Maitournam, PWR effect on crack initiation under equi-biaxial loading: Development of the experiment, Procedia Eng. 213 (2018) 571–580. doi:10.1016/j.proeng.2018.02.052.

[1.8] S. Asada, Y. Nomura, Development of New Design Fatigue Curves in Japan – Treatment of Variable Loading Amplitude Effect, in: Vol. 2 Comput. Technol. Bolted Joints; Des. Anal., American Society of Mechanical Engineers, 2021. doi:10.1115/PVP2021-60418.

[1.9] J. Colin, A. Fatemi, S. Taheri, Cyclic hardening and fatigue behavior of stainless steel 304L, J. Mater. Sci. 46 (2011) 145–154. doi:10.1007/s10853-010-4881-x.

[1.10] C. Currie, A. Morley, A. Mclennan, Suitably Accounting for Mean Stress Effects in Pseudo-Stress-Based Design Fatigue Curves, in: Vol. 1 Codes Stand., American Society of Mechanical Engineers, 2025. doi:10.1115/PVP2025-154711.

[1.11] O.K. Chopra, G.L. Stevens, NUREG/CR-6909,Rev.1; Effect of LWR Water Environments on the Fatigue Life of Reactor Materials. Final Report, 2018.

[1.12] J. Liao, J. Tan, X. Wu, D. Ning, G. Xue, W. Yao, Corrosion fatigue behavior of 304 stainless steel notched specimen in high-temperature pressurized water, Mater. Sci. Eng. A. 748 (2019) 137–145. doi:10.1016/j.msea.2019.01.090.

[1.13] K. Sakaguchi, Y. Asada, M. Itatani, T. Saito, Evaluation of Environmental Effects on the Fatigue of Notched Specimen of Austenitic Stainless Steel Using Modified Rate Approach

Method, in: Press. Vessel Pip. Codes Stand., ASMEDC, 2004: pp. 95–99. doi:10.1115/PVP2004-2678.

[1.14] ASME, Case N-905: Alternate Design Fatigue Curves to Those Given in For Section III Appendices, Mandatory Appendix I, Figures I-9.1 and I-9.1M Section III, Division 1, New York, 2020.

[1.15] ASME, Code Case N-792: Fatigue Evaluations Including Environmental Effects, Section III, Division 1, New York, 2020.

[1.16] ASME, Section VIII, Rules for Construction of Pressure Vessels, Division 1, Alternative Rules, New York, 2023.

[1.17] US-NRC, Regulatory Guide 1.207,Rev.1; Guidelines for evaluating the effects of Light-Water Reactor Water Environments in Fatigue Analyses of Metal Components, 2018.

[1.18] D. Tice, A. McLennan, P. Gill, Environmentally assisted fatigue (EAF) knowledge gap analysis: Update and revision of the EAF knowledge gaps, Palo Alto, CA, 2018.

[1.19] A. McLennan, A. Morley, S. Cuvilliez, Further Evidence of Margin for Environmental Effects, Termed Fen-Threshold, in the ASME Section III Design Fatigue Curve for Austenitic Stainless Steels Through the Interaction Between the PWR Environment and Surface Finish, in: Vol. 1 Codes Stand., American Society of Mechanical Engineers, 2020. doi:10.1115/PVP2020-21262.

[1.20] D.A. Steininger, K. Wright, M. Twite, A. Morley, T. Métais, G. Léopold, J.C. Le Roux, Component Testing Proposal to Quantify Margins in Existing Environmentally Assisted Fatigue (EAF) Requirements, in: Vol. 3B Des. Anal., American Society of Mechanical Engineers, 2017. doi:10.1115/PVP2017-65995.

[1.21] T. Métais, D. Tice, A. Morley, G.L. Stevens, L. de Baglion, S. Cuvilliez, Explicit quantification of the interaction between the PWR environment and component surface finish in environmental fatigue evaluation methods for austenitic stainless steels; PVP2018-84240, Am. Soc. Mech. Eng. Press. Vessel. Pip. Div. PVP. 1A-2018 (2018). doi:10.1115/PVP201884240.

[1.22] G. Blatman, T. Métais, J.-C. Le Roux, S. Cambier, Statistical analyses of high cycle fatigue French data for austenitic SS; PVP2014-28409, in: 2014. doi:10.1115/PVP2014-28409.

[1.23] INCEFA-PLUS Consortium, S. Arrieta, T. Austin, M. Bruchhausen, W.-J. Chitty, R. Cicero, S. Cicero, S. Cuvilliez, L. De Baglion, G. Dundulis, C. Gourdin, C. Huotilainen, J.-C. Le Roux, J. Mann, W. Mayinger, A. McLennan, T. Métais, E. Miroslava, K. Mottershead, R. Novotny, F.J. Perosanz López, N. Platts, I. Procopio, N. Prompt, P. Spätig, M. Twite, M. Vankeerberghen, INCEFA-PLUS findings on Environmental Fatigue, INCEFA-PLUS Project, 2020. doi:10.5281/zenodo.4243979.

[1.24] ASME, Nuclear Boiler and Pressure Vessel Code - Section III, (2007) edition with 2009 Addendum.

[1.25] B. Langer, Design of Pressure Vessels for Low-Cycle Fatigue, J. Basic Eng. (1962). doi:10.1115/1.3657332.

[1.26] T. Métais, S. Courtin, L. de Baglion, C. Gourdin, J.-C. Le Roux, ASME Code-Case Proposal to Explicitly Quantify the Interaction Between the PWR Environment and Component Surface Finish; PVP2017-65367, 2017. doi:10.1115/PVP2017-65367.

[1.27] C. Currie, A. Morley, N. Platts, M. Twite, K. Wright, Models for Calculating the Effect of Environment on Fatigue Life (Fen) for Complex Waveforms and/or Non-Isothermal Conditions, in: Vol. 1A Codes Stand., American Society of Mechanical Engineers, 2017. doi:10.1115/PVP2017-66030.

[1.28] J. Keisler, O.K. Chopra, W.J. Shack, NUREG/CR-6335 Fatigue Strain-Life Behavior of Carbon and Low-Alloy Steels, Austenitic Stainless Steels, and Alloy 600 in LWR Environments, 1995.

[1.29] A. Morley, A. McLennan, Statistical Analyses of Austenitic Stainless Steel High Cycle Fatigue Data to Support a Revised Design Factor for Design Fatigue Curve Development, in: Vol. 1 Codes Stand., American Society of Mechanical Engineers, 2022. doi:10.1115/PVP2022-84249.

[1.30] S. Asada, T. Nakamura, M. Kamaya, Y. Takahashi, Technical Revisions of Jsme Environmental Fatigue Evaluation Method, Am. Soc. Mech. Eng. Press. Vessel. Pip. Div. PVP. 1 (2023). doi:10.1115/PVP2023-102692.

[1.31] R. Smith, P. Watson, T. Topper, A stress–strain function for the fatigue of metal, J Mater. 5 (1970) 767–778.

CHAPTER 2 INCEFA-SCALE PROGRAM ON SOLID CYLINDRICAL SPECIMENS

This Chapter describes the baseline testing of solid specimens to evaluate critical hypotheses regarding mean stress, hardening effects, and variable amplitude loading through both mechanical results and detailed fractographic analysis, by Alec McLennan, Jack Beswick and Zaiqing Que.

2.1 INTRODUCTION

The INCEFA-SCALE test programme was designed to maximise the utility and value of the test data it produced. The data generated from the tests were envisioned to be used to explore design curves, develop fatigue models, and feed into materials characterisation to produce further data to support total life methodologies. To achieve this level of utility, and the broader aims of increasing mechanistic understanding, the testing was designed to initially be simple but severe and to cover a wide range of conditions that produce materials behaviour that fatigue models could be calibrated against. The ambition was that the complexity of the testing would be increased over time and produce data to study different aspects of the failure mechanism. This requires a combined approach of testing under reference conditions, variable loading, roughened surface finish, in air, and in PWR primary coolant environments. In this way the EAF design methods and main parameters of models could be evaluated such that a technical basis for new EAF methods could be created.

The ideal situation for the INCEFA-SCALE variable amplitude uniaxial programme would be to test spectrum loading as close to that seen in plant as possible. However, these types of tests are likely to be exceptionally difficult to interpret, have prohibitively long test times, and in the case of high temperature water testing impossible to set up for many laboratories given the technological limitations of the relevant equipment. This means that the variable amplitude waveforms had to be idealised to manage the limitations of laboratory testing. During the development of the test matrix the waveform pattern complexity, detection of difference between conditions, the coverage of conditions across the relevant space of conditions, laboratory equipment capability, and test times were considered.

The maximum strain amplitudes used were set to a practical bound to the ASME code (1%) based on what was observed in the Stepped Pipe experiments. The individual waveform pattens were balanced between strain amplitude, strain rate and test time so that the damage caused for each part of the pattern would enable analysis methods to evaluate the performance of the models used. By doing so, the tests were as complex and valuable as could be made within the limits of the testing capabilities.

However, one impact of these compromises was that the mean stresses for the tests were very high (see the Hypothesis 1, Section 2.2.3) and larger than is typically expected for civil plant. The benefits were that this magnified the differences between test conditions and allows different analytical methods to be compared without excessive numbers of tests.

Overcoming these compromises for future projects is non-trivial and would require:

- Significant upgrades to laboratory methods and equipment to enable test times greater than six months over a wider range of strain amplitudes.
- Development of extensometry to enable consistent testing methods across all fatigue testing in air and water environments.
- Software development to enhance data processing and interpretation.

To achieve the aims of the project as outlined above, several testing hypotheses were formulated to construct the INCEFA-SCALE test matrix.

2.1.1 THE NEGATIVE EFFECTS OF MEAN STRESS ON FATIGUE LIFE ARE RELATIVELY LESS DAMAGING AT HIGHER TEMPERATURES AND ARE CONSERVATIVELY ACCOUNTED FOR IN CURRENT DESIGN CODES

If a component or specimen is subject to multiple strain amplitudes within a single test, mean stresses will occur at the transition from one strain amplitude to another. The magnitude of these mean stresses is dependent on material properties, the magnitude of the preceding strain amplitude, the magnitude of the succeeding strain amplitude, the number of cycles at each strain amplitude, the temperature, and hold times. Furthermore, the environment may also influence the stresses that evolve during the test. These mean stresses, depending on the relative difference between the conditions at each strain amplitude, may be persistent or temporary. The mean stresses are simulated in laboratory testing by Variable Amplitude (VA) loading where multiple strain amplitudes are applied to the specimen during the experiment. The strain amplitudes can be applied in a variety of sequences or patterns as well as simulating random loading sequences. This ordering of strain amplitudes drives the evolution of mean stress.

This hypothesis is based on the ability of a specimen to support mean stresses due to VA loading being reduced at higher temperatures. For stainless steel, the material weakens as temperature increases and the amount of plastic damage for a given applied total strain increases. The increased plastic damage at high temperature means that mean stress will shake down to lower levels than for tests done at lower temperatures. This means that the negative effects of mean stress should be reduced for higher temperature tests.

To test this hypothesis several test waveforms were designed with a view to imparting and analysing transitional mean stresses, utilising a mean strain. A schematic of the strain waveforms applied in these tests is shown in Figure 2.1, named Periodic Overload (POL) and Periodic Underload (PUL). The ‘high’ and ‘low’ (‘low’ not shown in the figure) within the titles refer to the magnitude of the baseline strains, which were set at two levels with the aim to either maintain or shake down the mean stress developed by the position where the baselines departed the overload/underload cycles.

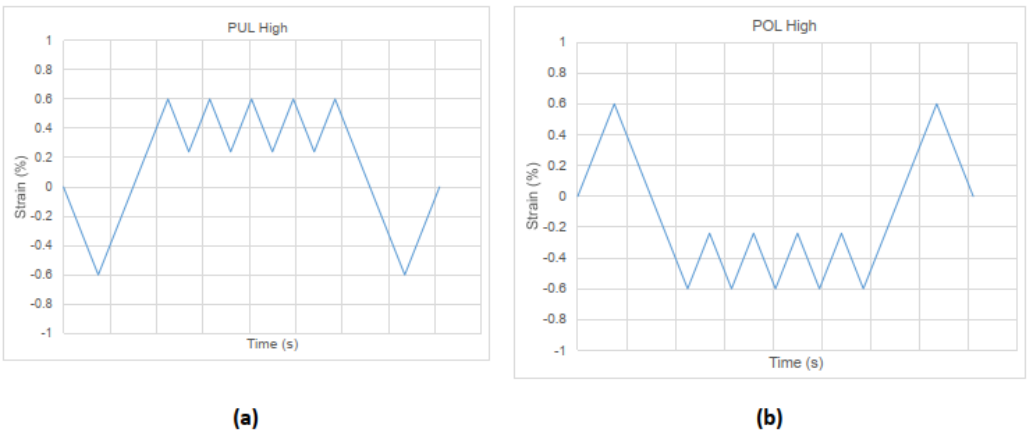

Figure 2.1. (a) PUL waveform and (b) POL waveform.

To fully test the hypothesis a series of tests were defined using the above waveforms with variations in temperature, environment, and baseline strain amplitude (between 'high' and 'low'). The matrix against the hypothesis is shown in Figure 2.2 with the testing logic included below:

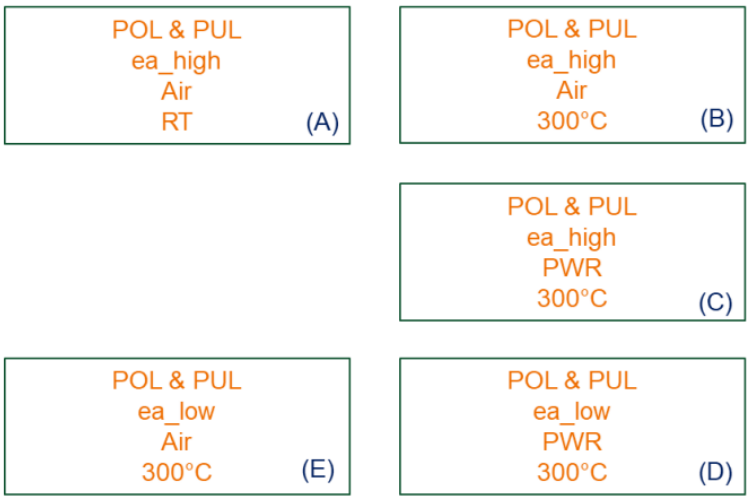

Figure 2.2. Schematic of logic for Phase I of the variable amplitude loading testing.

- Condition A is used to establish the VA behaviour in air and at room temperature, with "ea_high" being chosen to allow for significant mean stresses to persist throughout the loading block. According to Chopra et al. [2.1], it was anticipated that Condition A testing will show significant differences in the fatigue life between POL and PUL waveforms.
- Condition B is a repeat of Condition A but at an elevated temperature where the cyclic yield stress of the material will be lower. It was expected that this will would lead to less severe mean stresses and consequently a smaller difference in lifetimes under the POL and PUL waveforms. Condition B establishes the baseline air behaviour under VA loading for subsequent comparison to in-water testing.
- Condition C is a repeat of Condition B in a PWR water environment. These conditions will be used to develop the understanding of how a water environment might affect VA loading, whether there are any differences in environmental effects between POL and PUL waveforms, and whether the F_{en} methodology is suitable for this type of loading. As

in Condition B, it is expected that any differences in life between POL and PUL will be significantly smaller than in Condition A due to the more rapid shakedown of mean stresses.

- Condition D is a repeat of Condition C but using a lower strain amplitude for the baseline cycling to encourage the development of mean stresses throughout the loading block, even at this elevated temperature. This condition is used to provide further data on environmental effects under VA loading.
- Condition E represents a repeat of Condition D in an air environment, where mean stresses are expected to persist throughout a significant part of the loading block. This condition allows for a direct comparison with the environmental test under Condition D.

2.1.2 IN PWR ENVIRONMENTS, THE EFFECTS OF HARDENING ON FATIGUE LIFE SHOULD NOT BE TREATED AS ADDITIONAL TO EFFECTS OF ENVIRONMENT

In addition to mean stress, it is known that material hardening behaviour can affect fatigue lives [2.2,2.3]. A hardened material will have reduced levels of plastic strain compared to unhardened material for a given strain amplitude. However, reduced levels of plastic strain mean that the material can support higher levels of mean stress and stress amplitudes versus unhardened material. It is predicted, based on the observations reported in Fissolo et al. [2.3] that most of the effect from hardening would be on nucleation life and would not combine multiplicatively with the effects of environment, and would instead be dominated by the worse of the two effects, provided the effects of mean stress are negligible or suitably accounted for.

To assess these effects, a waveform was specified that would maximise hardening with negligible persistent mean stress according to ASME BPVC methods. This was predicted to be achievable using high over and underload cycles, set to a practical bound of the ASME BPVC, between blocks of baselines. By including similar baseline strain amplitudes to those in the POL/PUL tests described above it would be possible to obtain direct comparisons in lives between the tests with and without both significant hardening and mean stress. Therefore, a Periodic Over and Under Load (POUL) waveform was introduced in the testing with zero mean strain as shown schematically in Figure 2.3.

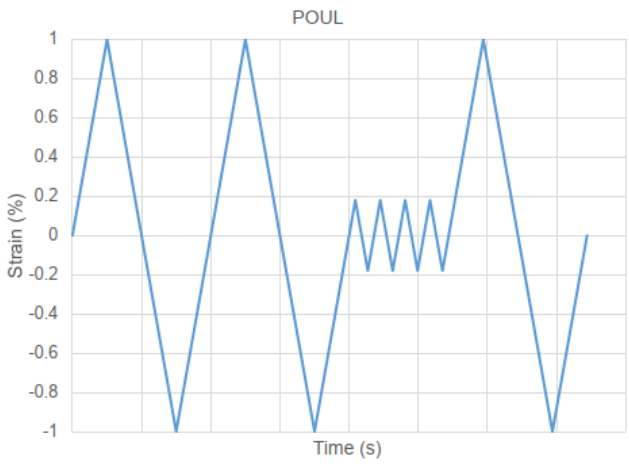

Figure 2.3. Representative POUL waveform.

2.1.2.1 THE LOWER STRAIN THRESHOLD FOR F_{EN} TO TAKE EFFECT IS GOVERNED BY PLASTIC STRAIN AND THEREFORE AFFECTED BY LOADING HISTORY

In addition to the above hypotheses defined above, observations from the initial tests, and data from other programmes, led to developments for Phase II. One observation was the possibility that environmental effects are potentially reduced or removed at higher strain amplitudes than the 0.1% threshold used in NUREG/CR-6909, Rev.1 [2.1], whereby increased hardening may alter the threshold at which F_{en} is applied due to a decrease in plastic strain reducing oxide layer breakage. This has led to the development of new POUL waveforms with either lower overload and underload or higher baseline strains to assess the effects of plastic strain amplitude on F_{en}. Accompanying this are Initial Over and Under Load (IOUL) tests, which assess if moving the over and under load cycles to the start of the tests shows an increase in F_{en} compared to the standard POUL through softening increasing plasticity as the test progresses.

All the above hypotheses were incorporated into tests as described above, namely POL, PUL, POUL, IOUL, and IHL/IHL-S (Initial-High-Low) tests, and were commissioned in both the first and second phases of the uniaxial testing programme. IHL/IHL-S and the tests aimed at Hypothesis 3 (Section 2.2.6) were introduced in Phase II and were carried out alongside repeats of the Phase I tests. All testing has been supported by fully reversed single strain amplitude tests to confirm the INCEFA-SCALE material's reference behaviour.

2.1.3 DESIGN GUIDANCE METHODS PROVIDE SUITABLE PROTECTION AGAINST SUB-ENDURANCE LIMIT SHORT CRACK GROWTH UNDER VARIABLE AMPLITUDE LOADING

A side effect of the adjustment factor on stress/strain is to effectively reduce the fatigue limit by the value of that factor. This offers protection against loading histories that could initiate a small fatigue crack with larger strain amplitudes that could then be grown to failure under subendurance limit cycling. As a reduction in the stress/strain factor would result in more transients not being counted, it is important to demonstrate that they would not otherwise contribute to this failure mode and result in a non-conservative position. This situation is an important consideration for assessing the appropriateness of the loading history subfactor and justifying any change to it. To achieve this understanding the Initial-High-Low and IHL-S waveforms was designed as shown schematically in Figure 2.4 and Figure 2.5.

The start of this waveform has large strain amplitudes designed to initiate a short defect. The amount of cycles here is based on the R5 [2.4] non-linear damage accumulation model which separates a fatigue life into the initiation and growth stages. The initial phase includes a specified number of cycles at a larger strain which, when considering the effects of environment, will nucleate a crack predicted to be 300 µm in length. The test then proceeds with 1000000 cycles at a baseline strain amplitude of 0.07%, which is predicted to have no effect on the subsequent life of the specimen-no crack growth is predicted. The value of 0.07% has been chosen as it is the NUREG/CR-6909, Rev.1 threshold limit of the specimen divided by 1.6, so would fall within the design curve with the proposed new factor on stress. This will support the challenge to the factor of 2 on stress as it is particularly concerned with the loading regime where the factor is influential. The subsequent life will be determined by testing to failure at a moderate strain amplitude. The IHL-S test which omits the 1000000 cycles allows direct comparison between the

lives of the specimens to determine the damage incurred by the baseline cycles. Tests in air and PWR conditions have been performed.

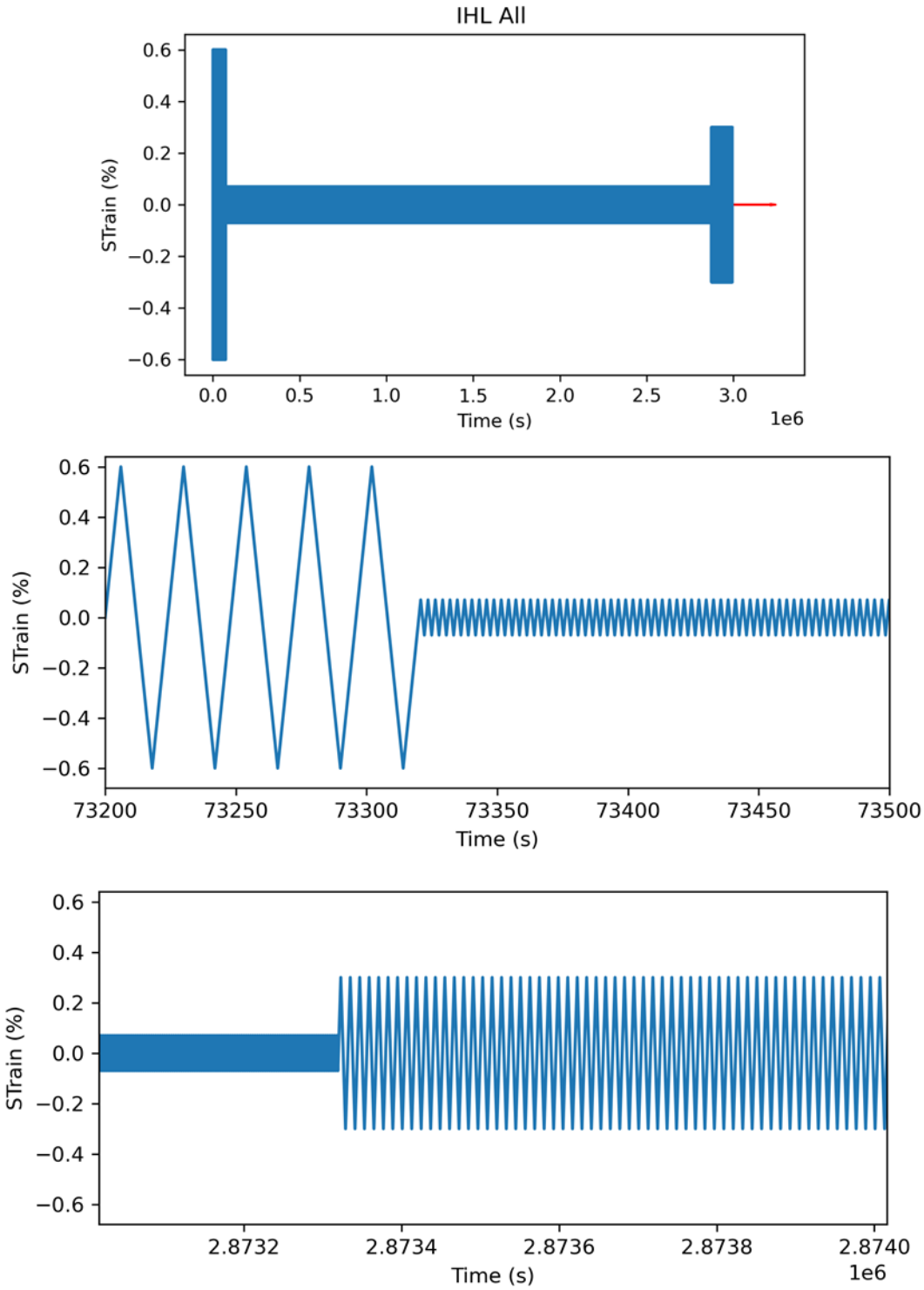

Figure 2.4. Representative IHL waveform (top), transition from 0.6% strain amplitude cycles to the 0.07% baseline (middle), and from 0.07% baseline cycles into the 0.3% final cycling to facilitate a test end withing the bounds of reasonable laboratory capability.

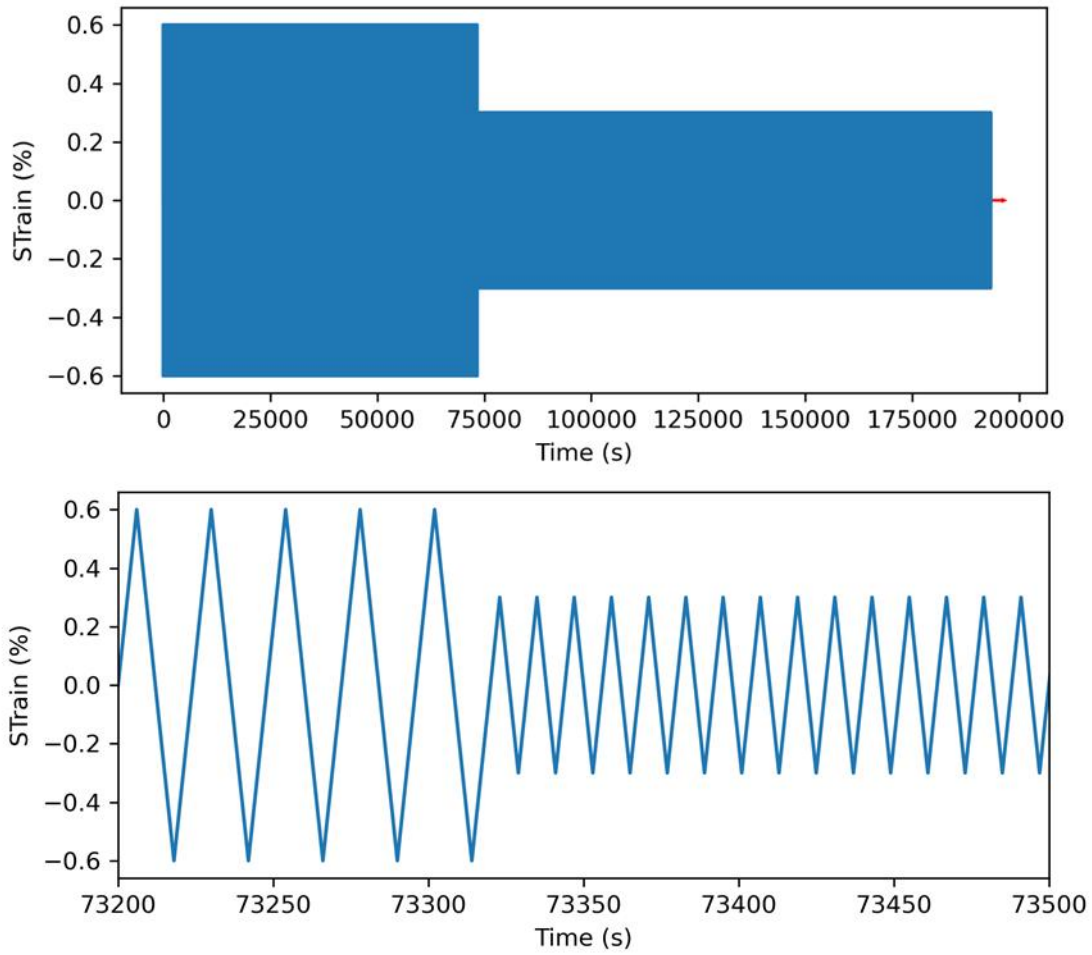

Figure 2.5. Representative IHL-S waveform (top), and transition from 0.6% strain amplitude cycles to the 0.3%.

2.1.4 IN PWR ENVIRONMENTS, NEGATIVE EFFECTS FROM HARDENING, ENVIRONMENT AND SURFACE ROUGHNESS ARE NOT MULTIPLICATIVE

INCEFA-PLUS and other international work showed that surface finish and environment are not independent and the associated subfactors on life should not be simply multiplied, with only the larger of the two effects (subfactors) contributing to the overall factor on life. The assumption is that the effect of environment on nucleation life (and hence on the factor on pseudo-stress/strain) is governed by the most onerous of hardening, environment, or surface roughness effects.

To assess this and support the INCEFA-PLUS findings [2.5], several specimens with surface finishes other than the standard polished roughness have been included in testing to allow direct comparison between the two.

2.2 RESULTS AND DISCUSSION

2.2.1 REFERENCE DATA

Low cycle fatigue of metals, such as stainless steel, is best characterised by plastic strain. However, the generation and analysis of LCF test data typically uses total strain control, using extensometry, because extraction of plastic strain from hysteresis loops can become cumbersome and unsuitable for experimental control. Total strain is comprised of elastic and plastic strain where the plastic contribution becomes increasingly dominant as total strain increases beyond the yield of the material. This means that material variability is a significant consideration in the analysis of fatigue endurance data as it can influence as the ratio of elastic to plastic strain and stress response for a given total strain as well as the material fatigue limit. Therefore, it is important to determine the baseline material properties done under standard test conditions prior to investigating more complex fatigue behaviour.

As this programme investigates variable amplitude loading and its influence on fatigue life of stainless steels, the “memory” effect of this material needs to be considered, whereby the past loading history of the material influences subsequent behaviour [2.3]. This, in theory, should be understandable by accounting for hardening, mean stress effects, and the influence of a crack on the threshold for crack growth during VA loading in addition to the underlying fatigue behaviour of the pristine material.

To produce adequate reference data that allows a reasonable description of the base fatigue properties to be evaluated, several experiments over a range of conditions were conducted. These experiments used fully reversed loading with strain amplitudes between 0.15% and 1.0% in air and simulated PWR primary coolant environments, which were relevant for the more complex testing.

Furthermore, the reference data can indicate any issues with aspects such as making comparisons across geometries and providing confidence that this material has similar behaviour to the INCEFA-PLUS common material with respect to surface finish.

The model selected to provide the fit to the reference data is the model reported by Currie et al. [2.6] and Asada et al. [2.7], which follows the shape of the original Langer curve. This model incorporates ultimate tensile strength into the determination of the model coefficients allowing aspects such as the temperature dependence on the shape of the curve to be accounted for. It provides a superior best-fit description of the fatigue behaviour of the material when dealing with datasets that have temperature as a variable compared to the model reported in NUREG/CR-6909, Rev.1 [2.8]. The material specific best-fit curve using the INCEFA-SCALE common material properties produces a reasonable fit to the polished reference data (Figure 2.6). The parameters were optimised using maximum likelihood estimation.

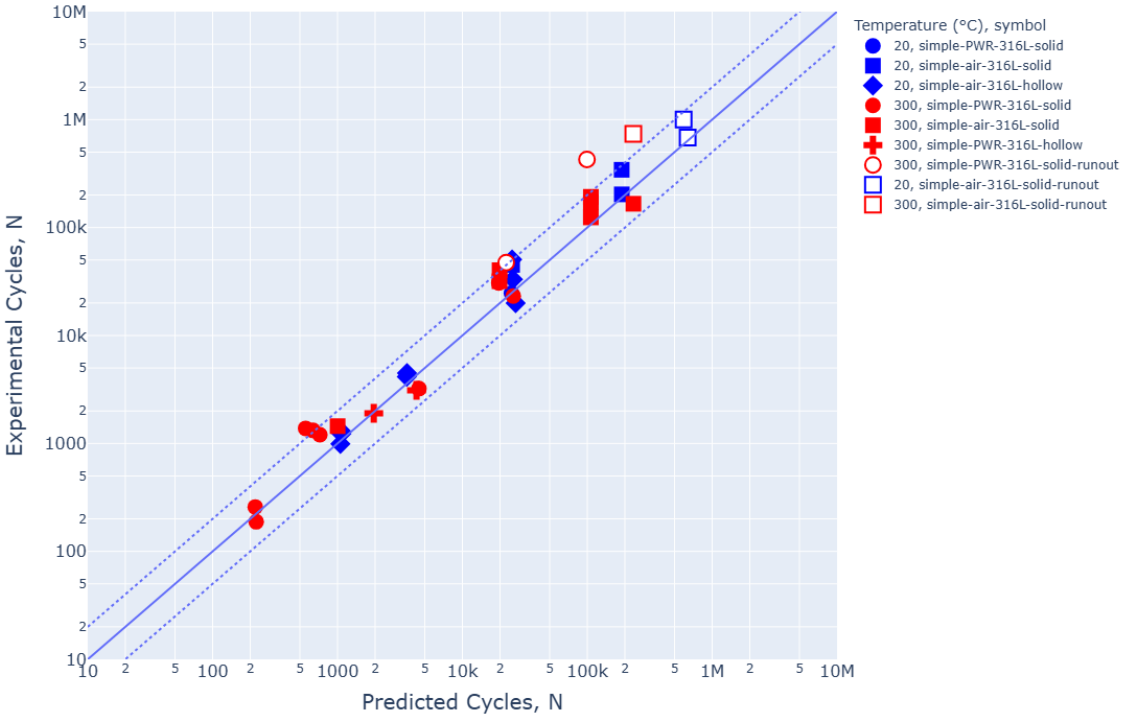

Figure 2.6. INCEFA-SCALE 316L using a material specific best-fit curve, defined in Currie et al. [2.6], based on the common material.

INCEFA-SCALE consists of test performed on hollow and solid specimens. In the past there has been a debate on how these two geometries can be compared within a single dataset [2.9]. To facilitate fair comparison between hollow specimen geometries, which do not all have 3 mm wall thicknesses, the method described by Hale et al. [2.10] and used in R5 [2.11] to adjust fatigue curves to a desired depth (N_0 using eq. 2.1 to eq. 2.7) [2.12,2.13]. Considering that the limited unpressurised (20 °C air data) appears to be well predicted by the model it indicates that the correction to bring the hollow and solid specimens into agreement may be temperature and pressure dependent. Because of this complexity, the reference data fit for INCEFA-SCALE was derived from data from solid specimens only. The investigation of hollow specimens and comparability to solid specimens within a single analysis is explored further in Chapter 3.

$$\ln(N_i) = \ln(N_l) - 8.06N_l^{-0.28} \quad \text{eq. 2.1}$$

$$N_g = N_l - N_i \quad \text{eq. 2.2}$$

$$N_g' = M \cdot N_g \quad \text{eq. 2.3}$$

$$D = a_{min} ln\left(\frac{a_l}{a_{min}}\right) + (a_{min} - a_i) \qquad \text{eq. 2.4}$$

$$M = \frac{a_{min} \ln\left(\frac{a_0}{a_{min}}\right) + (a_{min} - a_i)}{D} \quad \text{for } a_0 \geq a_{min} \qquad \text{eq. 2.5}$$

$$M = \frac{a_0 - a_{min}}{D} \quad \text{for } a_0 < a_{min} \qquad \text{eq. 2.6}$$

$$N_0 = N_i - N_g' \qquad \text{eq. 2.7}$$

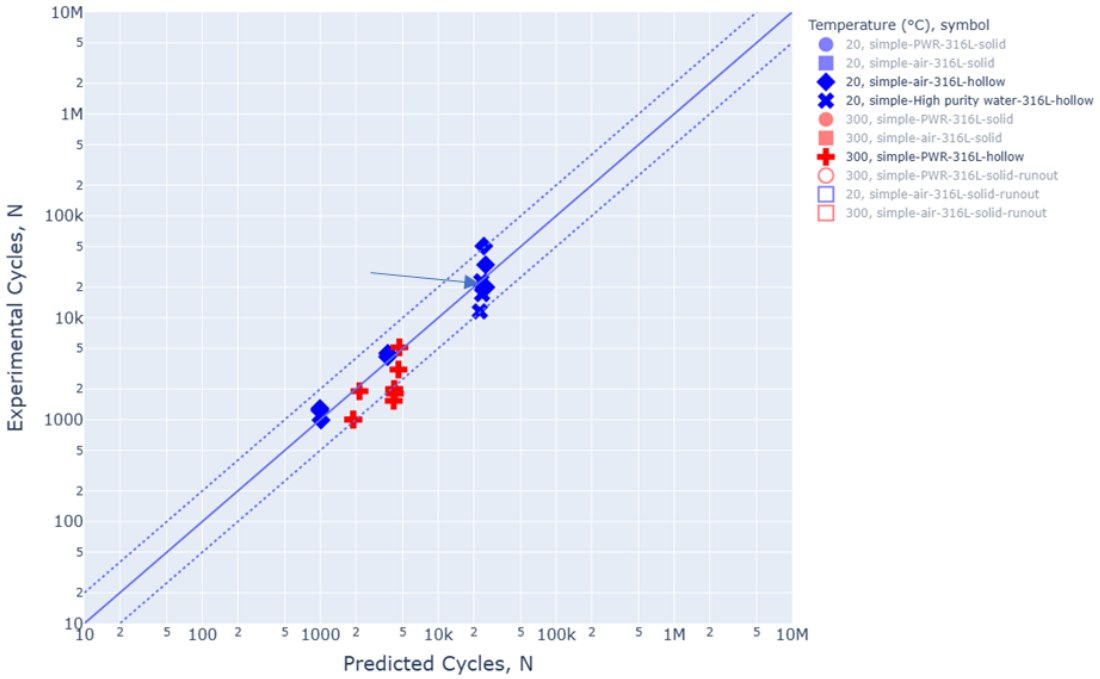

Figure 2.7. INCEFA-SCALE 316L assessed using a material specific best-fit curve, defined in Currie et al. [2.6], based on the common material. All 300 °C hollow specimen tests are pressurised and the high purity water tests were also pressurised except for the datapoint indicated by the arrow.

2.2.2 BEST ESTIMATE MODEL FOR VARIABLE AMPLITUDE DATA

Producing a best estimate model capable of analysing variable amplitude requires accounting for mean stress and the effect of a crack being initiated on the fatigue limit for subsequent cycles. Mean stress effects on the variable amplitude testing will be the most significant of these two effects.

The best estimate models used in the analysis of the INCEFA-SCALE data use the strain-based Smith-Watson-Topper (SWT) mean stress method. To account for the influence of a crack on the fatigue limit of the material during VA loading, the R5 method described in the previous section [2.4] is used to split the prediction of life into the life required to obtain a 200 µm crack using the model described in the reference data that has a fatigue limit. The prediction is then completed by calculating the number of cycles to grow the crack from 200 µm to 3 mm by using a model that has the fatigue limit removed and describes the slope of the data above 0.2% strain

amplitude. This is a simplification of the approach used by Kitigawa to describe the reduction of a fatigue limit due to the presence of a crack [2.14].

The impact on fatigue life of the presence of a crack during VA loading is biased towards lower strain amplitudes. Particularly tests with cycling at or around the fatigue limit. There are relatively few tests of this kind in INCEFA-SCALE, but this is important for evaluating the presence of a threshold for environmental effects such as the one described in NUREG/CR-6909, Rev.1 at 0.1% strain amplitude. Below this threshold the environmental effect was considered insignificant. It should be noted that the intended use of the threshold as described in NUREG/CR-6909, Rev.1 was that it should be applied not to the mean curve, but only with the design curves themselves. Considering the low strain amplitude value of this threshold, any unaccounted-for variable amplitude effects in this region would interfere with any conclusions regarding this threshold. Therefore, it is necessary to account for these variable amplitude effects to make the most out of the research data produced in this programme.

2.2.3 HYPOTHESIS 1: THE NEGATIVE EFFECTS OF MEAN STRESS ON FATIGUE ARE CONSERVATIVELY ACCOUNTED FOR IN CURRENT DESIGN CODES

As discussed in the Chapter 1, Currie et al. [2.6] highlighted the error in how Langer [2.15] applied the mean stress correction using pseudo stress and that this issue affects both the ASME mean stress correction and the SWT method described by Asada et al. [2.7]. The data produced in INCEFA-SCALE, with values taken from stabilized loops, illustrates the issue of the current assessment methods not applying the mean stress correction over a wide enough stress amplitude range as once converted to pseudo stress the data shows the presence of significant mean stresses persisting outside of the yield line used in ASME Section III (Figure 2.8). For these cases the mean stress correction would not be applied to the test result when it should be. This non-conservatism is offset by the application of conservative adjustment factors of 2 on stress/strain and 12 on cycles which contain a loading history subfactor so that the data is conservatively bound by the ASME design curves (Figure 2.9). However, substantial effort is being made globally to reduce these adjustment factors and provide more robust technical justification for the values they are set at. If benefit is to be gained from that work, it is argued that the mean stress must be treated differently using methods such as those described by Currie et al. [2.6] by calculating mean stress effects including plasticity considerations, in the detailed method, or by viewing the mean stress correction as a factor to apply to the endurance limit as in the simplified method. The effect of treating mean stress without converting from pseudo stress is illustrated in the Haigh diagram in Figure 2.10 where it is clear that the mean stress correction would be triggered for all datapoints using the hardened yield proposed by Currie et al. [2.6].

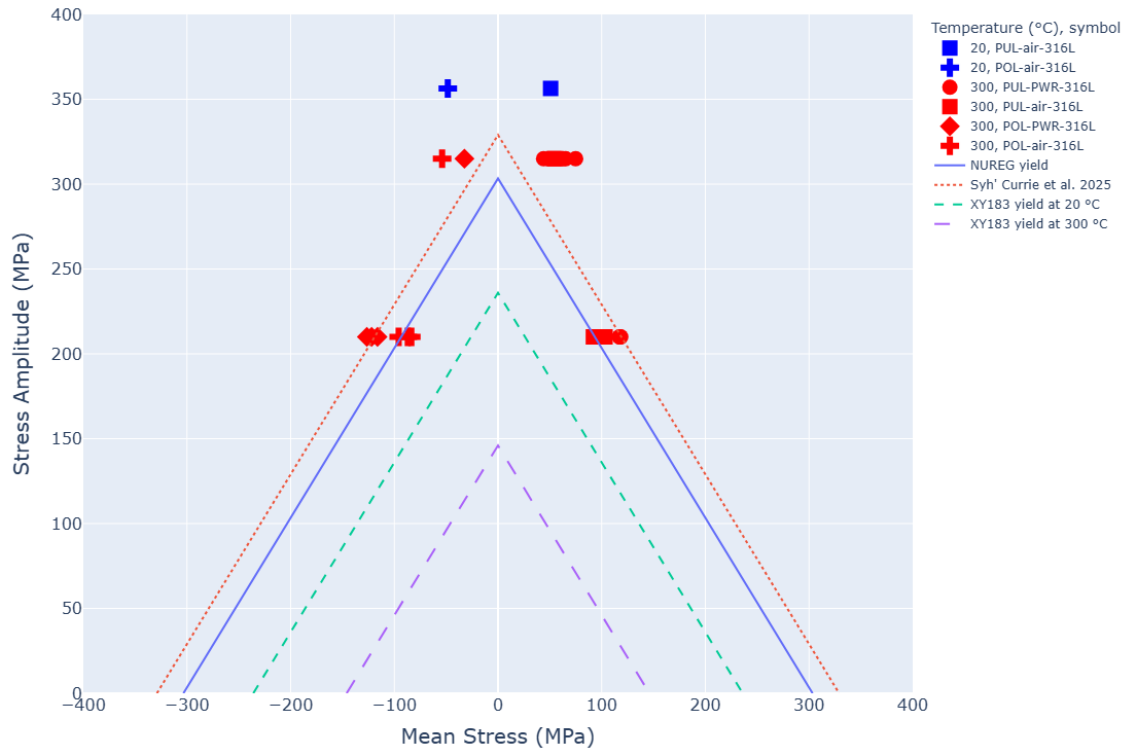

Figure 2.8. Haigh diagram stress amplitudes and mean stress magnitudes for the INCEFA-SCALE common material.

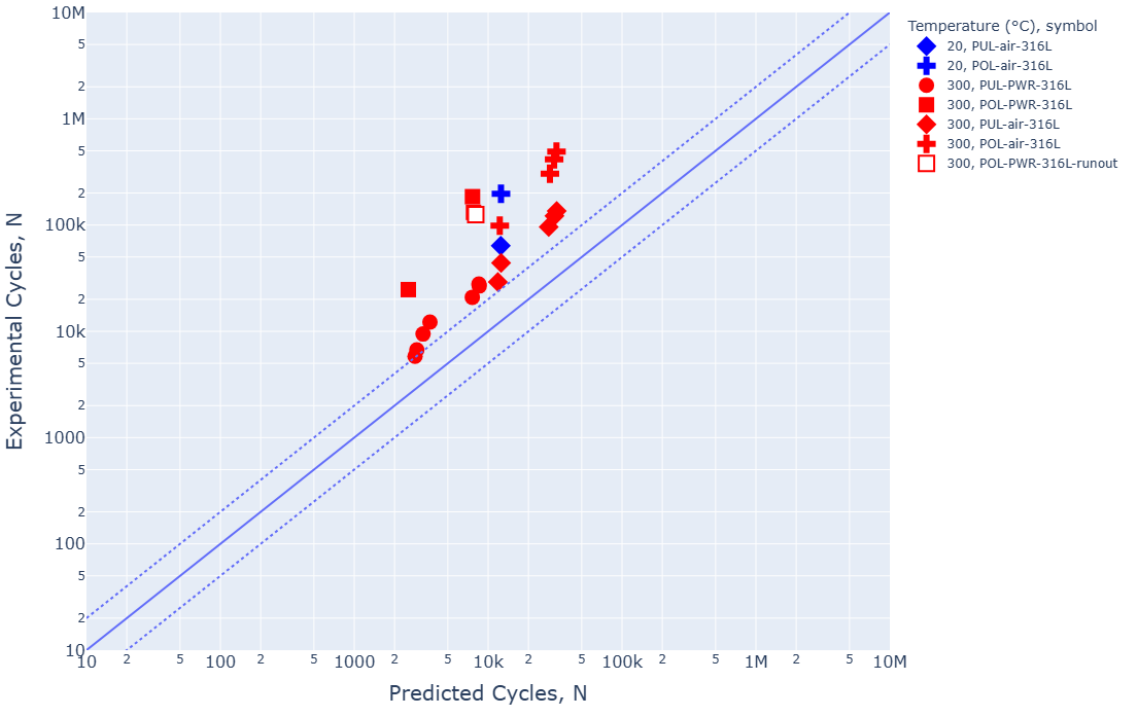

Figure 2.9. INCEFA-SCALE common material POL and PUL tests assessed using the method described in NUREG/CR-6909, Rev.1 with adjustment factors of 2 on stress/strain and 12 on cycles.

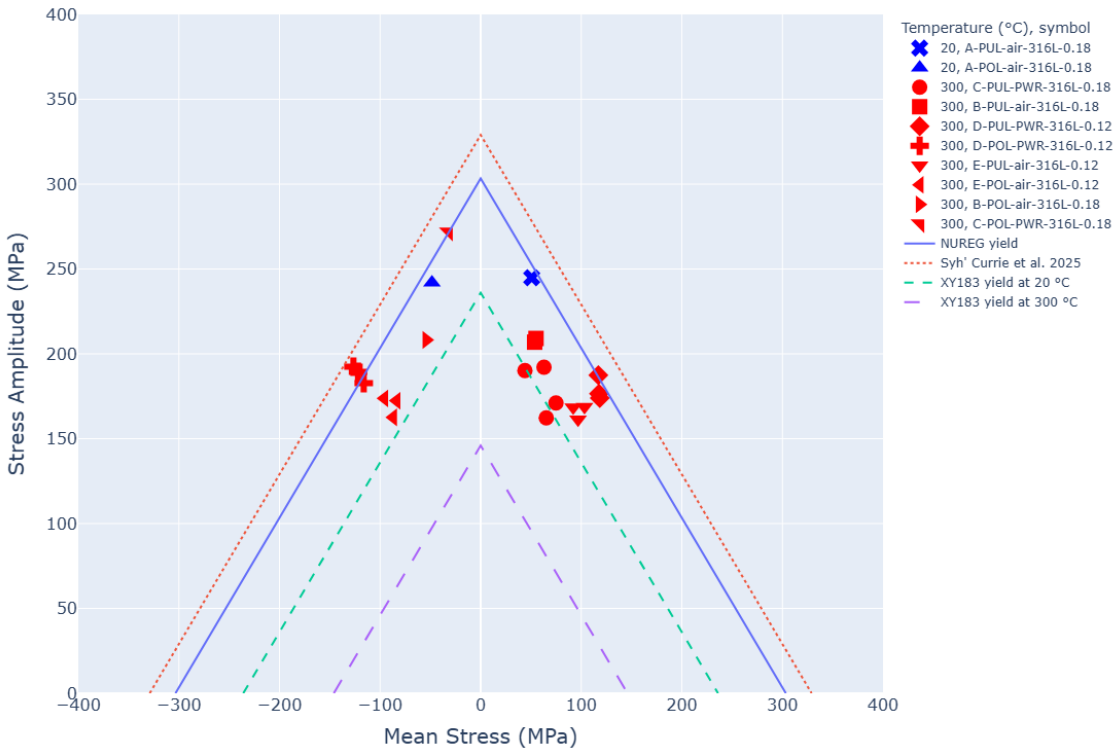

Figure 2.10. Haigh diagram showing experimentally observed in test stress amplitudes and mean stress magnitudes for the INCEFA-SCALE common material. The symbol is assigned based on a construction of subhypothesis, waveform, environment, material, and baseline strain amplitude.

In summary, the effects of mean stress for the tests conducted in INCEFA-SCALE are not conservatively accounted for in current design methods due to the use of pseudo stress amplitude combined with a yield that is not converted to pseudo stress. As well as the assumption of linearity between stress and strain from stainless steel materials. However, as demonstrated above, the fatigue design curves produce a conservative position through the application of the adjustment factors of 2 and 12. Without addressing the mean stress issue, reducing the adjustment factors will begin to reflect this non-conservatism.

2.2.4 HYPOTHESIS 1.1: THE NEGATIVE EFFECTS OF MEAN STRESS ON FATIGUE ARE RELATIVELY LESS DAMAGING AT HIGHER TEMPERATURES

The sets of Periodic Underloads and Periodic Overloads were designed so that each laboratory would be assigned these tests in pairs. This was specifically done to avoid lab-to-lab variation confounding with the comparison of the data generated from these tests. Conclusions could be drawn from comparing each POL and PUL pair from within a laboratory and would not be dependent on absolute values which are more influenced by lab-to-lab variation.

Figure 2.11 shows that the impact of the PUL vs. POL waveforms on fatigue life is less at higher temperatures (subhypothesis A vs. B see Figure 2.2). Comparing B and E in Figure 2.10 indicates that lower strain amplitudes can support larger mean stresses than larger strain amplitudes, which is logical as higher levels of plasticity would result in more shakedown. Figure 2.11 shows that the effect on life is larger for the POL/PUL pairs with a baseline strain amplitude of 0.12% which can be attributed to larger magnitude of mean stresses supportable by this loading pattern compared to the pattern used for B.

The influence of environment and mean stress can be visualised by comparing subhypotheses B vs. C and D vs. E (see Figure 2.2). However, there are pairs of finite datapoints available for condition C preventing a comparison between B and C on this basis. Comparing D and E, the difference in the ratio of life between POL and PUL is much greater for subhypothesis D than E. The tests in PWR conditions show a 30 to 40 MPa higher mean stress magnitude than the corresponding air tests based on taking values from half-life cycles during the test. Considering that PWR tests are much shorter than air tests under similar conditions due to environmental effects this gives the mean stresses less time to shake down and may have a larger influence on life than in the air tests. To produce a fair comparison the mean stress and stress values were also taken from earlier in the life of the air tests to correspond to a similar point in the PWR tests. This produced higher mean stresses and stress amplitudes for the air tests but were still less than those of the PWR tests. The mean stress of the air tests was approximately 25-30 MPa lower than the PWR equivalent. The reason behind such a difference in observed stresses is due to strain rate effects [2.16] which have been demonstrated to increase the stress amplitude of stainless steel in the temperature and strain rate range used for the INCEFA-SCALE PWR tests. The PWR tests were a mix of shoulder control with solid specimens and gauge control with hollow specimens which lowers the likelihood of it being a result of test type or geometry. Further data is required to fully evaluate the tests on this basis as the finite POL/PUL pairs for subhypothesis A, B, C, D, and E are 2, 1, 0, 1, and 1 respectively. Unfortunately, this level of data leaves analysis of the data in this manner vulnerable to laboratory variation and data scatter.

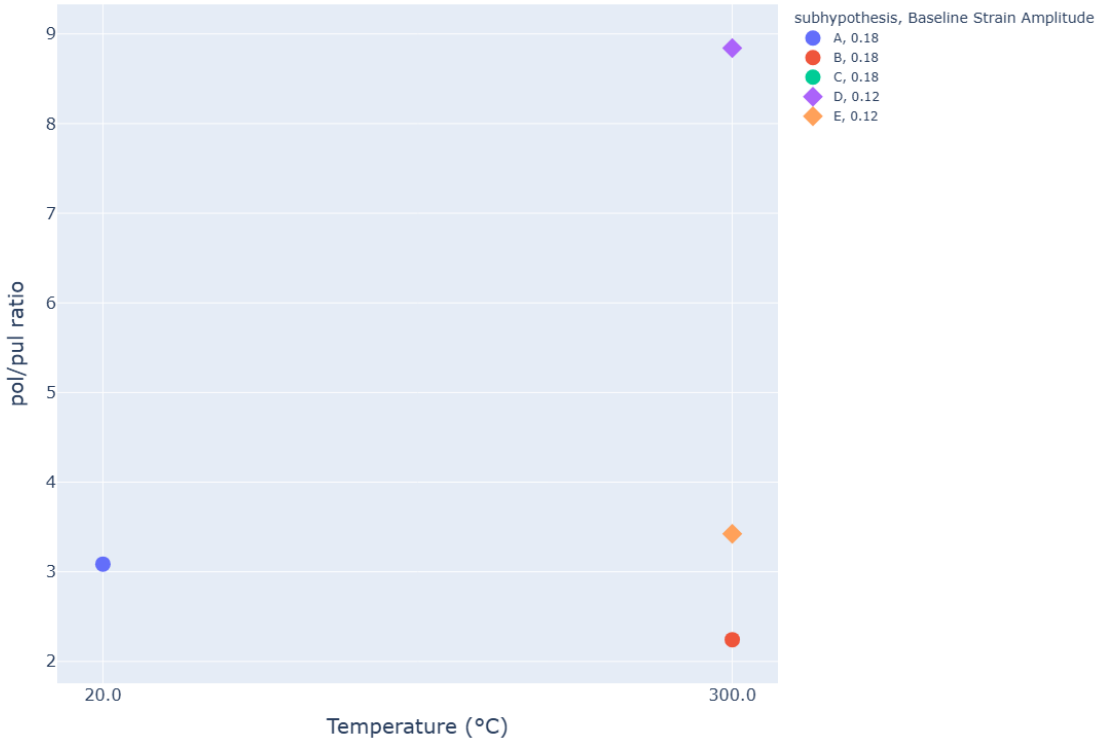

Figure 2.11. Ratio of POL and PUL experimental fatigue life vs. temperature by subhypothesis.

Using the best estimate approach detailed in Section 2.2.1 and Section 2.2.2 approach to describe the POL and PUL tests produces a reasonable fit to the finite data (Figure 2.12) vs. a fit using only mean stress correction and the Langer curve (Figure 2.13). The POL air data at high fatigue lives falling consistenly below the 1 to 1 line indicating that the parameters of the Langer

model may not be optimal for these cases. Which is possible as it was not reasonable to produce a full reference curve covering the full scope strain amplitudes near the fatigue limit as well as fully defining the shape of the curve in the transition from Low Cycle Fatigue (LCF) to High Cycle Fatigue (HCF, starting from 0.2% strain amplitude). This means that for tests with strain amplitudes in this region the Langer model may not describe the behaviour adequately. This is a reasonable observation as the data that is away from this region (above 0.2% and below 0.12%, see Section 2.2.5) is better described by the model. A possible way to explore this on a best-fit basis would be to produce individual bi-linear fits, for LCF and HCF, with a fit for each temperature. This would then remove any interference from the Langer curve not fitting data in the transition between LCF and HCF well and by temperature.

An analysis using a Coffin-Manson fit with the strain based SWT correction was also performed and achieved a better fit for these data (Figure 2.13). However, the reason this best estimate model was not more widely used in this analysis is because for other data it performed markedly worse than the one described at the start of this Section. This is because for the model used by Asada et al. there are constraints on the parameter optimisation that involve UTS and there are fewer steps in the parameter optimisation when compared to the fit in Figure 2.13. Unfortunately, the small amount of data below 0.2% strain impacts the ability to fit the HCF regime adequately. But, the analysis of the data using this fit highlights that the lower quality of fit to the data in this region can be resolved by increasing the amount of data in transition region or selection of a different model.

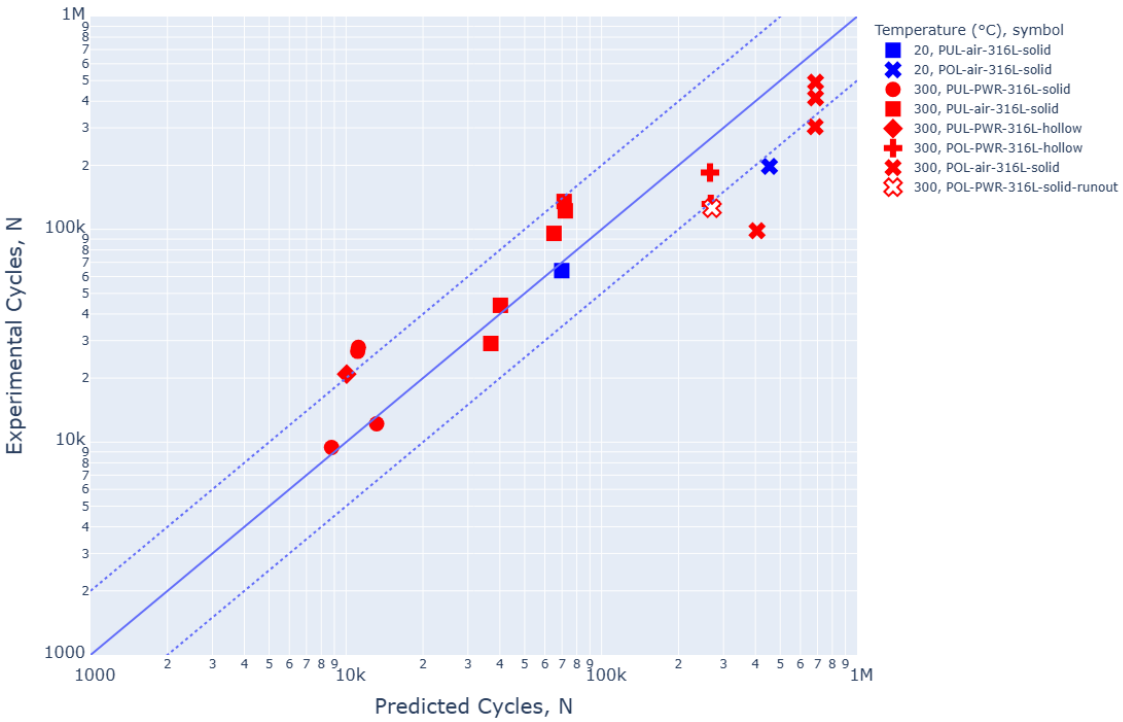

Figure 2.12. INCEFA-SCALE common material POL and PUL tests assessed using a material specific best-fit combined with the simplified Kitigawa approach [2.14] for accounting for the influence of a crack on the fatigue limit during VA tests.

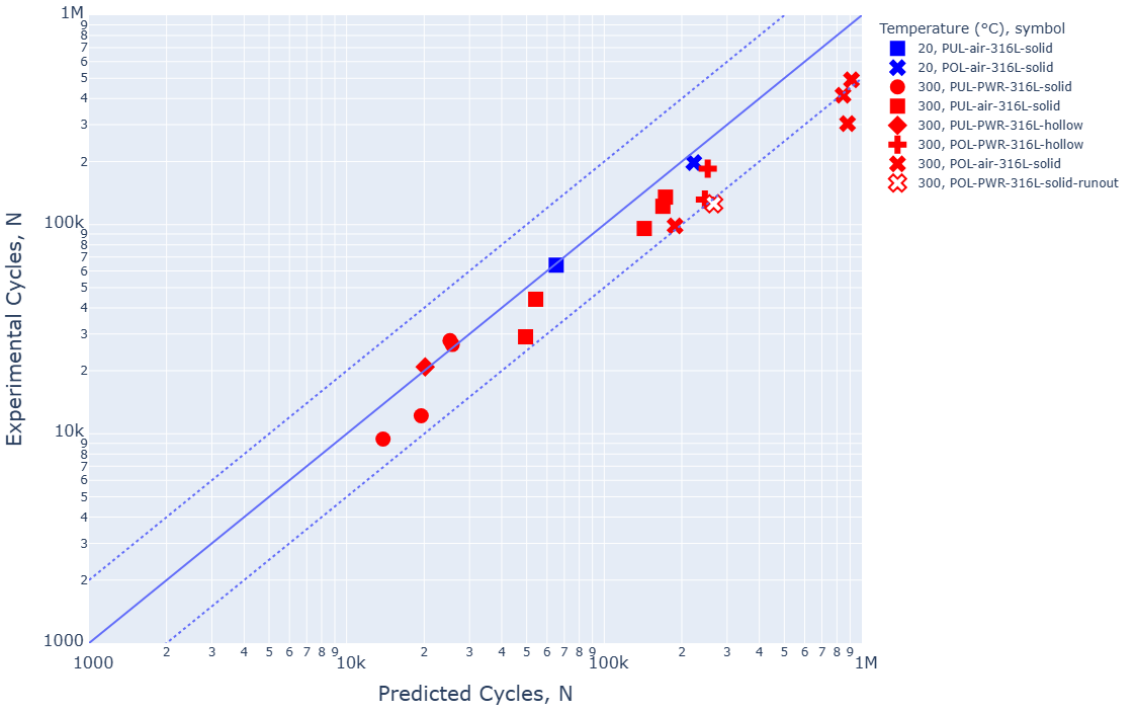

Figure 2.13. INCEFA-SCALE common material POL and PUL tests assessed using a material specific best-fit done using a Coffin-Manson strain based SWT analysis combined with the simplified Kitigawa approach [2.14] for accounting for the influence of a crack on the fatigue limit during VA tests.

2.2.5 HYPOTHESIS 2: IN PWR ENVIRONMENTS, THE EFFECTS OF HARDENING ON FATIGUE LIFE SHOULD NOT BE TREATED AS ADDITIONAL TO EFFECTS OF ENVIRONMENT

The POUL waveforms were designed to emphasise material hardening while minimising mean stress contributions. The initial POUL waveform consisted of two 1% strain amplitude cycles and a thousand 0.18% strain amplitude cycles in a repeating pattern. It was thought that the 0.18% cycles would have sufficient plasticity to cause reasonable shakedown of the mean stress produced from the 1% cycles, based on the original approach to mean stress described in the ASME BPVC. However, due to the issues with this approach, this was not the case, and the loading pattern was able to sustain mean stresses between ≈60 MPa and ≈80 MPa in the 0.18% strain amplitude cycles (Figure 2.14). Despite this, these tests are still useful as they provide insight into how the effects of material hardening and mean stress influence each other with respect to fatigue life.

Figure 2.15 indicates that the IOUL and POUL waveform 0.18% stain amplitude cycles have less plasticity than those of the constant amplitude tests at 300 °C. From the tests displayed, the POUL waveform baseline cycle shows the least plasticity. Neither the POUL nor IOUL baseline strain amplitudes cycle produces stress strain behaviour that fully shook down back to the corresponding constant amplitude reference tests. This indicates that the impact of preloading and repetitive overloading has a permanent effect on the material properties of these specimens.

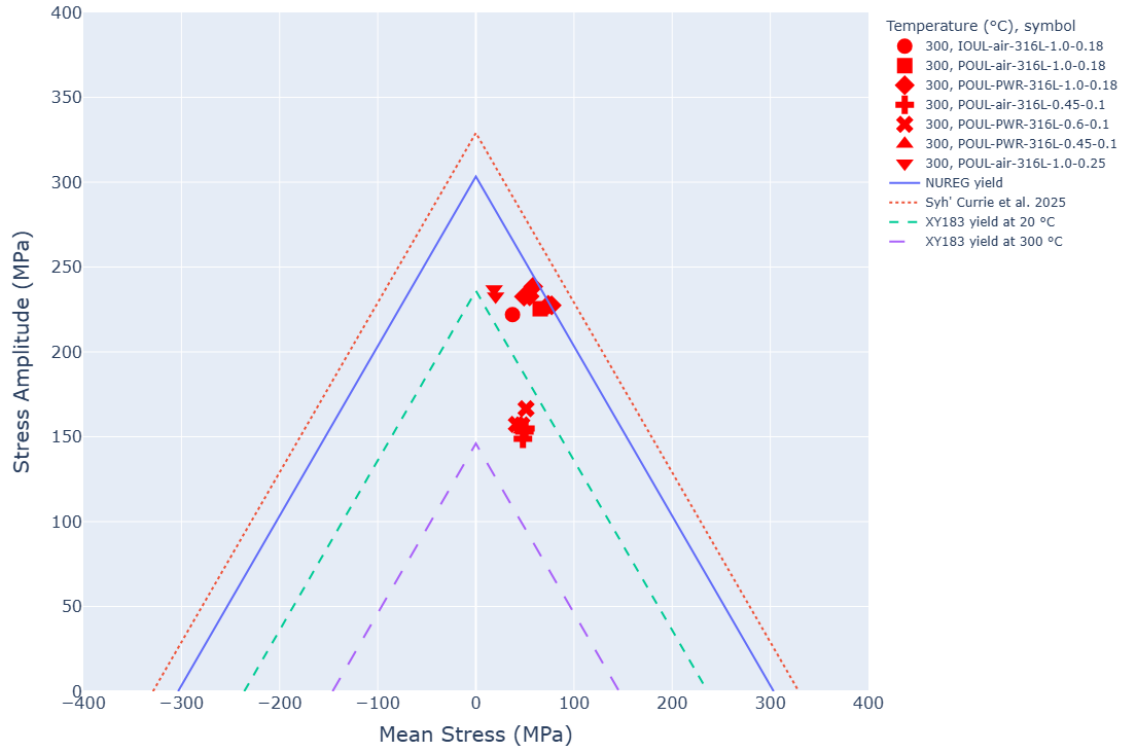

Figure 2.14. Haigh diagram showing experimentally observed in test stress amplitudes and mean stress magnitudes for the INCEFA SCALE common material for POUL loading pattern.

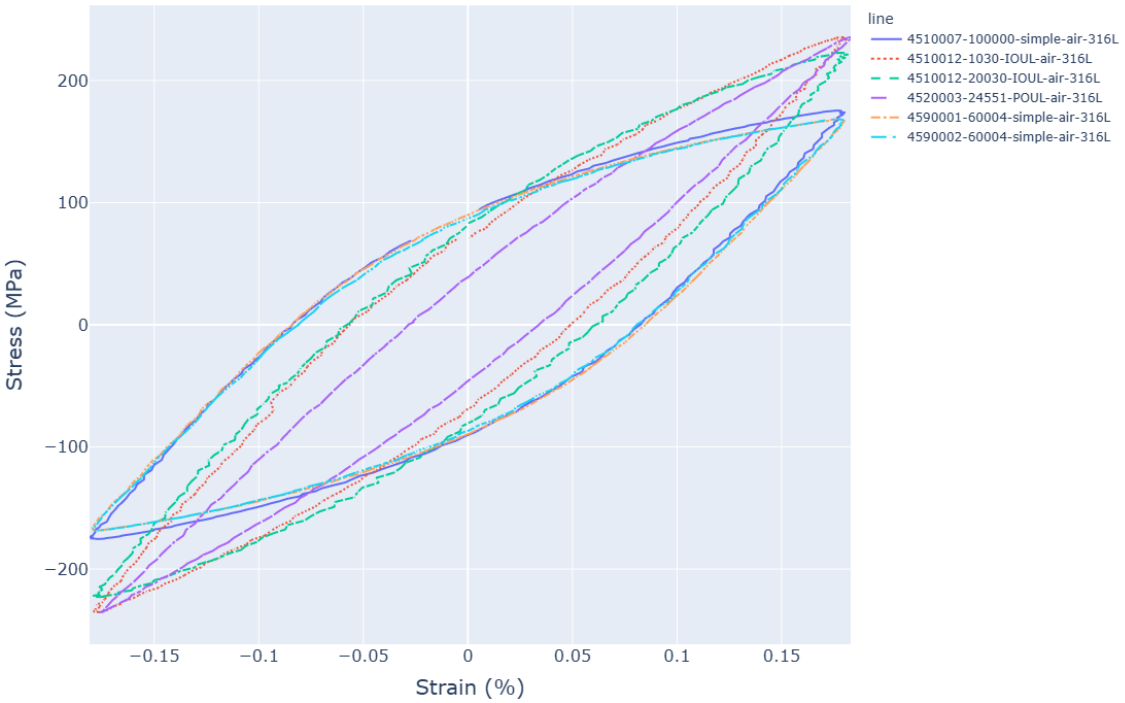

Figure 2.15. Hysteresis Loops for a cycle at near half-life with a strain amplitude 0.18% for 300 °C tests on the INCEFA-SCALE common material with a simple waveform, IOUL, or POUL. Three simple waveform tests are displayed to provide a guide to test-to-test variability under standard conditions. Mean stress has been subtracted from the hysteresis loops to provide a better comparison of the shapes from the different tests. The legend is TestID-cycle number-waveform-material.

To resolve the initial hypothesis, the POUL waveform was redesigned. Several options for relaxing the mean stress were considered, including ramping down the strain amplitude from the high value to the load in several stages. Ultimately, due to the experience of performing the variable amplitude tests the simpler option of reducing the high value (to 0.6% or 0.45%) or increasing the low value (0.18% to 0.25%) was selected. The POUL 1.0% - 0.25% air results indicate that raising the baseline strain amplitude is successful in minimising the magnitude of mean stress supported by the specimen during loading Figure 2.14.

Figure 2.16 shows that most POUL tests are reasonably well explained by the same method used to produce predictions for the VA tests in Hypothesis 1 and taking the stresses from the air tests at the same relative point in the specimen life as the PWR tests. There are two POUL PWR 1.0% - 0.18% tests that are outliers, these appear to have lower than expected stress amplitude and higher mean stresses that comparable tests. It is unknown why this is as the tests appear valid.

For the data in Figure 2.16 the F_{en} was set to be 1 for tests whose strain amplitude was less than or equal to 0.1%. By doing so the predictions of the POUL 0.45% - 0.1% PWR test are reasonably close to the corresponding air tests. For comparison, the data in Figure 2.17 have F_{en} calculated as per NUREG/CR-6909, Rev 1 and become outliers compared to the corresponding air tests. This gives indicates that the F_{en}-threshold proposed in NUREG/CR-6909, Rev.1 is applicable.

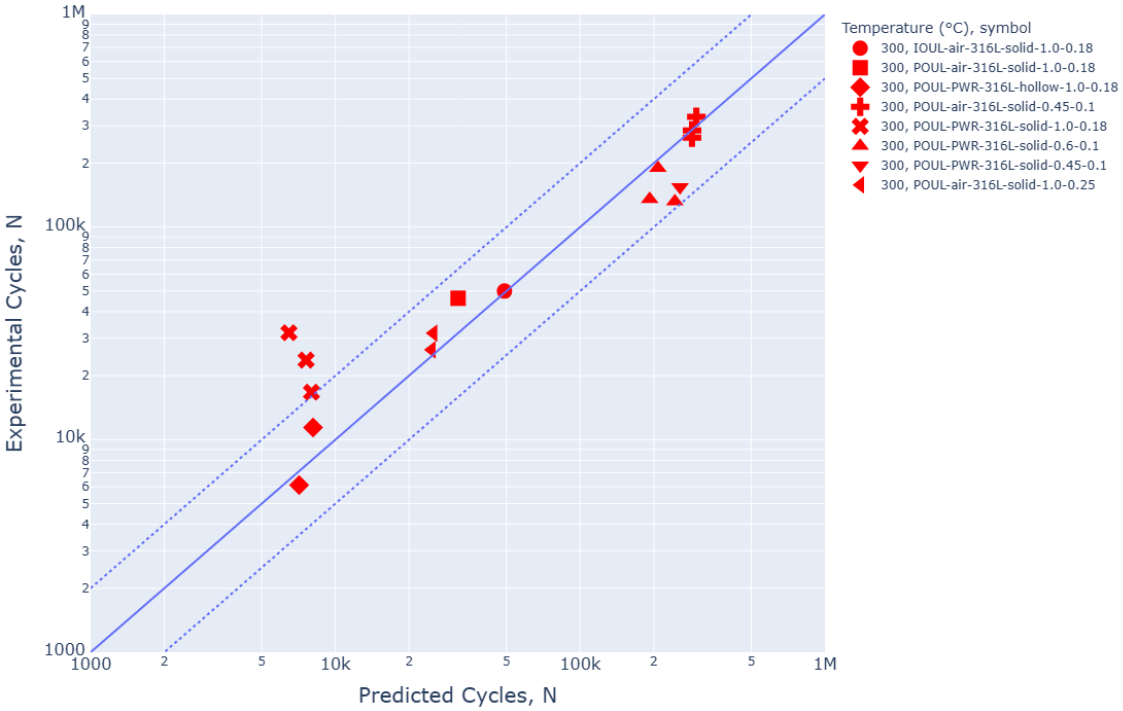

Figure 2.16. INCEFA-SCALE common material assessed using a material specific best-fit with F_{en} = 1 for strain amplitudes of 0.1% or below.

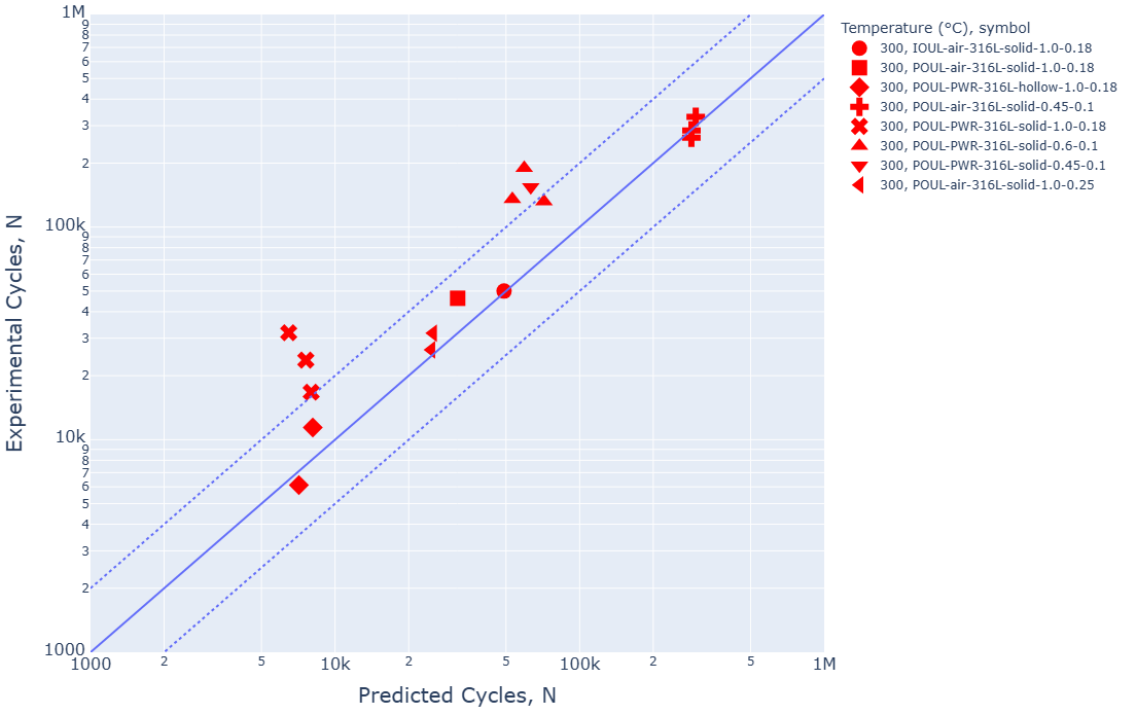

Figure 2.17. INCEFA-SCALE common material assessed using a material specific best-fit with F_{en} as calculated by NUREG/CR-6909, Rev.1 for strain amplitudes of 0.1% or below.

2.2.6 HYPOTHESIS 3: DESIGN GUIDANCE METHODS PROVIDE SUITABLE PROTECTION AGAINST SUB-ENDURANCE LIMIT SHORT CRACK GROWTH UNDER VARIABLE AMPLITUDE LOADING

As the nuclear industry attempts to redefine the adjustment factors for constructing design fatigue curves, it is important to explore edge cases that may challenge those new definitions. One such example is the initiation of a crack in a specimen with LCF cycling followed by cycling below the fatigue limit. As described by Kitigawa [2.14], the presence of a crack of suitable length causes a reduction in the crack growth threshold thereby increasing the damage of cycling done after the crack has been established. Therefore, the sub-endurance limit cycling may cause a failure of the specimen far sooner than is predicted or allowed for. As the adjustment factors applicable to the HCF regime affect the fatigue limit at which fatigue cycles start causing damage, it would cause non-conservatism if the sub-endurance limit cycling caused damage below the adjusted fatigue limit.

Unlike with the tests in Hypothesis 1 and 2, the baseline cycling here produces stress amplitudes near the elastic region of this material and within the boundary for applying the mean stress correction (Figure 2.18). This means that the issues identified previously, where the mean stress is not corrected and would be underestimated, is not applicable here. For the method described in NUREG/CR-6909, Rev.1 the modified Goodman mean stress method is active. Compared to other mean stress corrections this method is particularly conservative as it assumes the worst case mean stress. This results in a substantial amount of protection against this type of loading when applying this method (Figure 2.19).

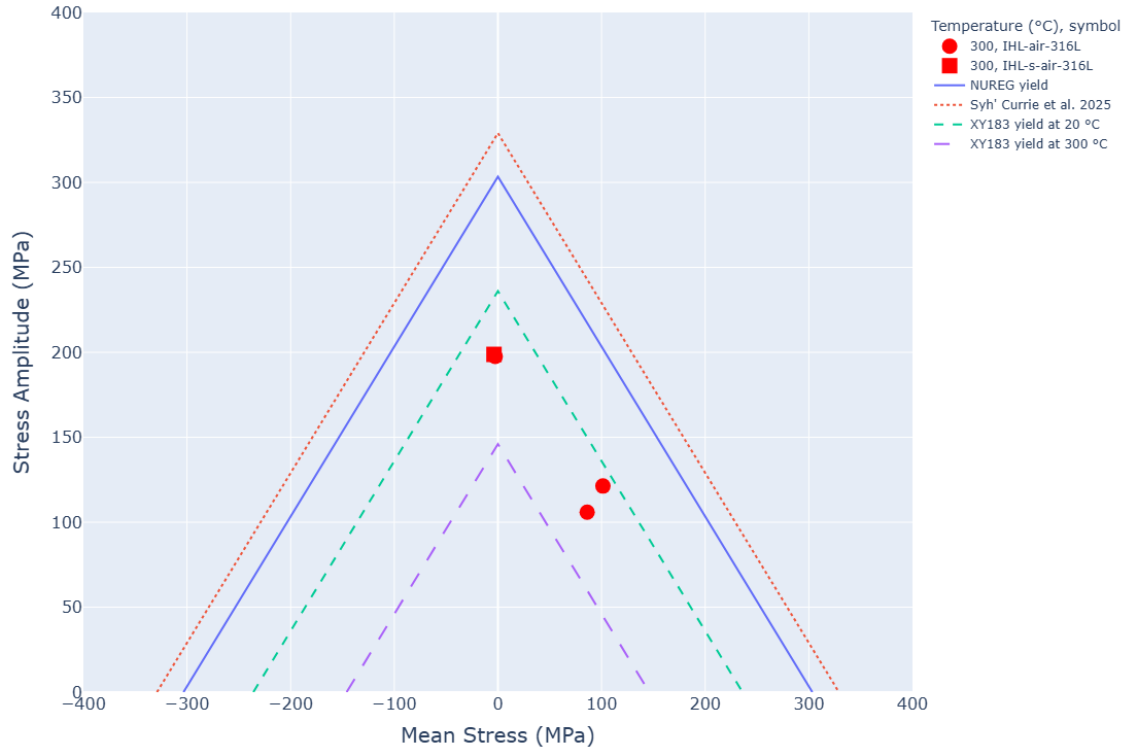

Figure 2.18. Haigh diagram showing the in-test stress amplitudes and mean stresses for the cycles applied in the IHL type tests.

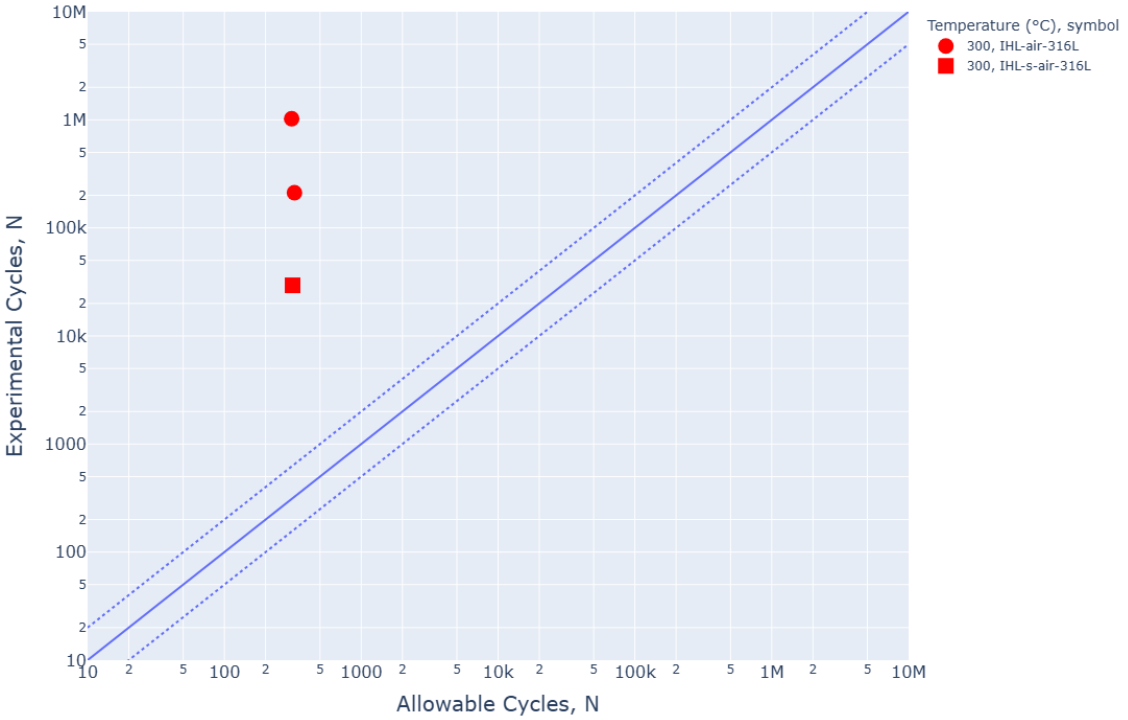

Figure 2.19. Allowable cycles calculated using the method defined in NUREG/CR-6909, Rev.1.

Additionally, the 0.3% cycles of both the IHL and the IHL-S do not have mean stress and the stress amplitude of these tests is approximately the same as the constant amplitude 0.3% tests. This indicates that after a certain amount of plasticity is present the baseline cycling can overcome the memory effect and the material shakes down to similar values to the constant

amplitude tests (Figure 2.18). This is also apparent from Figure 2.14 where the 1% tests have mean stresses of ≈55 MPa with 0.18% baseline cycles and ≈20 MPa with 0.25% baselines, although in this case full shakedown to constant amplitude behaviour in terms of stress amplitude was not achieved. For the IHL and IHL-S tests the shakedown occurred rapidly (Figure 2.20). This may provide information in how the definition hardening factor described by Currie et al. [2.6] can be improved as it is clear that for when the baseline cycling reaches 50% of the overloads in the IHL/IHL-S test the hardening factor should be 1. This is only considering two tests aimed at assessing a particular failure mode and a wider analysis investigating the dependence of stress amplitude on loading history is required to formulate a suitable relationship for design purposes.

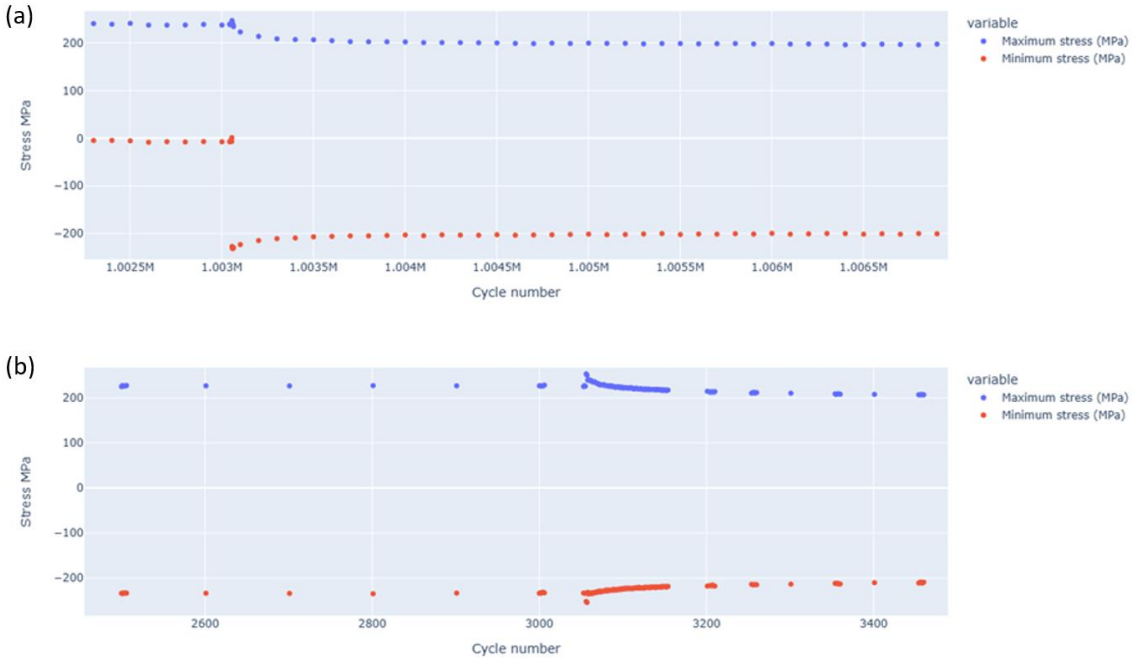

Figure 2.20. (a) IHL test transition into final 0.3% strain amplitude cycling showing shakedown within 200-500 cycles. (b) IHL-S tests transition from 0.6% cycles into 0.3% cycles showing shakedown within 200-500 cycles.

2.2.7 HYPOTHESIS 4: IN PWR ENVIRONMENTS, NEGATIVE EFFECTS FROM HARDENING, ENVIRONMENT, AND SURFACE ROUGHNESS ARE NOT MULTIPLICATIVE

To address Hypothesis 4, several roughened specimen tests with simple waveforms were commissioned to extend the reference dataset to include the behaviour of specimens with roughened surface finishes. Figure 2.22 shows that data tested with strain amplitudes equal to or above 0.3% have minimal surface finish effect, which aligns with observations from INCEFA-PLUS [2.5]. The tests conducted at 0.15% strain amplitude may show a negative impact of surface finish compared to the polished reference data (Figure 2.21). However, the number of datapoints is very limited for this condition. This was a necessary decision as test numbers are limited; 0.15% tests have very long run times for this material, and the surface finish programme for INCEFA-SCALE was only intended to be exploratory and not definitive.

To account for the surface finish effect at low strain amplitudes the fatigue limit of the best estimate model was reduced, and this produced an adequate fit for the 0.15% strain amplitude data (Figure 2.22). However, when considering the limited roughened specimen variable amplitude tests the same issue as described in Section 2.2.4 is met where there is insufficient data to describe the curvature of the model around the transition between LCF and HCF. The POLs are affected more than the corresponding PULs because of the SWT correction in the best estimate model reduce the strain amplitude in the presence of compressive mean stresses, with the opposite being true of the tensile mean stresses. This pushes the POL baseline amplitudes further into the problematic region and pushed the PUL baseline amplitudes further out of it. It should be noted that design methods do not have this issue as no benefit is obtained from compressive mean stresses. To highlight this the Coffin-Manson fit is shown in Figure 2.23 which does fit the data reasonably well.

In either case appears that surface finish has no additional influence on the fatigue life of specimens tested with the POL/PUL waveform when compared to the constant amplitude equivalent. As the prediction of the POL test is a similar distance from the 1 to 1 line as the polished equivalent in Figure 2.22 and is described as well as the constant amplitude data points in Figure 2.23.

This lends credibility to the idea that the effects on fatigue life of surface finish and the other conditions are not multiplicative and the larger of them is likely to dominate.

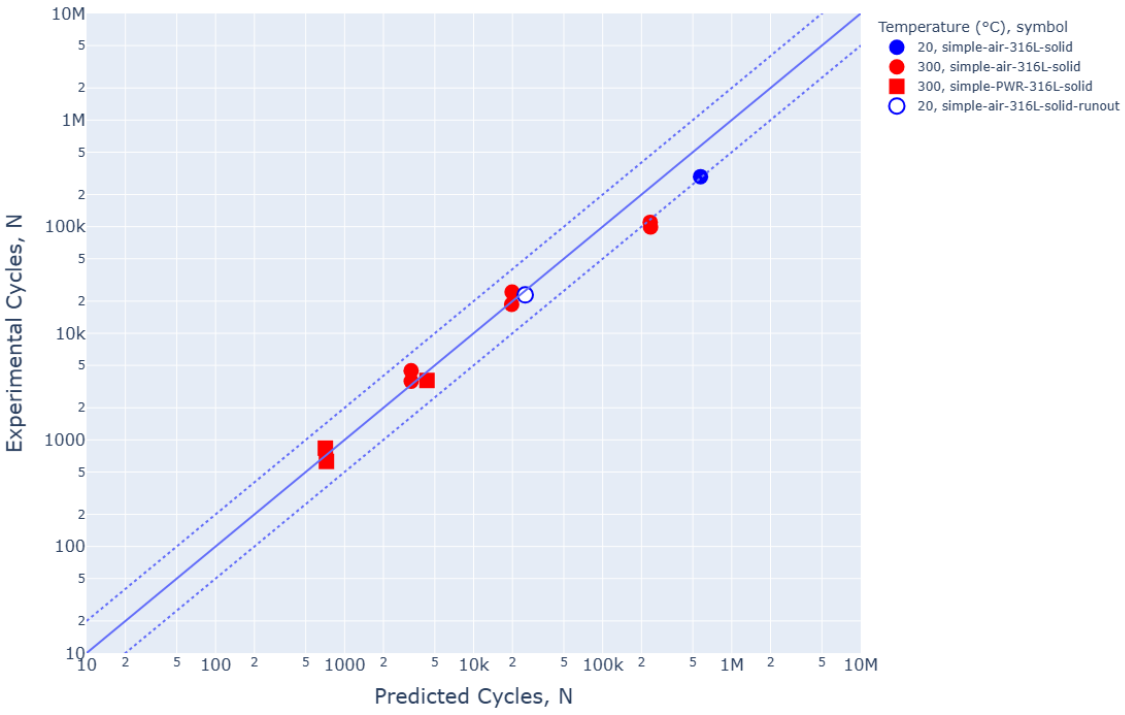

Figure 2.21. INCEFA-SCALE common material roughened specimens analysed using the material specific best-fit curve. The legend is temperature, waveform-environment-material-specimen type.

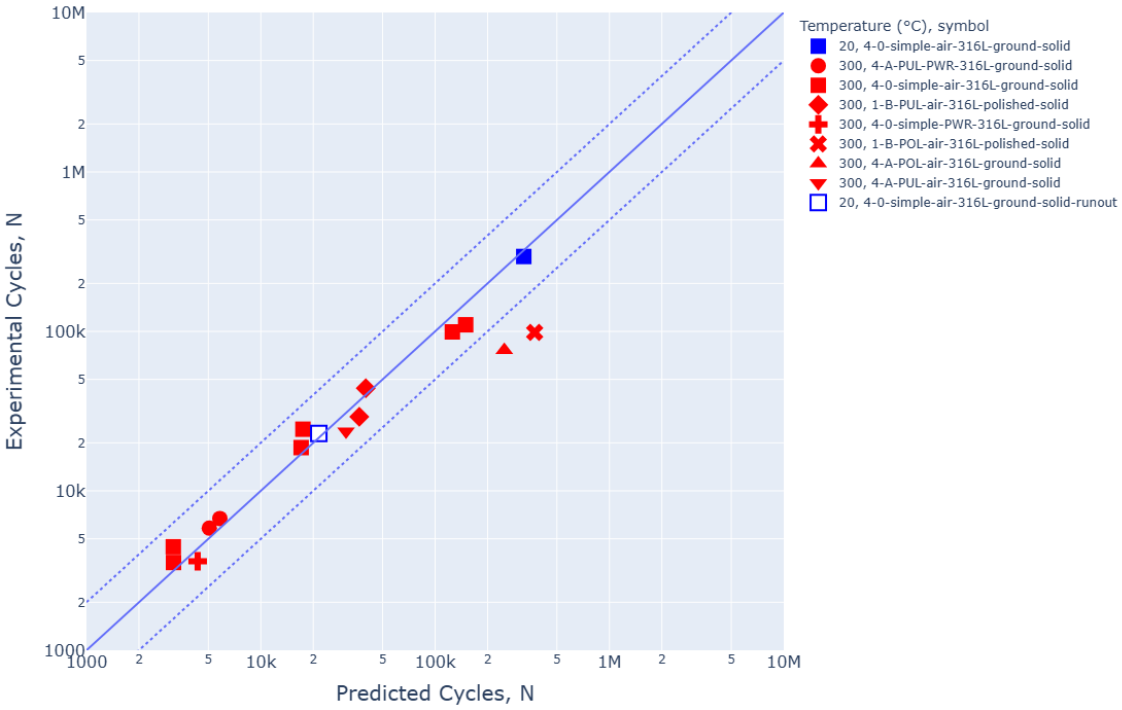

Figure 2.22. INCEFA-SCALE common material roughened specimens analysed using the material specific best-fit curve. The legend is temperature, hypothesis-subhypothesis-waveform-environment-material-specimen type-surface.

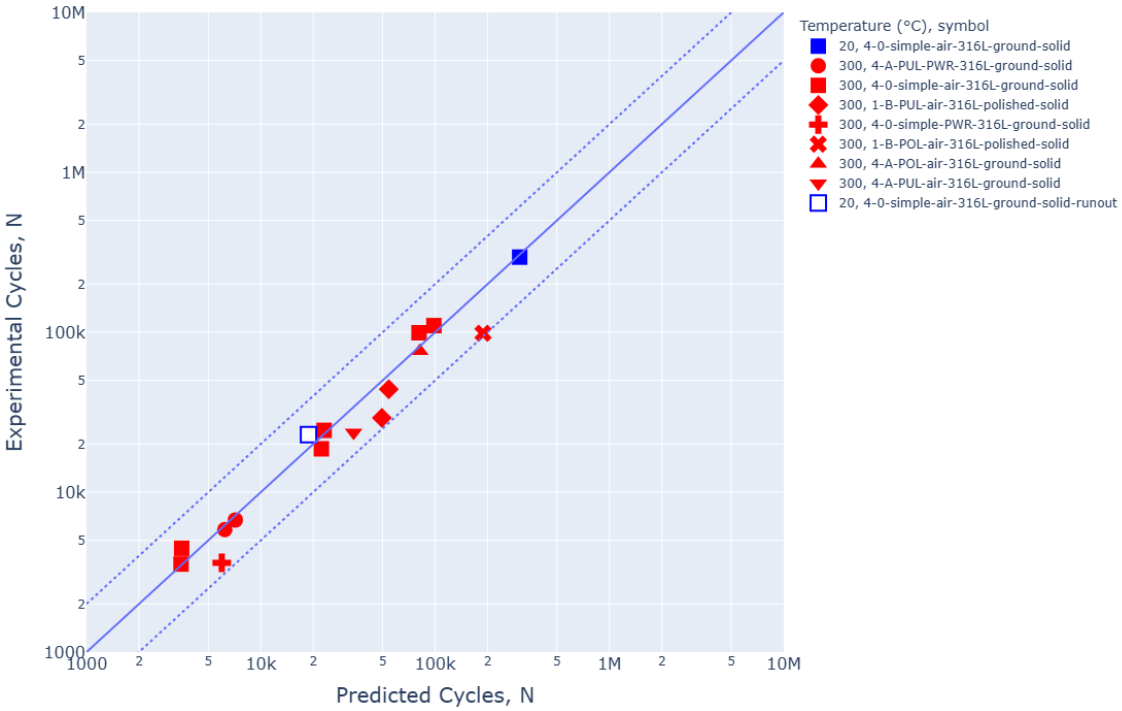

Figure 2.23. INCEFA-SCALE common material roughened specimens analysed using the material specific best-fit Coffin-Manson curve. The legend is temperature, hypothesis-subhypothesis-waveform-environment-material-specimen type-surface.

2.3 DESIGN CURVES

The fatigue community of the nuclear industry has proposed several revisions to the adjustment factor of 2 on stress or strain in the ASME design fatigue curves. Based on statistical analysis of material variability and data scatter factors of 1.6 [2.17] and 1.4 [2.18] have been proposed as alternatives to the factor of 2. Figure 2.24, Figure 2.25, and Figure 2.26 show that for each of these cases the INCEFA-SCALE test data, considered to be extreme in terms of severity of mean stress versus civil experience, is bounded conservatively by the proposed adjustment factors. The combination of these alternative adjustment factors and F_{en}-threshold has not yet been explored and is likely to have a lower amount of conservatism than the plots below show.

The INCEFA-SCALE data assessed by the simplified design curve method described in Currie et al. [2.6], and now part of a recently accepted ASME code-case, is shown in Figure 2.27. The 1 to 1 line in this method is the 95% percentile. This analysing the uniaxial data produced by INCEFA-SCALE Project using this method demonstrates that it provides margin against the design allowable cycles.

Furthermore, when considering surface finish in all cases the ground specimens are grouped with the corresponding polished data irrespective of waveform type. This indicates that each of the design methods handles the surface finish effect adequately. In the case of Currie et al. [2.6], the surface finish factor on life that was used in that method was the one described in the INCEFA-PLUS. This effect coupled with a reduction of the fatigue limit for mean stress effects and material variability and scatter is sufficient to account for the surface finish effect. This is strong evidence that the effect of environment, surface finish, and hardening are not multiplicative.

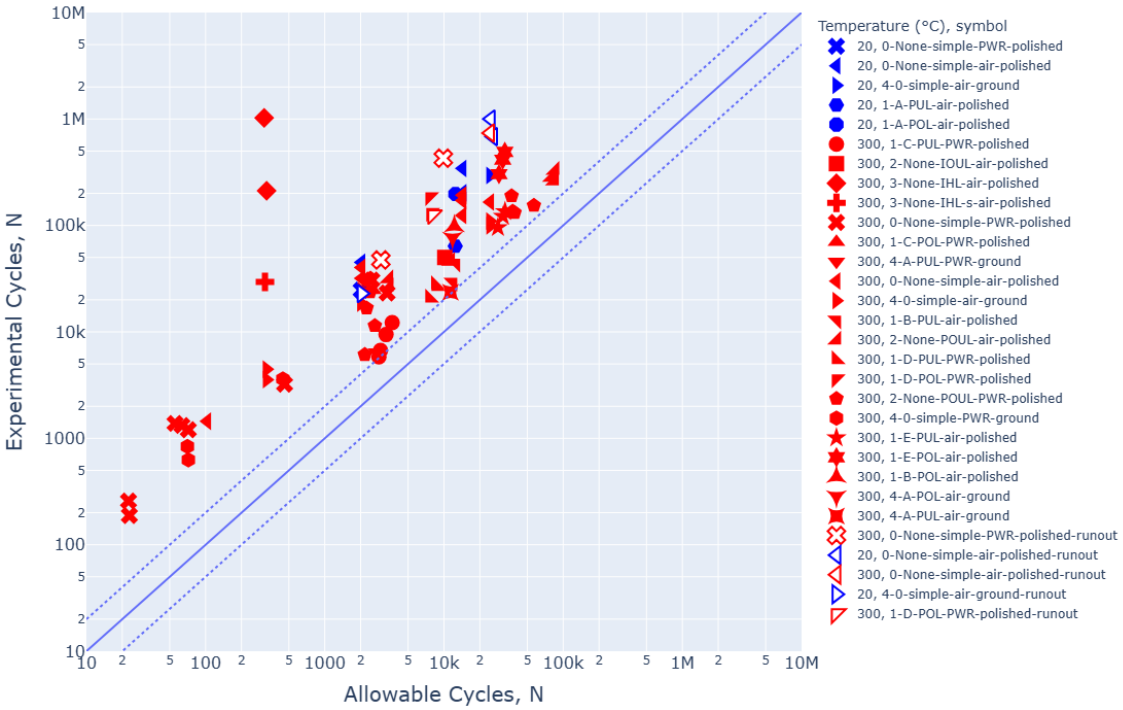

Figure 2.24. Allowable cycles calculated using the method defined in NUREG/CR-6909, Rev.1 with adjustment factors of 2 and 12.

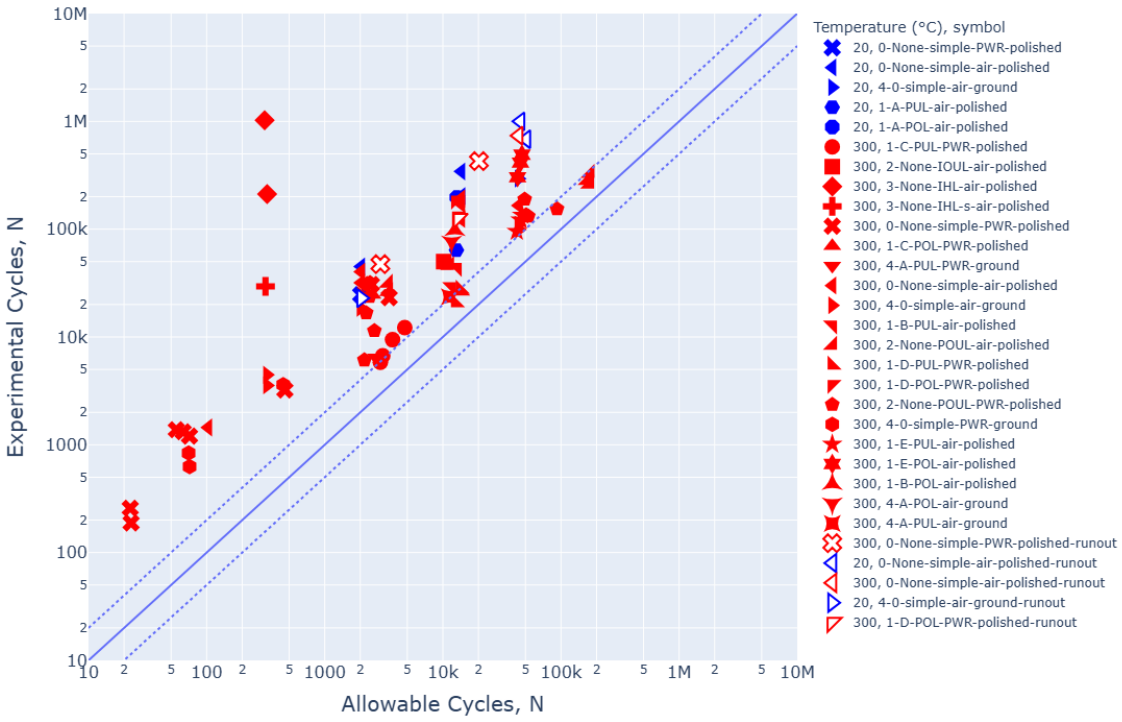

Figure 2.25. Allowable cycles calculated using the method defined in NUREG/CR-6909, Rev.1 with adjustment factors of 1.6 and 12.

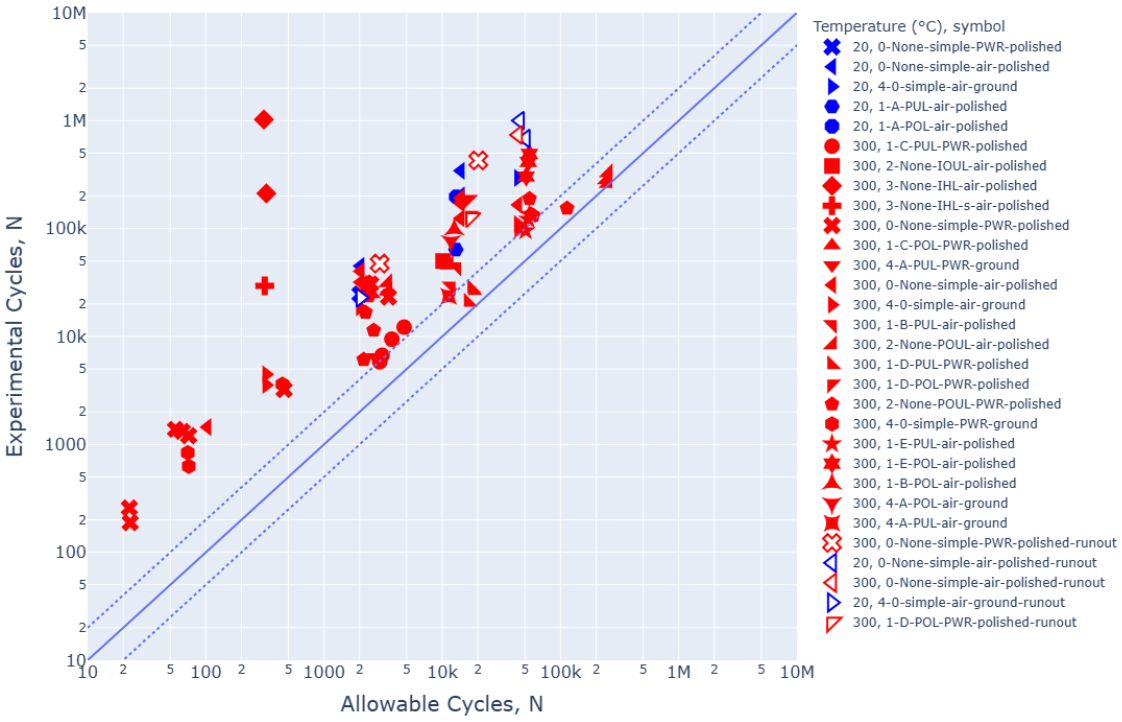

Figure 2.26. Allowable cycles calculated using the method defined in NUREG/CR-6909, Rev.1 with adjustment factors of 1.4 and 12.

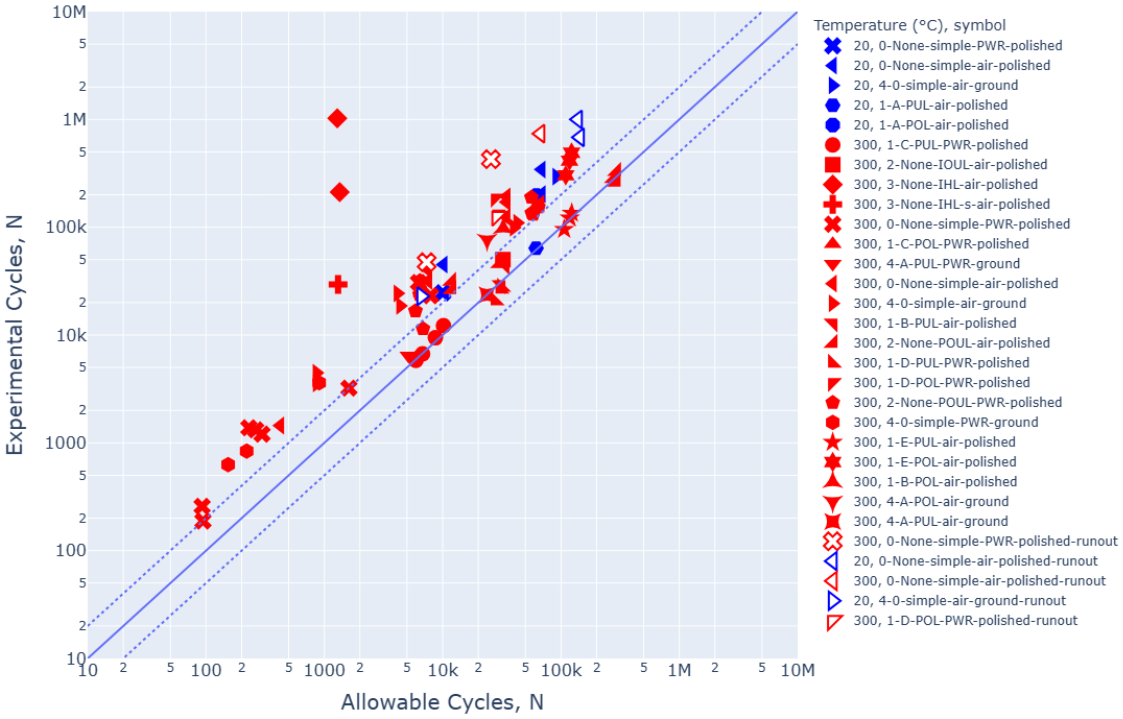

Figure 2.27. Allowable cycles calculated using the simplified method defined in Currie et al. [2.6].

2.4 MECHANISTIC UNDERSTANDING: FRACTOGRAPHIC EXAMINATION AND STRIATION COUNTING

The loading applied during the testing consisted of fully reversed (total-mean-strain of 0%) triangular or sawtooth CA waveforms, as well as either tensile or compressive dominant variable amplitude waveforms, i.e., PUL and POL, respectively. The PUL waveforms consisted of a single underload at 0.6% strain amplitude followed by a set of 200 tensile baseline cycles (with strain amplitudes of either 0.18% or 0.12%). Similarly, the POL waveforms consisted of a single overload at 0.6% strain amplitude followed by a set of 200 compressive baseline cycles (with strain amplitudes of either 0.18% or 0.12%). These loading blocks were repeated until the failure criterion was reached.

2.4.1 FRACTOGRAPHY AND STRIATION SPACING EVALUATION

Characterization of the fracture surfaces of the tested specimens aims to identify the primary initiation sites and final failure sites of the main fatigue cracks, which can then be used to identify the general crack propagation direction and assist in the selection of a suitable crack path for striation spacing evaluation [2.19]. The primary fatigue crack path was first identified on the fracture surface by Light Optical Microscopy (LOM), after which the average striation spacing (da/dN), i.e., Fatigue Crack Growth Rate (FCGR), was measured as a function of crack depth (a) from the Scanning Electron Microscope (SEM) observations. Ideally, there was a single primary fatigue crack that led to failure. If not, a suitable crack path for striation spacing evaluation was chosen based on the most dominant crack, associated with the largest area on the fracture surface, and the most dominant initiation site of such crack. The chosen crack path for each specimen extended from the identified primary initiation site to the region of the final fracture. Individual striation is generally orientated perpendicular to this path and can be used to

calculate the striation spacing. Although, for all specimens, the FCGR was determined on the whole fracture surface till the end of the main fatigue crack.

For specimens without VA loads, the striation spacing was evaluated by measuring the base load striations (only ones available). For specimens with VA loads, the striation spacing was evaluated using three methods, as shown in Figure 2.28.a. Method 1 is to measure striation spacing as an average over multiple VA blocks consisting of n·(base + VA) striations. Method 2 is to measure the distance between two adjacent VA-striations, excluding the VA-striations themselves, i.e., to measure the spacing of a known number of base load striations within a single block (assuming each load cycle produces a single striation). Method 3 measures the spacing of a selected number of base load striations in a chosen area.

In addition, for specimens tested with VA loads, periodic under/overloads were "mapped" on the fracture surface and used to evaluate striation spacing, as shown in Figure 2.28.b. This is a similar approach to Methods 1 and 2, i.e., the measurement is performed on a single block at a time (as in Method 2) but the VA-striation is also captured in the measurement (as in Method 1). The generated maps allow backward tracking of crack progression from the last underload/overload down to the initiation site. Such "VA-maps" can be used to evaluate both striation spacing, and cycles-to-depth (a direct method for estimating the total number of cycles to failure) for the VA specimens, as shown in Figure 2.28.b. This is possible because the number of base load cycles per block (200) is known.

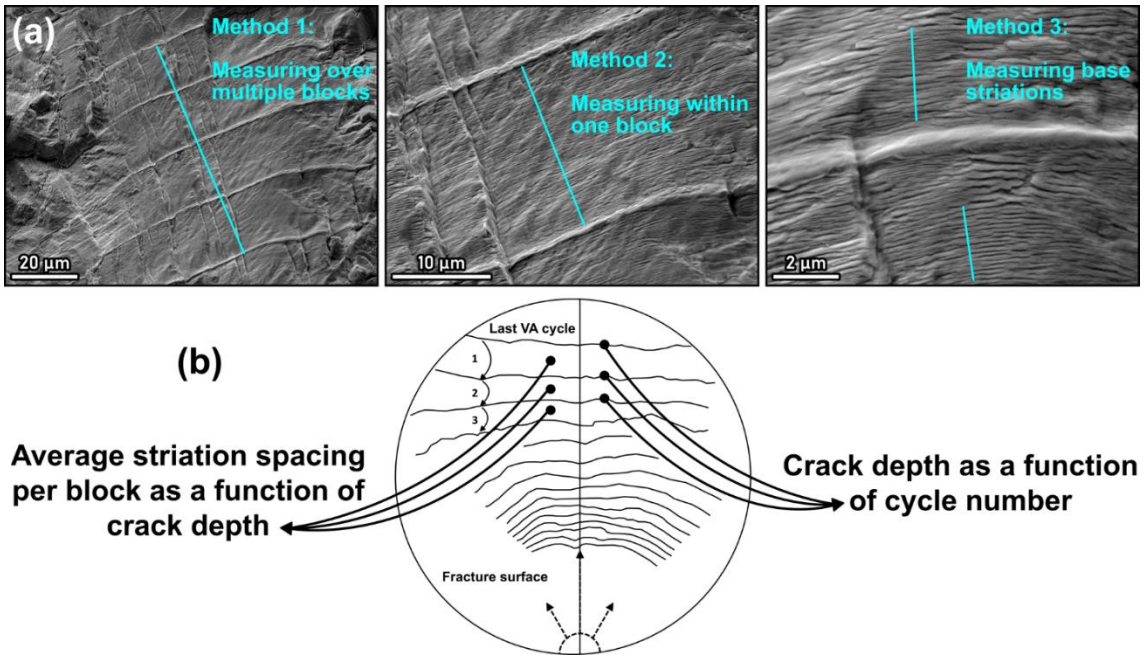

Figure 2.28. Striation counting and spacing evaluation. (a) Three methods of measuring striations from the fracture surfaces of VA specimens. (b) Schematic of periodic underload/overload striation mapping.

Furthermore, the striation spacing counting is used to evaluate the effective initiator size by the linear extrapolation of the crack depth – fatigue cycle plot (log-linear) [2.20,2.21]. The estimation tells the depth of the crack initiation location measured from the surface. If the initiator is at the surface, an estimation of the size of that initiator can be obtained, assuming crack propagation starts from the deepest point of the initiator. E.g., inclusion-matrix boundary behaving as an existing crack. However, the crack might initiate ahead of the initiator, or the

initiator might be located deeper in the material, in which case the estimation gives an effective size of an initiator that would be at the surface.

The striation spacings with respect to fatigue crack depth measured using the three methods are illustrated in Figure 2.29.b. Methods 1 (multiple blocks) and 2 (single block) yield similar results whereas Method 3 (base striations) shows higher variability (particularly in high crack depth regions) and tends to give higher spacing results than the other two methods, most likely due to the preferential/biased selection of easily visible (wider) striations. However, with the common guideline on the evaluation of base load striation spacings in LCF specimens, developed in the framework of the INCEFA-SCALE Project, the partners have obtained very similar striation spacing results for specimens tested with Constant Amplitude (CA) load spectrum, see Figure 2.29.a.

Furthermore, since Method 1 captures VA-striations themselves and Method 2 does not, it gives marginally higher results at high crack depths due to much wider VA-striations in comparison to base striations. However, Method 1 exhibits the least variation due to averaging over large number of striations, which can be observed in Figure 2.29.b.

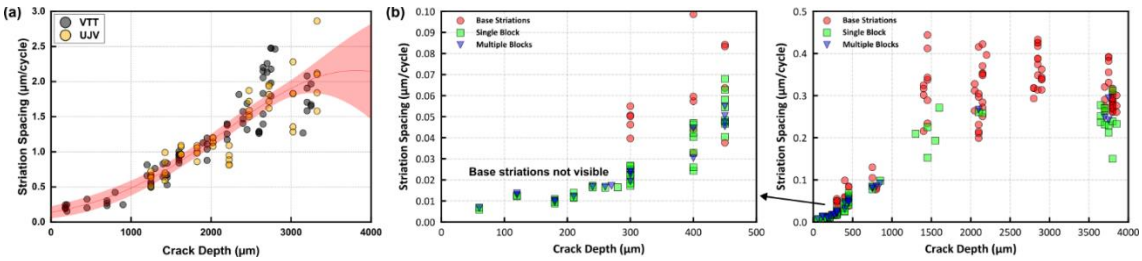

Figure 2.29. (a) Measured base load striation spacing as a function of crack depth (a < 4 mm) by individual organizations for UJV-2 specimens tested in PWR water (PWR CA 0.18%). (b) The striation spacing with respect to fatigue crack depth measured using three methods and shown in two scales for specimen VTTAIR-3 tested in RTA (RTA PUL 0.18% - 0.6%).

One evident benefit of using Methods 1 and 2 for evaluating the striation spacing is their ability to capture PUL/POL striations, which are visible a few tens of microns from the initiation sites, while base load striations are usually visible a couple of hundred microns from the initiator. As shown in Figure 2.29.b and Figure 2.30.b, PUL/POL striations are visible around 60 µm from the initiation sites, whereas base load striations are visible only beyond 300 µm from the initiator. It is noteworthy to mention that base load striations very close to the sample surface (a < 100 µm) were not observed in any specimen after testing in HTA or simulated PWR primary environments. Furthermore, although at higher crack depths, base load striations become visible, they can still be obscured by oxides/scales, particularly in heavily oxidized PWR-tested specimens. In contrast, PUL/POL striations with significantly larger block widths can be tracked more easily and consistently. It is also worth noting that PUL and POL striations are very similar in terms of how they look and how well they can be observed on the fracture surface.

Since the periodic under/overloads are clearly visible, they can be "mapped" on the fracture surface, which allows accurate measurement of crack depth as a function of cycle number as well as striation spacing estimations between a pair of under/overloads. The evaluation based on block spacing offers several key advantages:

- Consistency: Measurements can be consistently applied across the fracture surface.
- Efficiency: The procedure can be faster than measuring and averaging base load striations from multiple locations.
- Accessibility: The procedure can be performed to some extent using only macroscale LOM images (e.g., JAC-1 in Figure 2.30.a).

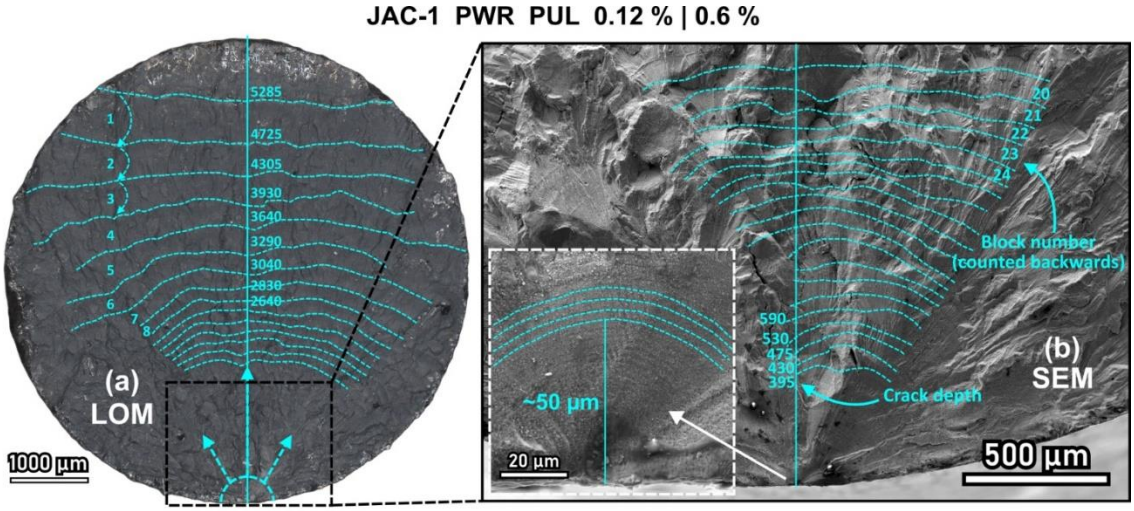

Figure 2.30. Example of periodic underload striation mapping from specimen JAC-1 tested in PWR (PWR PUL 0.12% - 0.6%). "VA-maps" can be used to evaluate striation spacing and cycles-to-depth for VA specimens. (a) Macroscale LOM image with mapping. (b) SEM image with mapping down to ≈50 µm from initiation site.

For the VA specimens evaluated in this study, all described methods were applied to each specimen to investigate the scatter of striation spacing data and to support the fitting of the FCGR curves. Two examples are given in Figure 2.31, emphasizing the benefits of using VA-maps in addition to the three methods of evaluating striation spacing. The VA-maps provide consistent and continuous measurements of crack progression without any gaps between the initiation and final failure sites, whereas the other three methods rely on a limited number of selected areas and thus leave gaps in the captured crack progression history. Eliminating the gaps with, for instance Method 3 (base striations) would require an infeasible number of measurements, especially if averaging per location is factored in. In addition, the VA-maps can be produced from a few high-resolution fractography images and since they cover the whole fracture surface, no additional SEM work is required later regardless of the chosen measurement location. Furthermore, the base load striations can become faint or invisible due to oxides/scales or local microstructure, which may result in a lack of reliable data points in some regions when performing the evaluation based on Method 3. This is not the case with VA-map analysis, as it is not necessary to see individual striations (same as with Methods 1 and 2). After filling in the additional striation spacing data from VA-maps, the striation spacing – crack depth profile becomes completer and more reliable, as shown in Figure 2.31.

In most LCF test specimens, the FCGR follows a logarithmic relationship. However, a decrease/plateau in striation spacing after reaching the middle range of crack depth (a ≥ 3-4 mm) was observed in some specimens, e.g., Figure 2.31.a, Figure 2.31.b, and Figure 2.32.e. This phenomenon can be explained either by multiple competing cracks in the gauge section or possibly specimen bending in relation to extensometer location, affecting the measured total-

strain, which in turn can cause sudden fluctuations in crack propagation rate due to the testing being total-strain-controlled.

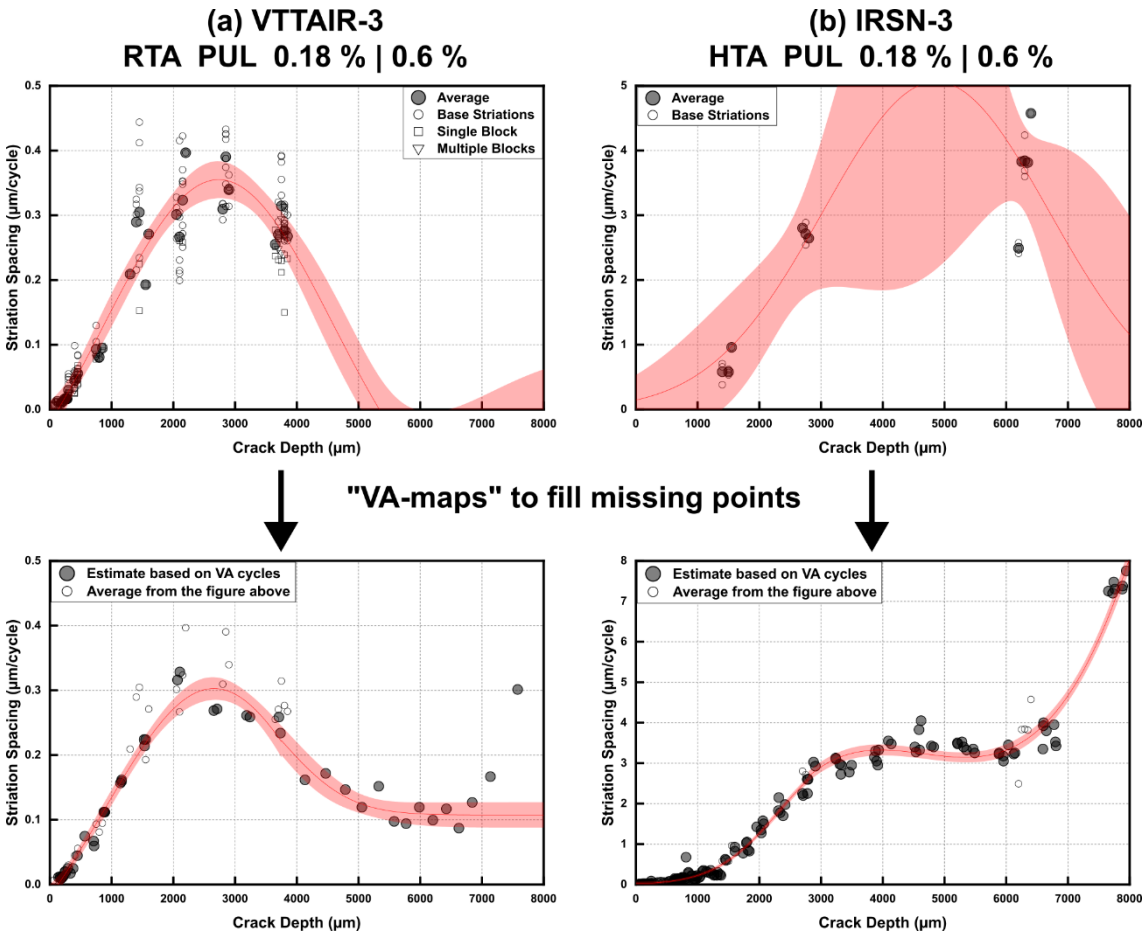

Figure 2.31. The striation spacing evaluation on VA specimens with and without the data filling from VA-maps with examples of (a) VTTAIR-3 (RTA PUL 0.18% - 0.6%) and (b) IRSN-3 (HTA PUL 0.18% - 0.6%). The red area should represent 95% confidence band of the fit.

Examples of the effective initiator size estimations are given in Figure 2.32. The effective initiator size of VTTAIR-3 was estimated to be around 15 µm, and with SEM, a relatively large (≈13 µm) inclusion at the immediate proximity of the surface at the initiation site of this specimen can be observed (Figure 2.32.b). This confirms the high accuracy of the application of this method for the estimation of effective initiator size. Although in Figure 2.32.a, there are data points down to ≈100 µm crack depth, similar and relatively reliable estimations by linear extrapolation could have been obtained already from several hundred microns away from the initiator. Figure 2.32.c shows that this primary initiator was enriched in Cr, O and Mn. Additionally, some elements like Al, Ti and Si are detected as well. Similar type of oxide-inclusion initiators was found in other specimens.

Plotting data in crack depth – fatigue cycle plots (linear-linear, and log-linear) is beneficial in the case of multiple major initiation sites. From the SEM image of the fracture surface in Figure 2.32.e, two major initiation sites can be identified. From each of the initiation sites, separate striations, indicating separate crack fronts, can be observed. The two crack fronts merged at a crack depth slightly beyond 1 mm. With a crack depth – fatigue cycle plot Figure 2.32.d, the crack

depth and the cycle number where the two fatigue crack fronts merged into one can be identified.

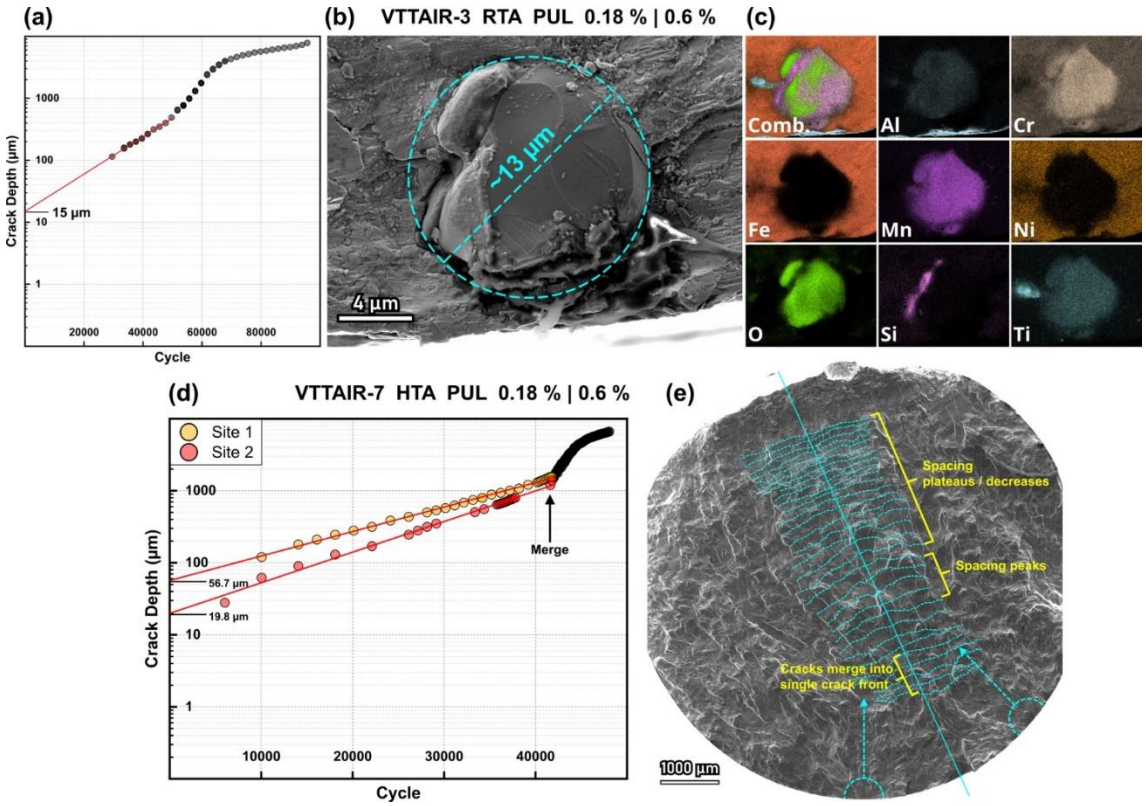

Figure 2.32. Estimation of the effective initiator size. (a) Linear extrapolation of the crack depth – fatigue cycle plot (log-linear) of specimen VTTAIR-3 tested in RTA (RTA PUL 0.18% - 0.6%). (b) SEM image of the initiator. (c) SEM-EDS of the initiator. (d) Linear extrapolation of the crack depth – fatigue cycle plot (log-linear) of VA specimen VTTAIR-7 tested in HTA (HTA PUL 0.18% - 0.6%), exhibiting two significant initiation sites. (e) SEM image of the fracture surface.

2.4.2 COMPARISON OF FATIGUE BEHAVIOR

It is possible to perform direct comparisons on these specimens, CA vs. PUL vs. POL (waveform). A negative impact of a PUL/POL test over a CA test on fatigue lifetime was found. Figure 2.33 depicts the comparison of spacing measurements in log-log scales and crack depth against cycle evaluation for these samples. For specimens tested in HTA, the waveform PUL/POL accelerates the FCGR compared to a CA loading (roughly 1-5x), particularly beyond a crack depth of 1 mm. Specifically, the striation spacing for PUL, POL and CA systems is 0.3 vs. 0.1 vs. 0.07 µm/cycle at a crack depth of 1.0 mm, respectively. In comparison, the striation spacing for PUL, POL and CA systems is 0.8 vs. 0.3 vs. 0.1 µm/cycle at a crack depth of 2 mm, respectively. Moreover, PUL/POL accelerates the initiation of fatigue crack in comparison to the CA specimens (3400 vs. 11250 vs. 188000 cycles).

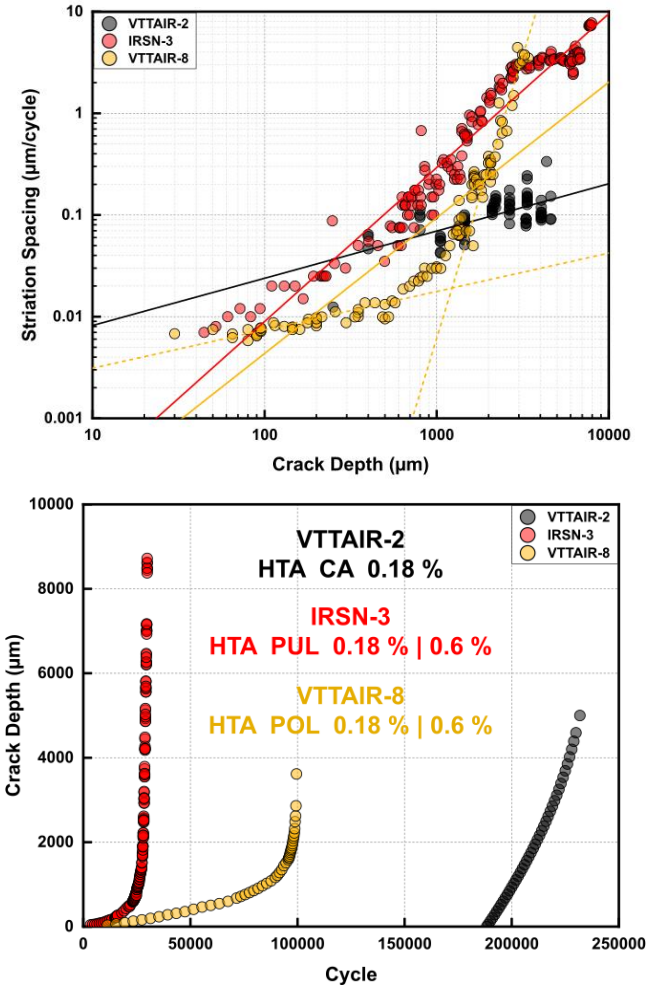

Figure 2.33. Striation spacing measurements (in log-log scales) and crack depth against cycle evaluation for CA vs. PUL vs. POL specimens.

2.4.2.1 CROSS-SECTIONAL CHARACTERIZATION

The SEM-BSE micrographs and Electron Backscatter Diffraction (EBSD) maps in Figure 2.34 reveal the deformed microstructures present in the vicinity of secondary fatigue cracks beneath the main fatigue fracture surface on the cross sections of specimens VTTAIR-2 (HTA CA) IRSN-3 (HTA PUL) and VTTAIR-8 (HTA POL). The crack tip in the VTTAIR-2 specimen that was tested in HTA with a CA loading mode is characterized by homogeneous dislocation cell structure (cells of size 200-300 nm), as a result of the planar plastic deformation during cyclic loading. The deformation accumulation beneath the main fatigue crack is around 10-15 µm. The crack tip in the IRSN-3 specimen that was tested in HTA with a PUL load spectrum is characterized by the formation of ultrafine grains and irregular cells ahead of the secondary fatigue crack and the formation of extensive shear bands. The irregular shape of the cells indicated a highly localized feature of deformation. Cells of 100-300 nm diameter adjacent to the secondary cracks and local formation of shear bands were observed on VTTAIR-8 (HTA POL). The plastic deformation accumulation beneath the main fatigue crack is of depth of 10, 20, and several hundred microns for specimens tested with waveforms of CA, PUL, and POL, respectively.

The micrograph results agree with the striation data, indicating that PUL waveform is worse than POL. In addition, it seems that PUL specimens tested in HTA have a similar behavior to the CA

specimens tested in PWR, and POL specimens tested in HTA have similar behavior to CA specimens tested in HTA (similar deformation, similar-sized cells).

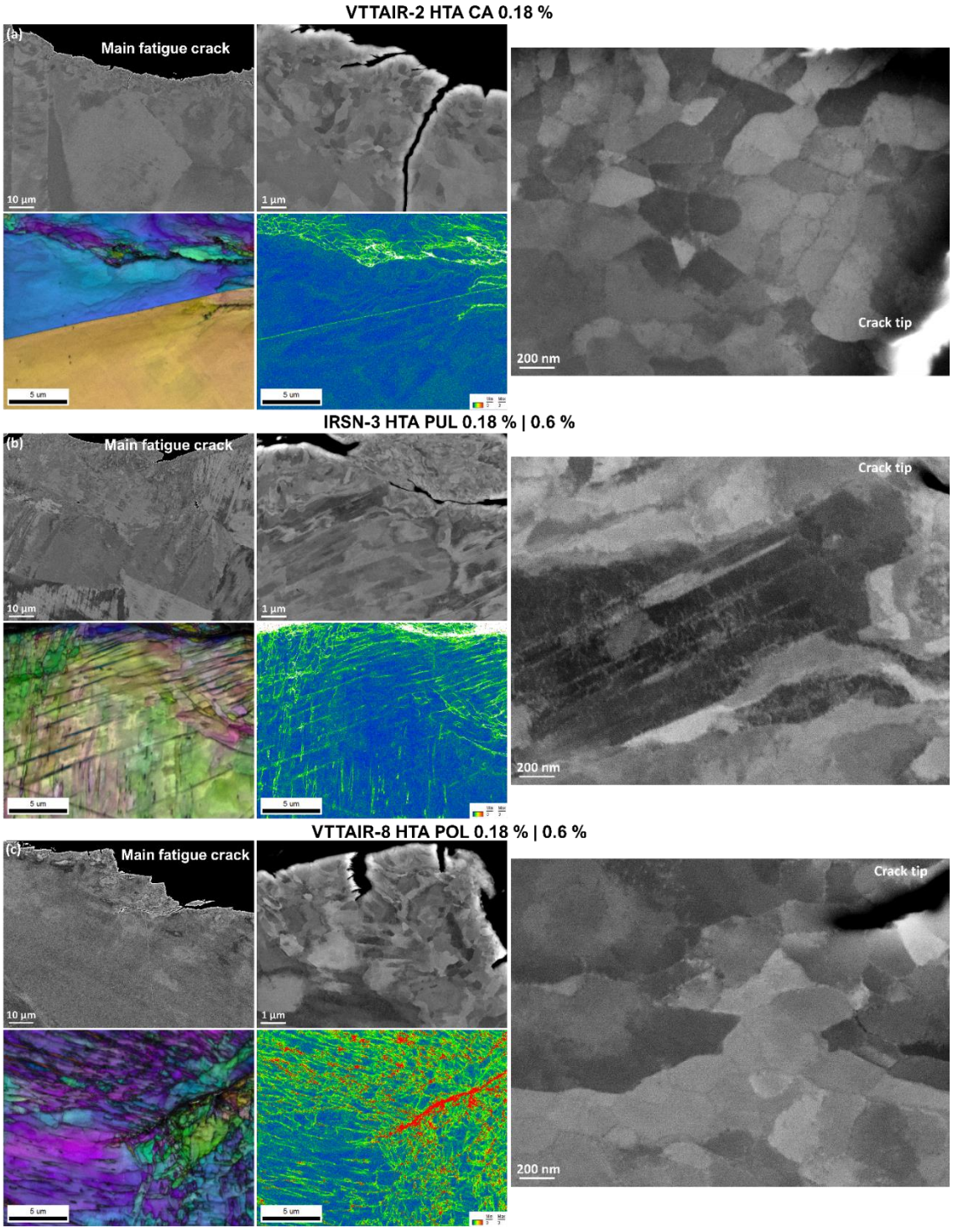

Figure 2.34. SEM-BSE, EBSD IPF and KAM maps. Microstructure observations in the vicinity of secondary crack tips beneath the fracture surface of specimens VTTAIR-2 (HTA CA), IRSN-3 (HTA PUL) and VTTAIR-8 (HTA POL).

2.4.2.2 DISCUSSION ON EFFECTS OF WAVEFORM

The N_{25} of the investigated PUL, POL, and CA specimens tested in HTA was 29090, 98600 and 192570, respectively. PUL/POL accelerated the FCGR compared to CA loading (0.3 vs. 0.1 vs. 0.07 µm/cycle at a crack depth of 1.0 mm and 0.8 vs. 0.3 vs. 0.1 µm/cycle at a crack depth of 2.0 mm).

Furthermore, PUL/POL accelerated the initiation of fatigue crack (N_I) in comparison to the CA specimens (3400 vs. 11250 vs. 188000 cycles).

The plastic deformation accumulation region beneath the main fatigue crack measured 10, 20, and several hundred microns in depth for HTA specimens tested with CA, POL, and PUL, respectively. For the specimen tested with CA, homogeneous cell formations of size of 200-300 nm were observed adjacent to the secondary cracks. For the specimen tested with POL, a local formation of shear bands was observed in addition to the formation of dislocation cells of size 100-300 nm adjacent to the secondary cracks. In contrast, extensive shear bands, ultrafine grains and irregular cells were formed ahead of the secondary fatigue crack of the specimen tested with PUL. The irregular shape of the deformed microstructure indicated a highly localized feature of deformation with high strain incompatibility.

Formation of shear bands was more prevalent in specimen IRSN-3 tested with a PUL load spectrum, which has a reduced fatigue life compared to VTTAIR-2 (HTA CA) and VTTAIR-8 (HTA POL), indicating a correlation between shear band formation and fatigue life. The correlation factor seems to be similar for both initiation and propagation. This is evident from the comparison between the PUL and POL striation data, indicating a factor of ≈3.4 in N_{25}, ≈3.3 in N_I and 2.7-3.0 in FCGR. Conversely, homogeneous cellular dislocation structure is more common in specimens tested with longer fatigue lifetimes. LCF waveform strongly influences the localization of plastic deformation and the residual stress state on and under the sample surface and therefore influences fatigue cracking propagation. In this work, the PUL has been found to induce more extensive slip bands and much deeper deformation beneath the fracture surface, compared to the POL and CA conditions. Cracking normally takes place preferentially in high-energy structural defects, like deformation bands or shear bands with a high density of dislocations.

The LCF waveform PUL/POL greatly advances the initiation cycle number of fatigue cracks in comparison to the CA specimens. This reflects the material's proneness to new crack initiation has increased. Faster crack initiation typically leads to decreased fatigue life, as the cycles to initiation often represents a significant portion of fatigue life, particularly in the case of the CA-tested specimen. The relative difficulty of fatigue crack initiation and propagation is expressed by the ratio of cycles to initiation/cycles to failure (N_I/N_{25}). The ratios from tests with waveforms of PUL/POL were much lower than the test with CA load spectrum. When both initiation and propagation processes are enhanced equally (i.e., N_I and N_{25} are reduced proportionally), the ratio remains stable. A lower N_I/N_{25} ratio suggests that the initiation is more significantly enhanced relative to the propagation in PUL/POL tests. This is evident from Figure 2.33, where the initiation of the POL specimen occurs very early, but the propagation is slow, taking almost 100000 cycles before failure.

Fatigue life is affected by the waveform and sequencing of the loading cycles, particularly when the cycle incorporates complex patterns of loading which can influence mean stress or the cyclic hardening behavior of the material. Moreover, an elevated stress concentration results in dislocation slip in the ductile bulk metal, which can accelerate cracking. VA fatigue is associated with situations where a component is subjected to different combinations of alternating loading at multiple different stress or strain amplitudes during operation. This more typically represents

the conditions experienced by an in-service plant (e.g., during load-follow) as opposed to the single CA loading conditions applied to test specimens, which are used for the development of standard fatigue endurance curves. This paper indicates that VA loading as a waveform relevant for NPP operation can alter fatigue endurance lifetimes and deserves more attention in future studies.

2.5 SUMMARY

The uniaxial testing programme of INCEFA-SCALE Project is focused on closing the gap between plant experience and laboratory testing. The specific testing goals and hypotheses were developed based on a review of the current industry position on many topics related to environmentally assisted fatigue assessment methods and the research required to develop a technical basis for the future. The research objectives for the uniaxial testing programme have been tailored to study the relationships between the loading history and surface finish subfactors of the adjustment factor of 2 on stress or strain in the ASME Boiler Pressure Vessel Code Section III, the environment, and mean stress. A crucial aspect of this work is understanding and identifying the ways that the complex effect of loading history within PWR coolant environments is accounted for. The hypotheses specific to the uniaxial testing are:

1. The negative effects of mean stress on fatigue life are relatively less damaging at higher temperatures and are conservatively accounted for in current design codes.
2. In PWR environments, the effects of hardening on fatigue life should not be treated as additional to effects of environment.
3. Design guidance methods provide suitable protection against sub-endurance limit short crack growth under VA loading.
4. In PWR environments, negative effects from hardening, environment and surface roughness are not multiplicative.

As the factor on stress or strain is defined by the largest of the subfactors, efforts to reduce this factor must consider the magnitude of the other subfactors involved as well as how the redefined factor will interact with other assessment approaches. Therefore, the results of these tests should ultimately be considered within the context of other efforts to influence assessment methods and the adjustment factors within design curves.

Analysis of the data indicates that the variable amplitude data can be conservatively bounded by the ASME BPVC design curves. However, the ASME design method does not conservatively handle mean stress effects observed in the INCEFA-SCALE test programme as it underestimates the magnitude of the mean stress effect and applies the correction over too small of a stress range. The adjustment factors of 12 on life and 2 on stress or strain and the inherent conservatisms in them are what compensate for the non-conservative mean stress correction for these data within this code. Therefore, work that seeks to reduce these factors must consider the mean stress issue and the expected severity of their plant loading to provide a suitably conservative set of design curves.

The Hypothesis 2 POUL tests show that in air and water at 300 °C for tests with strain amplitudes of 0.18% and above, a model that accounts for hardening and mean stress can adequately predict the fatigue lives of the common material specimens.

The exclusion of F_{en} for the tests with baseline strain amplitudes of 0.1% group this data with the corresponding air tests. This suggests that the F_{en}-threshold proposed by NUREG/CR-6909, Rev.1 is applicable.

The limited testing for Hypothesis 3 indicates that there is substantial margin in current assessment methods to protect against subendurance limit growth. Additionally, analysis of the stress amplitude and mean stress values from the 0.3% strain amplitude waveforms of these tests shows that these cycles rapidly shake the specimens down to constant amplitude behaviour with zero mean stress. This may aid the development of new hardening factors and the determination of where mean stress corrections are applicable based on loading history.

The surface finish tests conducted as part of Hypothesis 4 indicate that the effect of surface finish, environment, and hardening in air is not multiplicative. Considering the constant amplitude surface finish tests, these indicate that for strain amplitudes approaching the fatigue limit there is an effect of surface finish that is greater than observed in INCEFA-PLUS tests performed in the LCF regime at strain amplitudes of 0.15%. Furthermore, comparing the constant amplitude test data to that of the variable amplitude roughened specimen tests shows that there is no increase in surface finish effect for the variable amplitude tests. Using the appropriate best-fit model it can be shown that by accounting for the surface finish effect on life using the INCEFA-PLUS relationship and a reduction in fatigue limit the surface finish effect can be adequately described

When analysing the data produced by INCEFA-SCALE using various design curves the importance of adequately accounting for all variables affecting fatigue behaviour when refining adjustment factors becomes obvious. For example, although the surface finish effect appears to be larger towards the fatigue limit in the best estimate analysis, the design curves have adequate margin for this due to the adjustment factor on stress or strain. This indicates aspects that would influence the fatigue limit are not multiplicative with surface finish and are adequately described by adjusting the fatigue limit for mean stress and material variability and scatter.

REFERENCES

[2.1] O.K. Chopra, G.L. Stevens, NUREG/CR-6909,Rev.1; Effect of LWR Water Environments on the Fatigue Life of Reactor Materials. Final Report, 2018.

[2.2] J. Colin, A. Fatemi, S. Taheri, Cyclic hardening and fatigue behavior of stainless steel 304L, J. Mater. Sci. 46 (2011) 145–154. doi:10.1007/s10853-010-4881-x.

[2.3] A. Fissolo, J.M. Stelmaszyk, A First Investigation on Cumulative Fatigue Life for a Type 304-L Stainless Steel Used for Pressure Water Reactor, in: Vol. 3 Des. Anal., ASMEDC, 2009: pp. 263–272. doi:10.1115/PVP2009-77156.

[2.4] EDF, R5 - Procedures for Assessing Structural Integrity of Components under Creep and Creep-Fatigue Conditions, (2014).

[2.5] INCEFA-PLUS Consortium, S. Arrieta, T. Austin, M. Bruchhausen, W.-J. Chitty, R. Cicero, S. Cicero, S. Cuvilliez, L. De Baglion, G. Dundulis, C. Gourdin, C. Huotilainen, J.-C. Le Roux, J. Mann, W. Mayinger, A. McLennan, T. Métais, E. Miroslava, K. Mottershead, R. Novotny, F.J. Perosanz López, N. Platts, I. Procopio, N. Prompt, P. Spätig, M. Twite, M. Vankeerberghen, INCEFA-PLUS findings on Environmental Fatigue, INCEFA-PLUS Project,

2020. doi:10.5281/zenodo.4243979.

[2.6] C. Currie, A. Morley, A. Mclennan, Suitably Accounting for Mean Stress Effects in Pseudo-Stress-Based Design Fatigue Curves, in: Vol. 1 Codes Stand., American Society of Mechanical Engineers, 2025. doi:10.1115/PVP2025-154711.

[2.7] S. Asada, T. Nakamura, M. Kamaya, Y. Takahashi, Technical Revisions of Jsme Environmental Fatigue Evaluation Method, Am. Soc. Mech. Eng. Press. Vessel. Pip. Div. PVP. 1 (2023). doi:10.1115/PVP2023-102692.

[2.8] M. Nakane, Y. Wang, H. Hatoh, M. Yamamoto, A. Hirano, K. Hayashi, Development of New Design Fatigue Curves in Japan: Discussion of Effect of Surface Finish on Fatigue Strength of Nuclear Component Materials, in: Vol. 3 Des. Anal., American Society of Mechanical Engineers, 2019. doi:10.1115/PVP2019-93167.

[2.9] P. Gill, P. James, C. Currie, C. Madew, A. Morley, An investigation into the lifetimes of solid and hollow fatigue endurance specimens using cyclic hardening material models in finite element analysis; PVP2017-65975, Am. Soc. Mech. Eng. Press. Vessel. Pip. Div. PVP. 1A-2017 (2017). doi:10.1115/PVP2017-65975.

[2.10] R. Hales, R.A. Ainsworth, Multiaxial creep-fatigue rules, in: 11th Int. Conf. Struct. Mech. React. Technol. Post Semin. 5, 8th Int. Semin. Inelast. Anal. Fract. Predict., Tokyo, 1991: pp. 125–138.

[2.11] EDF, Assessment Procedure for the High Temperature Response of Structures R5, Issue 3, 2021.

[2.12] A. Pineau, High temperature fatigue behaviour of engineering materials in relation to microstructure, Fatigue High Temp. 14 (1983) 305–364.

[2.13] R. Hales, The role of stage I and stage II crack growth in the R5 procedures - NE Report TD/SID/MEM/0052, (1990).

[2.14] H. Kitagawa, S. Takahashi, Applicability of Fracture Mechanics to very Small Cracks or Cracks in the Early Stage BT - Proc. 2nd Int. Conf Mech. Behav. of Materials, (1976).

[2.15] B. Langer, Design of Pressure Vessels for Low-Cycle Fatigue, J. Basic Eng. (1962). doi:10.1115/1.3657332.

[2.16] L. De Baglion, J. Mendez, Low cycle fatigue behavior of a type 304L austenitic stainless steel in air or in vacuum, at 20 °C or at 300 °C: Relative effect of strain rate and environment, Procedia Eng. 2 (2010) 2171–2179. doi:10.1016/j.proeng.2010.03.233.

[2.17] A. Morley, A. McLennan, Statistical Analyses of Austenitic Stainless Steel High Cycle Fatigue Data to Support a Revised Design Factor for Design Fatigue Curve Development, in: Vol. 1 Codes Stand., American Society of Mechanical Engineers, 2022. doi:10.1115/PVP2022-84249.

[2.18] G. Blatman, T. Métais, J.-C. Le Roux, S. Cambier, Statistical analyses of high cycle fatigue French data for austenitic SS; PVP2014-28409, in: 2014. doi:10.1115/PVP2014-28409.

[2.19] J. a Le Duff, A. Lefrançois, J.P. Vernot, D. Bossu, A. Lefrancois, Effect of loading signal shape and of surface finish on the low cycle fatigue behavior of 304L stainless steel in PWR environment; PVP2010-26027, in: Proc. ASME PVP 2010, 2010. doi:10.1115/PVP2010-26027.

[2.20] EDF, Chemical and mechanical characterization of the materials purchased for the study of the fatigue behaviour of austenitic stainless steels, 2001.

[2.21] ASME, Section III Division 1, Rules for Construction of Nuclear Power Plant Components, in: Boil. Press. Vessel Code, American Society of Mechanical Engineers, New York, 2021.

CHAPTER 3 INCEFA-SCALE PROGRAM ON HOLLOW CYLINDRICAL SPECIMENS

This Chapter describes the influence of specimen geometry and internal pressure on fatigue life, focusing on the unique mechanistic drivers of crack growth and hoop stress within hollow specimen configurations, by Luc Doremus, Louise Casulli, and Zaiqing Que.

3.1 INTRODUCTION

Small specimen fatigue testing is challenging in simulated light water reactor (LWR) coolant environments at elevated temperatures and pressures. This occurs due to the challenges with using on-specimen extensometry in the wetted environment. Two approaches for isothermal uniaxial testing in such environments have been developed: use of an autoclave to contain the environment around the specimen, which is conventionally of a solid design (for example circular cross-section, parallel sided gauge length); and use of a thin-walled hollow or tubular specimen, where the coolant environment passes through the bore of the specimen.

It is often assumed that fatigue lives measured using these two specimen designs are equivalent. However, isothermal, strain-controlled, fatigue endurance tests on a single heat of Type 304L stainless steel showed fatigue lives differed between these specimen designs in high-temperature PWR coolant, with hollow specimens consistently giving shorter lives [3.1].

Furthermore, the INCEFA-PLUS Project reported a discrepancy, beyond typical laboratory to laboratory data scatter, between different laboratories using hollow specimens of different designs [3.2]. Two of the three laboratories produced hollow specimen data consistent with the observations of shorter life described in reference [3.3], with one laboratory showing data consistent with the average solid specimen fatigue life for a given strain amplitude. In addition, several studies showed opposite conclusions on this topic. Gill et al. [3.3] showed a difference between hollow and solid designs attributed to an effect of internal pressure and subsequent ratcheting under repeated plastic deformation. They also highlighted a geometrical feature which could contribute to reduce the fatigue lives: plastic strains exhibit a small increase in the region just after the shoulder. Bae et al. [3.4] agreed on the geometrical influence on fatigue life but pointed out that the difference on the crack propagation stage where a larger internal plastic strain near the crack tip on hollow specimens led to shorter lives. On the contrary, Asada et al. [3.5] and Kanasaki et al. [3.6] demonstrated that no differences should be expected between these two fatigue test approaches. This inconsistency is yet unresolved and it resulted at the end of the INCEFA-PLUS Project in the limited use of the hollow specimen data for model development.

INCEFA-SCALE has included a test programme designed to study geometrical differences between hollow specimen designs with the aim of generating sufficient understanding of the test method to enable full use of the data for model development. Furthermore, this research has provided additional data that can be used to define the influence of different small specimen geometries and highlight potential conservatism on the mean fatigue curve presented in NUREG/CR-6909, Rev.1 [3.7]. Indeed, most of the fatigue test results used in the NUREG/CR-6909, Rev.1 report to build the mean fatigue curve were produced using hollow specimens.

The testing has been carried out with different environments, specimen geometries, and internal pressure. The main focuses of the program have been to:

1. Evaluate the influence of internal pressure on the fatigue life.
2. Identify differences in the crack propagation stage due to geometrical features between hollow and solid designs.
3. Highlight the influence of hoop stress to explain the differences in fatigue lives between the hollow specimen designs.

3.2 DEFINITION OF THE EXPERIMENTAL PROGRAM

This experimental program has been entirely performed on INCEFA-SCALE common material Type 316L austenitic stainless steel.

Hollow specimen strain-controlled fatigue tests use a hollow cylindrical specimen (Figure 3.1) to contain the flowing simulated PWR primary coolant and are controlled by a gauge length extensometer.

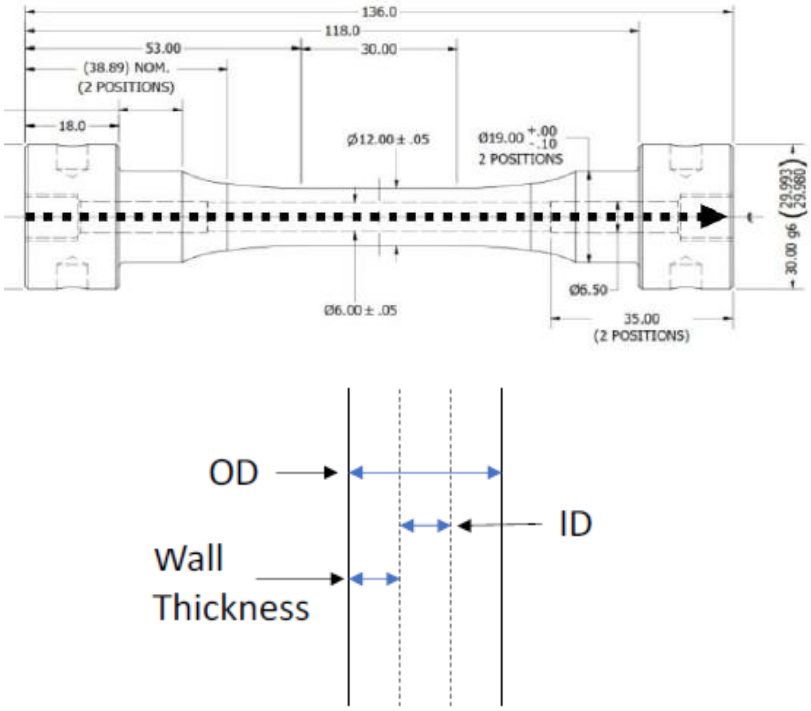

Figure 3.1. Hollow specimen.

As stated above, the testing program reported here is based on three hypotheses to evaluate the effect of specimen geometry and internal pressure/hoop stresses.

The first hypothesis infers that crack initiation is promoted on hollow specimens tested in PWR environments because of an increased Von Mises strain due to the contribution of radial and hoop stresses generated by internal pressure. This hypothesis has been analysed by testing hollow specimens with an internal pressure of 200 bar. To remove the influence of a corrosive PWR environment, tests were carried out in standard deoxygenated water at ambient temperature, which will still allow the internal pressures to be achieved. Table 3.1 gives the dedicated test matrix. For these tests, fatigue life is defined as the leakage occurs. Since the test

numbers were limited (6 tests), outer diameter and inner diameter were identical for all specimens. It has analytically been calculated using elastic theory that 200 bar generates radial stresses σ_r = -20 MPa and hoop stresses σ_θ = 43 MPa on this geometry. Two strain amplitudes are investigated: 0.3% and 0.6%. At 0.3%, the influence of internal pressure is expected to be more important because it should mainly affect the crack initiation stage which constitutes the larger part of the fatigue life at this strain amplitude. However, testing at 0.6% is of interest to evaluate the impact on fatigue life when the crack initiation stage has a lower impact on fatigue life.

One reference test without internal pressure was carried out at 0.3%. Other test results on the same hollow geometry, but in air (see second hypothesis below) were also used as reference. The aim of this reference air test alongside that in the deoxygenated water was to check the absence of the deoxygenated water environmental effect compared to air testing.

Strain amplitude (%)	Environment	Internal pressure (bar)	Temperature (°C)	wall thickness (mm)	OD (mm)	ID (mm)	σr (MPa)	σθ (MPa)	Surface finish in the OD
0,3	deoxygenated water	200	20	2	10	6	-20	43	Polished
0,3	deoxygenated water	200	20	2	10	6	-20	43	Polished
0,3	deoxygenated water	200	20	2	10	6	-20	43	Polished
0,6	deoxygenated water	200	20	2	10	6	-20	43	Polished
0,6	deoxygenated water	200	20	2	10	6	-20	43	Polished
0,3	deoxygenated water	-	20	2	10	6	-	-	Polished

Table 3.1. Test matrix to evaluate the influence of internal pressure.

The second hypothesis highlights that due to its specific geometry, crack propagation is shorter in a hollow specimen. Indeed, the wall thickness of hollow specimen is often below 3.0 mm, in comparison with solid specimen diameters (higher than 5.0 mm) [3.8]. The hollow geometry also generates differences in stress intensity factor which could lead to faster crack growth rate in the radial direction through the thickness than in the hoop direction at the surface. Table 3.2 presents the test matrix for this hypothesis. Tests were carried out at ambient temperature, with high strain amplitudes (0.6% and 1.0%) in order to reduce the scatter due to crack initiation. Different wall thicknesses (2.0 mm, 2.5 mm, and 4.0 mm) were tested to evaluate their impact on fatigue life on this geometry since no significant differences on fatigue lives were observed during the INCEFA-PLUS Project [3.2] where solid specimens with diameters varying from 5 mm to 9 mm were used. A strain amplitude of 0.3% has also been tested to serve as reference for the first hypothesis test matrix and evaluate the impact of the crack propagation stage at a lower strain amplitude. The fatigue life is defined here are as a 25% load drop since they are performed without internal pressure. Therefore, the comparison with solid specimens is based on the same fatigue life definition.

Strain amplitude (%)	Environment	Internal pressure (bar)	Temperature (°C)	wall thickness (mm)	OD (mm)	ID (mm)
0,3	air	-	20	2	10	6
0,3	air	-	20	2	10	6
0,6	air	-	20	2	10	6
0,6	air	-	20	2	10	6
1	air	-	20	2	10	6
1	air	-	20	2	10	6
0,3	air	-	20	2,5	10	5
1	air	-	20	2,5	10	5
1	air	-	20	2,5	10	5
0,3	air	-	20	4	12	4
0,6	air	-	20	4	12	4
0,6	air	-	20	4	12	4

Table 3.2.Test matrix to evaluate the influence of wall thickness and specimen design.

Finally, it is postulated that difference in lives with hollow specimens originate from differences in the hoop stresses on the specimens. Indeed, during the INCEFA-PLUS Project, the two labs showing comparable results used the same wall thickness for their specimens while the third lab using hollow geometry had a different wall thickness. Therefore, different hoop stresses were generated during the tests. Using the same experimental procedure and the same test conditions in specimens with different wall thicknesses should therefore generate different fatigue lives. The tests carried out to check this hypothesis are presented in Table 3.3.

Strain amplitude (%)	Environment	Internal pressure (bar)	Temperature (°C)	wall thickness (mm)	OD (mm)	ID (mm)	σr (MPa)	σθ (MPa)
0.3	PWR	150	300	3	12	6	-15	25
0.3	PWR	150	300	1.5	12	9	-15	54
0.3	PWR	150	300	1.5	12	9	-15	54
0.3	PWR	200	300	3	10	4	-20	28
0.3	PWR	200	300	1.4	10	7.2	-20	63
0.3	PWR	200	300	1.4	10	7.2	-20	63
0.4	PWR	150	300	3	12	6	-15	25
0.4	PWR	150	300	1.5	12	9	-15	54
0.4	PWR	150	300	1.5	12	9	-15	54
0.4	PWR	200	300	3	10	4	-20	28
0.4	PWR	200	300	1.4	10	7.2	-20	63
0.4	PWR	200	300	1.4	10	7.2	-20	63

Table 3.3. Test matrix to evaluate the influence of hoop stresses.

Tests were performed in PWR environment and two different ranges of hoop stresses were targeted: 25-30 MPa and 55-65 MPa. Two range of wall thickness (around 1.5 mm and 3.0 mm) and two values of internal pressure are used to achieve these range of hoop stresses. Two values of outer diameter (10 mm and 12 mm) were also used to evaluate their influence considering

identical values of wall thickness and hoop stress. It is noted that the PWR environment is used for these tests with the aim of producing some test results on hollow specimen to be used for model development. Fatigue life for PWR testing on hollow specimens is determined when leakage occurs.

3.3 EXPERIMENTAL FATIGUE LIFE RESULTS

The hypothesis that internal pressure promotes crack initiation appears to be verified by the results presented in Figure 3.2. In that, the hollow specimens tested in air or deoxygenated water at 1 bar generally show longer lives than those tested at 200 bar.

The reference test in deoxygenated water at 1 bar results in a comparable fatigue life to the tests in air, confirming the absence of an effect of the deoxygenated water environment on fatigue life. The effect of internal pressure is therefore evaluated by comparing tests at 200 bar in deoxygenated water and tests in air.

The decrease in fatigue life is on average 1.6 between pressurized and non-pressurized hollow specimens and it is comparable at both strain amplitudes.

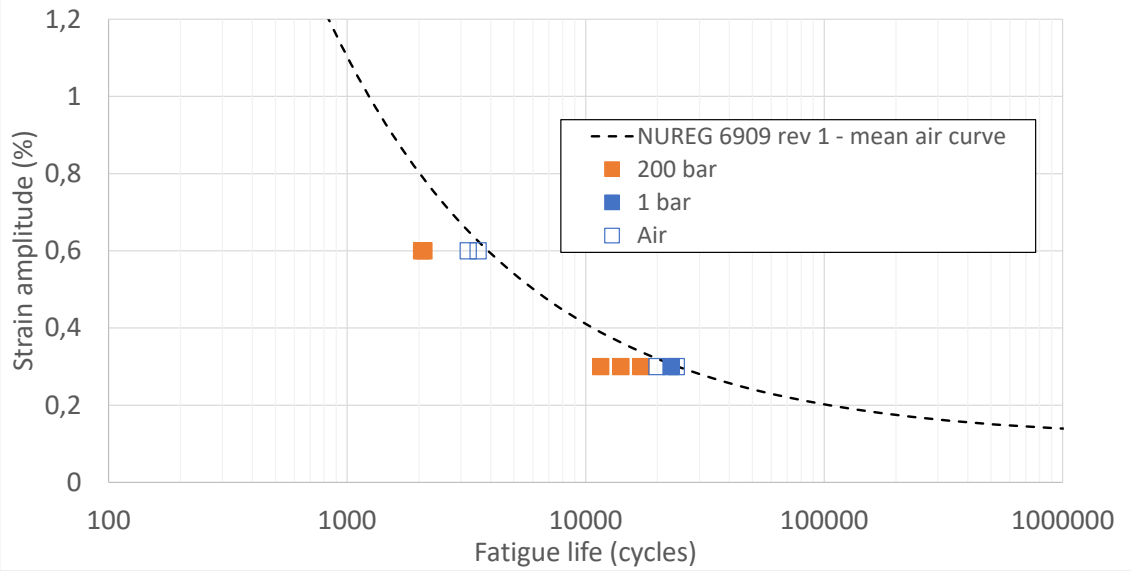

Figure 3.2. Influence of internal pressure.

Figure 3.3 shows the results aimed at evaluating the influence of hollow specimen geometry (especially wall thickness) versus solid specimens. Hollow specimens with wall thicknesses of 2.0 mm, 2.5 mm, and 4.0 mm have been tested in air at 1.0%, 0.6%, and 0.3% strain amplitudes. Fatigue tests on solid specimens with diameters of 8.0 and 9.0 mm were carried out in the framework of the general test program of INCEFA-SCALE are also provided for comparison.

The tests on hollow specimens with 2.0 mm and 2.5 mm wall thicknesses, at 1.0% strain amplitude, showed fatigue lives that were consistent with laboratory-to-laboratory variation. Because the difference in fatigue life was expected to affect the crack propagation stage, this strain amplitude was chosen in order to reduce the scatter inherent with crack initiation. The fatigue life at this high level of strain amplitude seems, however, too low to enable the separation of the influence of wall thickness from standard scatter.

At lower strain amplitudes such as 0.6% and 0.3%, differences due to specimen geometry are clearly visible between 2.0 mm and 4.0 mm wall thicknesses: the thicker the wall thickness, the higher the fatigue life. However, one specimen tested at 0.3% with a wall thickness of 2.5 mm exhibits the highest fatigue life. This could be due to the scatter on crack initiation duration inherent at that strain amplitude.

For all three strain amplitudes, solid specimens fatigue lives are higher than hollow specimens except for the hollow specimen tested at 0.3% with a wall thickness of 2.5 mm. This result highlights that even in an air environment the geometrical design of the specimen has a significant impact on the fatigue life. However, the origin of this result must be checked before being able to evaluate a conservatism in fatigue curves or models based on hollow specimens.

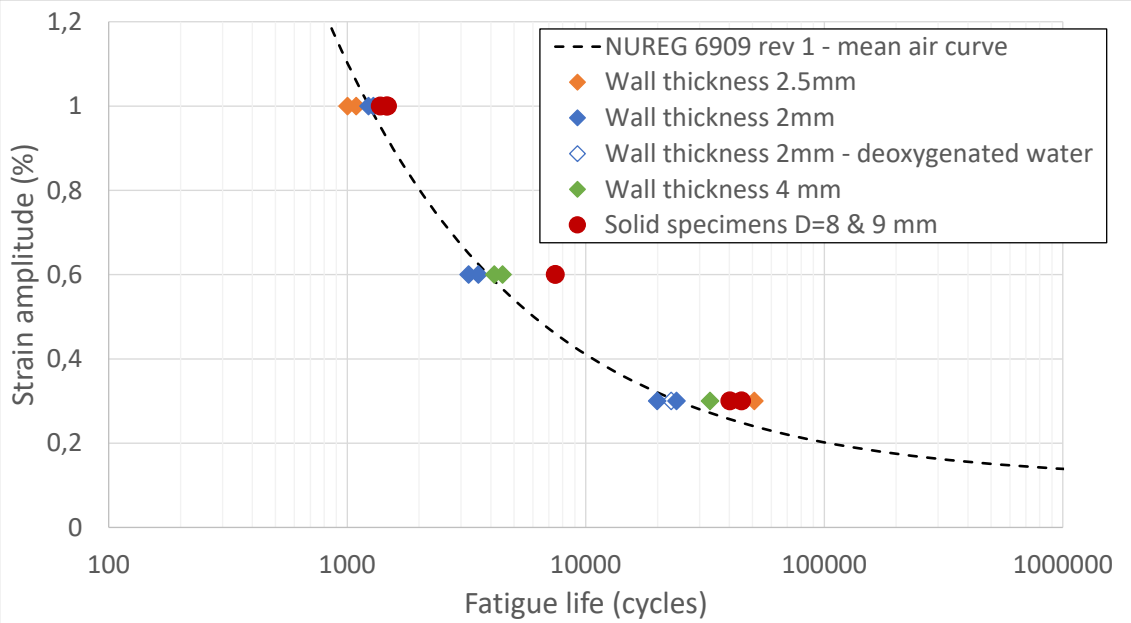

Figure 3.3. Influence of specimen geometry.

The third hypothesis under investigation states that hoop stresses promote crack initiation. Tests have been performed on hollow specimens in a PWR environment with different wall thicknesses and internal pressures, resulting to two ranges of hoop stresses: 25-30 MPa and 55-65 MPa. Results shown in Figure 3.4 confirm that the higher the hoop stress the lower the fatigue life for both strain amplitudes tested. The decrease in fatigue life is on average 2.3 at 0.3% strain amplitude and 1.9 at 0.4% strain amplitude between low and high ranges of hoop stresses. Finite element calculations and striation counting presented below were used to further analyse if hoop stresses are truly the origin of these results.

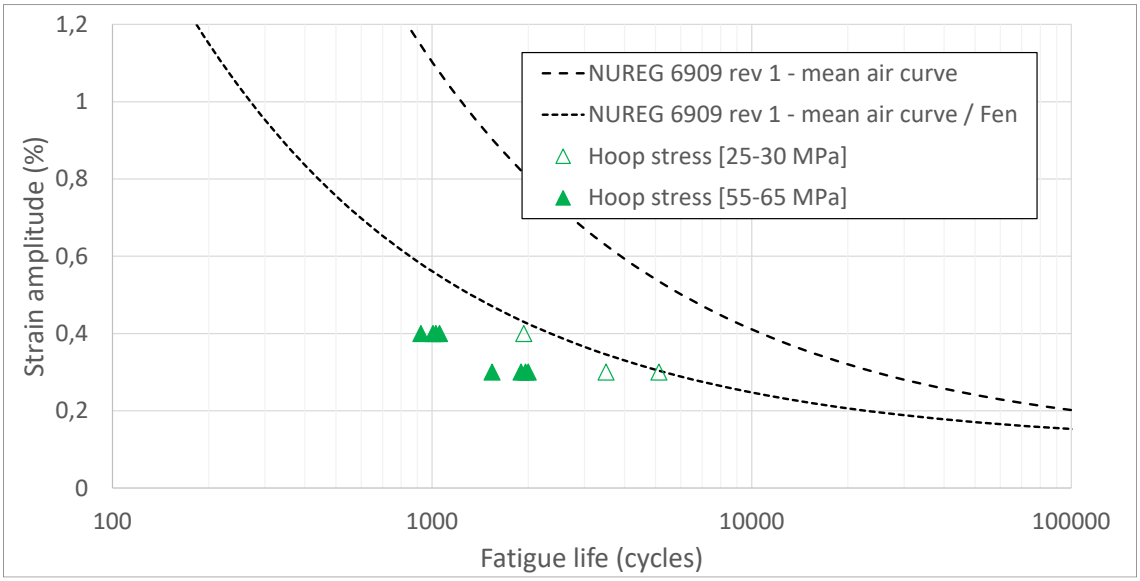

Figure 3.4. Influence of hoop stresses.

3.4 MODELLING AND MECHANISTIC UNDERSTANDING OF FATIGUE CRACK GROWTH IN HOLLOW SPECIMENS

3.4.1 MODELLING

Finite element analyses have been performed to model crack propagation to improve understanding of the test results and validate the experimental conjectures. The analyses have been performed with Cast3M software [3.9] using geometries of hollow specimens and a solid specimen to investigate the differences between them. The hollow designs are chosen from Table 3.1, Table 3.2, and Table 3.3. The test conditions were replicated in these numerical simulations. Calculations have been conducted with and without internal pressure to evaluate its effect on the fatigue lives (first hypothesis). Then, the crack propagation is compared for the different geometries (second hypothesis). Finally, the impact of hoop stresses is assessed on different specimens' fatigue lives (third hypothesis). Table 3.4 shows the analysed configurations.

Case	Strain amplitude (%)	Environment	Internal pressure (bar)	Temperature (°C)	Wall thickness (mm)	OD (mm)	ID (mm)
1	0.3	air	-	20	2	10	8
2	0.3	air	200	20	2	10	8
3	0.6	air	-	20	2	10	8
4	0.6	air	200	20	2	10	8
5	0.3	air	-	20	-	9	-
6	0.3	air	-	20	2	10	6
7	0.3	air	-	20	3	10	4
8	0.3	air	-	20	3	12	6
9	0.3	air	-	20	4	12	4
10	0.3	PWR	150	300	3	12	6
11	0.3	PWR	150	300	1.5	12	9
12	0.4	PWR	150	300	3	12	6
13	0.4	PWR	150	300	1.5	12	9

Table 3.4. Analysed configurations.

Similarly to experimental observations, an initial crack was modelled on the inner skin of the hollow specimens, to grow through the wall thickness. For the solid specimen, the crack is modelled on the external skin. The cracks were modelled as surface-breaking and semi-circular (a/c = 1) and with an initial depth of 0.5 mm.

A quarter of the geometry was modelled considering the symmetries. The model of the specimens was defined from the extensometer position plane (X = 5 mm) to the lateral symmetry plane (normal UX). It is assumed that the crack has no impact on the loading control, and it was verified on a model of the whole specimen that the strain is homogenous on the extensometer's position plane (see Figure 3.5). Figure 3.6 shows most of the studied geometries, described in Table 3.4.

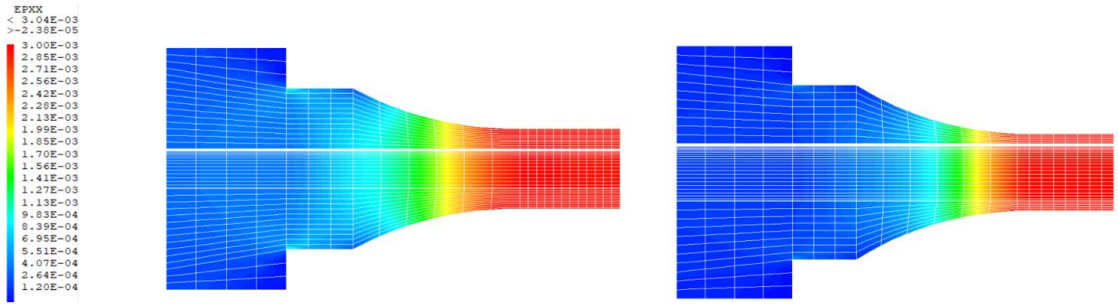

Figure 3.5. Homogeneous strain in the gage length.

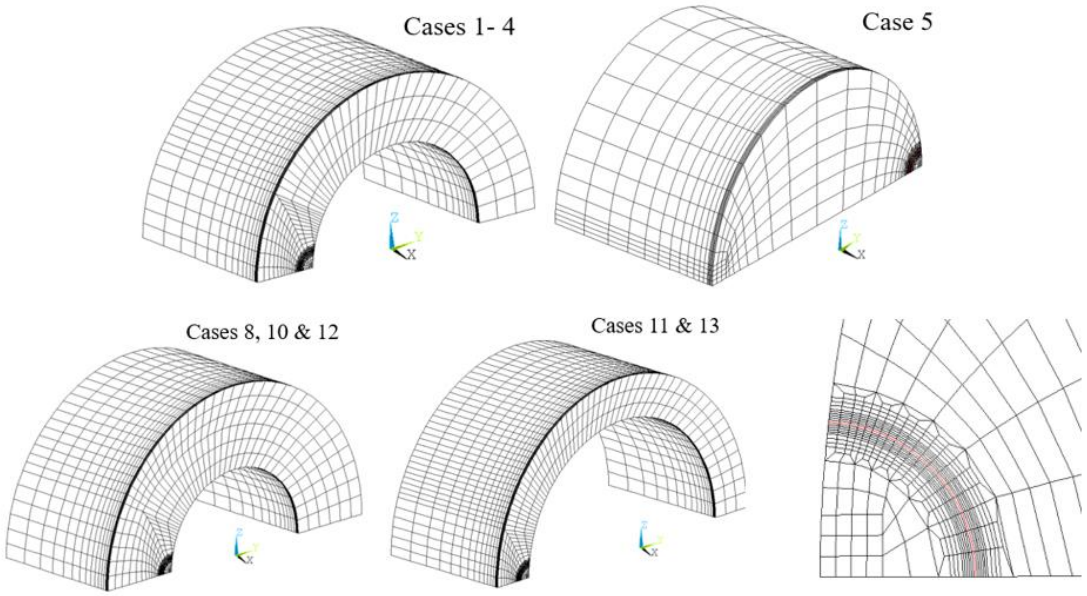

Figure 3.6. Some of the finite element models.

3D quadratic elements CU20 were mostly used. The mesh was refined around the crack tip, and the surrounding elements were defined perpendicular to crack direction. The mesh around the crack has been modelled similarly for all the studied geometries. The boundary conditions were as follows (see Figure 3.7):

- The axial displacement applied to the extensometer surface (UX direction).
- Symmetry conditions imposed on the axial symmetry plane (normal UZ) and on the lateral symmetry plane (normal UX), except for the crack surface.

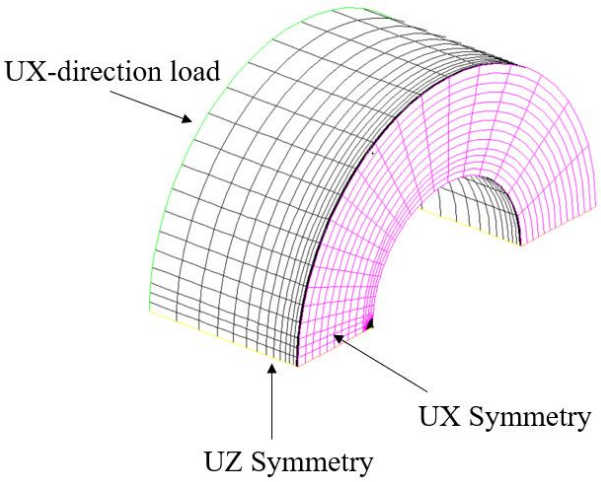

Figure 3.7. Boundary conditions.

The ΔJ approach was chosen to compute the iterative crack growth. Thus, the applied displacement corresponds to the experimental strain amplitude of a tension-compression cycle. The G-theta method is used to calculate the J-integral around the crack. The variation of the stress intensity factor is calculated from the following expression:

$$\Delta K_J = \sqrt{\Delta J \cdot E^*} \qquad \text{eq. 3.1}$$

with:

$$E^* = \frac{E}{1-\nu^2} \qquad \text{(for planar strain)} \qquad \text{eq. 3.2}$$

The effective variation of the stress intensity factor is calculated using the stress ratio ($R = K_{min}/K_{max}$); the load ratio function is provided in RSE-M Code, Appendix 5.6 [3.10].

$$\Delta K_{eff} = f(R)\Delta K = \frac{1}{1-\frac{R}{2}}\Delta K \qquad \text{eq. 3.3}$$

The stress ratio R is impacted by the pressure; this promotes crack propagation which contributes to reduce the fatigue life of specimens (in relation with the first hypothesis). To account for this effect, an elastic calculation was carried out to determine the minimum stress intensity factor K_{min} and the maximum stress intensity factor K_{max} considering the pressure applied to the inner skin and to the crack surface. The stress ratio R was then updated for each calculation step. For the calculations without the pressure, the stress ratio is R = -1 considering the conditions of symmetric tension-compression loading. These conditions also imply that the propagation mode I is preponderous.

The crack growth lengths (da) were then calculated with a Paris' law, with the coefficients C and n also extracted from RSE-M code, Appendix 5.6 [3.10] for PWR and air test conditions. The C coefficient is determined with the average law to be closer to the test results.

Paris' law	Austenitic steel – air	Austenitic steel – PWR environment
$\frac{da}{dN} = C \cdot \left(\Delta K_{eff}\right)^n$	Average law: $C = 2.7 \cdot 10^{-13}$	Average law: $C = 6.5 \cdot 10^{-13}$
	$n = 4$	$n = 4$

Table 3.5. Paris' law coefficients [3.10].

The G-theta method applies for monotonically increasing loadings only, therefore a reduced cyclic stress strain curve was used following ΔJ methodology [3.11]. The behaviour of 316L stainless steel under cyclic loadings is defined as elastic-plastic with kinematic hardening. Studies [3.12] have shown that 316L exhibits both cyclic hardening and cyclic softening under cyclic loading that makes the behaviour of this material difficult to model. The stress and strain amplitudes over the cycles are determined with stabilized states to consider the load history effect. The reduced cyclic curves were established from the stepped tests provided in [3.12].

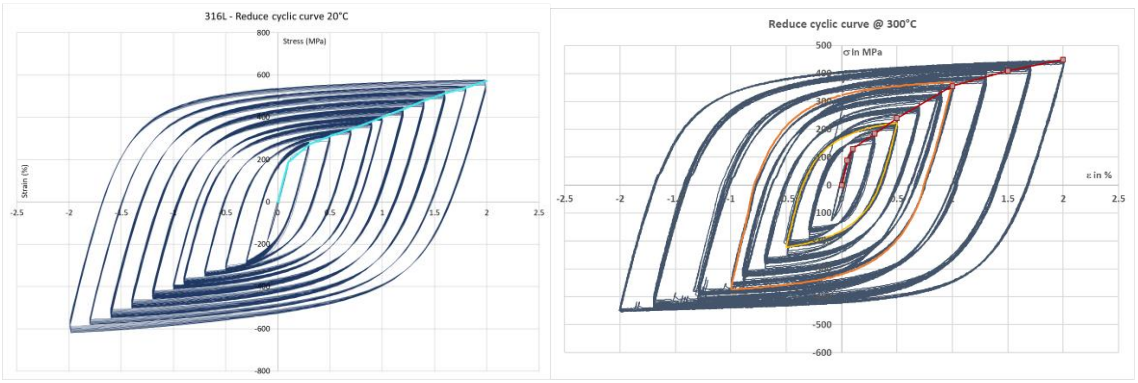

Figure 3.8. 316L - Reduced cyclic curves - 20 °C and 300 °C.

The J-integral values were smoothed along the crack tip to avoid excessive oscillations of the crack propagation. For each iteration, this maximal crack growth length determined the number of cycles (dN) considered. Then, for each individual node of the crack tip, the lengths da were applied in each normal plane to the crack tip updated at each iteration using the Gram-Schmidt orthonormalization procedure. The new crack is then adjusted with a polynomial function. This adjustment allows to add more nodes to the crack front to make it smoother. The propagation was modelled through remeshing which allows to update the crack shape.

The crack is incremented until it achieved 80% of the thickness. Figure 3.9 presents fractography of a hollow specimen with ID = 4.0 mm, wall thickness = 3.0 mm in PWR conditions as described in Table 3.4. To compare the fractography with the calculations, the crack front shape evolution is superimposed on Figure 3.9 for calculation case 8. The simulated crack front evolution appears globally consistent with the experimental observations: the crack propagation is fostered through the thickness.

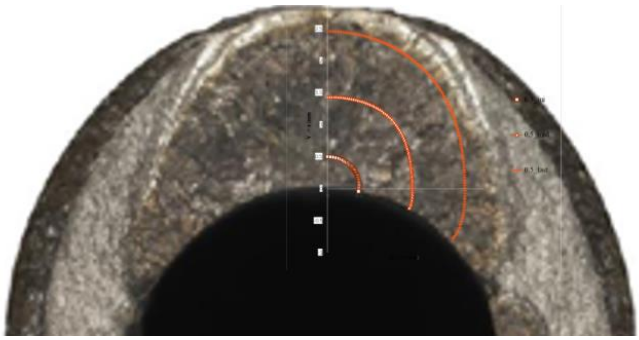

Figure 3.9. Fractography – ID = 4.0 mm – PWR – case 6 with three corresponding calculated crack front shapes.

Figure 3.10 presents a comparison between solid specimen's fractographies and the calculated crack front shape evolution. The calculated crack front evolution appears globally consistent with the experimental observations.

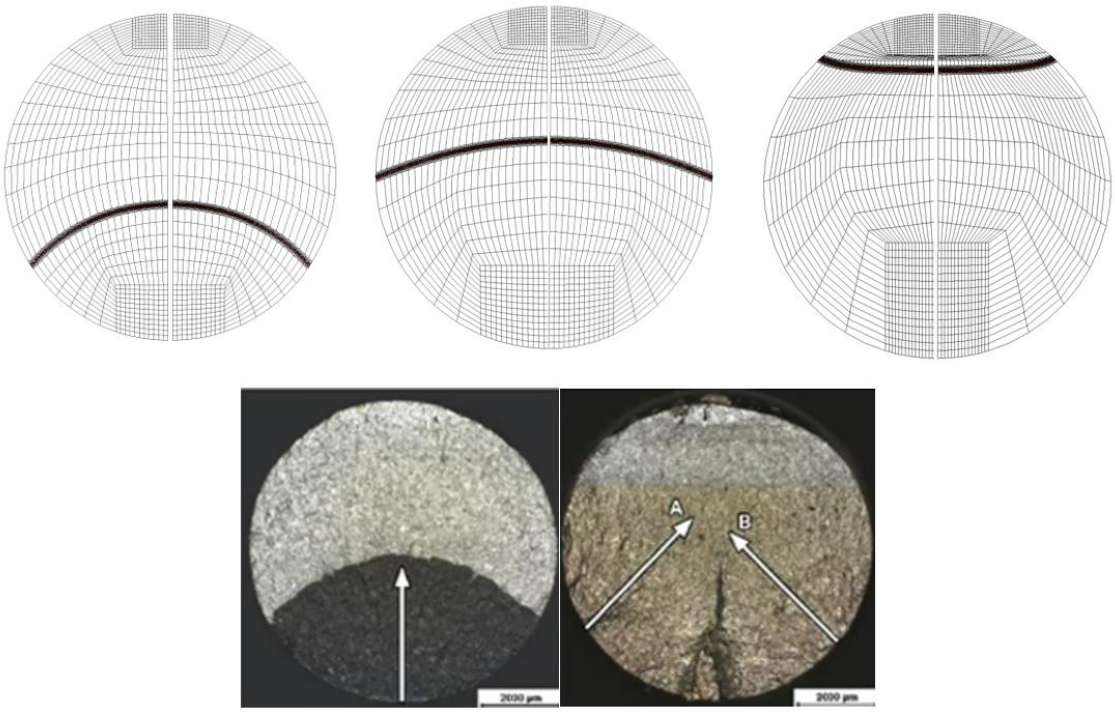

Figure 3.10. Solid specimen – Crack front shapes comparison between experiment and calculations.

3.4.2 MECHANISTIC UNDERSTANDING

The testing program was also be supported by mechanistic analysis including fractographic examination of the fracture surface to enable more detailed analysis of test results through enhanced understanding of the material behaviour.

The first aim was to identify initiation sites and overall crack morphology and to assess near surface deformation and interaction/correlation with nucleation. In addition, striation counting was performed on selected specimens to establish nucleation time to short defect depths and estimate fatigue crack growth rates. The intention was to assess if observed changes on fatigue life were due to shortened nucleation life, propagation life, or some combination of the two.

Striation counting is a widely applied technique in fatigue failure investigations where it is typically used to infer information on crack progression, including the estimation of propagation rates and number of applied loading cycles. For the INCEFA-SCALE Project, it was anticipated that a knowledge of the progression of cracks in fatigue specimens will be required to support the interpretation of test data. Indeed, the implementation of in-situ monitoring of crack growth during a fatigue test would be very complicated since no specific and unique crack starter could be identified before the test. Therefore, striation data represents a valuable way of reconstructing the crack history following the conclusion of the experiment. Moreover, striation results are expected to be robust since two round robins [3.13] between project partners were carried out at the beginning of the project resulting in a standardized procedure to perform this complex characterization.

However, the determination of the main crack path on the fracture surface was challenging for hollow specimens because several crack initiation sites from the inner surface were often observed, with an example shown in Figure 3.11. Therefore, the choice of the main crack path (red arrow in Figure 3.11) may differ from different SEM operators and influence the results comparison.

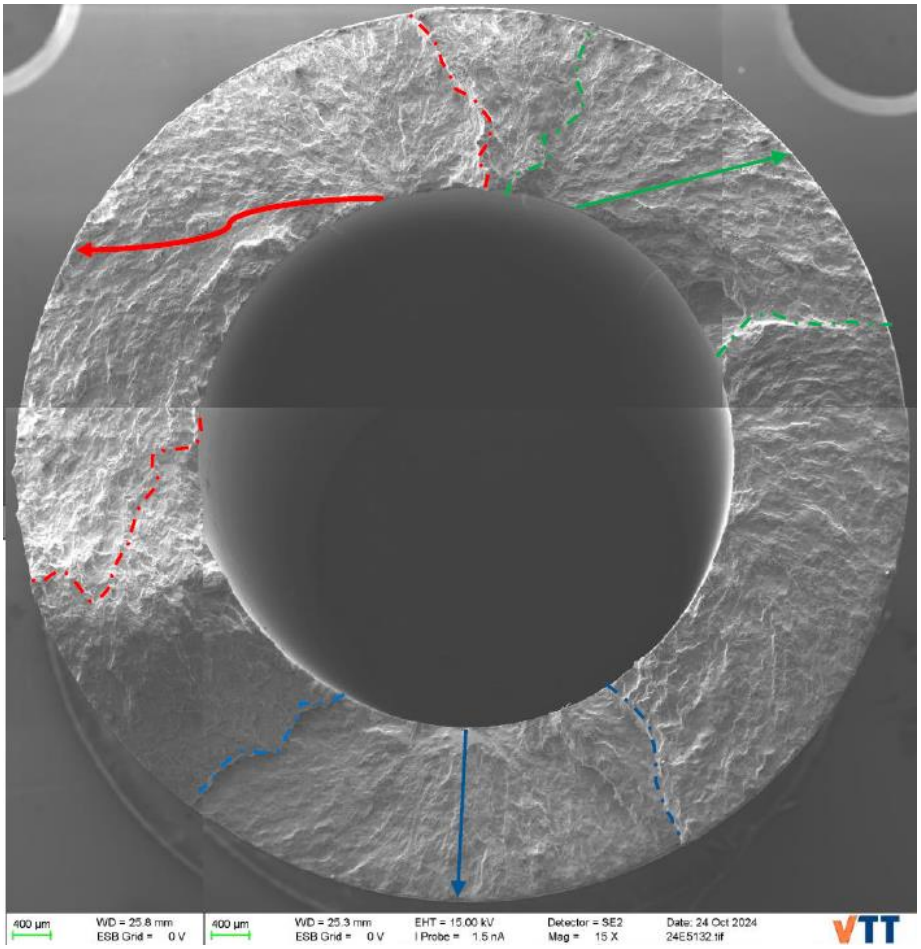

Figure 3.11. Determination of the main crack path on a hollow specimen.

Ratchetting is also a degradation mechanism that can happen during cycling of pressurized hollow specimens. Some experimental measurements were planned to assess its appearance. Pre and post-test dimension measurements of outer and inner diameter were requested to evaluate the evolution of the wall thickness during the fatigue test.

3.5 DISCUSSIONS

3.5.1 EFFECT OF INTERNAL PRESSURE

This Section aims to evaluate the effect of pressure on the crack propagation stage. It was expected that the pressure would slightly reduce the closure effect during the compressive part of the cycles, and so it may slightly reduce the crack propagation stage. This effect is shown by the reduction of the stress ratio R (calculated as explained in Section 3.4.1) which tended to decrease slightly the crack closure effect taken into account by the RSE-M R function (see Table 3.6).

Strain amplitude (%)	Pressure (bar)	Experimental number of cycles	Experimental Decrease of fatigue life (%)	Average stress ratio R	R function	Calculated decrease of fatigue life (%) – propagation stage
0.6%	200	≈2100	35%	-0.91	0.69	6%
	1	≈3300		-1.00	0.67	
0.3%	200	≈13000	40%	-0.95	0.68	11%
	1	≈22000		-1.00	0.67	

Table 3.6. Pressure effect - Comparison of fatigue life between experiment and calculations.

Figure 3.12 presents the FEA evolution of the crack depth a with and without pressure for the two strain amplitudes 0.3% and 0.6%. Figure 3.13 presents the crack growth rate da/dN against the crack depth a. These calculations underline that the crack propagation stage is not significantly impacted by pressure. Indeed, the percentages displayed in Table 3.6 indicate a small decrease in fatigue life for the propagation stage.

Table 3.6 indicates that the experimental decreases in total fatigue life due to internal pressure (initiation and propagation) were much higher: around 40% for the strain amplitude of 0.3% and about 35% for the strain amplitude of 0.6%. As a result, the fatigue life discrepancy between the experiment and the calculations suggests that the pressure impacts mainly the crack initiation stage.

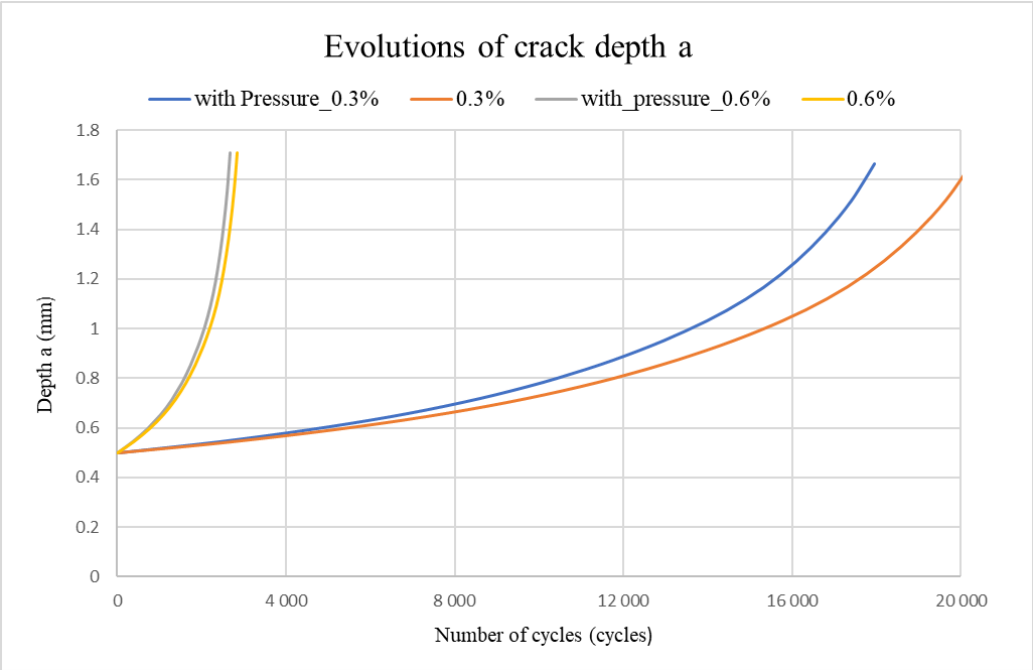

Figure 3.12. Crack depth evolutions with and without pressure for two strain amplitudes of 0.3% and 0.6%.

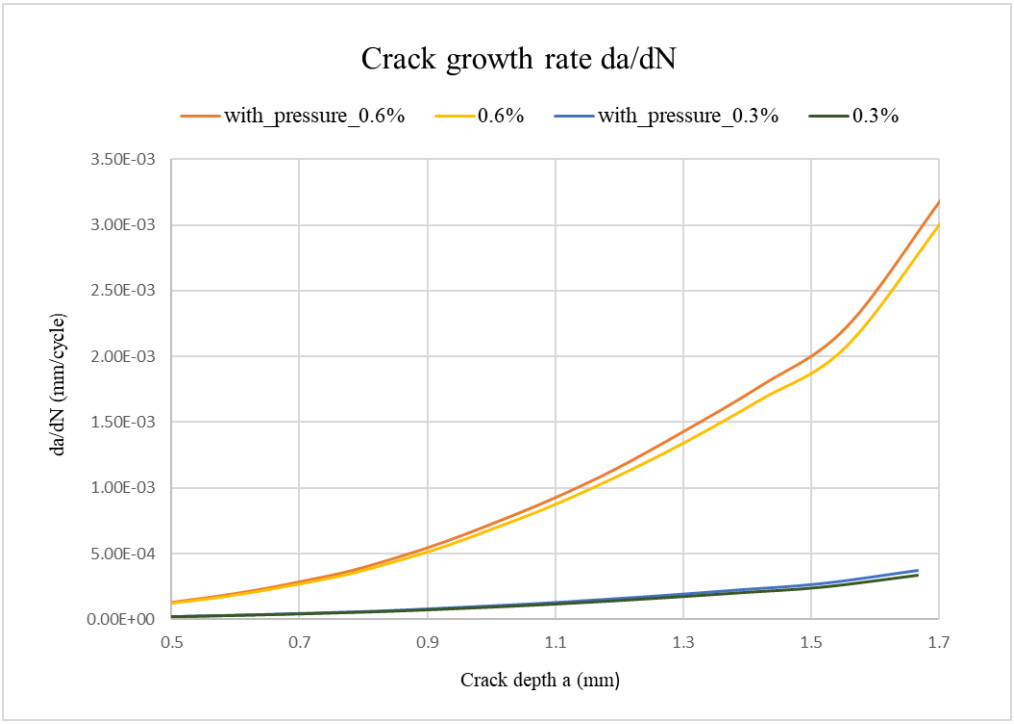

Figure 3.13. Crack growth rates with and without pressure for two strain amplitudes of 0.3% and 0.6%.

Therefore, this assumption was assessed using the striation counting performed on the fractured specimens. Figure 3.14 presents the striation counting for the specimen geometry types in Table 3.1 for two different test conditions:

- PSIPWR-11: pressure 1 bar in deoxygenated water;
- PSIPWR-10: pressure 200 bar in deoxygenated water.

The striation spacing evolutions were quite similar for the tests in deoxygenated water with and without pressure (see Figure 3.14) which supports that the crack propagation is not significantly impacted by the pressure.

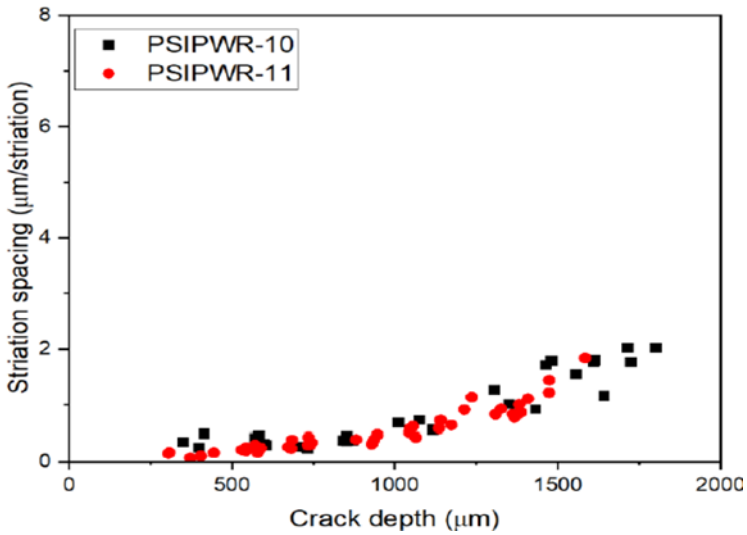

Figure 3.14. Evolution of striation spacing with and without pressure.

Thus, the experimental fatigue lives demonstrate that the pressure impacts significantly the initiation stage but not the propagation stage. The possible explanation is that crack initiation is promoted on hollow specimens because of an increased von Mises strain due to the contribution of the radial and hoop stresses generated by the internal pressure.

3.5.2 EFFECT OF SPECIMEN GEOMETRY

This Section aims to evaluate the effect of specimen geometry on the crack propagation stage. Three wall thicknesses of 2.0 mm, 3.0 mm, and 4.0 mm of hollow specimen geometry and one solid specimen are compared in air environment for two strain amplitudes: 0.6% and 0.3%. Table 3.7 compares the specimen's geometries.

Case	Specimen	Outer Diameter OD (mm)	Wall thickness t (mm)	ID/2t	Cross-section (mm²)
5	D9mm	9	-	-	63.6
6	TH_2mm	10	2	1.50	50.3
7	TH_3mm_OD10mm	10	3	0.67	66.0
8	TH_3mm_OD12mm	12	3	1.00	84.8
9	TH_4mm	12	4	0.50	100.5

Table 3.7. Geometry effect - Comparison of dimensions.

Figure 3.15 presents the crack growth rate da/dN over the crack depth a. For the hollow specimens, it was observed that the thicker the wall thickness, the slower the fatigue crack growth and the higher the fatigue life. It is interesting to note that for the same wall thickness, the smaller outer diameter implies a higher fatigue life. Case 7 shows a calculated propagation duration 7% longer than case 8.

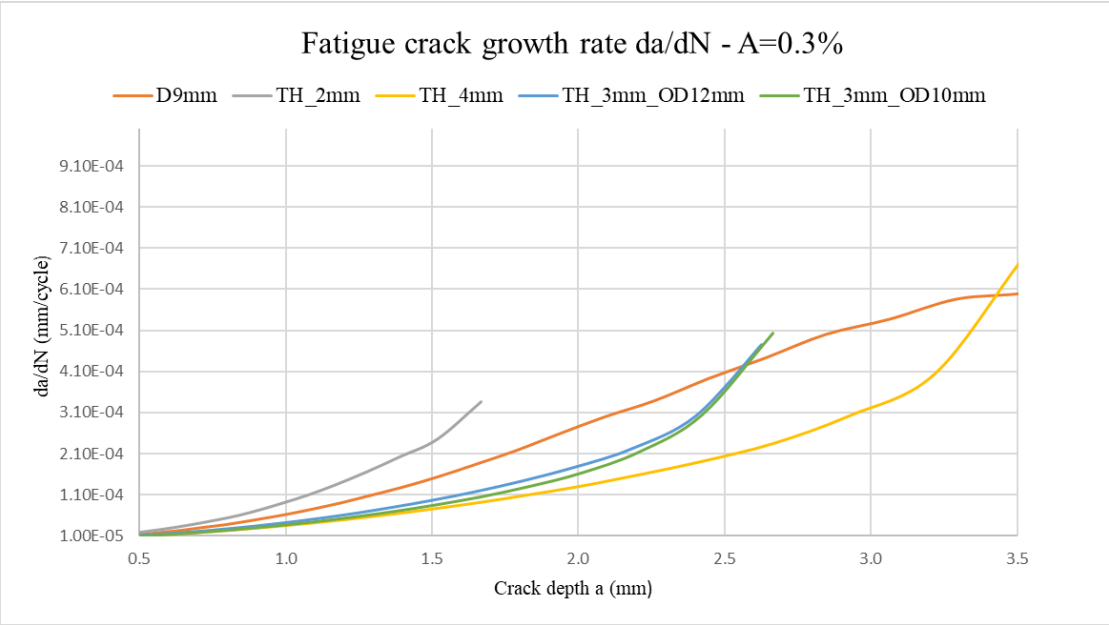

Figure 3.15. Crack growth rates for three hollow specimen geometries and one solid specimen under a strain amplitude of 0.3%.

Figure 3.16 presents the evolutions of striation spacing for two hollow specimens of thickness 3.0 mm (IRSN-18) and 2.0 mm (PSIPWR-8), both in air environment at 20 °C and under a strain amplitude of 0.3%. Table 3.8 presents the comparison between the experimental fatigue lives and the calculated propagation durations for these two specimens. The striation spacing confirms that the crack propagation rate is lower in a thicker hollow specimen, which leads to higher fatigue lives as displayed in Table 3.8.

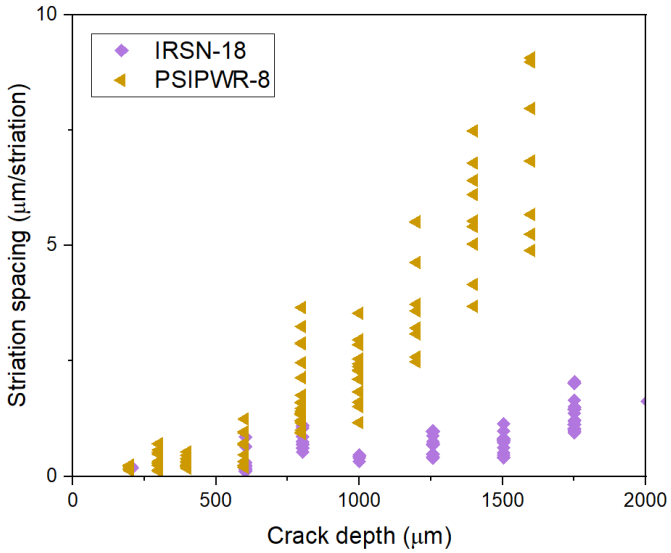

Figure 3.16. Evolution of striation spacing for two hollow geometry of thickness 2 mm and 4 mm.

Strain amplitude (%)	Geometry	Experimental number of cycles	Decrease of fatigue life (%)	Calculated number of cycles	Decrease of fatigue life (%) – propagation stage
0.3%	Th_3mm (IRSN-18)	50699	61%	45610	56%
	Th_2mm (PSIPWR-8)	19953		19975	

Table 3.8. Comparison of fatigue life between experiment and calculations for the two hollow specimens of thickness 3 mm (IRSN-18) and 2 mm (PSIPWR-8).

Figure 3.17 presents the evolution of the crack depth (a) between the 2.0 mm thick hollow specimen and a solid specimen of diameter 9.0 mm under a strain amplitude of 0.3%. The propagation duration is much higher in a solid specimen of diameter 9.0 mm than a hollow specimen with a wall thickness of 2.0 mm. This can be explained by the mechanism of fracture for hollow specimens: the fracture of one ligament triggers the total fracture of the hollow specimen, whereas for solid specimens, the distance for the crack to cover implies an increase of the propagation duration. On Figure 3.15, it can be noted that the crack growth rate evolution differs between the hollow specimens and the solid specimens.

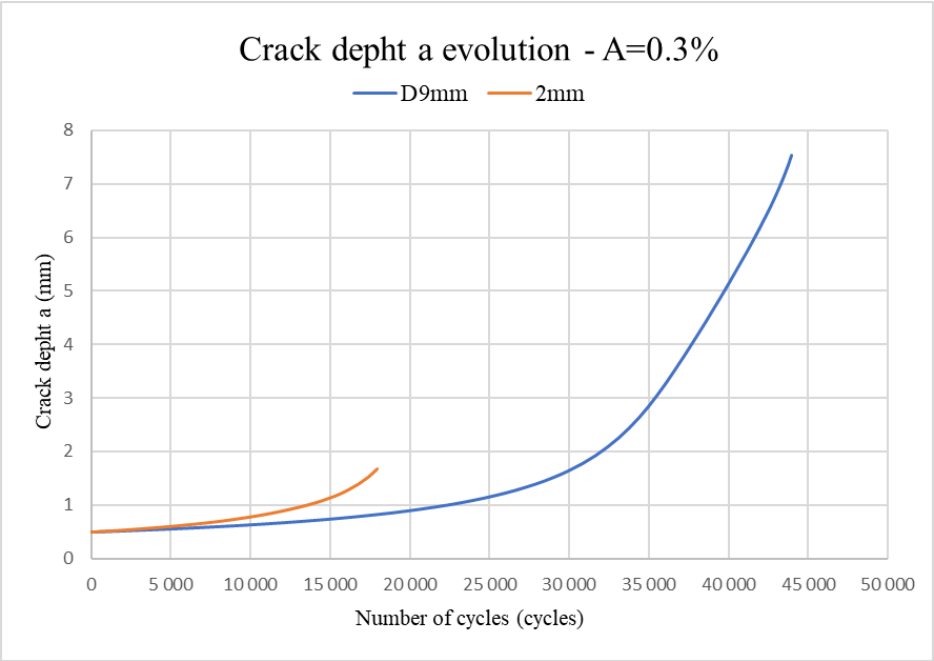

Figure 3.17. Crack depth evolutions between the 2.0 mm-thick hollow specimen and a solid specimen of diameter 9 mm under a strain amplitude of 0.3%.

Table 3.9 presents a comparison between the 2.0 mm-thick hollow specimen and a solid specimen of diameter 9.0 mm for the fatigue tests and the calculations. The calculated decreases of propagation duration are close to the experimental decreases of total fatigue life (initiation and propagation). It suggests that the experimental differences between hollow and solid specimens on fatigue lives are mainly due to the crack propagation stage.

Strain amplitude (%)	Geometry	Experimental number of cycles	Decrease of fatigue life (%)	Decrease of fatigue life (%) –propagation stage
0.6%	Solid_D9mm	≈7500	56%	45%
	Hollow_th2mm	≈3300		
0.3%	Solid_D9mm	≈42000	42%	40%
	Hollow_th2mm	≈22000		

Table 3.9. Comparison of fatigue life between experiment and calculations for 2.0 mm-thick hollow specimen and a solid specimen of diameter 9.0 mm.

These results support the hypothesis that the geometrical design of the specimen has a significant impact on the propagation stage and on the fatigue life.

3.5.3 EFFECT OF HOOP STRESS

This Section aims to evaluate the effect of hoop stresses on the crack propagation stage. Two hollow specimen geometries with wall thicknesses of 3.0 mm and 1.5 mm (see Table 3.3) are compared in PWR environment (150 bar) for two strain amplitudes: 0.4% and 0.3%. The two ranges of hoop stresses are then compared: 25-35 MPa (wall thickness of 3.0 mm) and 55-65 MPa (wall thickness of 1.5 mm). The calculated decreases of propagation duration of Table 3.10 are close to the experimental decreases of fatigue life (initiation and propagation). It suggests that the experimental differences on fatigue lives are mainly due to the crack propagation stage.

Strain amplitude (%)	Wall thickness (mm)	Experimental number of cycles	Experimental Decrease of fatigue life (%)	Average stress ratio R	R function	Calculated decrease of fatigue life (%) – propagation stage
0.3%	3.0	≈4250	55%	-0.93	0.683	40%
	1.5	≈1900		-9.90	0.690	
0.4%	3.0	≈2000	50%	-0.95	0.678	44%
	1.5	≈950		-9.93	0.683	

Table 3.10. Hoop stress effect - Comparison of fatigue life between experiment and calculations.

Figure 3.18 presents the crack growth rate da/dN over the crack depth a. The thickness effect is similar to the results presented in Section 3.5.2, Figure 3.15.

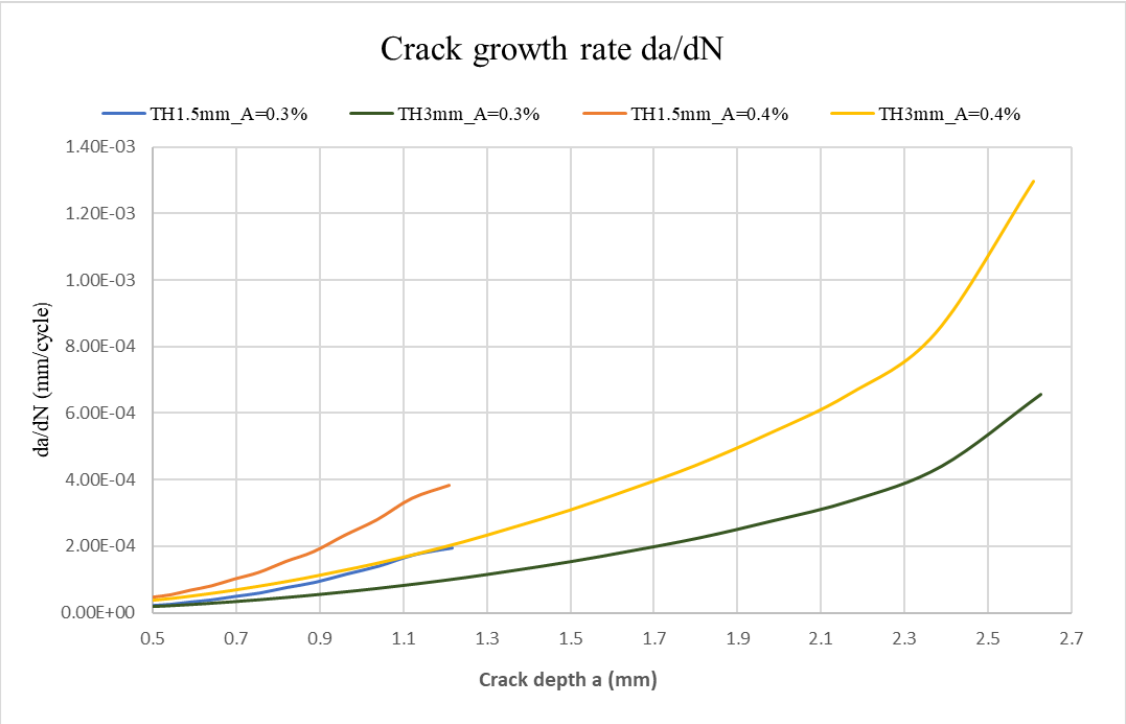

Figure 3.18. Crack growth rates for two hollow specimen geometries and one solid specimen under a strain amplitude of 0.3% and 0.6%.

Figure 3.19 presents the evolutions of striation spacing for two hollow geometries of thickness 1.5 mm (EDF_PWR_9) and 3.0 mm (EDF_PWR_6), both in PWR environment (300 °C and 150 bar) and under a strain amplitude of 0.3%. The striation spacing supports the hypothesis that the crack propagation rate is lower in a thicker hollow specimen, which leads to higher fatigue lives. Section 3.5.1 has shown that the pressure has a negligible impact on the propagation stage, the crack growth rate differences are then mainly due to the thickness differences, as presented in Section 3.5.2.

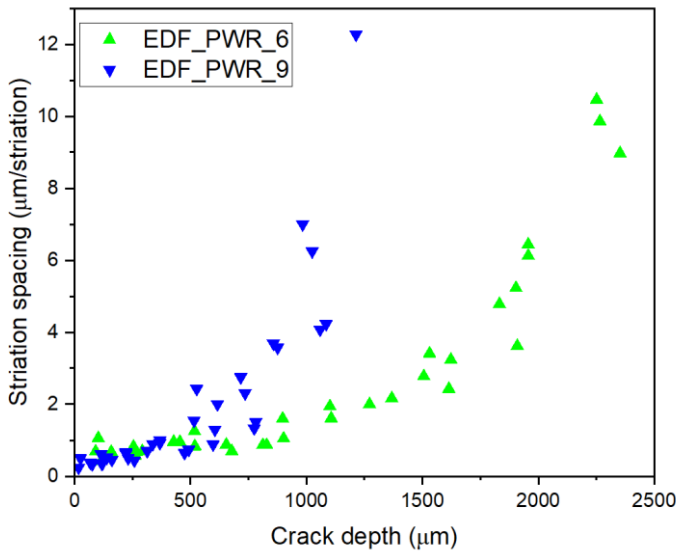

Figure 3.19. Evolution of striation spacing for two hollow geometry of thickness 1.5 mm and 3.0 mm.

3.6 CONCLUSIONS

A test program on hollow specimens combined with Finite Element Analysis and striation counting with the aim to evaluate several hypotheses enabled to highlight some differences in fatigue lives between solid and hollow specimens. The use of a hollow design may have a substantial influence on fatigue life because of the negative effect of hoop stresses (internal pressure) on the initiation stage and the important impact of specimen geometry (especially wall thickness) on the propagation stage. The crack initiation duration may also differ between a hollow and a solid specimen which could be an additional source of discrepancy between the hollow and the solid specimens. In conclusion, the use of hollow specimen geometries in fatigue design curve can be a source of conservatism.

REFERENCES

[3.1] M. Twite, N. Platts, A. McLennan, J. Meldrum, A. McMinn, Variations in Measured Fatigue Life in LWR Coolant Environments due to Different Small Specimen Geometries, in: Vol. 1A Codes Stand., American Society of Mechanical Engineers, 2016. doi:10.1115/PVP2016-63584.

[3.2] INCEFA-PLUS Consortium, S. Arrieta, T. Austin, M. Bruchhausen, W.-J. Chitty, R. Cicero, S. Cicero, S. Cuvilliez, L. De Baglion, G. Dundulis, C. Gourdin, C. Huotilainen, J.-C. Le Roux, J. Mann, W. Mayinger, A. McLennan, T. Métais, E. Miroslava, K. Mottershead, R. Novotny, F.J. Perosanz López, N. Platts, I. Procopio, N. Prompt, P. Spätig, M. Twite, M. Vankeerberghen, INCEFA-PLUS findings on Environmental Fatigue, INCEFA-PLUS Project, 2020. doi:10.5281/zenodo.4243979.

[3.3] P. Gill, P. James, C. Currie, C. Madew, A. Morley, An investigation into the lifetimes of solid and hollow fatigue endurance specimens using cyclic hardening material models in finite element analysis; PVP2017-65975, Am. Soc. Mech. Eng. Press. Vessel. Pip. Div. PVP. 1A-2017 (2017). doi:10.1115/PVP2017-65975.

[3.4] K.-H. Bae, S.-B. Lee, The effect of specimen geometry on the low cycle fatigue life of metallic materials, Mater. High Temp. 28 (2011) 33–39. doi:10.1179/096034011x12982896521562.

[3.5] S. Asada, K. Tsutsumi, Y. Fukuta, H. Kanasaki, Applicability of hollow cylindrical specimens to environmental assisted fatigue tests; PVP2017-65514, Am. Soc. Mech. Eng. Press. Vessel. Pip. Div. PVP. 1A-2017 (2017). doi:10.1115/PVP2017-65514.

[3.6] H. Kanasaki, I. Satoh, M. Koyama, T. Okubo, T.R. Mager, R.G. Lott, Fatigue and Stress Corrosion Cracking Behaviors of Irradiated Stainless Steels in PWR Primary Water, in: Fifth Int. Conf. Nucl. Eng. (ICONE 5), Nice, 1997.

[3.7] O.K. Chopra, G.L. Stevens, NUREG/CR-6909,Rev.1; Effect of LWR Water Environments on the Fatigue Life of Reactor Materials. Final Report, 2018.

[3.8] J.L. Smith, O.K. Chopra, Crack initiation in smooth fatigue specimens of austenitic stainless steel in light water reactor environments, Am. Soc. Mech. Eng. Press. Vessel. Pip. Div. PVP. 395 (1999) 235–242. https://www.osti.gov/biblio/12388.

[3.9] CEA, Cast3M, (2003). https://www-cast3m.cea.fr/.

[3.10] AFCEN, RSE-M 2020. In-service inspection, installation and maintenance rules for mechanical components of PWR, 2020.

[3.11] J. Li, O. Ancelet, A. Double, S. Chapuliot, Evaluation of Fatigue Crack Propagation by ΔJ Approach, in: Vol. 3 Des. Anal., American Society of Mechanical Engineers, 2019.

doi:10.1115/PVP2019-93555.

[3.12] W. Zhang, Fatigue crack growth in large scale yielding condition, Université Paris Saclay (COmUE), 2016.

[3.13] B. Howe, J. Mann, Z. Que, C. Huotilainen, F. Scenini, G. Burke, Development of a Robust Procedure for the Evaluation of Striation Spacings in Low Cycle Fatigue Specimens Tested in a Simulated PWR Environment, in: Vol. 4A Mater. Fabr., American Society of Mechanical Engineers, Las Vegas, Nevada, USA, 2022. doi:10.1115/PVP2022-84027.

This page intentionally left blank.

CHAPTER 4 INCEFA-SCALE PROGRAM ON NOTCHED CYLINDRICAL SPECIMENS

This Chapter describes the fatigue response of specimens including stress concentrations using notched geometries, considering the impact of strain uncertainties, specimen size effects, and the transition from air to PWR environments, by Luc Doremus, Louise Casulli, and Zaiqing Que.

4.1 INTRODUCTION

Geometrical discontinuities such as welds, bolt holes, threads, etc. are generally treated as notches in assessment. These features create stress concentrations that may decrease the fatigue life of the component and are often the site for nucleation and growth of fatigue cracks in components subject to cyclic loading [4.1,4.2]. Assessing components with these features within a fatigue assessment is challenging and can have substantial implications for obtaining acceptable results from the assessment.

The ASME Boiler and Pressure Vessel Code (BPVC) [4.3] provides an engineering method to account for the effect of notch-like features on fatigue behaviour that uses Stress Concentration Factors (SCFs) and Fatigue Strength Reduction Factors (FSRFs) to represent the effect of these features on fatigue initiation life [4.4]. FSRFs and SCFs are related to each other by the notch sensitivity of the material (eq. 4.1).

$$q = \frac{K_f - 1}{K_t - 1} \qquad \text{eq. 4.1}$$

where q is notch sensitivity as a function of FSRF (K_f) and SCF (K_t). A q of 0 indicates no notch sensitivity where K_f is then 0. A q of 1 indicated full notch sensitivity where K_f is then equal to K_t.

ASME Section III provides values for certain features: for example, an FSRF of 4 for thread root radii and in NB-3600 stress indices are given (which are like FSRFs) for piping components. The ASME BPVC Section III recognizes that SCFs greater than 5 are not likely and, as a result, limits FSRFs to 5 [4.4]. ASME BPVC Section VIII sets the largest FSRF at 4 [4.5]. However, FSRF testing rarely sees values greater than 3 for stainless steel [4.6,4.7], which indicates a level of conservatism in the codes for stainless steel. The most onerous features tend to be small blend radii in vessels and small diameter measurement nozzles, for which there are no generic FSRFs.

ASME Section III Appendices allow bespoke component feature testing to derive FSRFs (II-1600), but they cannot be easily transferred to other geometries or types of loading [4.4] due to the challenge of justifying the transfer of a complex stress state from one specific geometry/loading combination to another. Significant testing data is available in air and PWR environments for undressed pipe girth welds, which supports the existing ASME Section III NB-3600 stress index of 1.8 with some possible conservatism for high quality weld roots [4.6–4.8]. There are limited additional austenitic stainless steel data in air and Light Water Reactor conditions for certain geometries and notches [4.9–4.11], but it is difficult to transfer the results to other geometries and loading.

The SCFs or FSRFs are applied to the stress amplitudes produced from an analysis along with a plasticity correction factor, if appropriate. The resulting stress amplitude, once corrected for

differences between reference and elastic moduli, can then be entered into a stress-cycles fatigue life curve such as the ASME design curve.

More complex methods for analysing notches include determination of the local notch stresses and strains followed by life prediction based on strain life equations. The determination of stresses and strains can be carried out using analytical models including elastic stress concentration factors combined with the linear rule, Neuber's rule, strain energy density or Glinka's rule. Finite Element Analysis (FEA) may also be used in conjunction with a reasonable representation of the nonlinear stress-strain behaviour.

NUREG/CR-6909, Rev.1 references some notched specimen tests carried out on SA106-B steel in air [4.12] and simulated PWR primary coolant [4.2] but did not actively include them in the analysis [4.13]. The notch specimens were designed to have K_t values of 2, 3, and 6 and tested under load control in air at room temperature and 288 °C and in simulated PWR primary coolant at 288 °C. The notched tests were analysed analytically using a modified version of Neuber's Rule (eq. 4.2) to enable comparison with results from smooth specimens. Notch stresses and strains were also calculated using the modified Neuber's Rule and a Ramberg-Osgood model for stress-strain behaviour. The results of the PWR tests indicated that the margin from the factors of 2 on stress and 20 on life were nearly used up, but it should be noted that environmental effects were not accounted for in the analysis.

$$\sigma_a \varepsilon_a = \frac{(K_f S_a)^2}{E} \qquad \text{eq. 4.2}$$

where σ_a and ε_a are the stress and strain amplitudes at the notch tip. K_f is the fatigue notch factor, S_a is the stress amplitude uncorrected for notch effects and E is the Young's Modulus.

Some notched testing has also been carried out on type 300 stainless steel [4.10,4.11] in room temperature air and in simulated PWR primary coolant at 280 °C and 325 °C. The notched specimens had a K_t value of 2.58. These specimens were tested under stress control, fully reversed, and the notch strain was determined by FEA. Details of the FEA analysis were not presented. By comparing the strain amplitudes at the notch root to data generated on smooth specimens these studies indicated that there was either minimal effect of the notch or that the life of notched specimens was longer than those of smooth specimens for the same level of strain.

Further testing has been performed for carbon steel [4.14], stainless steel [4.15], and nickel-based alloy NCF600 (Alloy 600) plate [4.16] on circumferentially notched specimens with K_t values of 1.4 and 3.0 in simulated Boiling Water Reactor (BWR) water. The notch root strain-time history was calculated using elastic-plastic FEA. Axi-symmetric models were used with the nominal stresses being applied far from the loaded section. These studies focussed on the applicability of the modified rate approach [4.13] for calculating an effective strain rate to use in the environmental factor (F_{en}) calculations. The modified rate approach was proposed as under stress control the strain rate of at the root of the notch is not constant and will influence the magnitude of F_{en} for these experiments. These studies indicated that modified rate approach was a reasonable method for calculating the transformed strain rate parameter of F_{en}. However, the specimens with a notch K_t value of 3.0 had lives, after multiplying the lives by F_{en}, that were slightly longer but within the scatter of the air data and substantially longer than specimens with

K_t value of 1.4. It was concluded that for these notches the discrepancy is driven by the difference in crack propagation from the stress distribution analysis. The analysis of the stress at the notch root from the FEA indicated that the stress for the specimens with a K_t value of 3.0 becomes considerably smaller than the blunter notch specimens. It has been observed before that notched specimens initiate almost immediately [4.2] and this difference in stress behaviour between the specimen types is likely to be the cause of the sharper notched specimens having longer lives.

For stainless steel, notch radii less than 1.0 mm to 2.0 mm tend to have FSRFs substantially less than the elastically calculated SCFs due to notch sensitivity effects. A potential approach, for INCEFA-SCALE to take, may be to attempt to generate sufficient data to determine FSRFs for a particular feature with the aspiration of covering a limited number of plant locations.

To achieve this a range of challenges would need to be overcome. First, a small number of features need to be defined and parameterized. Second, a suitable test method needs to be selected that is applicable for testing in air and in an autoclave containing simulated PWR primary coolant. Third, a program of testing is required that can incorporate results from various specimen designs across multiple laboratories.

The main notch testing aims at understanding mechanisms and current assessment methods are detailed at a high level as below:

1. Improve the understanding of crack initiation and growth behaviour in a stress concentration area.
2. Evaluate the reliability of assessment design rules in stress concentration areas.
3. Obtain experimental fatigue life data for stress concentrations in a PWR environment.

The improved understanding of SCF effects on initiation and growth may also be used in tandem with the multiaxial testing data to validate assessment rules and novel strain-energy based damage quantification methods for complex stress fields. This analysis, combined with addition of data in PWR environments will also enable validation of methods of assessing the environmental impact on the features, such as the NUREG/CR-6909, Rev.1 F_{en} methodology, for these complex stress fields.

4.2 DEFINITION OF THE EXPERIMENTAL PROGRAM

4.2.1 TESTING PROGRAM

This experimental program on notched specimen was entirely performed on INCEFA-SCALE common material Type 316L austenitic stainless steel.

The notched fatigue tests were being performed on circumferentially notched specimens (Figure 4.1). INCEFA-SCALE testing was carried out at several different laboratories with differing specimen design requirements. To produce comparable data across those designs, the notch dimensions were specified to have radii of 0.5 mm and 2.0 mm with a maximum $K_t \approx 4$, representative of threads and bolts. The K_t calculation is based on the analysis shown in the “Notched design procedure” (Section 4.2.2). This meant that although some dimensions were

fixed, the notch depth could be tuned and specified for each specimen design producing consistent K_t values and comparable results (as specified in Table 4.1).

Fatigue testing in PWR relevant environments is challenging and requires compromises in testing methods. One of these compromises is in the measurement or control of the displacement or strain resulting from standard extensometer generally not being suitable for use in an autoclave. This has resulted in many laboratories using displacement control at the shoulders of the specimen to perform the testing. The implication for notch testing is that the measurements are too remote from the notch to be reasonably used for the control of PWR testing. To facilitate test control and the production of comparable test results, especially on PWR rigs, the tests were performed in load control mode.

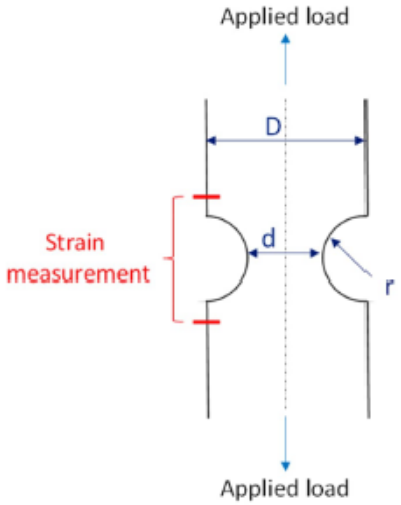

Figure 4.1. Circumferentially notched specimen.

4.2.2 NOTCH DESIGN PROCEDURE

To design the notched testing program, several considerations were made. FEA was used in the initial planning of the tests to define notch geometries based on the pre-defined major diameters (D in Figure 4.1) specified by the different laboratories. The notch geometries were defined using elastic analyses.

Using the Cast3M software [4.17], preliminary elastic calculations were carried out to initially assess stress concentration and triaxiality levels based on notch geometries. The initial calculations were based on major diameter (D in Figure 4.1 and eq. 4.3) values between 6.0 mm and 9.0 mm. Specimens gauge lengths were modelled as cylinders loaded in tension, using axisymmetric elements. A representative Young's Modulus of 197 GPa was applied in the isotropic material definition.

A parametric study on notch geometry was then carried out with minor diameters between 4.0 mm and 8.0 mm and notch radii of 0.5, 1.0, 2.0, and 5.0 mm. Two values were calculated from the modelling: K_t (stress concentration factor as per the French RCC-M design code) (eq. 4.4) and Tr (SCF normalized using the ratio of specimen gauge diameter and the notched section diameter) (eq. 4.5), as defined below:

$$\Delta = \frac{D}{d} \quad \text{eq. 4.3}$$

$$K_t = \frac{\sigma_{tresca,max}}{\sigma_{nominal}} \quad \text{eq. 4.4}$$

$$Tr = \frac{K_t}{\Delta^2} \quad \text{eq. 4.5}$$

From an initial simulation of loading of a 9.0 mm diameter specimen, it was observed that the K_t factor was a function of both d and r (notch radii), as shown in Figure 4.2. The stress concentration increases as the notch radius reduces and the minor diameter reduces; intuitively as the notch essentially tends towards a deep, sharp crack. Stress triaxiality at the notch tip was predicted to drive crack initiation and growth. Therefore, the triaxiality parameter (Tr) was calculated by normalizing K_t by the section area ratio for the various notch geometries in the parametric study, shown in Figure 4.3.

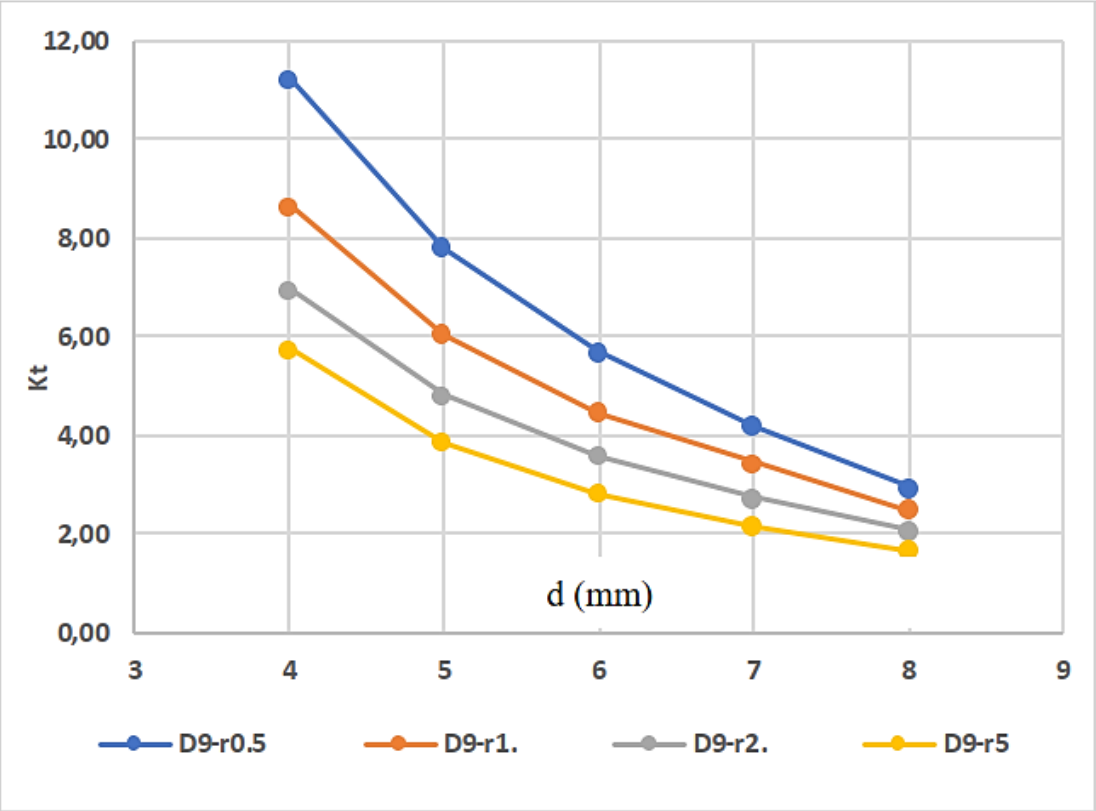

Figure 4.2. Evolution of K_t for a 9.0 mm diameter specimen.

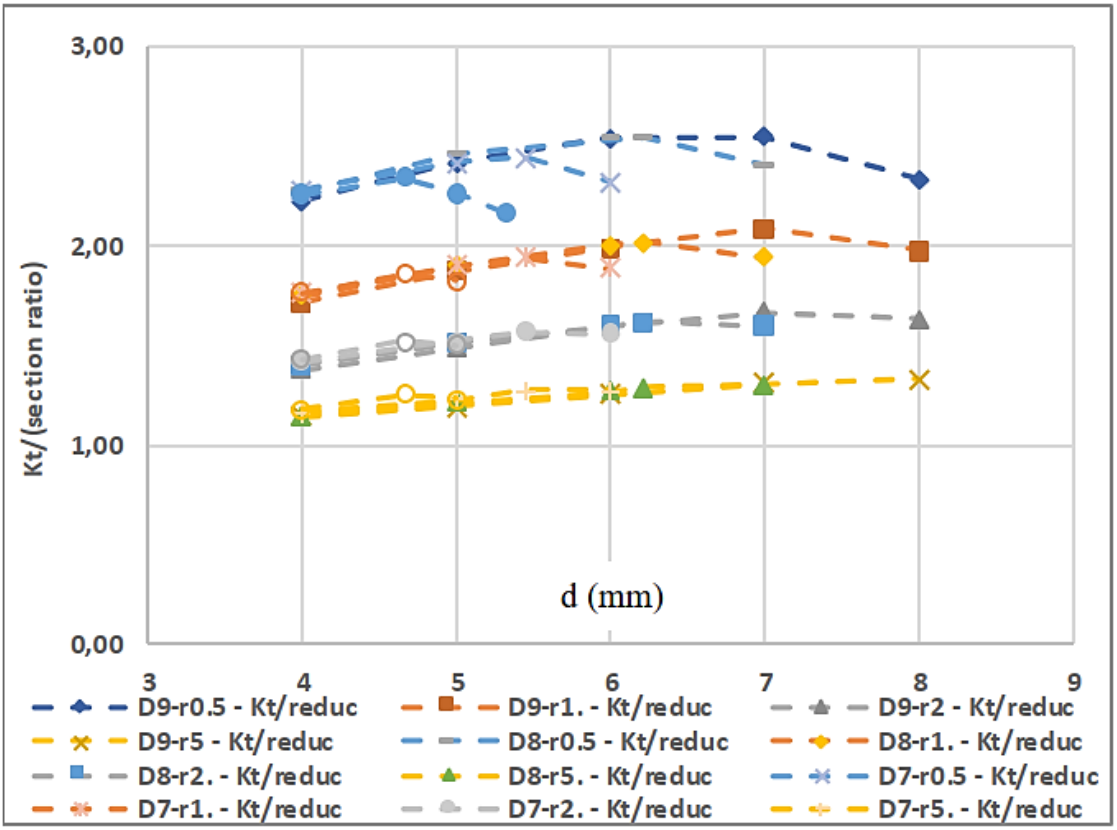

Figure 4.3. Evolution of the triaxiality parameter for various notch radii and specimen diameters.

Here it can be seen that the Tr factor (K_t/section ratio Δ) is generally constant for a given major diameter and notch radius. Through this normalization process, it was discerned that for a constant Δ, the Tr parameter is only influenced by the notch radii. By rationalizing the K_t in this way, the parameters could be limited within this study to manage the impact that laboratory to laboratory variation, particularly the number of different specimen geometries, would have on the results of the testing. Two notch radii, 2.0 mm and 0.5 mm were chosen for features for the specimens. The values of K_t and Tr for both notch radii are shown in Table 4.1. The K_t values for the smaller radius (0.5 mm) are towards the limit of the upper FSRF values of 4 and 5 for ASME BPVC Section VIII and Section III respectively. The larger radius predicts intermediate K_t values according to the ASME BPVC.

D (mm)	d (mm)	r (mm)	K_t	Tr
9	7.00	0.5	4.20	2.54
8	6.22	0.5	4.19	2.53
7	5.44	0.5	4.02	2.43
6	4.67	0.5	3.86	2.33
9	7.00	2.0	2.74	1.66
8	6.22	2.0	2.67	1.61
7	5.44	2.0	2.59	1.57
6	4.67	2.0	2.51	1.52

Table 4.1. K_t and Tr for the various notch geometries.

4.2.3 LOAD DEFINITION

The use of load control as a compromise for the type of testing requires calibrations to be performed to translate the desired notch tip strain from an alternating load using finite element calculations. Elastic-plastic modelling was used to define the loads at which the main testing would be carried out.

For most of the laboratories involved in INCEFA-SCALE Project, gauge length extensometry is not possible in simulated PWR environment test rigs. Therefore, it was decided that the notched testing would be conducted under load control to enable consistency across the testing program (for example, both air and PWR environments). To enable comparison with the uniaxial testing the loads were defined to introduce a notch tip equivalent strain amplitude equal to those in the fully reversed reference tests carried out in the project. This equivalent strain $\varepsilon_{tot\text{-}eq}$ is calculated with the following equation:

$$\varepsilon_{tot-eq} = \varepsilon_{pl-eq} + \frac{2}{3}(1+\upsilon)\frac{\sigma_{VM}}{E} \qquad \text{eq. 4.6}$$

Determination of the testing loads to apply to the specimens required accurate modelling of the notched specimens with consideration of the effects of plasticity. Notch strain amplitudes of 0.6% and 0.3% were targeted for the testing, as shown in Figure 4.4, to pair with the uniaxial reference testing at the same strain amplitudes. As the uniaxial reference data for this material is substantial, there is a tolerance for deviation from the specified strain amplitudes as a material specific reference curve may be used in place of specific test results. The deviation may come from determining the reference curve via different methods or experimental considerations.

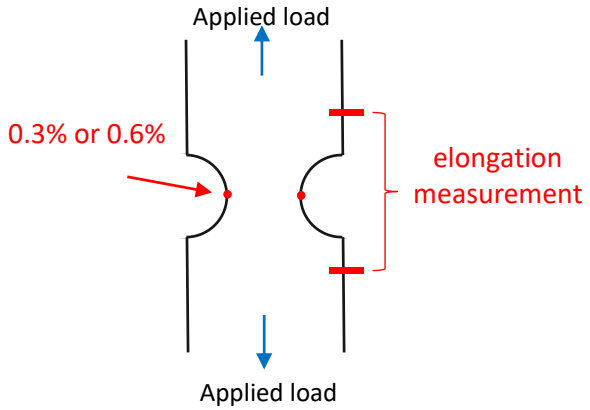

Figure 4.4. Targeted strain location and extensometer position.

For simplicity, stabilized state plasticity estimates were incorporated into the material model. These included a cyclic stress strain curve input as monotonic tensile data, and a non-linear kinematic hardening model. The models were designed to reproduce uniaxial, fully reversed test data. Both models under either monotonic or cyclic loading are shown in Figure 4.5 and compared to experimental hysteresis loops in Figure 4.6.

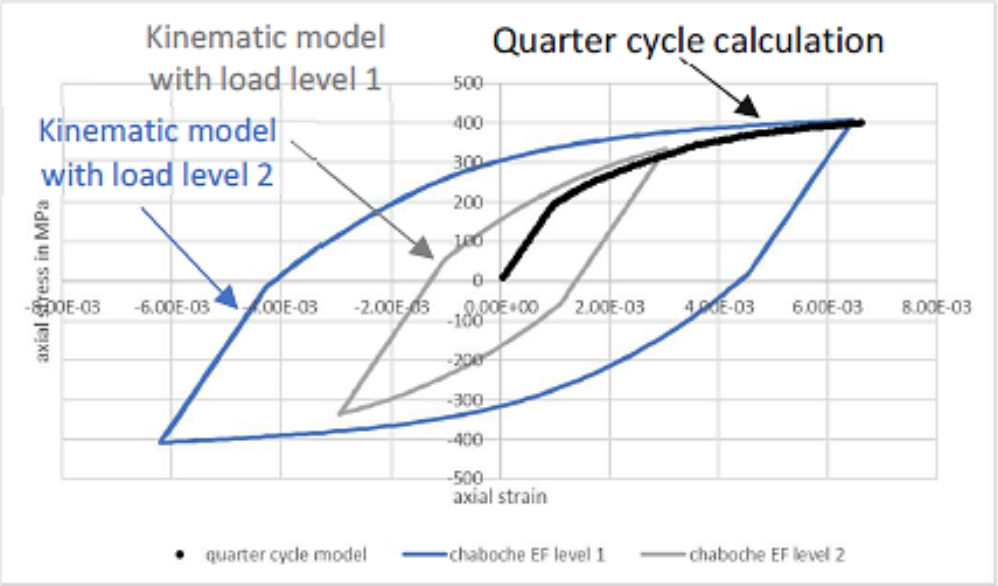

Figure 4.5. Cyclic and monotonic material model behaviour.

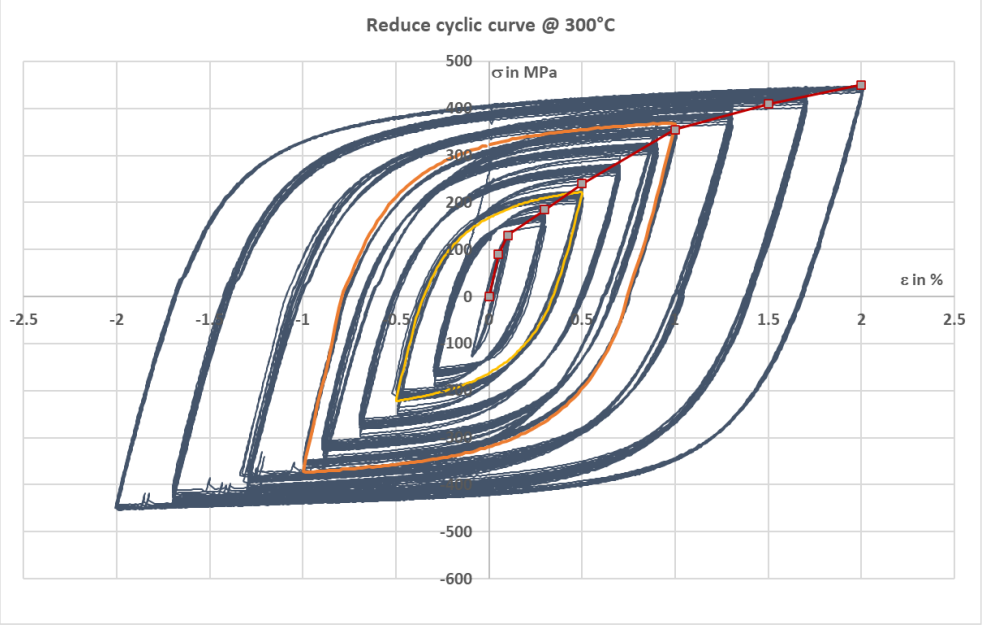

Figure 4.6. Comparison of material model behaviour with experimental data.

It is evident from Figure 4.6 that the reduced cyclic curve performs well in matching the tips of the hysteresis loops from stabilized behaviour. This implies that to predict stabilized strains at the notch tip the reduced cyclic curve could be applied under monotonic loading to predict the maximum equivalent strain at the notch tip. The models of each specimen, with geometry according to Table 4.1, were loaded in tension for a quarter cycle according to the RCC-M methodology and plots such as that in Figure 4.7 were produced.

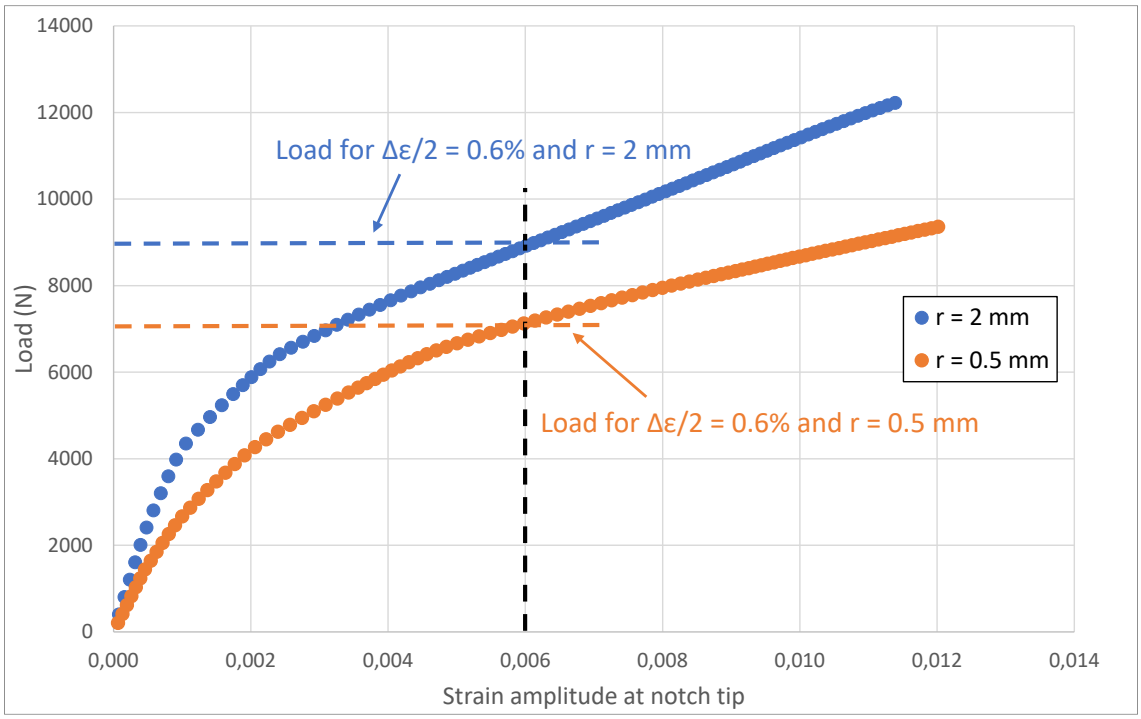

Figure 4.7. Example of load versus notch tip equivalent strain for 9.0 mm diameter specimen.

Using the data obtained from these simulations it was possible to define fully reversed loading conditions which provided best estimates to introduce the desired strain amplitudes at the notch tip.

4.2.4 TEST MATRIX

The final test matrix is given in Table 4.2. 45 tests were performed in air. In that environment, the test frequency is 1 Hz with a triangular waveform. Sawtooth waveform is allowed to speed the test duration but the rising time should be identical to the one of a triangular waveform at 1 Hz. Test temperature is 300 °C for all tests. Finally, some additional tests were added to the test matrix:

- One laboratory offered to perform another notch radius of 1.0 mm. Therefore 4 tests were performed: 2 tests per strain amplitude targeted at the notch tip.
- First results highlighted the influence of specimen diameter. Therefore 8 tests were performed on very large diameter specimen (18 mm) on two different labs: 2 per strain amplitude targeted at the notch tip for each notch radius and each lab.

20 tests were planned in PWR environment and 13 performed due to experimental issues and delay in some laboratories. The testing frequency was calculated to reproduce the duration of a strain-controlled fatigue test cycle with a strain rate of 0.01 %/s leading to an environmental factor F_{en} = 4.57 according to NUREG/CR-6909, Rev.1 [4.13]. The waveform is here mandatory triangular. In the PWR environment, only standard specimens' diameters (6.0 mm and 9.0 mm) were used. The notch radii are limited to the two initial planned: 0.5 mm and 2.0 mm.

Load amplitude (N)	Frequency (Hz)	Environment	Temperature (°C)	Targeted strain at notch tip (%)	Notch radius (mm)	D (mm)	d (mm)
5167	1	Air	300	0.30	0.5	9	7.00
5167	1	Air	300	0.30	0.5	9	7.00
7131	1	Air	300	0.60	0.5	9	7.00
7131	1	Air	300	0.60	0.5	9	7.00
7131	1	Air	300	0.60	0.5	9	7.00
7304	1	Air	300	0.64	0.5	9	7.00
4212	1	Air	300	0.30	0.5	8	6.22
4212	1	Air	300	0.30	0.5	8	6.22
4212	1	Air	300	0.30	0.5	8	6.22
4212	1	Air	300	0.30	0.5	8	6.22
5758	1	Air	300	0.60	0.5	8	6.22
5758	1	Air	300	0.60	0.5	8	6.22
5758	1	Air	300	0.60	0.5	8	6.22
5758	1	Air	300	0.60	0.5	8	6.22
1862	1	Air	300	0.30	0.5	5	3.89
1862	1	Air	300	0.30	0.5	5	3.89
2447	1	Air	300	0.60	0.5	5	3.89
16750	1	Air	300	0.30	0.5	18	14.00
16750	1	Air	300	0.30	0.5	18	14.00
24085	1	Air	300	0.60	0.5	18	14.00
24085	1	Air	300	0.60	0.5	18	14.00
6185	1	Air	300	0.30	1.0	9	7.00
6185	1	Air	300	0.30	1.0	9	7.00
8055	1	Air	300	0.60	1.0	9	7.00
8055	1	Air	300	0.60	1.0	9	7.00
6895	1	Air	300	0.30	2.0	9	7.00
6895	1	Air	300	0.30	2.0	9	7.00
6895	1	Air	300	0.30	2.0	9	7.00
8908	1	Air	300	0.60	2.0	9	7.00
8908	1	Air	300	0.60	2.0	9	7.00
8908	1	Air	300	0.60	2.0	9	7.00
5516	1	Air	300	0.30	2.0	8	6.22
5516	1	Air	300	0.30	2.0	8	6.22
5516	1	Air	300	0.30	2.0	8	6.22
7147	1	Air	300	0.60	2.0	8	6.22
7147	1	Air	300	0.60	2.0	8	6.22
7147	1	Air	300	0.60	2.0	8	6.22
2245	1	Air	300	0.30	2.0	5	3.89
2245	1	Air	300	0.30	2.0	5	3.89
2958	1	Air	300	0.60	2.0	5	3.89
2958	1	Air	300	0.60	2.0	5	3.89

24700	1	Air	300	0.30	2.0	18	14.00
24700	1	Air	300	0.30	2.0	18	14.00
32000	1	Air	300	0.60	2.0	18	14.00
32000	1	Air	300	0.60	2.0	18	14.00
7131	0.00417	PWR	300	0.60	0.5	9	7.00
7131	0.00417	PWR	300	0.60	0.5	9	7.00
2560	0.00833	PWR	300	0.30	0.5	6	4.67
3417	0.00417	PWR	300	0.60	0.5	6	4.67
3417	0.00417	PWR	300	0.60	0.5	6	4.67
3417	0.00417	PWR	300	0.60	0.5	6	4.67
3417	0.00417	PWR	300	0.60	0.5	6	4.67
3417	0.00417	PWR	300	0.60	0.5	6	4.67
3417	0.00417	PWR	300	0.60	0.5	6	4.67
3417	0.00417	PWR	300	0.60	0.5	6	4.67
3417	0.00417	PWR	300	0.60	0.5	6	4.67
6895	0.00833	PWR	300	0.30	2.0	9	7.00
6895	0.00833	PWR	300	0.30	2.0	9	7.00
3191	0.00833	PWR	300	0.30	2.0	6	4.67
3191	0.00833	PWR	300	0.30	2.0	6	4.67
3191	0.00833	PWR	300	0.30	2.0	6	4.67
3191	0.00833	PWR	300	0.30	2.0	6	4.67
4175	0.00417	PWR	300	0.60	2.0	6	4.67
4175	0.00417	PWR	300	0.60	2.0	6	4.67
4175	0.00417	PWR	300	0.60	2.0	6	4.67
4175	0.00417	PWR	300	0.60	2.0	6	4.67

Table 4.2. Test matrix for notched specimens.

4.3 EXPERIMENTAL FATIGUE LIFE RESULTS

4.3.1 RESULTS IN AIR

Based on the notch strain amplitudes as determined by FEA, almost all tests performed in air environment have a higher fatigue life than predicted by NUREG/CR-6909, Rev.1 [4.13] mean curve for stainless steel (see Figure 4.8). Some tests were stopped and considered as run out because of the very long test duration. All fatigue lives above 2000000 cycles were considered as run outs.

It appears that for both strain amplitudes, the higher the notch radius the lower the fatigue life. This is highlighted in Figure 4.9 with the average fatigue lives depending upon notch radius for each strain amplitude. It means that the higher the stress concentration factor, the higher the fatigue life.

The other main result is the large scatter observed at the same FEA predicted strain amplitude. This scatter is more important than a standard laboratory-to-laboratory variation. As shown in Figure 4.10 and Figure 4.11, the influence of specimen diameter does not completely explain this scatter since depending upon the strain amplitude and the notch radius, opposite trend of diameter influence is observed.

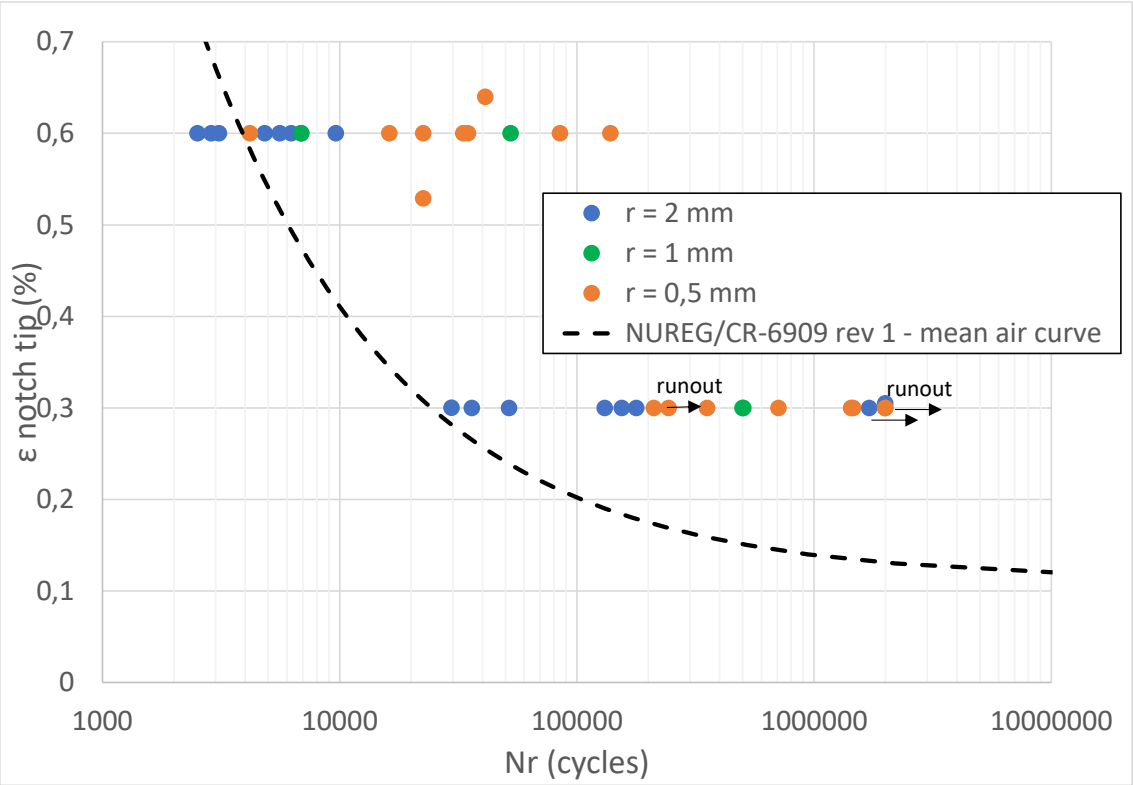

Figure 4.8. Fatigue lives of notched specimens in air.

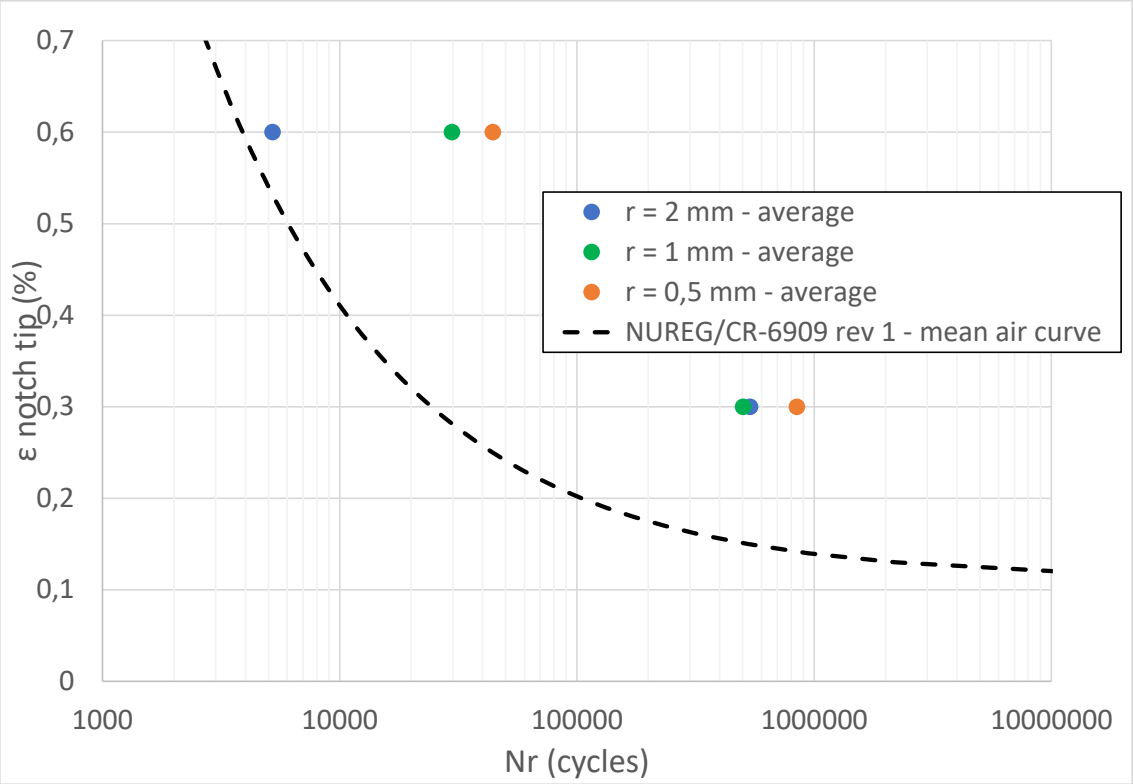

Figure 4.9. Average fatigue lives of notched specimens in air depending upon notch radius and strain amplitude.

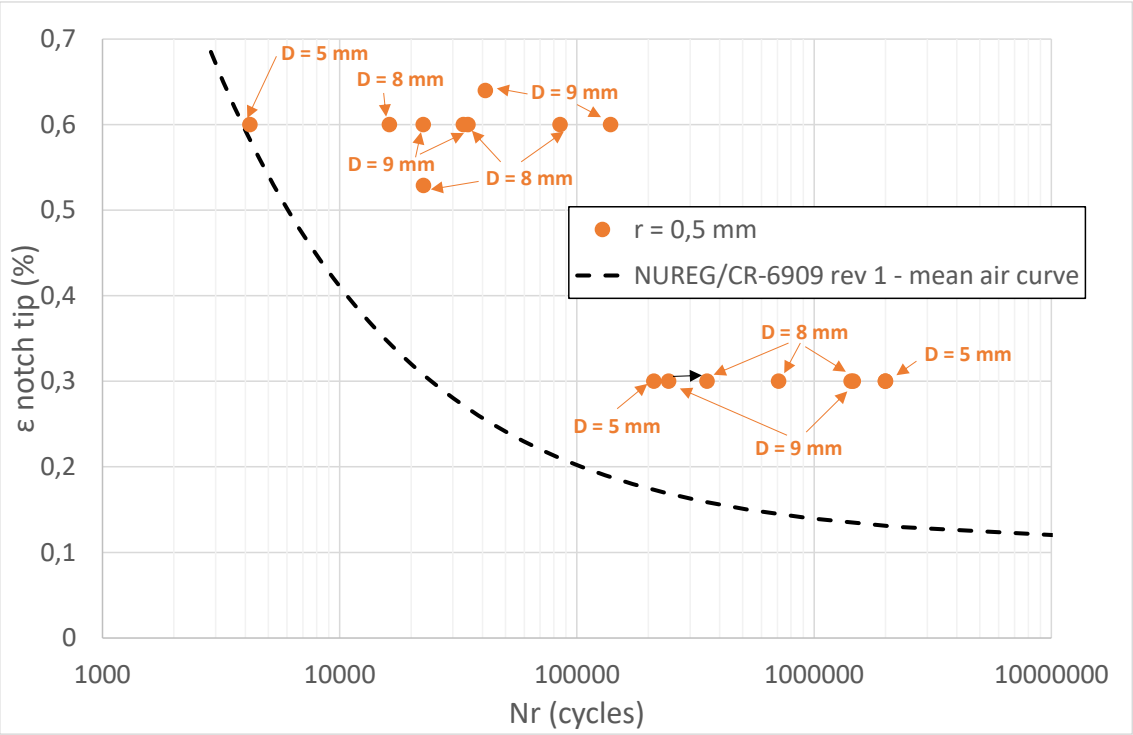

Figure 4.10. Influence of specimen diameter – 0.5 mm notch radius.

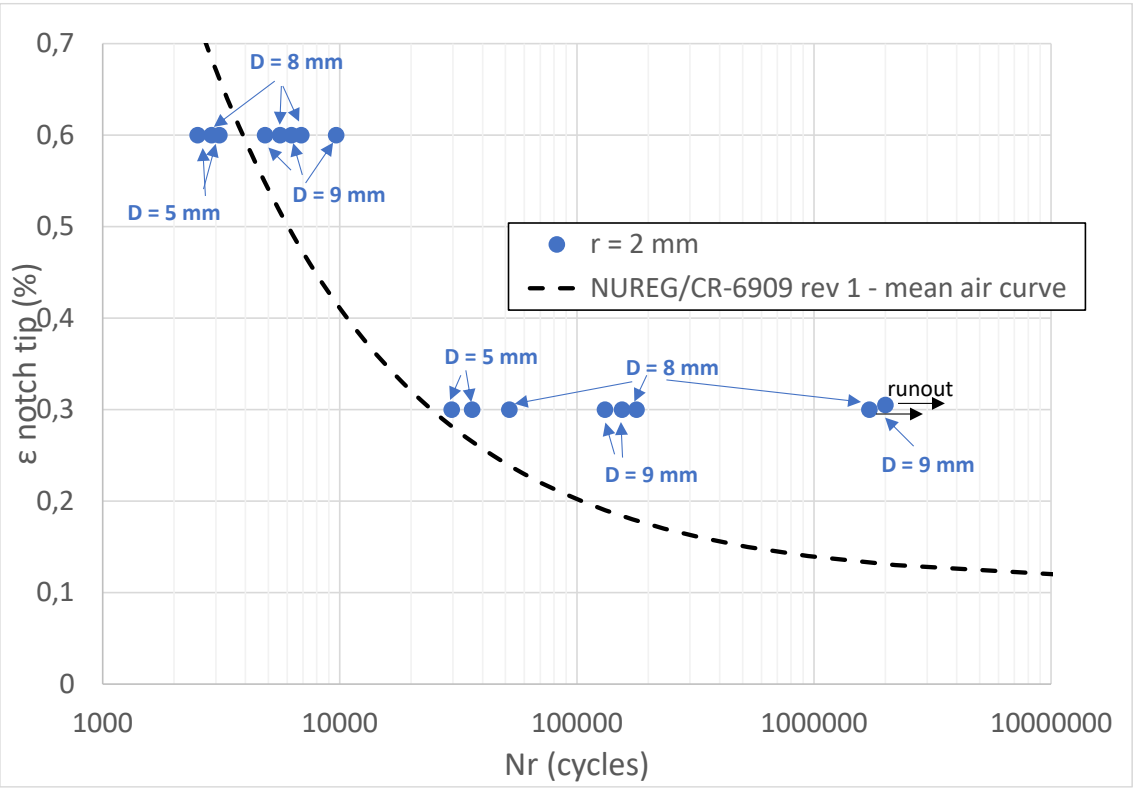

Figure 4.11. Influence of specimen diameter – 2.0 mm notch radius.

More analyses are needed to explain these results. The two main hypotheses are:

1. The uncertainty on the strain at the notch tip which leads to different strains depending upon the specimen geometry/diameter.
2. The differences on the crack growth stage due to strain gradient and specimen diameter.

These hypotheses are discussed in the next Sections.

4.3.2 RESULTS IN AIR ON LARGE DIAMETER SPECIMENS

Figure 4.12 and Figure 4.13 compares the fatigue lives on notched specimens in air for standard and large diameter specimens. At 0.3% strain amplitude similar conclusions can be drawn from large diameter specimens' results: the higher the stress concentration, the higher the fatigue life. It is also observed that large diameter specimens have lower fatigue lives than standard diameter specimens. These conclusions are not as pronounced at 0.6% strain amplitude, which can be mainly explained by the low number of test results with large diameter specimens and the obtaining of an important fatigue life for one of the two large diameter specimens with a 2.0 mm notch radius tested at 0.6% strain amplitude.

The impact of the specimens' diameter is discussed in the next Sections.

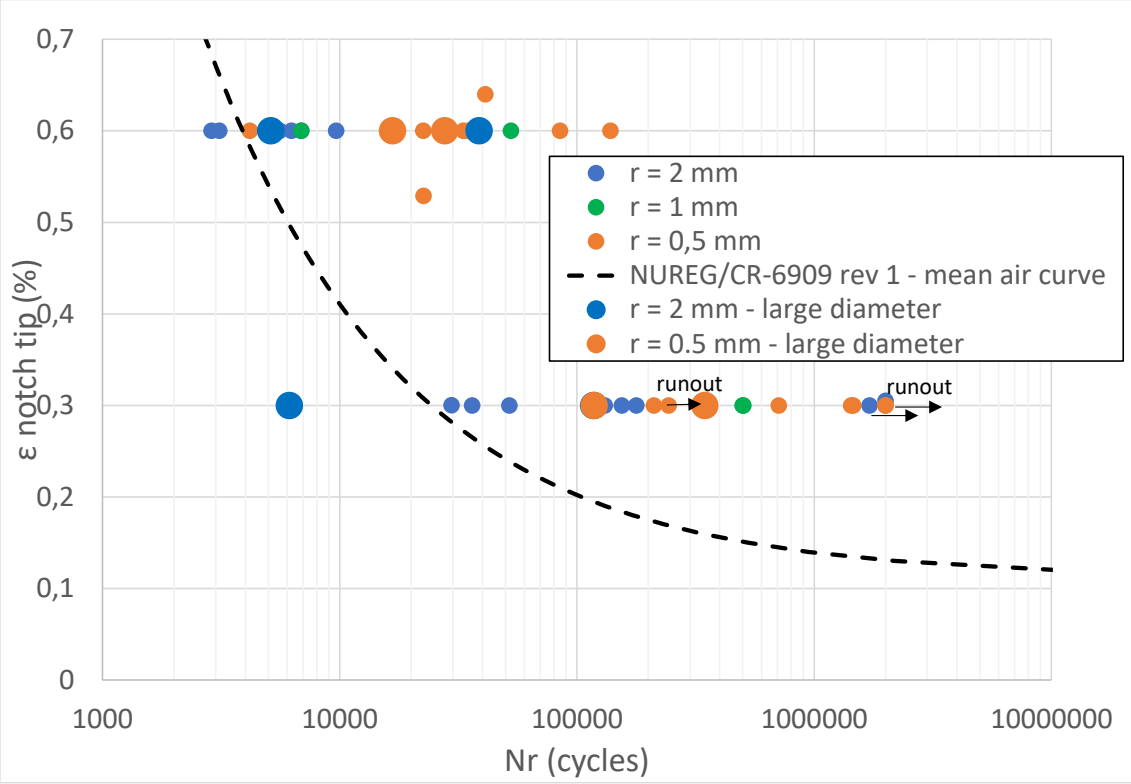

Figure 4.12. Fatigue lives on notched specimens in air for standard and large diameter specimens.

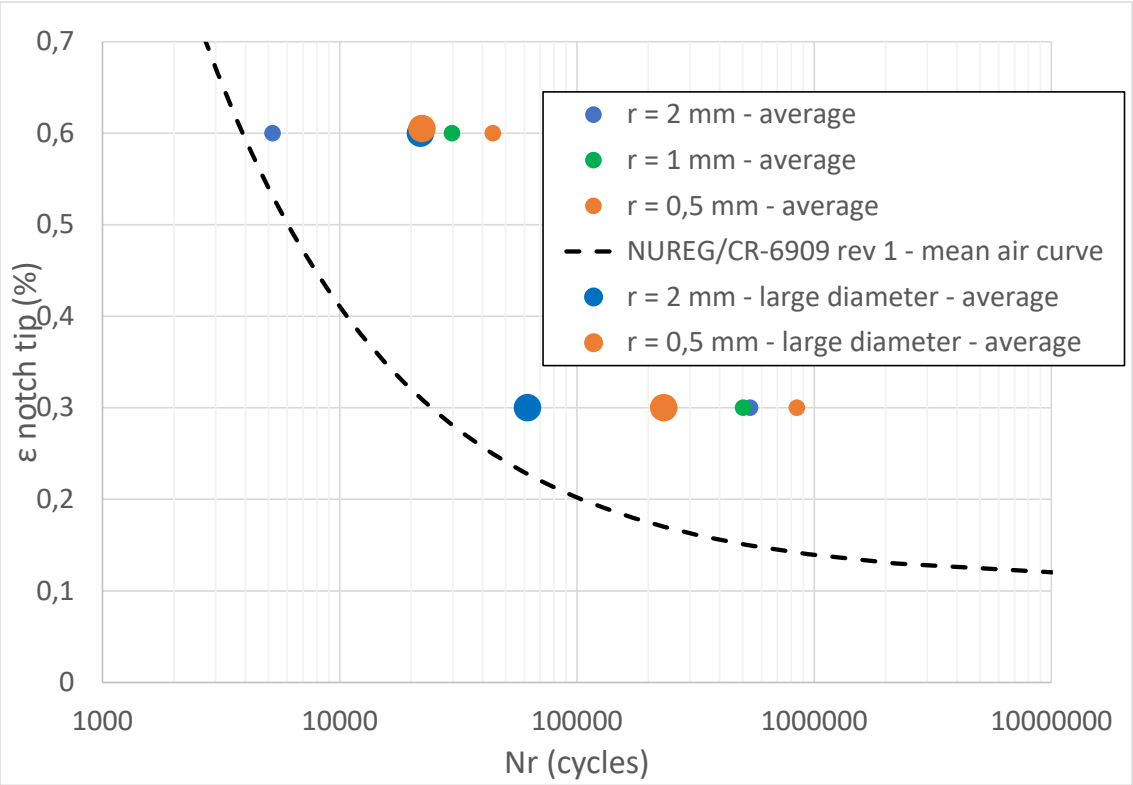

Figure 4.13. Average fatigue lives on notched specimens in air for standard and large diameter specimens.

4.3.3 RESULTS IN PWR ENVIRONMENT

Figure 4.14 compares the fatigue lives on notched specimens in air and in PWR environment.

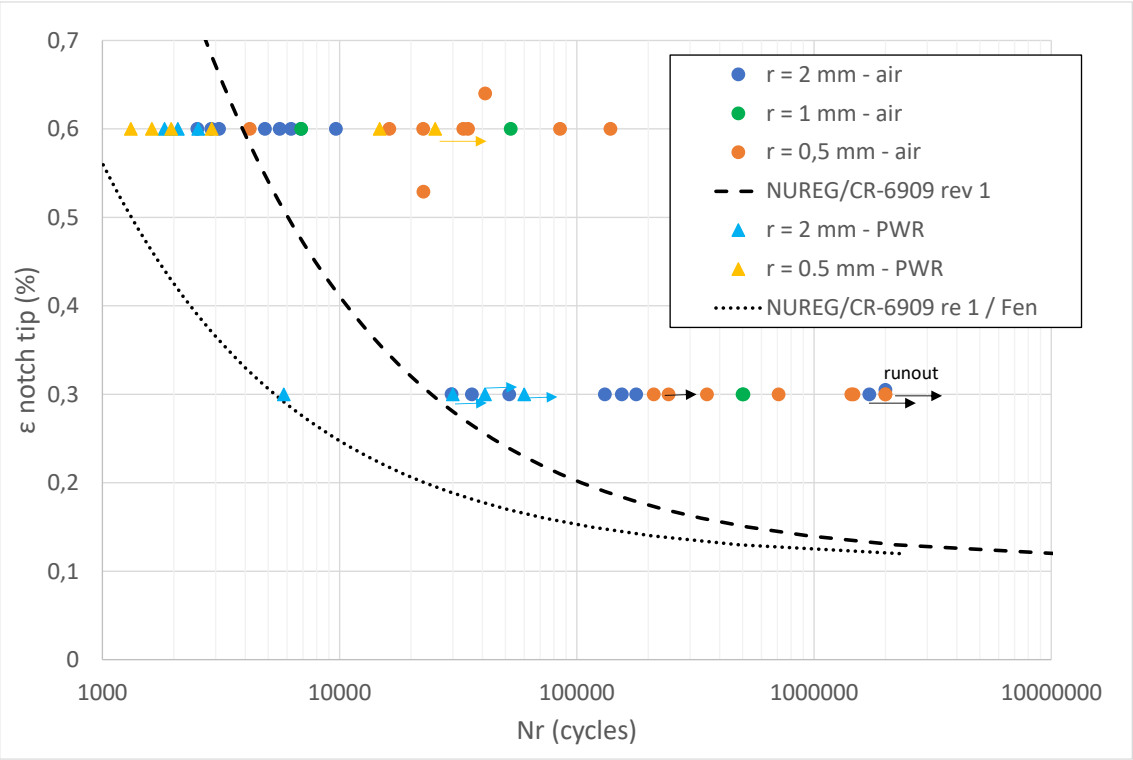

Figure 4.14. Fatigue lives on notched specimens in air and PWR environment.

Similarly to air environment, almost all tests performed in PWR environment have a higher fatigue life than predicted by NUREG/CR-6909, Rev.1 and considering the environmental factor. Some tests were stopped and considered as run outs because of the very long test duration. A large scatter is also observed for fatigue lives obtained in the same loading conditions.

The average fatigue lives in air and PWR environment are compared in Figure 4.15. In average, the fatigue life reduction in PWR environment is 5.6 for 0.5 mm notches and 2.4 for 2.0 mm notches tested at 0.6% strain amplitude. This is close to the expected theoretical F_{en}. For 2.0 mm notches tested at 0.3% strain amplitude, the fatigue life reduction cannot be determined because of the high number of run outs in the test results.

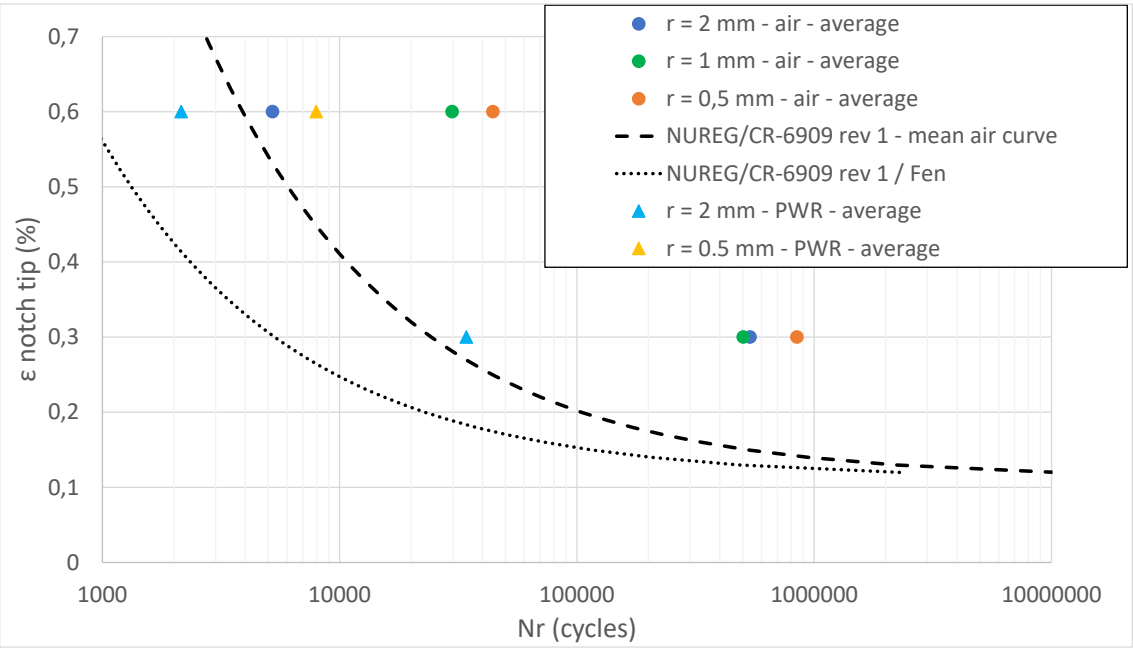

Figure 4.15. Average fatigue lives on notched specimens in air and PWR environment.

4.4 DISCUSSIONS ON STRAIN UNCERTAINTIES

4.4.1 INFLUENCE OF REAL NOTCH DIMENSIONS

A pragmatic first step is to examine and remeasure the notch dimensions for each specimen to check for consistency of notch profile. Although reasonable efforts were made to produce a manufacturing process that produced consistently acceptable notches within the specimens, it was unreasonable to trial these methods across all geometries. If the manufacturing method produces a sufficiently large variation in notch geometry, then this will need to be accounted for in the determination of the stress concentration factor K_t and strain at the notch tip to provide a consistent way of interpreting the test results. Examples of notch radius measurements are given in Figure 4.16.

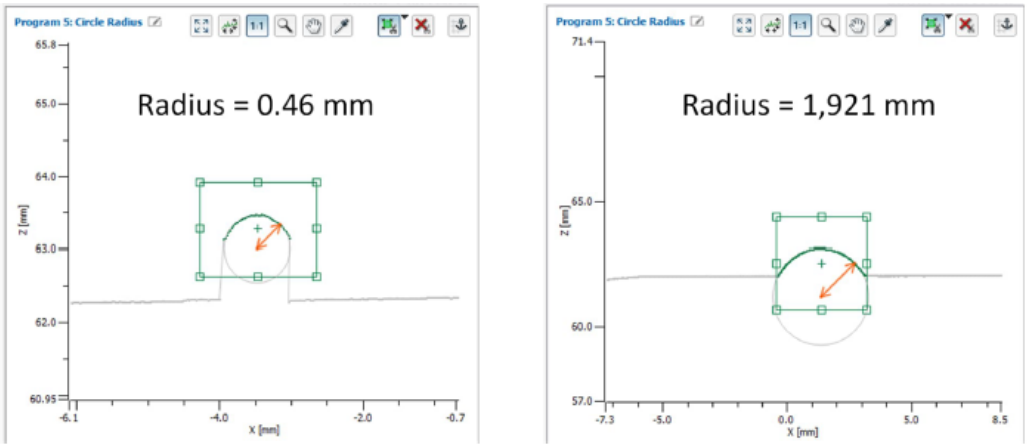

Figure 4.16. Example of notch radius measurements.

Figure 4.17 and Figure 4.18 present the fatigue lives in air versus the measured notch radius respectively for 0.5 mm and 2.0 mm radii. No trend is visible on the fatigue lives for 0.5 mm notch radii. A slight trend is observed for 2.0 mm notch radii tested at 0.3% strain amplitude: the lower the radius (equal to the higher the K_t) the higher the fatigue life. However, when the nominal diameter D and the diameter inside the notch d are considered to calculate an analytical stress concentration K_0 value based on the eq. 4.7, this trend does not appear anymore (see Figure 4.19). Therefore, it seems that the consideration of real notch dimensions does not explain the scatter on the fatigue lives.

$$K_0 = 1 + \left[\frac{1}{1.55\,\Delta - 1.3} \cdot \frac{h}{r}\right]^n \qquad \text{eq. 4.7}$$

$$n = \frac{(\Delta - 1) + 0.5\sqrt{\frac{h}{r}}}{(\Delta - 1) + \sqrt{\frac{h}{r}}} \qquad \text{eq. 4.8}$$

$$\Delta = \frac{D}{d} \qquad \text{eq. 4.9}$$

$$h = \frac{D - d}{2} \qquad \text{eq. 4.10}$$

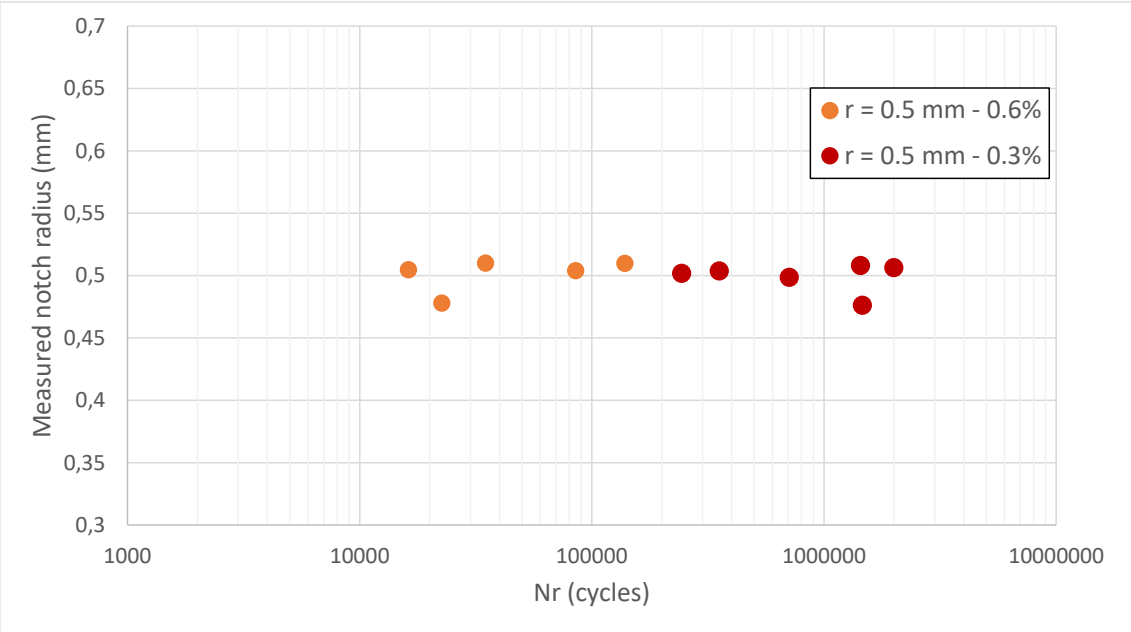

Figure 4.17. Influence of real notch radius – 0.5 mm.

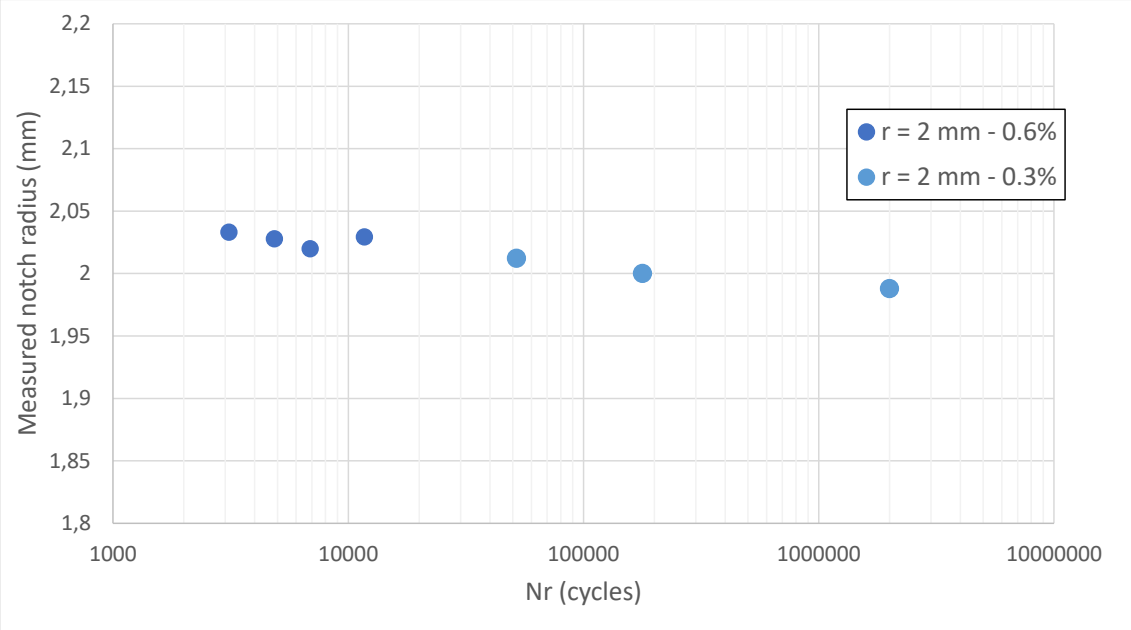

Figure 4.18. Influence of real notch radius – 2.0 mm.

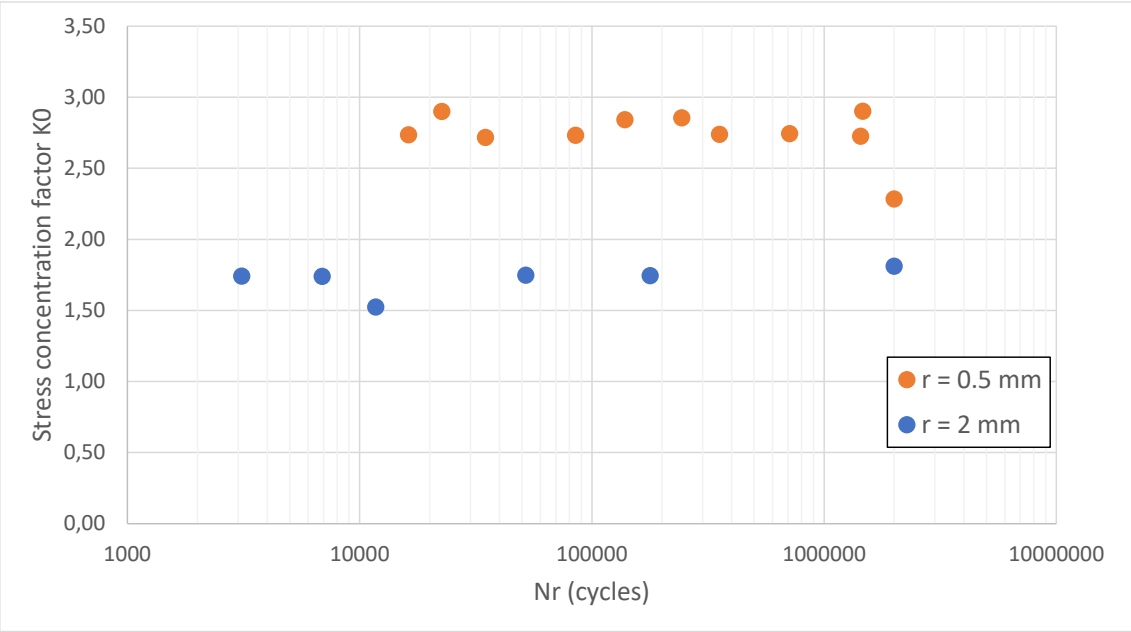

Figure 4.19. Influence of real stress concentration factor.

4.4.2 EFFECT OF STRAIN/LOAD CALIBRATION

Another important factor is the FEA strain/load calibration. Even if FEA calculations show a reasonable agreement with experimental extensometer measurements (see Figure 4.20). FEA adjustments might be needed to re-evaluate the strain at the notch tip and ensure accuracy for all specimen geometries.

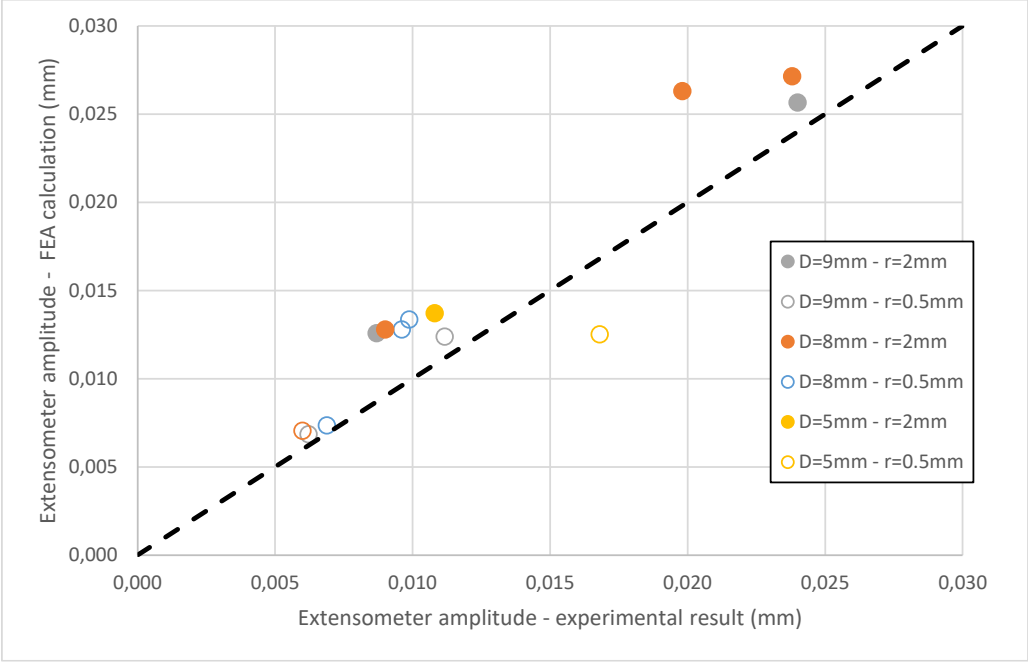

Figure 4.20. Comparison between FEA and experimental extensometer amplitudes.

Further analyses have then been carried out to quantify the effect of the FEA strain/load calibration. First another elastic-plastic reduced cyclic curve has been considered to perform 1/4 cycle modelling for load definition (see Figure 4.21). The objective was to evaluate the impact

on the strain/load calibration of the uncertainty on the cyclic curve. Note that the initial one used for load definition was more representative of the maximal hardening observed in the experimental data, whereas the new curve considered in this paragraph is closer to half-life experimental data.

The comparisons on the extensometer amplitudes, for several tests conditions and specimen geometries, showed the following results:

- Differences in the range [-16%; +8%] between the uses of the initial curve and of the new one.
- Differences in the range [-37%; +18%] between the use of the new curve and the experimental data, whereas the use of the initial one lead to differences in the range [-26%; +36%].

Finally, no clear conclusion could be drawn about the most relevant cyclic curve to represent experimental data. Note that the latter also include some uncertainties that makes these comparisons difficult.

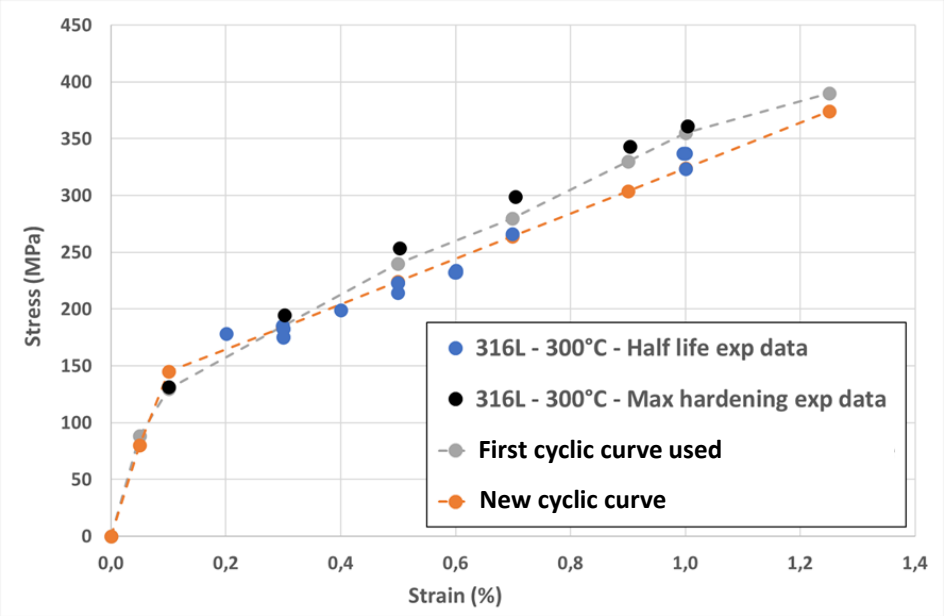

Figure 4.21. Elastic-plastic reduced cyclic curves considered for 1/4 cycle modelling.

For the prediction of the maximal strain at the notch root, the differences between the uses of the initial curve and of the new one were in the range [-14%; 0%]. This indicate that the initial calibration might have underestimated the strain loading in the tests.

To go further, non-linear kinematic and isotropic hardening modelling has been performed by two different project partners, but similar significant differences between numerical results and experimental data were observed for extensometer amplitudes: differences in the range [-22%; +40%] for the partner A modelling, and in the range [-25%; +34%] for the partner B modelling. The possible underestimation of the strain amplitude at the notch tip was also confirmed since the differences between the partner B modelling results and the experimental targets were in the range [-18%; +5%]. Note that these non-linear kinematic and isotropic hardening modelling also showed that the strain ratio during cycling, at the notch tip, was likely not be equal to -1, a

mean strain appearing in the numerical hysteresis loops and increasing according to the load level of the tests up to 0.06% for a maximum strain amplitude of 0.6% (see Figure 4.22).

As a conclusion, uncertainties on experimental data and material behaviour have surely led to uncertainties on the strain amplitude at the notch tip. Further work is required to quantitatively determine the errors made on the strain amplitude with the testing in load control and the initial FEA strain/load calibration.

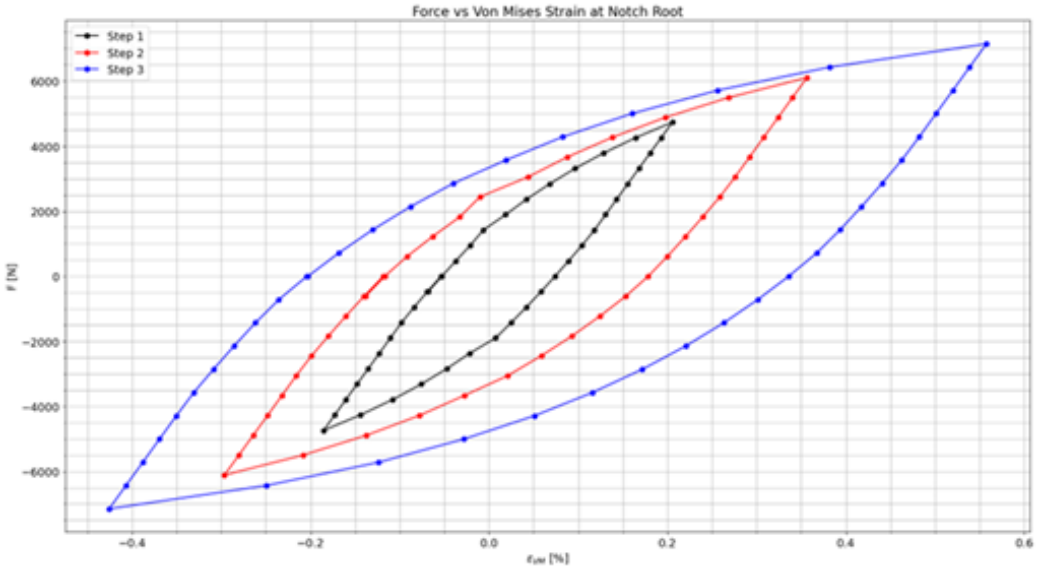

Figure 4.22. Numerical hysteresis loops at the notch tip for 0.2%, 0.4%, and 0.6% maximum strain amplitude targeted at the notch tip.

4.5 MODELLING AND MECHANISTIC UNDERSTANDING OF FATIGUE CRACK GROWTH IN NOTCHED SPECIMENS

4.5.1 MODELLING

Similarly as in Section 3.4.1, FEA have been performed to model the crack propagation to understand better the test results and to validate the experimental conjectures. The test conditions are replicated in these numerical simulations. Calculations are conducted in air environment. The crack propagation is compared for the different geometries and notch radius and specimen sizes. Table 4.3 shows the analysed configurations.

Case	Strain amplitude (%)	Environment	Temperature (°C)	Notch radius (mm)	D1 (mm)	D2 (mm)
1	0.3	air	300	2	9	7
2	0.3	air	300	0.5	9	7
3	0.6	air	300	2	9	7
4	0.6	air	300	0.5	9	7
5	0.3	air	300	2	8	6.22
6	0.3	air	300	0.5	8	6.22
7	0.6	air	300	2	8	6.22
8	0.6	air	300	0.5	8	6.22
9	0.3	air	300	2	5	3.89
10	0.6	air	300	0.5	5	3.89

Table 4.3. Analysed configurations.

Figure 4.23 shows most of studied geometries, described in Table 4.3.

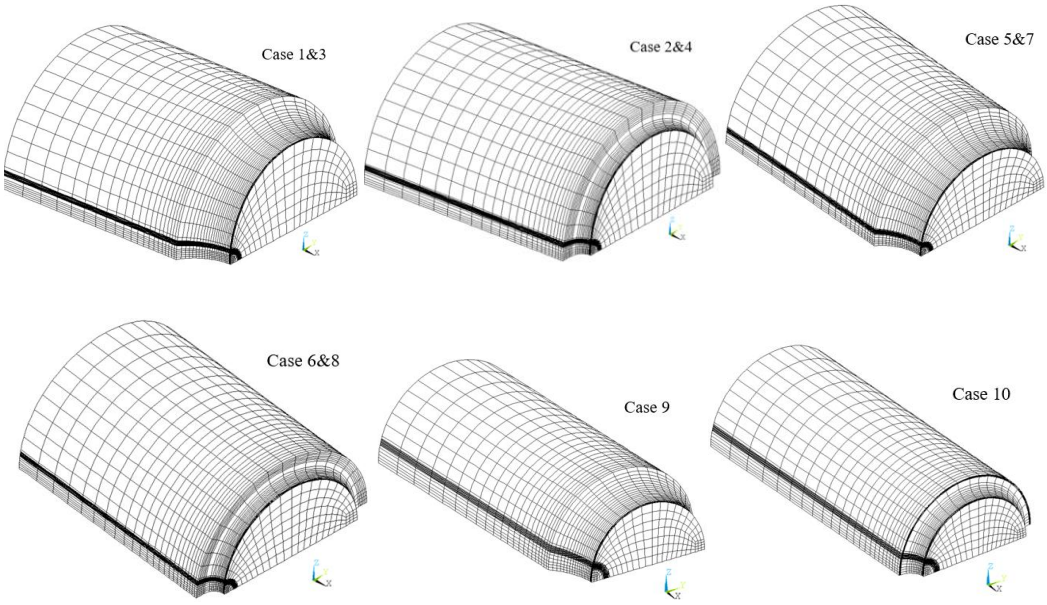

Figure 4.23. Finite element models.

The assumptions about the initial crack and the boundary conditions are identical to the ones presented in Section 3.4.1. The loadings have been determined as explained in Section 4.2.3, according to the specimen dimensions and the notch radius. They are applied as a pressure on the end of the specimen (see Figure 4.24).

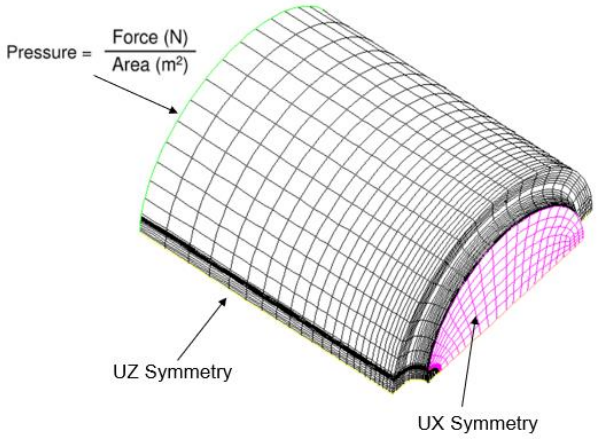

Figure 4.24 Load and boundary conditions.

The ΔJ approach and the material data are used as detailed in Section 3.4.1. The crack growth is calculated as explained previously and with the parameters of RSE-M Code [4.18] as described in Section 3.4.1.

The crack front shape is compared to the experimental results for the specimen size D1 = 9.0 mm; d2 = 7.0 mm (see Figure 4.25). The crack propagation is fostered on the circumference due to the stress concentration in that area. The calculated crack front evolution seems globally consistent with the experimental observations. Nevertheless, a significant number of specimens have developed multiple initiation sites; this case scenario has not been analysed by the calculations.

Notched radius R = 0.5 mm	Notched radius R = 2 mm
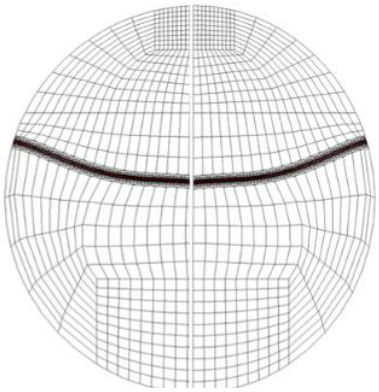	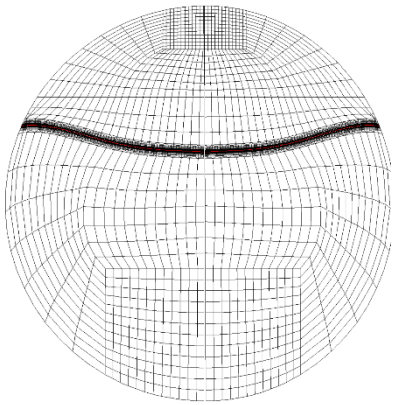
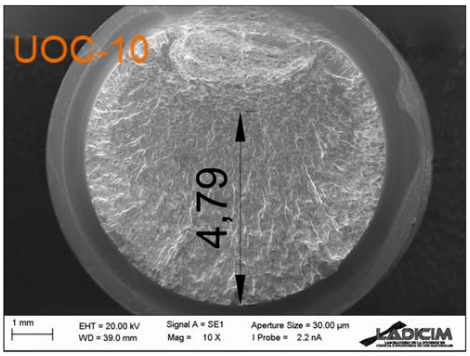	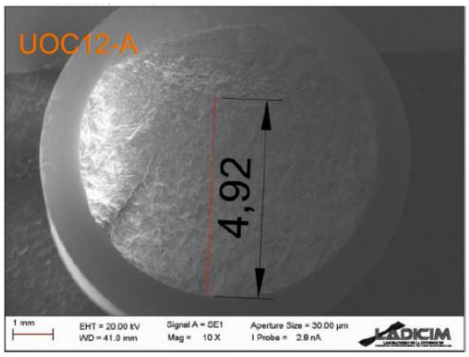

Figure 4.25. Notched specimens – Crack front shapes comparison between experiment and calculations.

4.5.2 MECHANISTIC UNDERSTANDING

As for hollow specimens (see Section 3.4.2), this testing program is supported by fractographic examination of the fracture surface. An example of the overall crack morphology is presented on Figure 4.26. In almost all cases, multiple crack initiations sites are identified along the notch circumference. Striations counting is performed only through the major fatigue crack (large arrow on Figure 4.26). Therefore, these data have to be analysed with caution since there could be potential significant contributions from others cracks to the crack growth.

In addition, another experimental technique is used to help reconstruct the crack history. Some labs used Direct Current Potential Drop (DCPD) technique to detect crack initiation and follow crack growth in air and in PWR environment. The set-up includes 3 or 4 measurement channels positioned at equally angular distance along the specimen diameter (see Figure 4.27). This set-up is illustrated in Figure 4.28 for air and PWR testing. Crack initiation can be detected although the determination of the exact crack length would necessitate a dedicated calibration. This was not done since it is not possible to predict the exact initiation point on a circumferential notch. The same issue happens for the crack growth rate determination. Results are then analysed only to provide an indicative number of cycles to initiate a crack which is still highly valuable to understand the crack history.

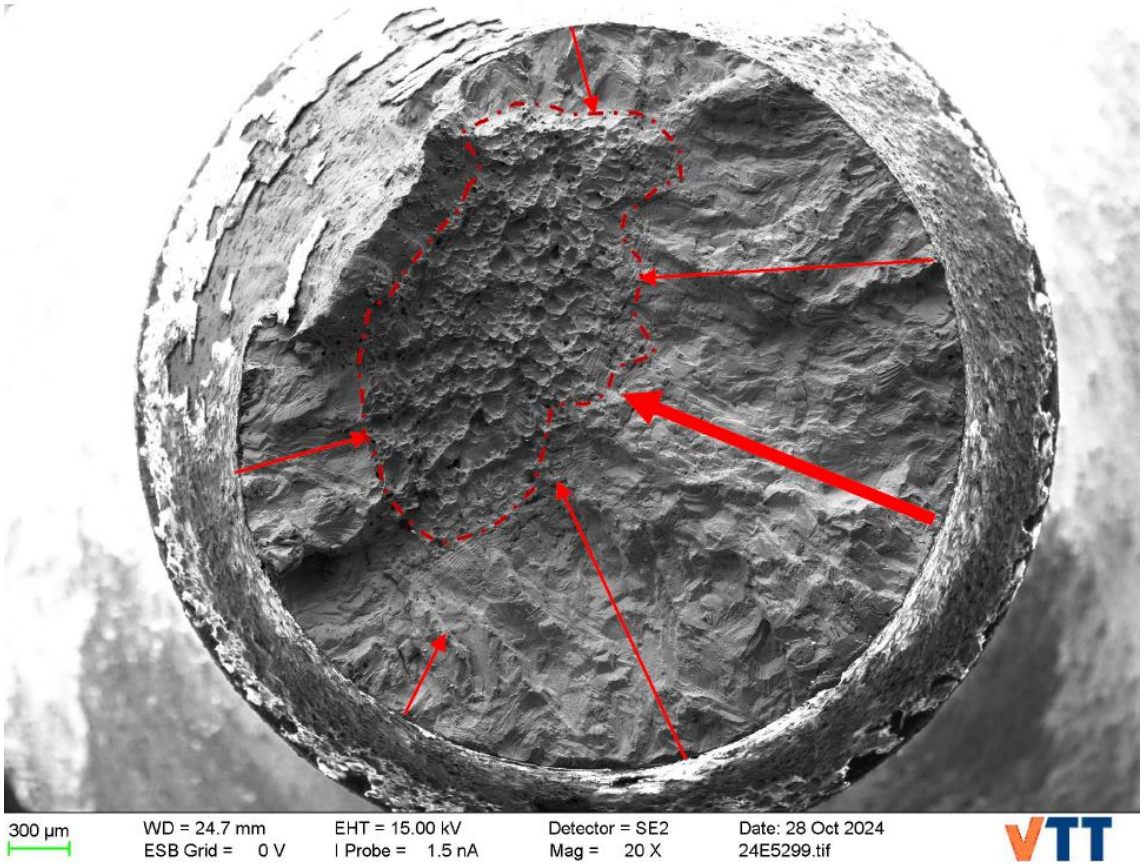

Figure 4.26. Example of the crack morphology on a notched specimen.

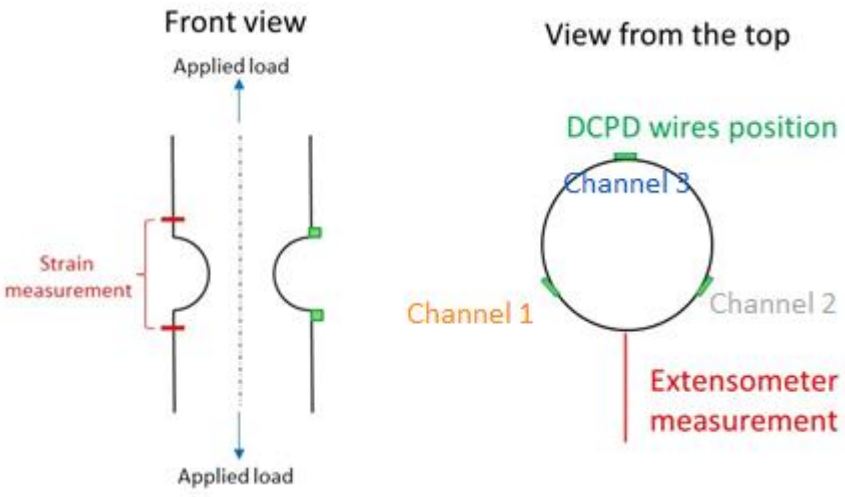

Figure 4.27. Description of the DCPD set-up.

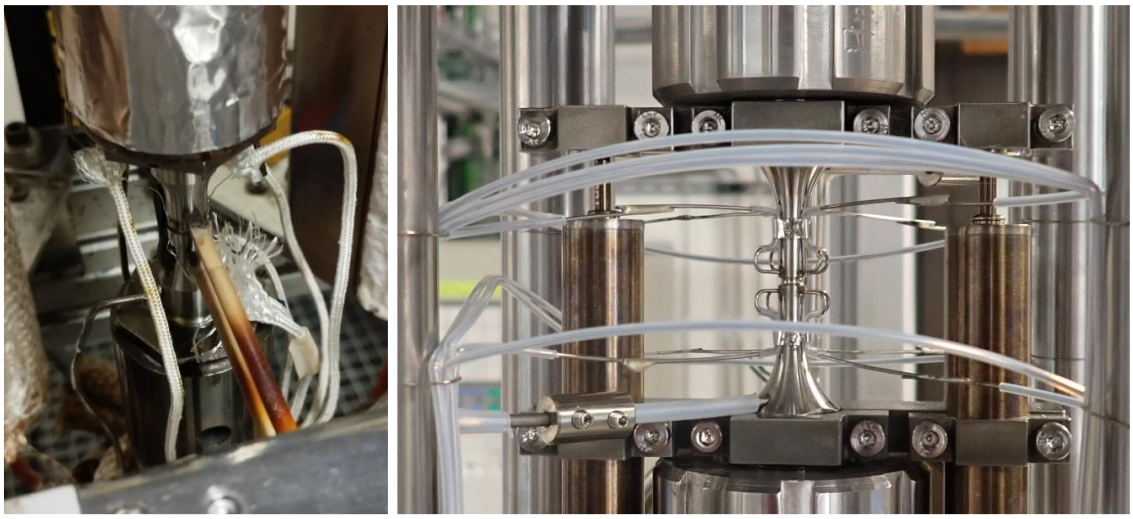

Figure 4.28. DCPD set-up in air (left) and PWR (right) environment.

4.6 DISCUSSIONS

4.6.1 EFFECT OF STRAIN GRADIENT

This Section aims at evaluating the effect of the stress concentration factor which is related to the notch radius on crack propagation stage. Two notched radii of 2.0 mm and 0.5 mm are compared in air environment under a strain amplitude of 0.6%.

Figure 4.29 presents the crack growth rate da/dN over the crack depth a. The effect of the notched radius as discussed above is considered: the higher the notch radius, the higher the crack growth rate and consequently the lower the fatigue life. It is consistent with the experimental results although there is significant scatter in the fatigue life results (see Figure 4.8). Striation counting has been performed on some fractured specimens. Figure 4.30 presents the evolutions of striation spacing for notched radii of 2.0 mm (UOC-11) and 0.5 mm (UOC-10), both in air environment at 300 °C and under a strain amplitude of 0.6%. The striation spacing confirms that the crack propagation rate is lower in a smaller notched radius which leads to higher fatigue life. The test results scatter may be due to the initiation stage. In addition, the multiplicity of the crack initiation sites along the notch circumference induces variability in the total fatigue life.

The effect of the stress concentration factor is related to the strain gradient in the specimens. Figure 4.31 presents the equivalent von Mises strain gradient for the notched radii of 2.0 mm, 1.0 mm, and 0.5 mm and two targeted strain amplitudes at the notch tip: 0.3% and 0.6% in a specimen without any crack. For a small notch radius, the strain decreases substantially just after the notch tip, especially for a strain amplitude of 0.6% at the notch tip. Thus, it tends to slow down the crack growth rate during the propagation.

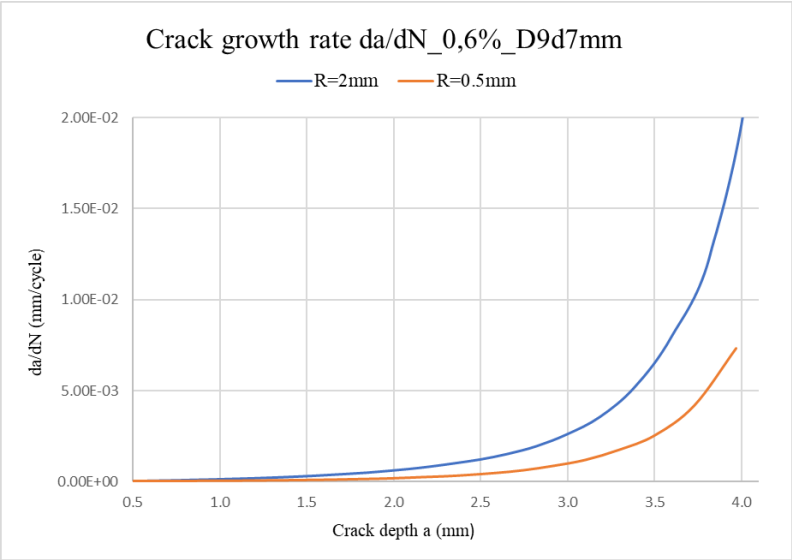

Figure 4.29. Crack growth rate for two notched radii under a strain amplitude of 0.6%.

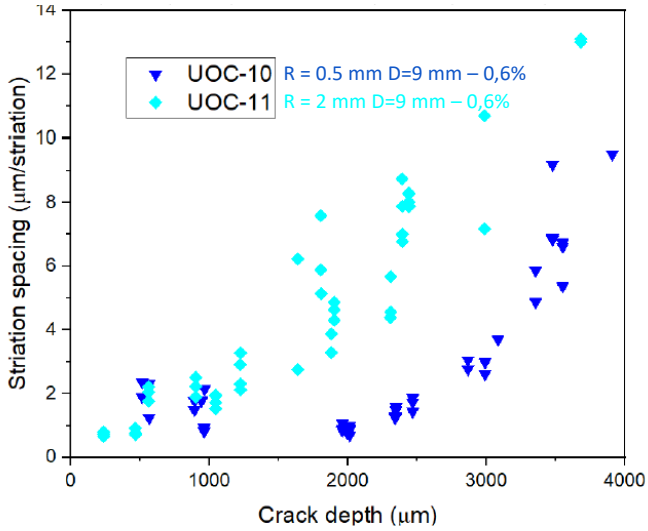

Figure 4.30. Crack growth rates for two notched radii under a strain amplitude of 0.6%.

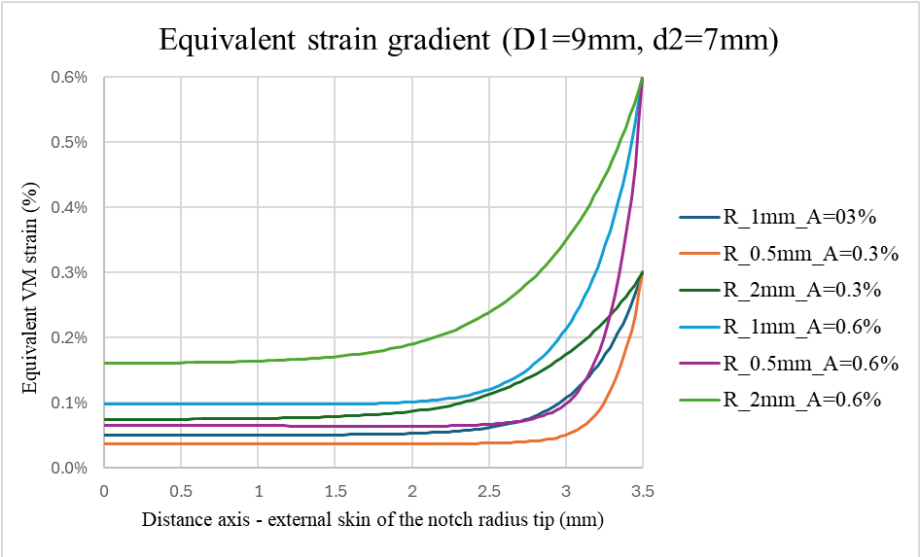

Figure 4.31. Equivalent von Mises strain gradient for two notched radii and two targeted strain amplitude at the notch tip: 0.3% and 0.6%.

4.6.2 EFFECT OF SPECIMEN SIZE

This Section aims at evaluating the effect of the specimen size on crack propagation stage. Three geometries with a notched radius of 0.5 mm are compared in air environment under a strain amplitude of 0.6%.

Figure 4.32 presents the crack growth rate da/dN over the crack depth a. The effect of the geometry of the notched specimen implies a higher crack growth rate for small geometries. Even if the experimental results show a high dispersion, it is consistent with the trend identified on the average fatigue lives (see Figure 4.9). Moreover, the striation counting performed on some fractured specimens are in good agreement with the calculations results.

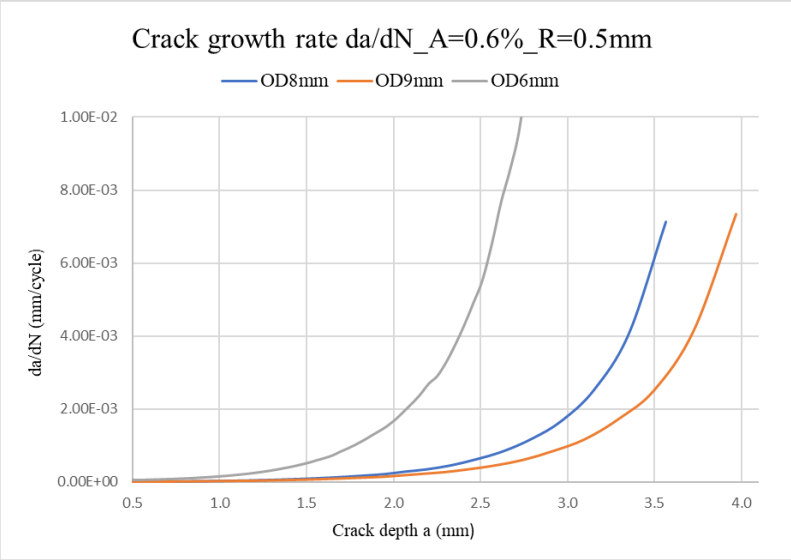

Figure 4.32. Crack growth rate for three geometries of notched specimen (R = 0.5 mm) under a strain amplitude of 0.6%.

Figure 4.33 presents the evolutions of striation spacing for three specimens with a notched radius of 0.5 mm with the following dimensions:

- VTT-AIR17: outer diameter of 8.0 mm and inner diameter of 6.22 mm, under a strain amplitude of 0.3**%.**
- KTU-13: outer diameter of 5.0 mm and inner diameter of 3.9 mm, under a strain amplitude of 0.6%.
- UOC-10: outer diameter of 9.0 mm and inner diameter of 7.0 mm, under a strain amplitude of 0.6%.

All the specimens were tested in air environment at 300 °C. The comparison of the striation spacing for the two specimens which have a strain amplitude of 0.6% at the notch tip confirms that the crack propagation rate is lower in a bigger specimen which leads to higher fatigue life.

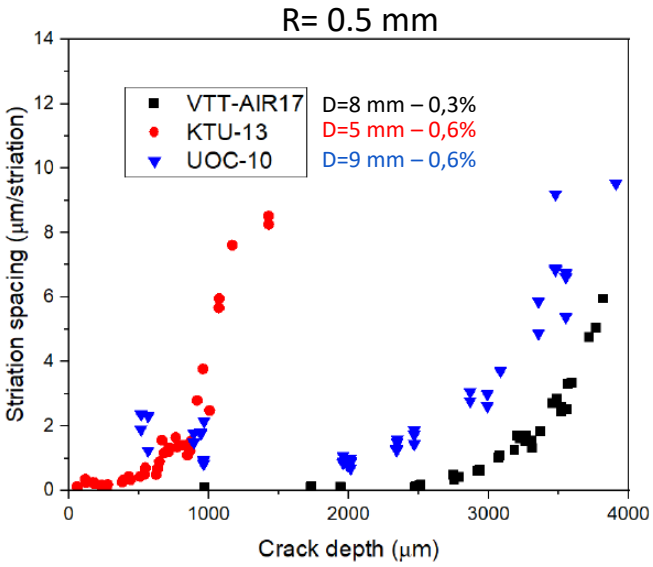

Figure 4.33. Striation spacing for three notched specimens.

As mentioned in the previous paragraph, the effect of the geometry on the crack propagation is related to the strain gradient in the specimens. Figure 4.34 underlines that for a bigger diameter, the strain decreases more than for a smaller diameter. Thus, the strain decrease impacts the crack growth rate during the propagation and leads to higher fatigue life. In addition, the crack growth duration is higher in a bigger specimen which increase slightly the fatigue life.

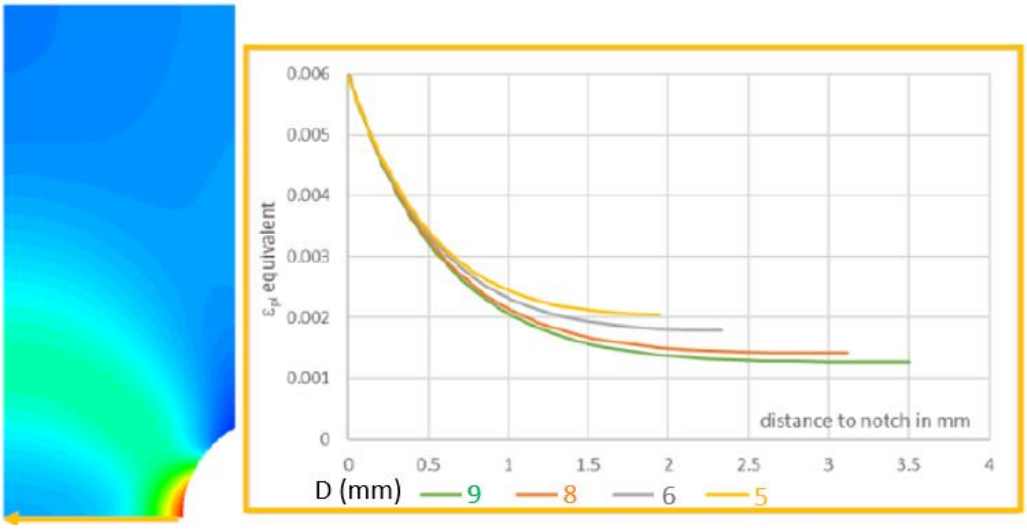

Figure 4.34. Equivalent von Mises strain gradient for different geometries with a notched radius of 2.0 mm and a strain amplitude at the notch tip of 0.6%.

Figure 4.35 compares the evolution of the equivalent strain gradient on the crack depth axis during the crack propagation for a notched radius of 2 mm between two specimen sizes: D1 = 9.0 mm; d2 = 7.0 mm; and D1 = 8.0 mm; d2 = 6.22 mm. Figure 4.36 compares the evolution of the equivalent strain gradient on the crack depth axis during the crack propagation for a notched radius of 0.5 mm between the two specimen sizes. The displayed iterations have been chosen to get the closest crack depth a between the two specimen sizes. Thus, for a similar crack depth a. the bigger specimen shows a lower strain along the crack depth axis which tends to decrease the fatigue crack growth rate. The minimum strain discrepancy between the two geometry

increases over the propagation for both notched radius: for the first iteration, the strain discrepancy is about 5% and for a crack depth close to 2.75 mm, it is about 20%.

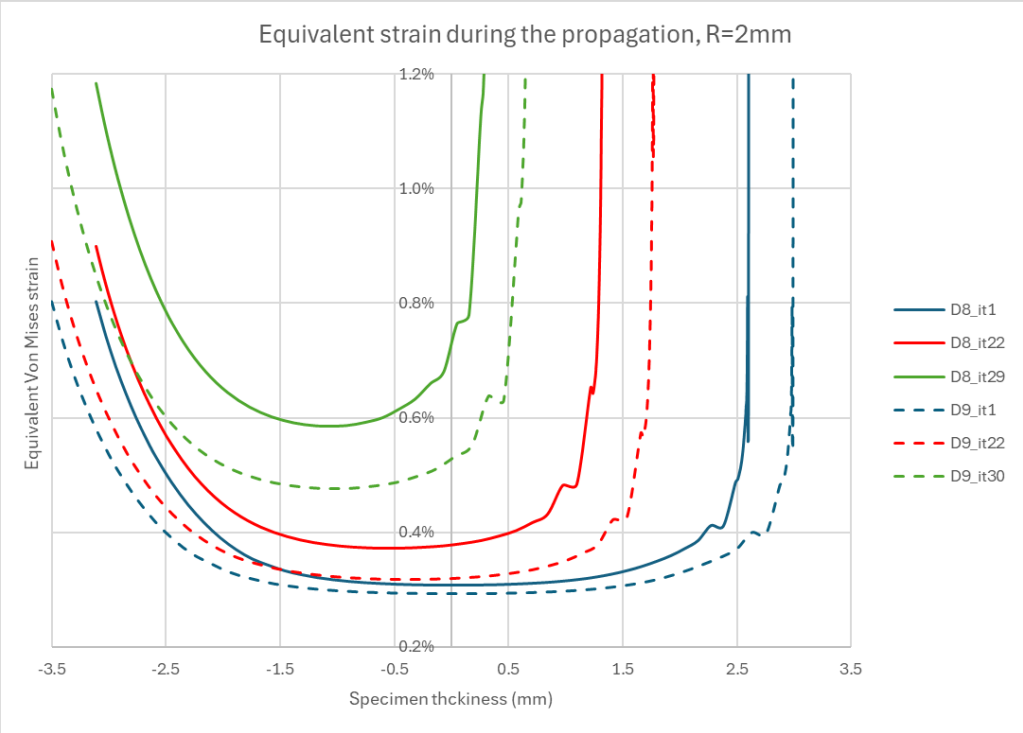

Figure 4.35. Equivalent von Mises strain gradient for a notched radius of 2.0 mm under a strain amplitude at the notch tip of 0.3% during the propagation.

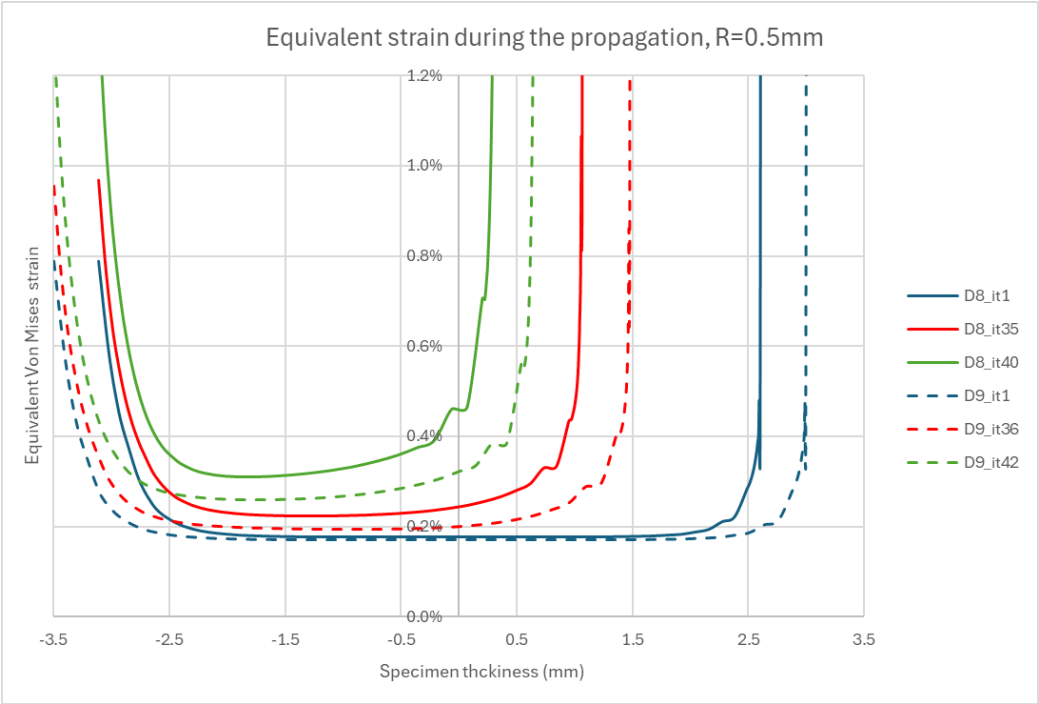

Figure 4.36. Equivalent von Mises strain gradient for a notched radius of 0.5 mm under a strain amplitude at the notch tip of 0.3% during the propagation.

The calculations and the striation counting demonstrate that the notched specimen geometry impacts the propagation stage: the crack growth rate is higher for smaller specimens which lead to lower fatigue lives. It mainly is related to the strain gradient. On the contrary, regarding the initiation stage, the bigger specimen dimensions are supposed to foster the crack initiation due to the highest probability to find irregularities in the material surface. Experimental fatigue life results of Figure 4.10 and Figure 4.11 show an important scatter which might be explained by the opposite effects on the initiation and the propagation. This opposite effect might also explain the lower averaged fatigue lives for large diameter notched specimens (see Figure 4.13). For these large diameter specimens, the crack initiation reduction due to the bigger diameter was certainly more important than the increase of crack growth stage duration, leading finally to lower total fatigue lives. In addition, it can also be noted that the multiplicity of crack initiations sites along the notch circumference induces variability in the crack propagation stage thus in the total fatigue life.

4.7 CONCLUSIONS

A testing program on notched specimens was defined with the aim to better understand and assess the fatigue lives from stress concentration areas. Results in air and in PWR environment showed that almost all fatigue lives are higher than the ones predicted by the NUREG/CR-6909, Rev.1 mean air curve for tests in air and the latter divided by the corresponding F_{en} value for PWR tests. The effect of specimen size and strain gradient has been highlighted and explain the highest fatigue lives obtained for the highest stress concentration factor configurations at a given notch tip strain amplitude. However, a large scatter on the results leads to question the reliability of the notch tip strain used for the analyses. In addition, the effect of the specimen size may induce opposite effects for the initiation stage and the propagation stage, and the multiplicity of the crack initiations sites along the notch circumference induces variability in the total fatigue life. Further analyses are needed to understand better the potential origins of the experimental scatter.

The work on notched specimens in the INCEFA-SCALE Project focused on understanding differences in fatigue life for several notch geometries tested at similar notch tip strain amplitude. However, it is important to note that another perspective of this work would be to analyse the test results with the methods described in the codes, meaning using the nominal stresses on the unnotched part of the specimens. Figure 4.37 highlights that in a stress space, higher stress concentrations are leading to lower fatigue lives as expected. The perspective would be to evaluate if the fatigue life reduction due to the notch is similar to the K_t value. Thus, potential conservatisms in code's approaches could be highlighted.

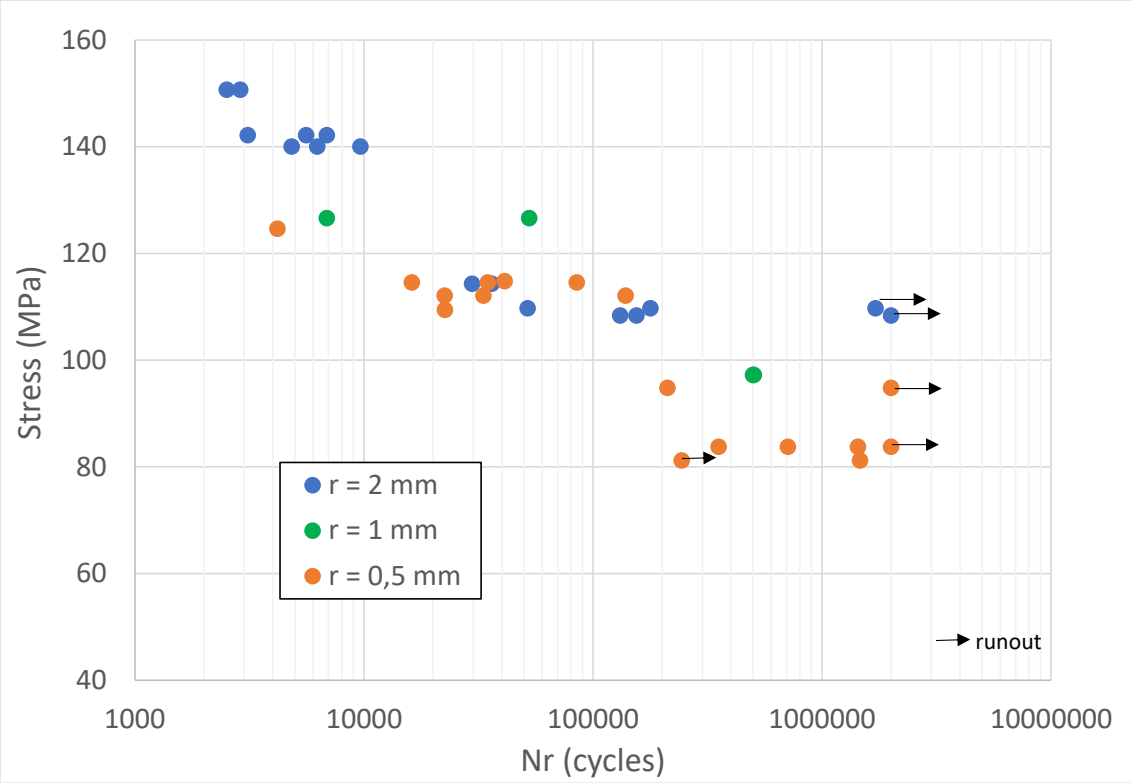

Figure 4.37. Notched fatigue lives versus nominal stress on the unnotched part of the specimens.

REFERENCES

[4.1] J.B. Terrell, Use of Neuber's rule to estimate the fatigue life of notched specimens of ASME SA 106-B steel piping in 288°C air, Int. J. Press. Vessel. Pip. 40 (1989) 17–40. doi:10.1016/0308-0161(89)90122-1.

[4.2] J.B. Terrell, Fatigue life response of ASME SA 106-B steel in pressurized water reactor environments, Int. J. Press. Vessel. Pip. 39 (1989) 345–374. doi:10.1016/0308-0161(89)90107-5.

[4.3] ASME, Boiler and Pressure Vessel Code, New York, 2009.

[4.4] ASME, Section III Division 1, Rules for Construction of Nuclear Power Plant Components, in: Boil. Press. Vessel Code, American Society of Mechanical Engineers, New York, 2021.

[4.5] ASME, Section VIII, Rules for Construction of Pressure Vessels, Division 1, Alternative Rules, New York, 2023.

[4.6] C.E. Jaske, J.L. Hechmer, E.J. Kuhn, WRC 432 Fatigue Strength Reduction and Stress Concentration Factors for Welds in Pressure Vessels and Piping: Part 1 & Part 2, 1998.

[4.7] E.C. Rodabaugh, S.E. Moore, Stress indices for girth welded joints, including radial weld shrinkage, mismatch and tapered-wall transitions, US-NRC, 1978. doi:10.2172/6518357.

[4.8] ASME, Division I - Subsection NB Class 1 Components, 2023.

[4.9] K. Kishida, M. Higuchi, M. Fukuzawa, High cycle fatigue strength of butt welded joints of small diameter pipes, Int. J. Press. Vessel. Pip. 55 (1993) 375–383. doi:10.1016/0308-0161(93)90058-2.

[4.10] J. Liao, J. Tan, X. Wu, D. Ning, G. Xue, W. Yao, Corrosion fatigue behavior of 304 stainless steel notched specimen in high-temperature pressurized water, Mater. Sci. Eng. A. 748 (2019) 137–145. doi:10.1016/j.msea.2019.01.090.

[4.11] J. Tan, Z. Zhang, H. Zheng, X. Wang, J. Gao, X. Wu, E.-H. Han, S. Yang, P. Huang, Corrosion fatigue model of austenitic stainless steels used in pressurized water reactor nuclear power plants, J. Nucl. Mater. 541 (2020) 152407. doi:10.1016/j.jnucmat.2020.152407.

[4.12] J.B. Terrell, NUREG/CR-5013 MEA-2232: Fatigue Life Characterisation of Smooth and Notched Piping Steel Specimens in 288 °C Air Environments, 1998.

[4.13] O.K. Chopra, G.L. Stevens, NUREG/CR-6909,Rev.1; Effect of LWR Water Environments on the Fatigue Life of Reactor Materials. Final Report, 2018.

[4.14] M. Itatani, K. Iida, K. Ogawa, Effect of loading rate on the fatigue strength of notched carbon steel in high temperature water, Am. Soc. Mech. Eng. Press. Vessel. Pip. Div. PVP. 374 (1998) 261–266.

[4.15] K. Sakaguchi, Y. Asada, M. Itatani, T. Saito, Evaluation of Environmental Effects on the Fatigue of Notched Specimen of Austenitic Stainless Steel Using Modified Rate Approach Method, in: Press. Vessel Pip. Codes Stand., ASMEDC, 2004: pp. 95–99. doi:10.1115/PVP2004-2678.

[4.16] M. Itatani, K. Sakaguchi, T. Saito, T. Hayashi, Evaluation for Environmental Fatigue of Notched Specimen of Ni-Base Alloy, in: Vol. 1 Codes Stand., ASMEDC, 2007: pp. 213–218. doi:10.1115/PVP2007-26379.

[4.17] CEA, Cast3M, (2003). https://www-cast3m.cea.fr/.

[4.18] AFCEN, RSE-M 2020. In-service inspection, installation and maintenance rules for mechanical components of PWR, 2020.

CHAPTER 5 INCEFA-SCALE BIAXIAL FATIGUE PROGRAM

This Chapter describes equi-biaxial feature testing conducted to assess whether variable amplitude loading impacts in-phase biaxial states significantly differently than standard uniaxial conditions, by Clémentine Jacquemoud.

5.1 INTRODUCTION

It is well understood that the in-plane loading of components would affect the fatigue initiation time of an unflawed surface. However, strains in other directions may also affect the initiation time. The influence of strain in other directions must be combined into a single scalar strain amplitude for use in fatigue assessment methods such as the ASME design curves. Several methods exist to account for the effect of multiaxial loading and produce a single scalar value to use with fatigue methods. ASME Section III uses the Tresca yield criterion (eq. 5.1) [5.1] to define an effective stress range for multiaxial loading. Other examples of these are the plastically corrected von Mises (eq. 5.2) [5.1], and the Maximum Total Principal strain (eq. 5.3).

$$\Delta\sigma_{eq} = max\{|\Delta\sigma_1 - \Delta\sigma_2|, |\Delta\sigma_2 - \Delta\sigma_3|, |\Delta\sigma_3 - \Delta\sigma_1|\} \quad \text{eq. 5.1}$$

$$\Delta\varepsilon_{ETSR} = \frac{\sqrt{2}}{2(1+\nu^*)}\left[(\Delta\varepsilon_1 - \Delta\varepsilon_2)^2 + (\Delta\varepsilon_2 - \Delta\varepsilon_3)^2 + (\Delta\varepsilon_3 - \Delta\varepsilon_1)^2 + \frac{3}{2}\left(\Delta{\gamma_{12}}^2 + \Delta{\gamma_{32}}^2 + \Delta{\gamma_{31}}^2\right)\right]^{1/2} \quad \text{eq. 5.2}$$

$$\Delta\varepsilon_{MTP} = (|\Delta\varepsilon_1|, |\Delta\varepsilon_3|) \quad \text{eq. 5.3}$$

A particular issue with these methods, and others, was noted by Reinhardt [5.2] where they would all predict the same life for specimens under uniaxial and equi-biaxial loading. This is not the observed behaviour for experiments conducted in low cycle fatigue. This highlights an issue with multiaxial models, which is that their validation is difficult due to the availability of test data under relevant conditions.

The relevant data that does exist indicates that for biaxial loading that is rationalized in terms of von Mises equivalent strain, there is little additional impact on the fatigue life of stainless steels [5.3]. This is further supported by the biaxial disc and uniaxial experiments reported by Gourdin et al. [5.4]. There is also an identifiable environmental effect of simulated PWR primary coolant conditions [5.5] that initially appears to be consistent with the environmental correction factor (F_{en}) definition of NUREG/CR-6909, Rev.1 [5.6]. Relevant data under LWR conditions beyond equi-biaxial loading has not been findable through reasonable efforts.

More complex models exist to address some of the short comings of the above methods. Critical plane methods are one such class consisting of the model by Jiang [5.7] and Critical Plane Strain Range models such as those presented by Leary et al. [5.8] and Yang et al. [5.9]. Like with the models stated above, these complex models are also difficult to differentiate between and validate. These types of methods have been compared by Leary et al. [5.8] and Hales et al. [5.10] based on a reanalysis of historic component scale data and found to be less conservative than the simple methods described above.

The simpler methods used for combining multiaxial loads are overly conservative and exploration and development of improved models may result in better predicted or allowable lifetimes in assessments. Aside from the combination of multiaxial loads, how these models handle other relevant parameters such as variable amplitude loading, surface finish, and environment is not well understood but is necessary for fully understanding the performance of these models in fatigue assessments.

Understanding of multi-axial and plant relevant loading is also a significant consideration for interpreting and analysing modern data collected on large-scale test pieces such as the stepped pipe [5.11] or the EPRI large-scale test [5.12]. The different analyses that have been performed on the data produced during the stepped pipe experiment, which produced a wide range of values for the predicted life of the test piece, highlight the deficiency in current assessment methods and the need for improved understanding of multi-axial fatigue [5.13].

5.2 DEFINITION OF THE EXPERIMENTAL PROGRAM

The purpose of this experimental program was to generate new test data in equi-biaxial loading conditions to improve the understanding of environmental low cycle fatigue in these complex conditions, specifically in the case of overloads.

5.2.1 UPGRADES OF THE FABIME2E TEST RIG

CEA is equipped with an equi-biaxial fatigue test rig called FABIME2e, initially developed to assess the equi-biaxial loading effect on fatigue life at constant strain amplitude [5.14].

Within the rig, a disc-shaped specimen is clamped between two half-shells called the fatigue cell (Figure 5.1.a). This cell contains either distilled water or PWR fluid. A pressure gradient (up to 10 MPa) applied alternatively on each side of the specimen creates a bending cyclic loading with a load ratio that can be either positive or negative. An initial operating pressure higher than 15 MPa on each side of the specimen is required to ensure that the PWR fluid remains monophasic. Practically, a pressure of 30 MPa is convenient to stay below the device limit of 35 MPa during a test.

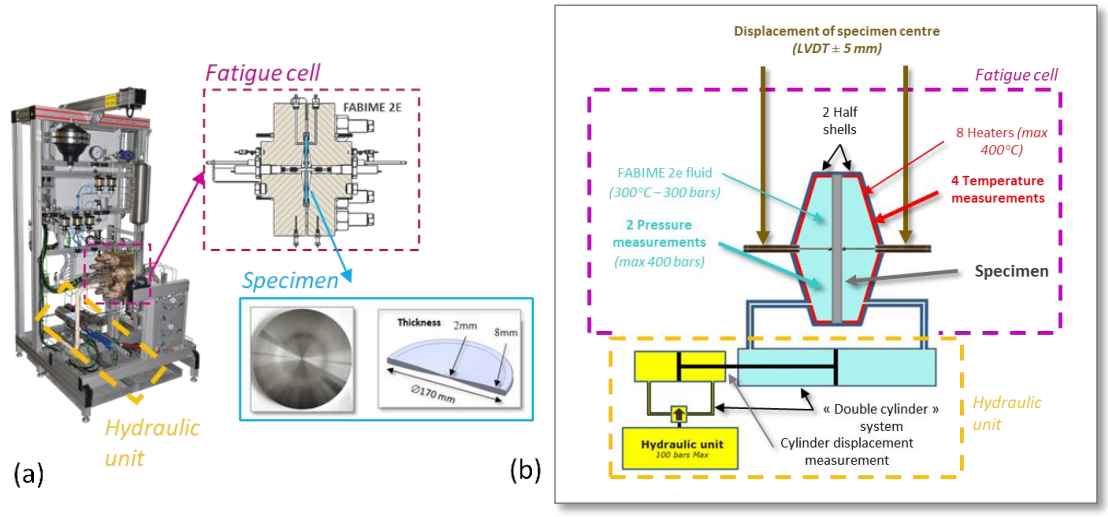

Figure 5.1. (a) FABIME2e test rig and the disc specimen geometry. (b) Rig instrumentation shown on a schematic.

A double-cylinder system ensures a pressure variation in the PWR fluid between the two half-shells. This double-cylinder connects the PWR fluid loop (in blue in Figure 5.1.b) to the hydraulic loop in oil (in yellow in Figure 5.1.b). Indeed, two hydraulic loops were required to isolate the PWR fluid from the rest of the hydraulic unit. The movement of this double-acting cylinder is controlled by the hydraulic unit (pressure-controlled). Then, its mechanical movement acts on the pressure of the PWR loop by modifying the fluid volume in each half-shell (using water incompressibility).

An efficient heating system composed of eight heating cartridges (250 W each) can conduct tests up to 340 °C. It is worth noting that only the fatigue cell and the PWR fluid supply pipes directly attached to the cell are maintained at the test temperature. The rest of the PWR loop must be at room temperature, especially the double-cylinder connected to the hydraulic loop. A secondary temperature loop control is dedicated to this part of the test rig.

The high-pressure high-temperature device results in a fatigue cell (two half-shells containing the specimen) with large dimensions for safety purposes (Figure 5.1.a). Sealing is a technological challenge by itself in such operating conditions. The PWR loop requires metallic sealing (EYTOR O-rings) compatible with the PWR environment and temperature.

Each half-shell of the fatigue cell is equipped with the following sensors (Figure 5.1.b):

- Type K thermocouples allow an accurate measurement of the temperature gradient, as a small variation in temperature (of about 1 °C) can have a high impact on the pressure level (up to a few megapascals).
- Pressure sensors with a capacity of 40 MPa.
- A Linear Variable Displacement Transducer (LVDT) to measure the specimen centre displacement. These types of displacement sensors support PWR environment conditions and have a measuring range of ±5 mm.

The disc-shaped specimen dedicated to FABIME2e tests has an optimised geometry (Figure 5.1.a) with a reduced thickness of 2.0 mm at the centre (on a 10 mm diameter area) to concentrate strain and ensure the crack initiates in the central part.

The control software of the device was developed in-house by CEA for Environmental-Assisted biaxial low cycle fatigue at constant amplitude loading. Despite its high flexibility and efficiency as required in such complex test conditions, the control software had to be upgraded to enable the variable amplitude loadings with high overloads (compared to baseline strain amplitude) planned in the INCEFA-SCALE Project. The improvements, presented in [5.5], mainly concern the device capability:

- to reach high overload ($\Delta\varepsilon/2 = \pm 1\%$), which is the highest value tested in the WP3.4 work package of the INCEFA-SCALE Project;
- to conduct tests at a low strain rate, inducing Proportional-Integral-Derivative optimisation of the signal and control mode modifications compared to previous tests at higher rates;
- to manage leakage via a new procedure and the temperature stability in the transition phase between overloads and baseline;
- to assure the reliability of the equipment for very long tests (months long).

These modifications have been successfully validated in [5.5]: the set point (displacement) was perfectly reached either on baseline or overload cycles for the POUL test at low strain rates; meanwhile, the micro-leaks were perfectly handled by the software using a pressure adjustment procedure.

5.2.2 FINITE ELEMENT MODEL FOR THE TEST DESIGN AND ANALISYS

Due to the PWR environment in the fatigue cell, no direct strain measurement is possible during the test. Nevertheless, predictions of the strain in the specimen were required which relied on Finite Element (FE) simulations.

A 3D mesh of one-quarter of the specimen was used in the FE simulations. The boundary conditions are illustrated in Figure 5.3.a. They were optimised to represent the experimental test conditions, particularly the clamping conditions, which affect the results. An elastoplastic Chaboche-type model was incorporated to account for the material hardening and softening behaviour. The model implemented in Cast3M CEA FE software [5.15] includes isotropic hardening and a kinematic hardening with two back stresses. The material parameters for the INCEFA-SCALE material have been calibrated at room temperature and 300 °C in Work Package 4 (WP4) based on uniaxial data at strain amplitudes of 0.5% and 1.0% corresponding to the half-life cycles. As illustrated in Figure 5.2.b and Figure 5.2.d, the material parameters listed in Figure 5.2-a and Figure 5.2.c fit the 0.5% strain data but do not accurately model the 1.0% strain data.

(a) T = 300°C

E (Gpa)	nu	
160	0.3	
C1 (Pa)	γ1	
1.36E+11	1200	
C2 (Pa)	γ2	
3.64E+10	303.194	
Psi	Omega	
1	0	
R0 (Pa)	RM (Pa)	b
5.00E+06	5.00E+06	1

(b)

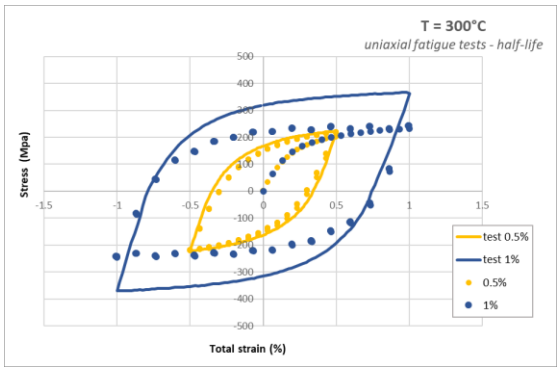

(c) T = 20°C

E (Gpa)	nu	
160	0.3	
C1 (Pa)	γ1	
5.26E+10	600	
C2 (Pa)	γ2	
2.87E+10	202.99	
Psi	Omega	
1	0	
R0 (Pa)	RM (Pa)	b
5.00E+06	5.00E+06	1

(d)

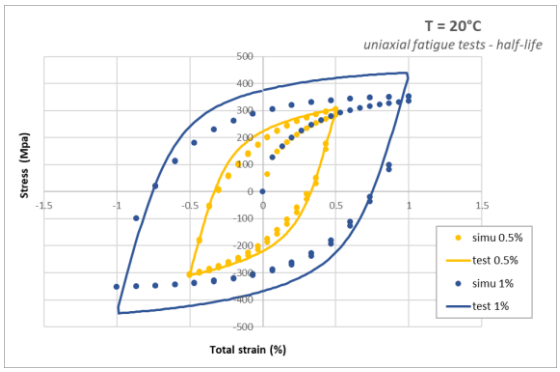

Figure 5.2. Material parameters calibrated for the Chaboche model at room temperature and 300 °C – INCEFA-SCALE material.

To replicate the experimental loading conditions, a loading optimisation procedure (Figure 5.3.b) was developed to iteratively calculate the pressure (P_{up} and P_{down}) that would be applied to match the required displacement (LVDT value at the specimen centre = U_z) for each cycle N

for a given waveform. The minimisation problem is solved by a Levenberg-Marquardt algorithm. It is a pressure-controlled procedure where the pressure is adjusted to reach the required experimental displacement, exactly as the experiments were conducted.

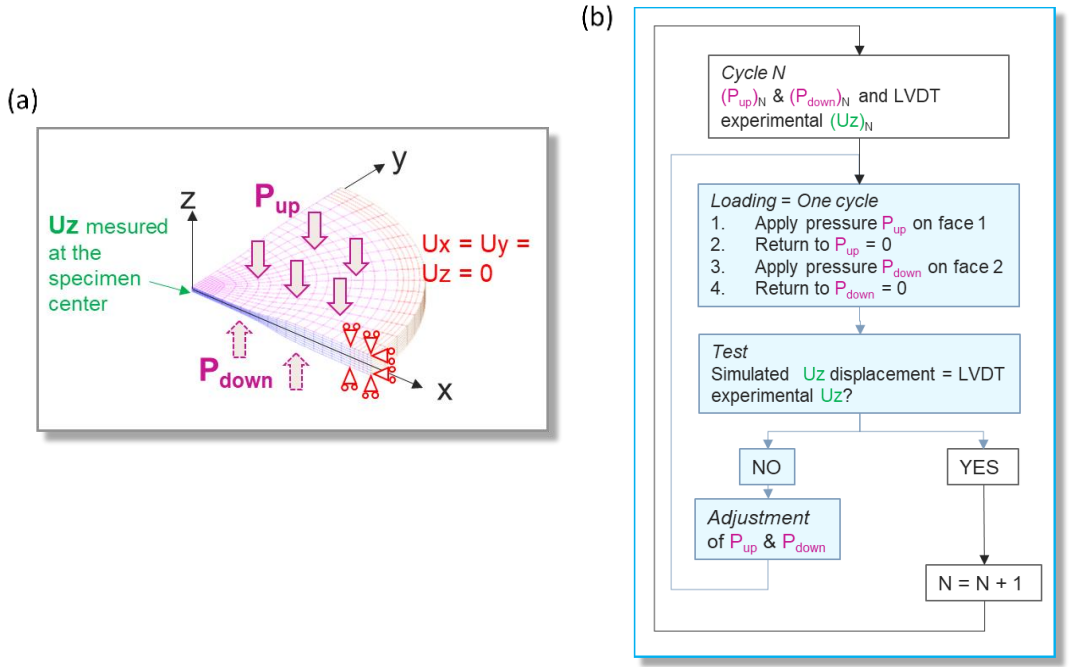

Figure 5.3. (a) FE mesh of 1/4 of the disc specimen with the boundary conditions and (b) optimisation procedure used for the simulations.

Simulations using this Finite Element Model (FEM) were dedicated to the test design and analysis. First, to define the loading conditions in terms of strain values, as described in Table 5.1, a specific calibration method was developed to link the simulated strain to the experimental displacement measured by the LVDT at the specimen centre. A dedicated experiment consists of a specific test rig with only one half-shell as described in [5.14] and illustrated in Figure 5.4.a.

Digital Image Correlation (DIC) was also used to measure the radial strain on the specimen surface during a half-cycle. The maximum radial strain at the specimen centre was plotted as a function of the displacement measured by the LVDT at the specimen centre (Figure 5.4.b). This experiment was then simulated using the FEM as described previously. The simulation output allowed the definition of a calibration curve linking the radial strain amplitude ($\Delta\varepsilon_{rr}/2$) to the displacement amplitude ($\Delta U_z/2$). Figure 5.4.b shows a good correlation between the experimental data coming from the DIC measurements.

This validated the use of the same simulation to establish, in a second step, the relationship between the radial strain (ε_{rr}) and the equivalent von Mises strain (ε_{eq}). Indeed, the FABIME2e test analysis aimed to compare the data (strain amplitude versus fatigue life) obtained in uniaxial and equi-biaxial loading conditions. Previous work by CEA [5.16] has already validated the use of the von Mises strain as an equivalent strain value in multiaxial PWR environments and the French design code RCC-MRx recommends the use of von Mises strain equivalent. For the INCEFA-SCALE Project, it was agreed to base the analysis on the von Mises equivalent strain for multi-axial loadings. Therefore, each test was simulated, and the maximum equivalent von Mises strain at the specimen centre was calculated.

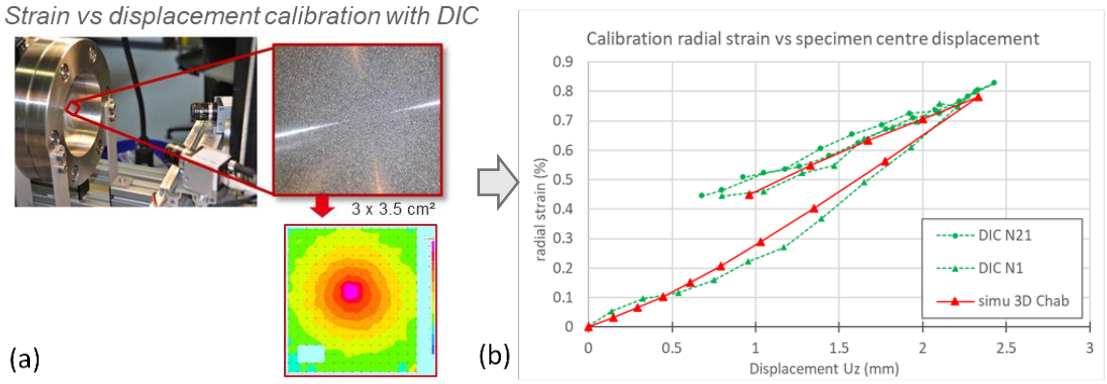

Figure 5.4. Calibration of the radial strain evolution with the specimen centre displacement using DIC measurement (in green) and comparison to FE simulations (in red).

5.2.3 THE EXPERIMENTAL TESTING PROGRAM

The testing program aimed to explore the combined effect of an overload and PWR environment in equi-biaxial loading conditions. CEA, tested the Periodic Over and Underload (POUL) sequence in biaxial conditions, with a focus on a 1.0% strain amplitude for the overload for comparison to the uniaxial test conditions.

Two different heats of 316L stainless steel were used:

- The INCEFA-SCALE common material, denoted “INCEFA”;
- The 316L used in [5.16] provided by EDF, denoted “EDF 316L”.

To evaluate whether the effects of VA loading we similar in equi-biaxial loadings and uniaxial loadings, loading conditions were prescribed to be equivalent. In uniaxial conditions, the POUL sequences (with a 1.0% strain overload) included baseline phases at a strain amplitude of 0.25%. with the same waveform selected for the biaxial tests. Complementary tests with constant amplitude loadings were also performed with a triangular waveform to evaluate the overload effect. The list of all biaxial tests carried out is given in Table 5.1:

				Cycle type - Over/Under load			Cycle type - Baseline		
Material	Waveform	Environment type	T (°C)	strain amplitude Δε/2 (%)	strain rate (%/s)	number of cycles / sequence	strain amplitude Δε/2 (%)	strain rate (%/s)	number of cycles / sequence
EDF 316L *(743BS)*	triangular	water	20				**0.6**	0.3	
EDF 316L *(743BP)*	POUL	water	20	**1**	0.1	2	**0.6**	0.3	1000
INCEFA *(816-C)*	POUL	PWR	300	**1**	0.1	2	**0.6**	0.1	1000
INCEFA *(816-H)*	POUL	water	20	**1**	0.1	2	**0.25**	0.25	1000
INCEFA *(816-B)*	POUL	PWR	300	**1**	0.1	2	**0.25**	0.01	1000

Table 5.1. Equi-biaxial test matrix – theoretical strain amplitudes.

Because the tests were displacement-controlled, the equivalent displacement amplitude and displacement rate were calculated using the FEM defined in Section 5.2.2 and the calibration procedure for the strain values. For the EDF 316L material, the Chaboche model parameters used in the simulations had been calibrated in [5.16]. The displacement at the specimen centre, as given in Table 5.2, was calculated to match the theoretical strain amplitude of Table 5.1 after 2 cycles, in terms of equivalent von Mises strain (as explained in Section 5.2.2).

				Cycle type - Over/Under load			Cycle type - Baseline		
material	Waveform	Environment type	T (°C)	displacement amplitude (mm)	rate (mm/s)	number of cycles / sequence	displacement amplitude (mm)	rate (mm/s)	number of cycles / sequence
EDF 316L (743BS)	triangular	water	20				+/- 1.2	0.6	
EDF 316L (743BP)	POUL	water	20	+/- 1.8	0.6	2	+/- 1.2	0.6	1000
INCEFA (816-C)	POUL	PWR	300	+/- 1.8	0.18	2	+/- 1.2	0.2	1000
INCEFA (816-B)	POUL	PWR	300	+/- 1.8	0.18	2	+/- 0.65	0.026	1000
INCEFA (816-H)	POUL	water	20	+/- 1.8	0.18	2	+/- 0.65	0.6	1000

Table 5.2. Equi-biaxial test matrix – displacement amplitudes and displacement rates calculated by FE.

5.3 EXPERIMENTAL RESULTS

Figure 5.5 to Figure 5.8 illustrate the experimental results obtained for the five tests listed in Table 5.1:

- (a) The pressure variation on each side of the specimen is plotted as a function of the number of cycles (orange curve = face 1, and blue curve = face 2). This graph enables the definition of the number of cycles at crack initiation, N_f.
- (b) The post-mortem photos of each specimen were taken at the end of the tests. The number of cycles indicated correspond to the final stop of the test.

5.3.1 CRACK INITIATION DETECTION

Detection of crack initiation was achieved using the method described in [5.5] based on the pressure variation drop, as no direct observation of the crack initiation is possible due to the PWR fluid.

The pressure variation on each face of the specimen shows a sudden decrease around 16000 cycles, as illustrated in Figure 5.5.a, for the constant amplitude test. Red dashed lines represent the mean slope of both parts of the curves (pre and post pressure drop); the lines' intersection corresponds to the number of cycles at crack initiation. The same pressure drop is observed on the POUL type test in Figure 5.6.a, which confirms that this method can be applied to both constant and variable amplitude loading tests to define the fatigue life.

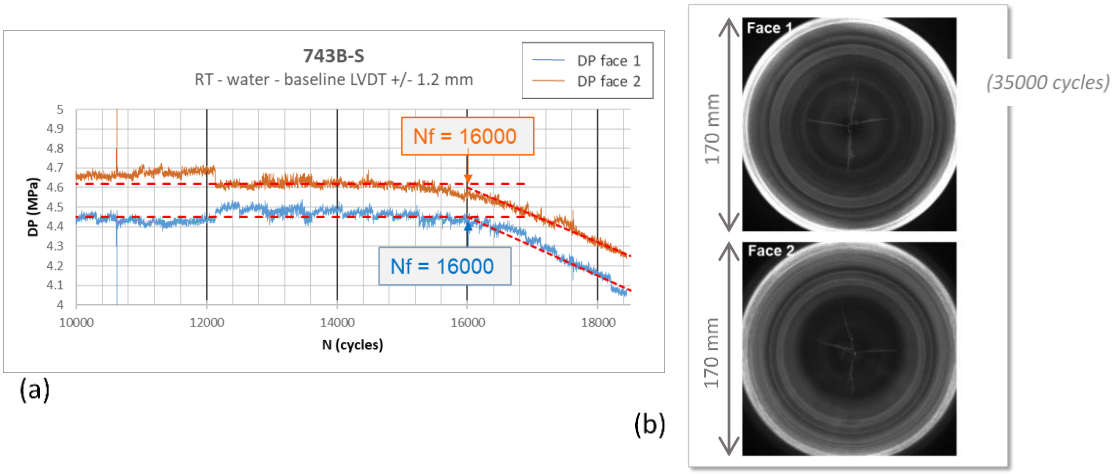

Figure 5.5. Results of triangular test 743B-S – water 20 °C – 0.6% - EDF 316L material.

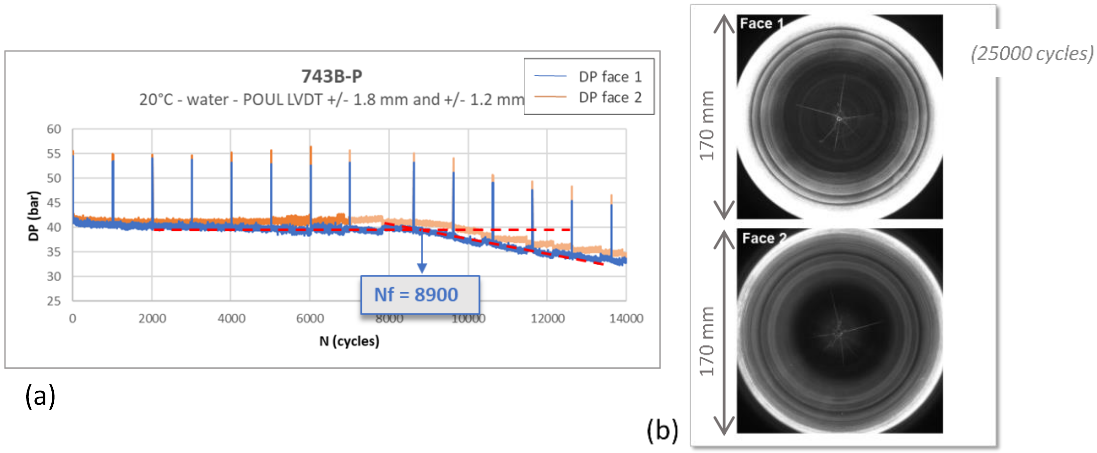

Figure 5.6. Results of POUL test 743B-P – water 20 °C – 1.0% - 0.6% - EDF 316L material.

The results of tests 816-H and 816-B further validate this method. On the one hand, in Figure 5.7.a, the slope change in the pressure curve is clearly defined (at N_f = 67500), and after a 5% pressure decrease, cracks around 10 mm in length are observed on each face of the specimen. On the other hand, in Figure 5.8.a, the pressure shows a small fluctuation at ≈42500 cycles, but remains generally constant till the end of the test. In this case, the surface crack measured is about 4-5 mm in length on each face of the specimen.

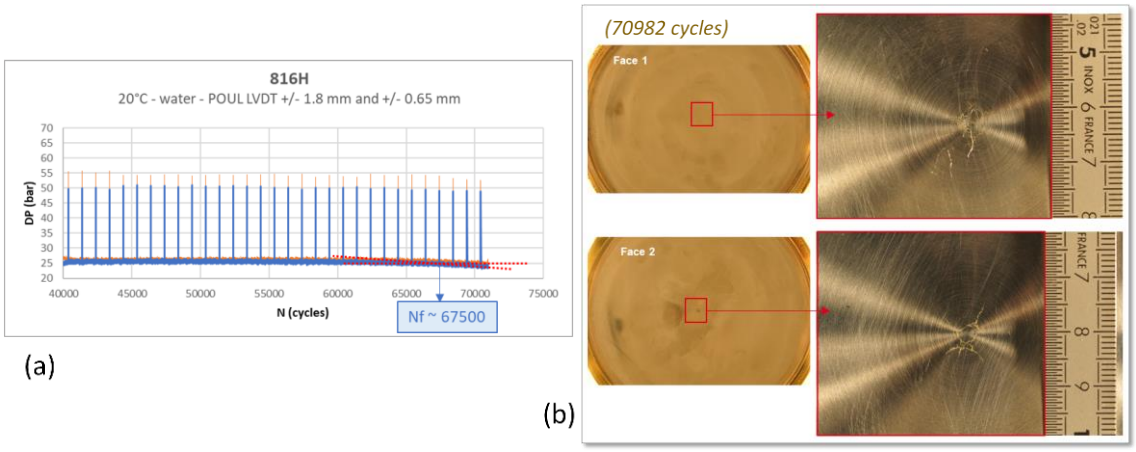

Figure 5.7. Results of POUL test 816-H – water 20 °C – 1.0% - 0.25% - INCEFA-SCALE material.

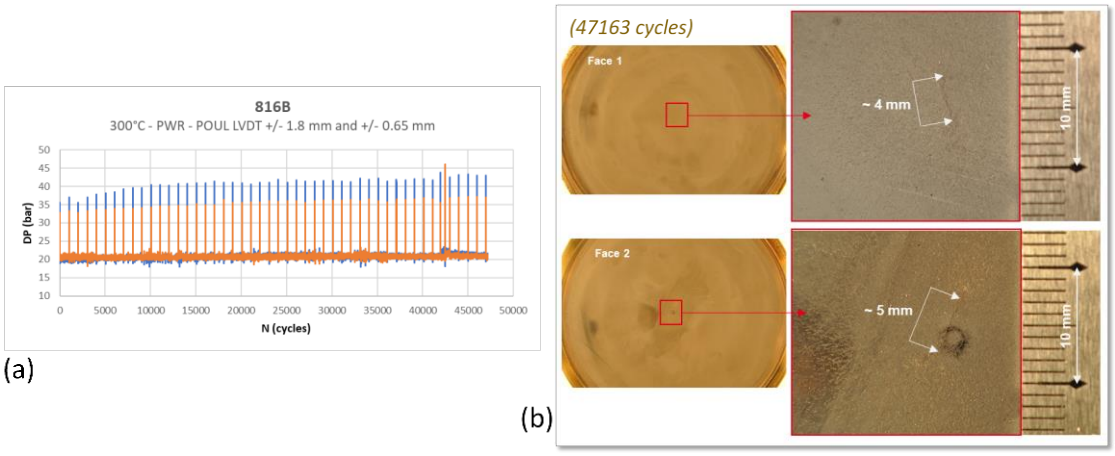

Figure 5.8. Results of POUL test 816-B – PWR 300 °C – 1.0% - 0.25% - INCEFA-SCALE material.

This led to the conclusion that the N_f values defined (at the start of the pressure drop) on these four tests (743B-P, 743B-S, 816-H and 816-B) correspond to a surface crack of about 4-5 mm on both faces of the specimens, based on test 816-B being considered the initial pressure fluctuation at initiation which showed cracks this length following examination.

Test 816-C (Figure 5.9.a) is an isolated case. The baseline pressure seems to decrease right after each overload and then remains constant for the following 1000 cycles of the baseline, resulting in a stepwise progression of the pressure making initiation becomes more challenging to define. However, as can be seen with the scale zoomed in Figure 5.9.c, the pressure starts to decrease between 2000 and 3000 cycles, reaching the 5% drop limit as defined above before a third step down at 3000 cycles, of more than 8%, suggesting a larger crack than 5 mm long. Consequently, the N_f value for this test is then set in the range of 2000 to 3000 cycles.

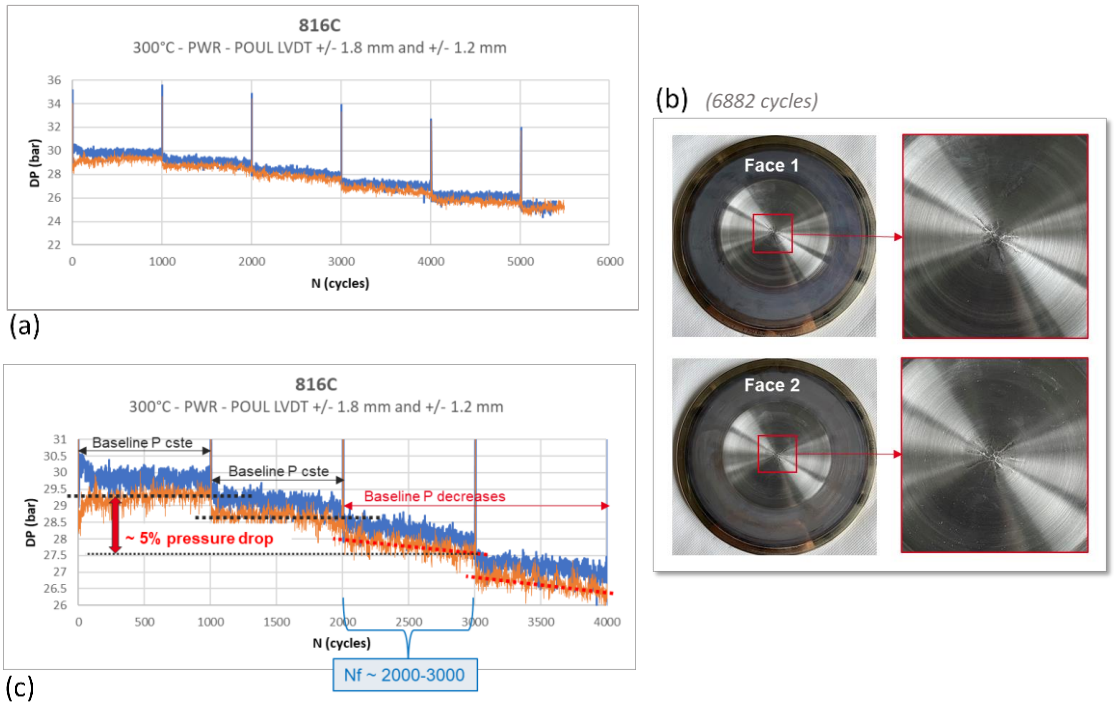

Figure 5.9. Results of POUL test 816-C – PWR 300 °C – 1.0% - 0.6% - INCEFA-SCALE material.

The fractography suggests that initiation had occurred on both faces of the specimen, at the number of cycles defining initiation, although the cracks had not interacted. The N_f values therefore could be slightly different on each face, but not significantly different when the R ratio is -1.

5.3.2 FATIGUE LIFE RESULTS

Based on the crack detection method presented above, fatigue life results (N_f) are summarised in Table 5.3 for the five equi-biaxial tests.

				Cycle type - Over/Under load			Cycle type - Baseline			
Material	Waveform	Environment type	T (°C)	strain amplitude Δε/2 (%)	strain rate (%/s)	number of cycles / sequence	strain amplitude Δε/2 (%)	strain rate (%/s)	number of cycles / sequence	Nf
EDF 316L *(743BS)*	triangular	water	20				**0.6**	0.3		16000
EDF 316L *(743BP)*	POUL	water	20	**1**	0.1	2	**0.6**	0.3	1000	8900
INCEFA *(816-C)*	POUL	PWR	300	**1**	0.1	2	**0.6**	0.1	1000	2000-3000
INCEFA *(816-H)*	POUL	water	20	**1**	0.1	2	**0.25**	0.25	1000	67500
INCEFA *(816-B)*	POUL	PWR	300	**1**	0.1	2	**0.25**	0.01	1000	47163

Table 5.3. Equi-biaxial test results.

These experimental results can be plotted on a displacement amplitude versus number of cycles graph (Figure 5.10). Tests circled by black dashed lines were performed during the INCEFA-SCALE Project (listed in Table 5.3). They are compared to previous data from tests at constant amplitude loading performed on the EDF 316L material, in distilled water either at room temperature (blue triangles) or at 300 °C (red triangles).

Since the POUL test in a PWR environment and with a 0.6% baseline strain (816-C) has been complex to analyse, the range of N_f values (N_f = 2000-3000 cycles) is represented by two red dots in Figure 5.10.

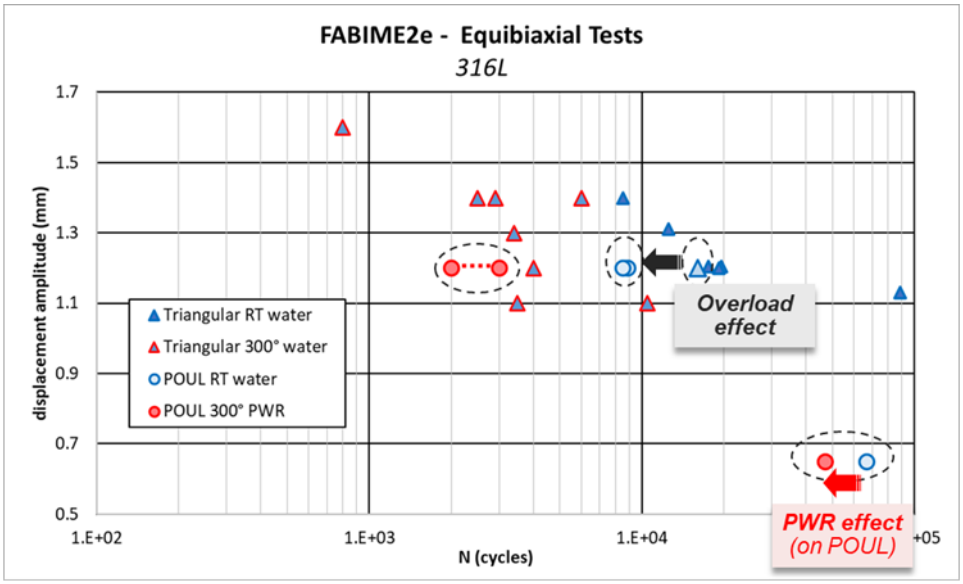

Figure 5.10. Fatigue life for equi-biaxial tests performed in the INCEFA-SCALE Project (circled by black dashed lines) compared to existing data [5.16] at constant amplitude loadings (triangles).

In equi-biaxial testing conditions:

- Overload effect in distilled water at room temperature (RT):

  Overloads in the POUL 1.0% - 0.6% test tend to reduce the fatigue life at room temperature by ≈1/2 in distilled water compared to constant amplitude loading tests with the same baseline amplitude of 0.6%. These tests were not carried out on the INCEFA-SCALE common material so direct comparisons with the uniaxial test data cannot be drawn, especially considering this waveform was not completed in the uniaxial test programme.

It is noted that however that the fatigue life for the constant amplitude test in the room temperature water test is significantly longer (≈3.5x on average) than those carried out with uniaxial specimens in air. This may suggest a smaller equivalent strain amplitude was achieved at the notch tip than the DIC/FE results would suggest. It is difficult to draw further conclusions without further testing.

- PWR effect on POUL test:

  For the comparable pair of POUL 1.0% - 0.25% tests, the PWR environment reduces the fatigue life. This effect can be quantified through the environmental correction factor. An experimental value of the F_{en} was calculated using eq. 1.1 for the POUL test with baseline strain amplitude level of 0.25%.

$$F_{en\ exp} = \frac{N_{f,water}}{N_{f,PWR}} \qquad \text{eq. 5.4}$$

  The experimental F_{en} values in Table 5.4 demonstrate different PWR environment effects for both low and high baseline strain levels.

Loading type	Test conditions	N_f exp.	F_{en} exp.
Overload 1% **Baseline 0.25%**	Water – 20 °C	67434	**1.43**
	PWR – 300 °C	47163	

Table 5.4. Summary of the F_{en} values for POUL tests.

The experimental F_{en} values are then higher than the theoretical value of F_{en}, which is 4.57 for a strain rate of 0.01 %/s. This may be due to simple scatter in that the PWR test showed a longer life than would be expected, although further testing and more detail multiaxial strain rate calculations would need to be carried out to further support this hypothesis.

This combined with the discrepancy in the lives at constant amplitude test suggests that there may be some inaccuracy in comparing the equivalent strain method used here and the uniaxial test data to predict fatigue lives. The longer lives provided by the biaxial tests however suggest this method is conservative, albeit overly so. Further analysis with critical plane approaches such as suggested in the introduction would also be desirable to further understanding of these fatigue lives.

5.4 DISCUSSION AND CONCLUSION

The FABIME2e equi-biaxial fatigue test rig has been successfully upgraded to achieve VA loading in PWR conditions. Nevertheless, very low strain levels leading to very long test durations have highlighted the rig limits: tests are highly damaging to the machine, leaks need to be managed during the tests, and seals and parts must be fixed or replaced during one test.

However, the five equi-biaxial tests have generated valuable data to draft the first conclusions:

- Overloads reduce fatigue life by ≈1/2 compared to constant 0.6% strain amplitude loadings.
- In POUL tests, the PWR environment reduces fatigue life, compared to water at RT.

- The fatigue lifetime is seemingly much higher in equi-biaxial conditions compared to uniaxial tests in the same conditions. Unfortunately, this comparison is only based on a very limited dataset.

REFERENCES

[5.1] ASME, Section VIII, Rules for Construction of Pressure Vessels, Division 1, Alternative Rules, New York, 2023.

[5.2] W. Reinhardt, Strain Measures for Fatigue Assessment Using Elastic-Plastic FEA, in: Vol. 2 Comput. Technol., ASMEDC, 2005: pp. 223–231. doi:10.1115/PVP2005-71547.

[5.3] D. Tice, A. McLennan, P. Gill, Environmentally assisted fatigue (EAF) knowledge gap analysis: Update and revision of the EAF knowledge gaps, Palo Alto, CA, 2018.

[5.4] C. Gourdin, G. Perez, H. Dhahri, L. De Baglion, J.-C. Le Roux, Environmental Effect on Fatigue Crack Initiation under Equi-Biaxial Loading of an Austenitic Stainless Steel, Metals (Basel). 11 (2021) 203. doi:10.3390/met11020203.

[5.5] C. Jacquemoud, C. Gourdin, G. Perez, L. Doremus, Biaxial Fatigue Tests in PWR Environment, in: Vol. 1 Codes Stand., American Society of Mechanical Engineers, 2025. doi:10.1115/PVP2025-151549.

[5.6] O.K. Chopra, G.L. Stevens, NUREG/CR-6909,Rev.1; Effect of LWR Water Environments on the Fatigue Life of Reactor Materials. Final Report, 2018.

[5.7] Y. Jiang, H. Sehitoglu, Modeling of cyclic ratchetting plasticity, part i: Development of constitutive relations, J. Appl. Mech. Trans. ASME. 63 (1996) 720–725. doi:10.1115/1.2823355.

[5.8] D. Leary, C. Currie, K. Wright, Critical Review of Strain Measures for Characterisation of Fatigue Damage in ASME Section III Fatigue Assessments, in: Vol. 1 Codes Stand., American Society of Mechanical Engineers, 2019. doi:10.1115/PVP2019-93849.

[5.9] F.P. Yang, X.G. Yuan, Z.B. Kuang, Influence of loading path on fatigue crack growth under multiaxial loading condition, Fatigue Fract. Eng. Mater. Struct. 35 (2012) 425–432. doi:10.1111/j.1460-2695.2011.01633.x.

[5.10] R. Hales, Multiaxial creep-fatigue rules, Nucl. Eng. Des. 153 (1995) 257–264. doi:10.1016/0029-5493(94)00832-J.

[5.11] D.P. Jones, J.E. Holliday, T.R. Leax, J.L. Gordon, Analysis of a Thermal Fatigue Test of a Stepped Pipe, in: Proc. ASME/JSME 2004 Press. Vessel. Pip. Conf. Comput. Technol. Appl., ASMEDC, 2004: pp. 67–77. doi:10.1115/PVP2004-2748.

[5.12] D. Bellett, F. Morel, A. Morel, J. -L. Lebrun, A Biaxial Fatigue Specimen for Uniaxial Loading, Strain. 47 (2011) 227–240. doi:10.1111/j.1475-1305.2009.00674.x.

[5.13] J. Mann, M. Twite, M.G. Burke, Analysis of Fatigue Crack Growth in Standard Endurance Test Specimens in Support of Total Life Approaches to Fatigue Assessment, in: Vol. 5 High-Pressure Technol. Rudy Scavuzzo Student Pap. Symp. 24th Annu. Student Pap. Compet. ASME Nondestruct. Eval. Diagnosis Progn. Div. (NDPD); Electr. Power Res. Inst. Creep Fatigue Work., American Society of Mechanical Engineers, 2016. doi:10.1115/PVP2016-63238.

[5.14] C. Gourdin, G. Perez, H. Dhahri, S. Courtin, J.C. Le Roux, H. Maitournam, PWR effect on crack initiation under equi-biaxial loading development of the experiment, Mech. Ind. 20 (2019) 619. doi:10.1051/meca/2019060.

[5.15] CEA, Cast3M, (2003). https://www-cast3m.cea.fr/.

[5.16] H. Dhahri, Endommagement en fatigue multiaxiale avec effet d'environnement REP. Matériaux et structures en mécanique, Université Paris-Saclay, 2019.

This page intentionally left blank.

CHAPTER 6 INCEFA-SCALE DATA ANALYSIS

This Chapter describes the establishment of a data-driven framework and the International Fatigue Database designed to bridge knowledge gaps between laboratory data and NPP component lifetimes, by Petra Gee, Roman Cicero, and Tim Austin.

6.1 INTRODUCTION

This Chapter provides a comprehensive overview of the data-driven framework established to advance the prediction of NPP component lifetimes under environmentally assisted fatigue loading. A central challenge in current nuclear safety assessments is the significant "knowledge gap" regarding the transferability of small-scale laboratory test data to real-world component geometries and complex loading conditions.

To address this, the INCEFA-SCALE Project focuses on the development of a robust data infrastructure and advanced analytical methodologies. This Chapter details the management and harmonization of vast datasets, including the creation of the International Fatigue Database. This repository integrates historical data from NUREG/CR-6909, Rev.1 [6.1], results from the predecessor INCEFA-PLUS Project, and recent contributions from international third-party sources.

The following Sections will outline the procedures for data curation, the selection of critical variables—ranging from common environmental parameters to specialized project-specific metrics—and the overarching strategy for utilizing this data to reduce unnecessary conservatism in safety cases while maintaining the highest standards of structural integrity.

6.2 DATA CURATION

An established engineering materials database application [6.2] was adopted as the INCEFA-SCALE data repository. The mentioned database application (MatDB [6.3]) is one of a handful of systems ranked by the JRC FAIR Data Guidelines [6.4] as being compliant with the highest level of the FAIR data maturity model [6.5] and as such is optimised for data sharing and reuse. The system was thus well-suited to supporting the scientific objectives of INCEFA-SCALE by ensuring test results were readily accessible to all project partners. An underlying principle of the data curation was that any individual test result was entered into the database in a timely manner, which as well as enabling analysis of the entire collection of test results as they became available, allowed sufficient time to correct any shortcomings in data quality and completeness. This contrasts to giving data curation towards project term simply to ensure data are preserved, which although having some merit, risks creating a silo of poor-quality data.

6.2 STATISTICAL ANALYSIS

The development of accurate life-prediction models for nuclear components requires a systematic statistical approach to interpret the complex interactions between mechanical loading and environmental effects. By applying advanced analytical techniques to the expanded International Fatigue Database (IFD) [6.6], this analysis aims to move beyond purely empirical observations toward a deeper mechanistic understanding of fatigue degradation. The following

study evaluates various modelling architectures, ranging from traditional linear regression to sophisticated neural networks, to identify the most robust predictors of fatigue endurance. These statistical efforts are essential for validating new sensitivities and establishing a more realistic, data-driven foundation for nuclear safety standards. For the simplicity of this demonstration of model development using the INCEFA-SCALE tool the models are restricted to the linear range of the low cycle fatigue regime.

6.2.1 DATA REPOSITORY

This Section outlines the centralized data repository developed to support the project's analytical goals. The IFD compiles historical benchmarks, project-specific experimental results, and international third-party data into a harmonized structure for robust fatigue life prediction.

6.2.1.1 FATIGUE DESIGN CURVES AND ENVIRONMENTAL EFFECT

The fatigue design curves in the ASME code are derived from strain-controlled fatigue tests conducted on small, polished specimens at room temperature in air. These curves were developed using best-fit correlations to experimental fatigue ε-N data, expressed through the Langer equation. During the 1990s, a comprehensive effort was undertaken to compile and analyse existing strain-life (ε-N) fatigue data from various institutions and research laboratories worldwide, primarily in the United States and Japan. Fatigue tests recorded not only the strain amplitude and the number of cycles to failure but also parameters such as specimen diameter, temperature, strain rate, environmental characteristics, and material grade. These data were systematically compiled in NUREG documents (USNRC), with significant information consolidated in NUREG/CR-6909, Rev.1 [6.1].

The predictive model based of this environmental factor outlined in the NUREG/CR-6909, Rev.1 for stainless steels was established based on various tests conducted in air (770) and in LWR environments (683, of which approximately 570 were under PWR environmental conditions).

The method described by Currie et al. [6.7] and Asada et al. [6.8] (the former is the basis of a recently accepted ASME code-case and the latter is now part of the JSME code) are based on a subset of the NUREG/CR-6909, Rev.1 database with some additional data covering aspects such as variable amplitude effects on fatigue limit. This overlap in datasets between these methods is the result of data sharing between the USNRC and Japan during the development of NUREG/CR-6909, Rev.1. Therefore, the methods are often compared to each other when new behaviour is accounted for to highlight the original gap and the effect of it being resolved. Furthermore, independent development of methods from shared datasets lends strength to them where they agree and supports continuous improvement efforts to provide methods with appropriate margin.

6.2.1.2 NEW FATIGUE DATA DEVELOPED DURING INCEFA-PLUS AND INCEFA-SCALE PROJECTS

During the INCEFA-PLUS Project, additional key factors influencing fatigue behavior, such as mean strain/stress, hold times, and surface roughness, were systematically investigated in austenitic stainless steel [6.9]. A comprehensive series of 260 fatigue tests was performed,

comprising of 103 tests conducted in air and 157 in PWR environment. Detailed measurements were taken, including hysteresis loops and cyclic curves (ε-N) at specific cycles for all tests.

The resulting fatigue data provided valuable insights. These findings not only highlighted potential gaps requiring further analysis but also significantly expanded the statistical dataset, enabling the development of more robust and reliable predictive models.

The INCEFA-SCALE Project contributes 110 new validated fatigue tests (58 in air and 52 in PWR environment). This new dataset was designed with the aim of significantly contribute to a deeper understanding of the fatigue process. Among other relevant factors, the project places particular emphasis on the interaction between waveform and mean strain.

6.2.1.3 INTERNATIONAL FATIGUE DATABASE (IFD)

Since the publication of NUREG/CR-6909, Rev.1 [6.1], a substantial body of international data and research has emerged, significantly enhancing the understanding of fatigue degradation mechanisms in the nuclear industry. This progress has contributed to a more robust foundation for assessing and mitigating fatigue-related aging in critical NPP components.

In addition to the data generated through the INCEFA-PLUS and INCEFA-SCALE projects, contributions from third-party institutions have recently further enriched the fatigue database. Notable sources include Mitsubishi Heavy Industries (Japan) and PreussenElektra (Germany), as well as proprietary data from laboratories currently involved in the INCEFA-SCALE Project.

At the conclusion of the INCEFA-PLUS Project, and especially during the development of the INCEFA-SCALE Project, a significant effort was made by various organizations to compile fatigue data coming from various sources worldwide into a single database: the International Fatigue Database [6.6].

The origins of the IFD can be traced back to a publication on the topic of an EDF/NRC High-Cycle Fatigue Database Proposal [6.10], the authors of which participates in the INCEFA-PLUS and INCEFA-SCALE projects. Although the eventual focus of the IFD is EAF rather than high cycle fatigue, the underlying principles outlined in the publication are unchanged insofar as particular attention is given to data fields of particular relevance and data quality.

The legal framework on which the IFD is based anticipates the accession of new organisations and continued contributions at intervals by existing signatories, so that the total body of test results will increase (and new releases of the IFD published) over time. The first release of the IFD is available at [6.11] and Table 6.1 summarizes the quantity of available fatigue data for stainless steels, noting that the total IFD count does not include data provided by KAERI.

Data Source	Air	PWR	Total
NUREG/CR-6909	818	613	1431
INCEFA-PLUS	102	131	233
INCEFA-SCALE	58	52	110
Third Sources	86	187	273
TOTAL (IFD)	1064	983	2047

Table 6.1. Summary of fatigue data sources for stainless steel.

6.2.1.4 VARIABLES RECORDED IN THE DATABASE

The number of variables recorded varies depending on the source of information and, fundamentally, the year in which the tests were conducted. All fatigue datasets include values for a common set of variables, as shown in Table 6.2:

Variable	Description	Unit
Material Grade	AISI 316, AISI 304L…	--
Environment	Air, PWR, BWR	--
Temperature	Real Value	ºC
Strain ratio	Real Value	--
Waveform	Triangular, Sawtooth…	--
Hold Time	Yes/No	--
Strain Rate	Real Value	·/s
Surface Finish	Rough, Smooth	--
Specimen Type	Bar, Hollow, Plain	--
Strain Range	Real Value	%

Table 6.2. Common variables recorded in all datasets.

However, in the case of fatigue tests conducted within the INCEFA-PLUS Project (and INCEFA-SCALE), a greater number of variables were recorded. These additional variables are presented in Table 5.4:

Variable	Description	Unit
Diameter	Real Value	mm
Average Roughness	Real Value	µm
Max. Rough. Height	Real Value	µm
Env. Pressure	Real Value	MPa
B Content	Real Value	ppm
Li Content	Real Value	ppm
Dissolved H2	Inlet value	cc/kg
Dissolved O2	Average value	ppb
Conductivity	Inlet value	mS/cm
pH	Average value	--

Table 6.3. Additional variables recorded in INCEFA-PLUS and INCEFA-SCALE.

Even for common variables like waveform, the new test programs include more variety and complexity. In fact, a detailed analysis of the waveform's interaction with other factors is a primary focus of the INCEFA-SCALE Project (IHL, IHL-S, IOUL, POL, POUL, and PUL).

The combined INCEFA-PLUS and INCEFA-SCALE projects have yielded richer datasets, enabling a more nuanced analysis. Analysts can choose between two primary approaches: using the full IFD dataset (approximately 2000 tests) with 10 common variables to identify broad trends, or employing a focused subset (approximately 350 tests from the two projects) with over 20 variables to investigate specific damage mechanisms in greater detail.

6.2.2 DATA MINING APPLICATION

Work Package 2 (WP2) within the INCEFA-SCALE Project is dedicated to data mining. As part of this effort, a web application was developed to facilitate comprehensive analysis of fatigue data [6.12].

The primary goal of this application is to analyse existing fatigue datasets and accommodate future data generated in subsequent years. Currently, access to the application is available to all members of the International Fatigue Data group, with plans to expand access to the general public based on user type.

The web application utilizes two types of models: linear regression and a neural network with nine neurons. It enables the analysis of various fatigue parameters that influence or may influence the fatigue life of steels.

Specifically, two distinct linear regression architectures are available for selection. The first is a standard linear model, while the second utilizes the NUREG/CR-6909, Rev.1 fatigue life predictive model expression [6.1] (also described in Section 1.3):

$$ln(N) = A - Bln(\varepsilon_a - C) \quad \text{eq. 6.1}$$

where A, B, and C are model coefficients, N is the fatigue life, and ε_a is the strain amplitude. Note that for the so-called standard linear regression model, the parameter "C" has a value of zero. The linear regression model has been the most widely used so far for two main reasons:

1. it has proven to be as accurate as the models obtained with the neural network, and;
2. it provides an analytical expression that can be directly applied in fatigue calculations. The inability of the neural network to return an analytical expression makes the model harder to interpret and utilize in future predictions.

The models enable users to evaluate their accuracy based on various predictor variables and interactions. The accuracy and reliability of the models are assessed using the following metrics:

- MAE (Mean Absolute Error): Measures the average error in model predictions, calculated as the sum of absolute errors divided by the sample size.
- R^2 (Coefficient of Determination): Represents the proportion of variance explained by the model, serving as an indicator of its explanatory power.
- VIF (Variance Inflation Factor): Assesses the degree of multicollinearity among predictor variables.
- ANOVA (Analysis of Variance): Evaluates the significance of variance within the model.
- p-value: provide statistical significance for all predictor variables.

The application integrates a range of analytical functionalities to facilitate the comprehensive evaluation of experimental results. The primary features available to the analyst are detailed below:

- Variable selection: Allows the user to load only the variables required for evaluation or use in dataset filtering (Figure 6.1).

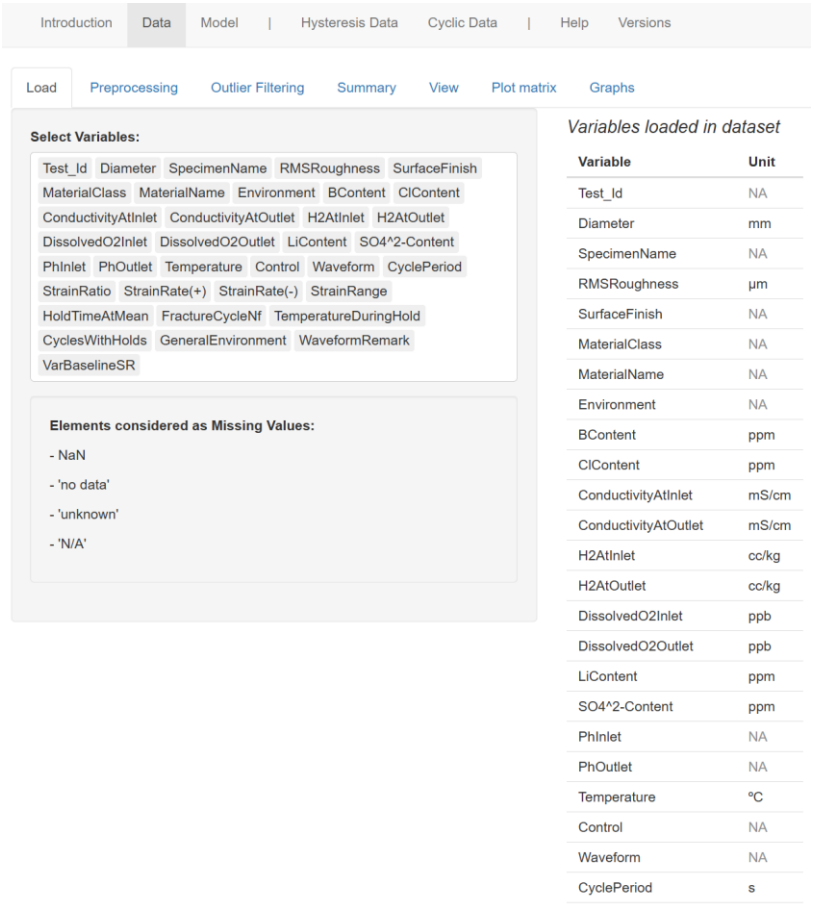

Figure 6.1. Variable selection.

- Data Pre-processing: Filters the data based on the loaded variables to further refine the desired dataset. (Figure 6.2).

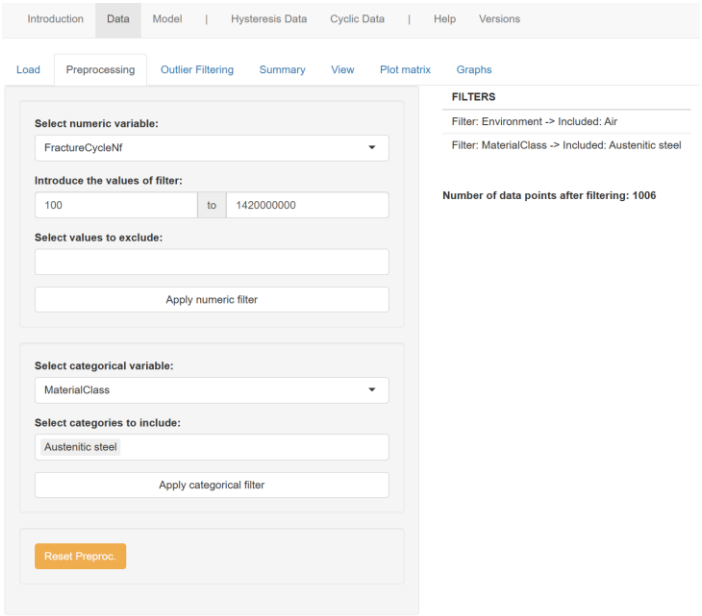

Figure 6.2. Data filtering and pre-processing.

- Outlier Detection: Identifies potential anomalies by calculating z-scores for each material class-environment pair within the refined dataset. Data points falling outside a

user-defined threshold are flagged as potential outliers, providing the analyst with the necessary criteria to decide on the inclusion or exclusion of suspicious data. (Figure 6.3).

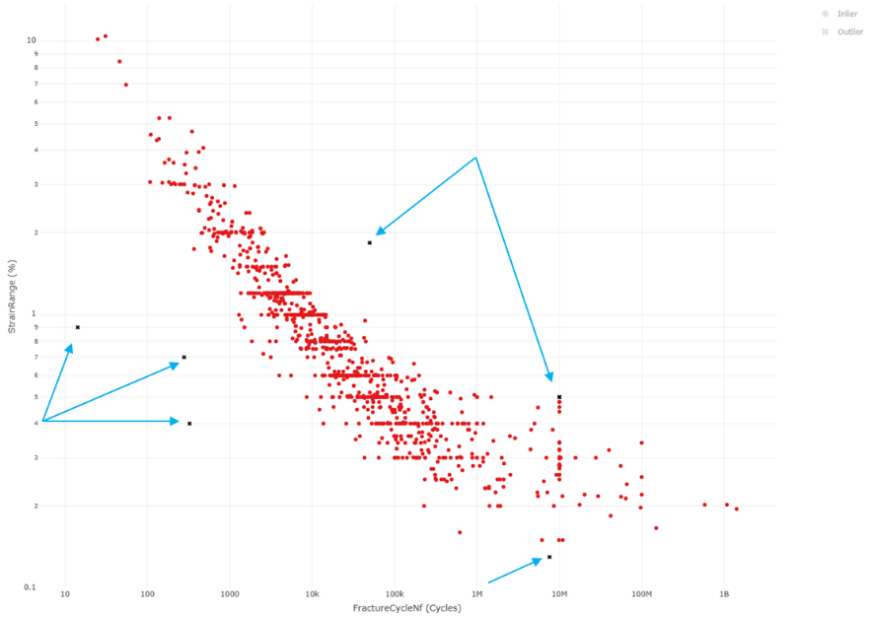

Figure 6.3. Outlier Detection: potential outliers highlighted in blue.

- Graphical Visualization of the Dataset: The tool plots the data and applies color-coding based on user-selected parameters, such as material class, environment, or temperature. Standard reference curves (ASME, NUREG/CR-6909, Rev.1, and RCC-M) can be overlaid to provide a direct visual comparison (Figure 6.4). The interface features interactive tooltips that display the fracture cycle and strain range by default; however, users have the flexibility to customize these settings to visualize any of the defined variables associated with a data point simply by positioning the cursor over it (Figure 6.4).

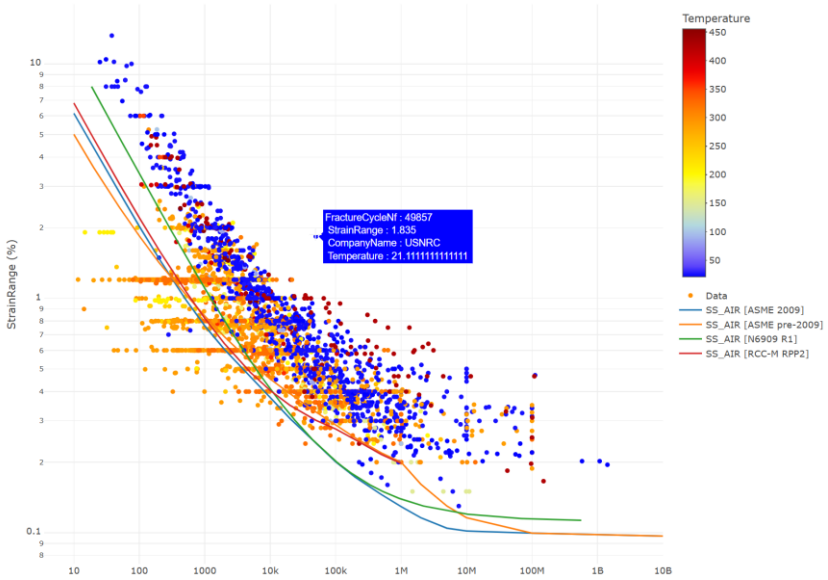

Figure 6.4. Graphical visualization of the dataset.

- Plot Matrix: The application provides a high-level overview of the experimental space, enabling analysts to rapidly identify existing data gaps between chosen variables. By visualizing these voids, the matrix serves as a strategic guide for prioritizing future test campaigns, ensuring that new experimental efforts are targeted toward areas where data is deemed necessary to eliminate critical knowledge gaps (Figure 6.5).

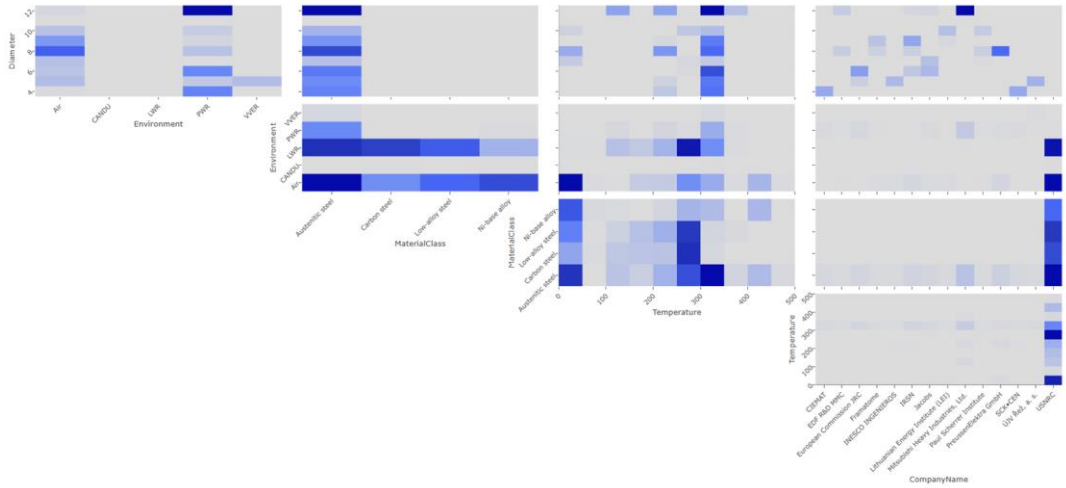

Figure 6.5. Plot matrix.

- Model Summary: Provides a systematic workflow for generating customized fatigue life models. The user first selects the specific environment for data analysis (AIR, PWR, or BWR) to ensure the model's relevance to operational conditions. Subsequently, the analyst defines the explanatory variables, where the strain range is automatically retained as a mandatory default predictor due to its primary influence on fatigue life. Based on these selections, the application calculates a mathematical expression using a linear regression model to predict the number of cycles to failure. To evaluate performance, the fitted model and its predicted points are visualized against the experimental data cloud, allowing for a clear assessment of the model's fit and statistical accuracy (Figure 6.6).
- Graphical Visualization of the Model: Utilizing the specific predictive equations derived from the developed model, this tool generates a visual representation of predicted fatigue life values across the experimental strain range. It allows for a direct benchmark comparison between the model's predictions and established international fatigue design curves, such as ASME, NUREG/CR-6909, Rev.1, and RCC-M (Figure 6.7). By overlaying these predefined standards, the analyst can visually quantify the degree of conservatism in existing regulations and evaluate the predictive accuracy of the project-derived models compared to current industry benchmarks.

$$\ln(N_f) = B_0 + B_1 \cdot \ln(StrainRange) + B_2 \cdot Temperature$$

Coefficient	Value
B0	9.368
B1	-3.439
B2	-0.001739

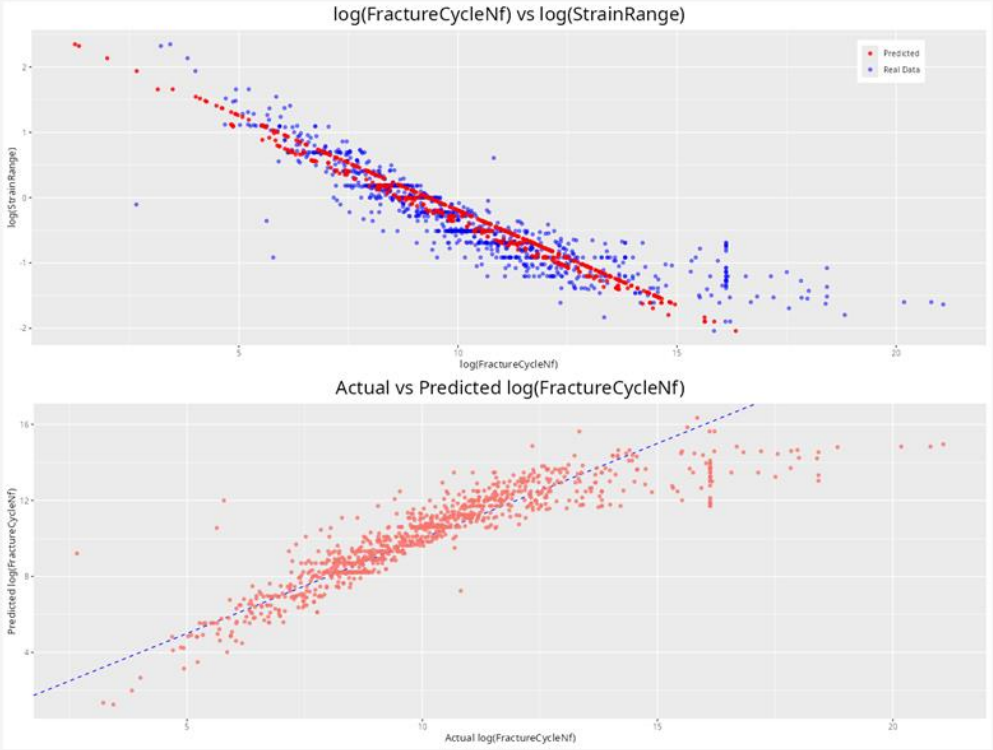

Figure 6.6. Model summary.

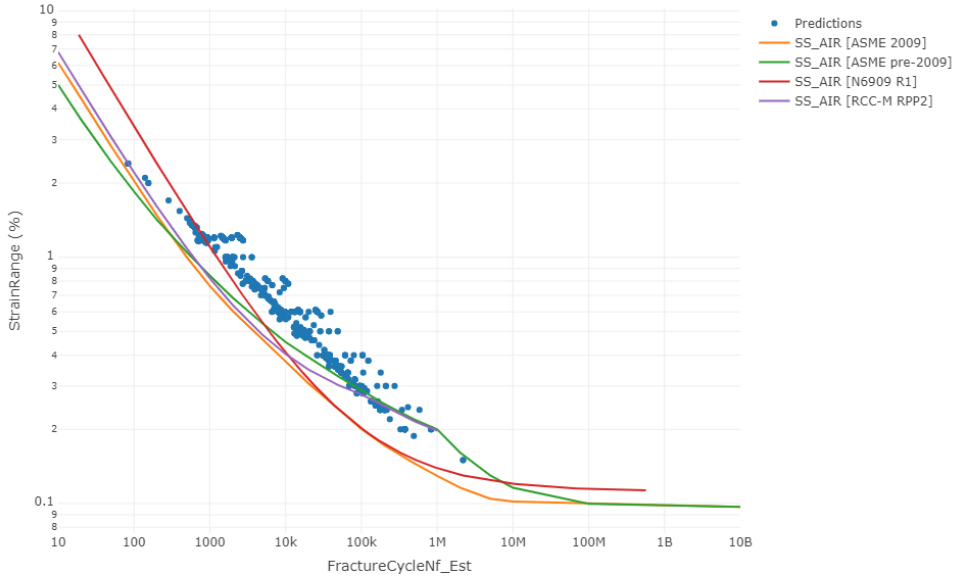

Figure 6.7. Model graphical visualization.

- Hysteresis Data Visualization: Provides a direct visualization of the stress-strain mechanical response recorded during experimental testing. For test IDs where data points were registered at specific intervals, the application displays hysteresis loops corresponding to different cycle numbers throughout the fatigue life (Figure 6.8). This functionality allows for the identification of cyclic material behavior, such as hardening or softening, which is essential for the development and parameterization of the material laws utilized in subsequent fatigue calculations.

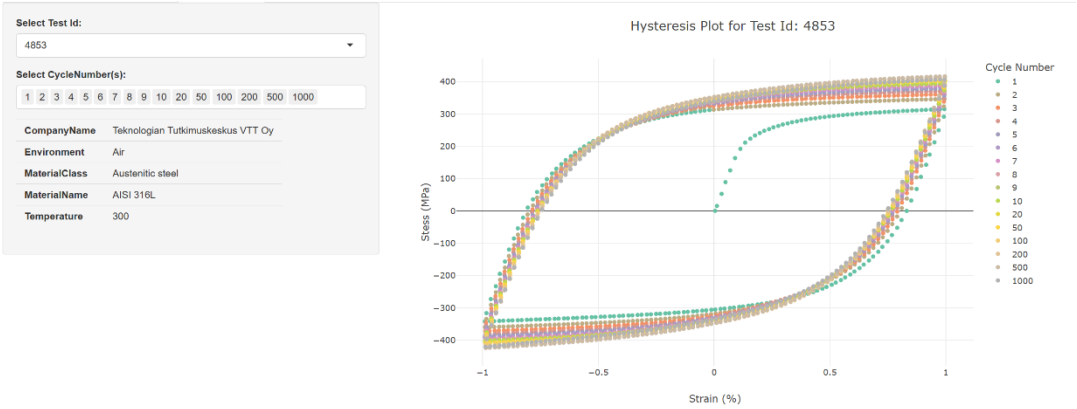

Figure 6.8. Hysteresis data visualization.

- Cyclic Data Visualization: Displays the evolution of stress levels (specifically maximum, minimum, and mean values) against the number of cycles for a given test. By focusing on stress response rather than strain, this functionality allows for a clearer identification of cyclic phenomena, such as material hardening or softening, over the entire duration of the fatigue life (Figure 6.9).

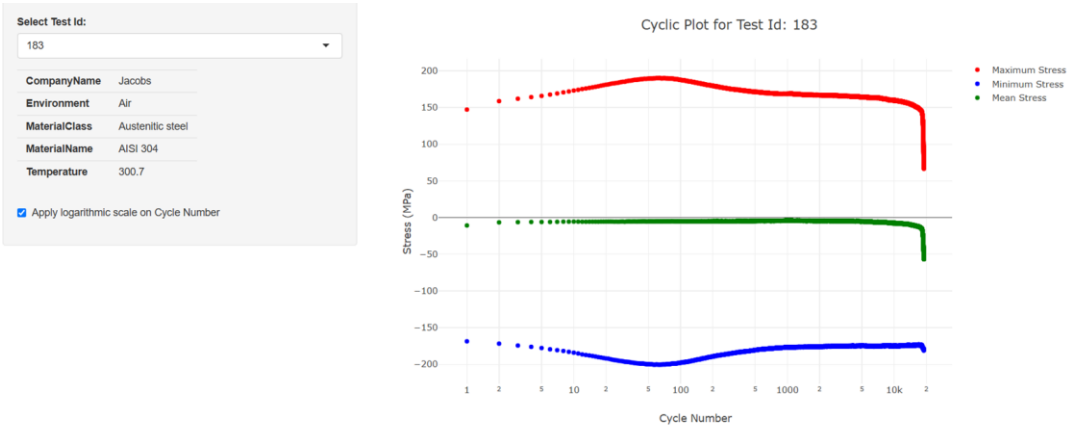

Figure 6.9. Cyclic data visualization.

6.2.3 DATA ANALYSIS

Utilizing the data compiled through the INCEFA-SCALE and INCEFA-PLUS projects—including internal experimental results and external third-party contributions—a series of predictive linear regression models has been developed by leveraging the analytical tools integrated within the project's dedicated web application. This analysis utilized datasets of increasing size and complexity to ensure predictive robustness. The initial dataset centred on the high-quality results from the INCEFA-PLUS and INCEFA-SCALE experimental campaigns. The second dataset

was expanded to incorporate additional data from various international third-party sources. Finally, the most comprehensive dataset integrated all INCEFA data with third-party results and the NUREG/CR-6909, Rev.1 [6.1] database, forming the current IFD. This stepwise methodology was adopted to facilitate a systematic evaluation of model performance as the data pool grew in both size and diversity.

The distribution and cumulative evolution of the datasets utilized in this analysis are visualized as follows:

- Figure 6.10 presents the initial dataset, which consists of the combined INCEFA-PLUS and INCEFA-SCALE results. It differentiates between tests conducted in air and those in light water reactor environments (including PWR and VVER), and is predominantly composed of tests at two targeted strain ranges: 0.3% and 0.6%.
- Figure 6.11 illustrates the second dataset, which expands upon the previous internal data by incorporating international third-party sources. These additions feature a higher density of data points for air environments, while the PWR data in this expanded set remain largely concentrated in low strain ranges.
- Figure 6.12 compiles the most comprehensive dataset by integrating all previous project and third-party data with the NUREG/CR-6909, Rev.1 database. This final assembly, representing the current IFD, demonstrates a significantly broader range of strain values.

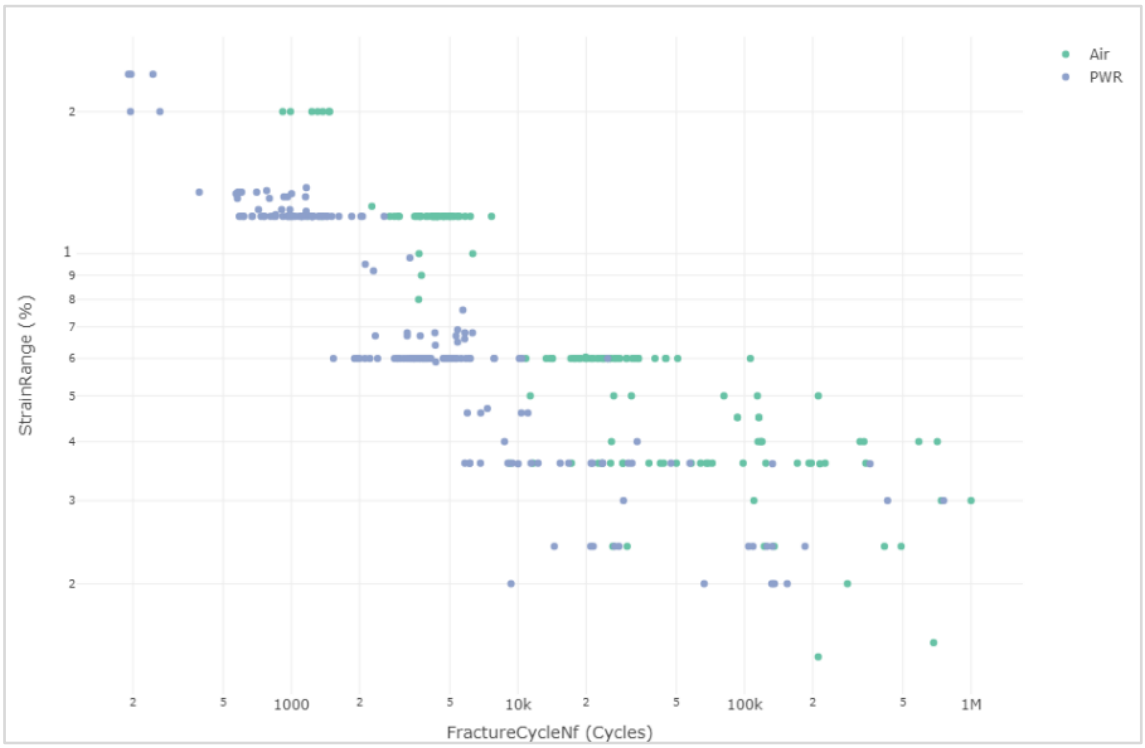

Figure 6.10. Data from INCEFA-PLUS and INCEFA-SCALE projects.

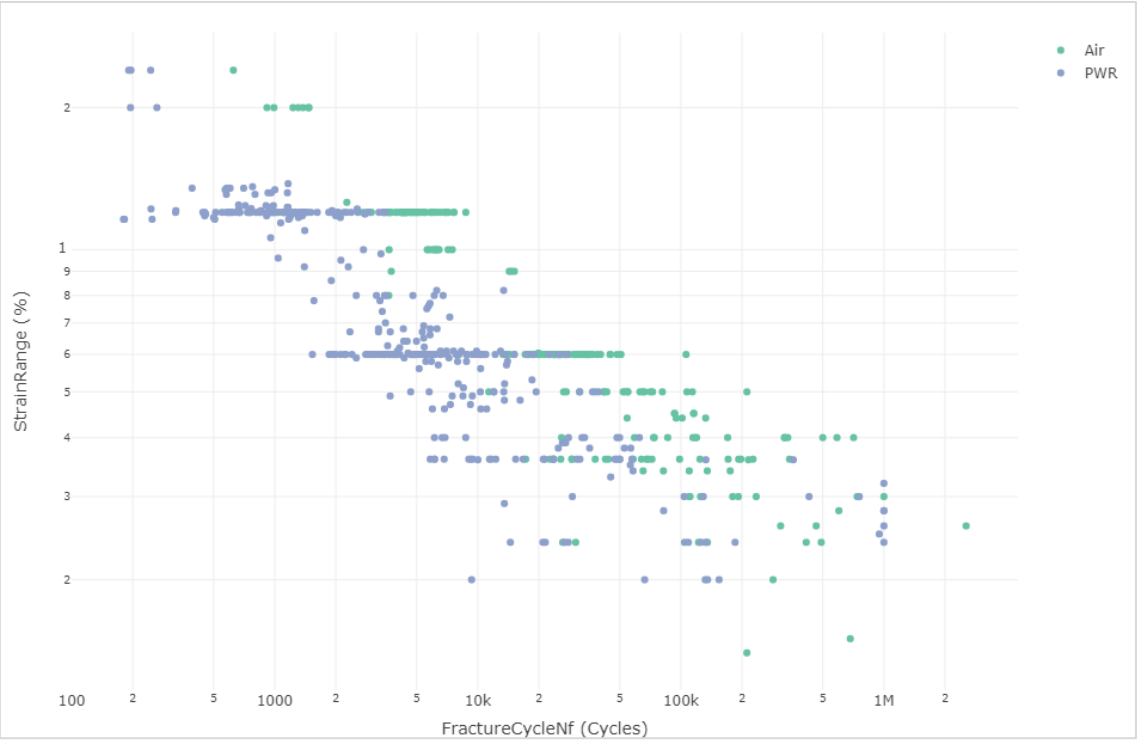

Figure 6.11. Data from INCEFA-PLUS and INCEFA-SCALE projects plus third-party sources.

Figure 6.12. Data from INCEFA-PLUS and INCEFA-SCALE projects, third-parties, and NUREG/CR-6909, Rev.1 (IFD).

6.2.3.1 MODEL FOR CONDITIONS IN AIR

The statistical evaluation of austenitic stainless steels begins with an exclusive focus on fatigue behavior under air conditions. The analysis follows a cumulative sequence, starting with the high-quality experimental data generated within the INCEFA-PLUS and INCEFA-SCALE projects before expanding to broader international datasets.

INCEFA-PLUS and INCEFA-SCALE Data Analysis: Figure 6.13 displays the fatigue curve data in air derived solely from the INCEFA-PLUS and INCEFA-SCALE campaigns, categorized by temperature. This dataset consists of 160 data points, with the number of cycles ranging from 900 to 1000000. To ensure a consistent and robust evaluation across all predictive models, this specific cycle range is maintained throughout the subsequent comparative analyses.

The methodology for model generation involved an iterative evaluation of potential explanatory variables. The selection process was guided by identifying which variables effectively minimized the MAE and maximized the R^2. Throughout this process, the statistical significance of each variable was verified using p-values. Predictors with high p-values were excluded from the final expressions, as they indicated a negligible influence on the model's accuracy. Conversely, a low p-value confirmed that a variable exerted a statistically significant effect on fatigue endurance.

Table 6.4 presents the two primary models derived from internal data. The results indicate that temperature is the only explanatory variable whose inclusion significantly enhances predictive accuracy alongside the mandatory strain range parameter.

Cumulative Dataset Expansion: Following the initial internal analysis, the study incorporated broader datasets to assess model performance at a global scale.

- Table 6.5 and Figure 6.14 present models expanded to include third-party data, totaling 244 data points.
- Table 6.6 and Figure 6.15 represent the most comprehensive analysis, integrating the previous sources with the NUREG/CR-6909, Rev.1 database to reach 906 data points.

In both expanded cases, temperature remains the sole significant predictive variable beyond the strain range.

Interpretation of Model Performance: A comparison of these models reveals that incorporating the vast amount of fatigue data from NUREG/CR-6909, Rev.1 (e.g., comparing Model 6 with Model 2 or 4) does not necessarily result in a reduction of the MAE. While an initial observation might suggest that the model with more data is less precise due to a slightly higher error, this is a natural consequence of the increased variability inherent in a large-scale, heterogeneous international database.

Crucially, the inclusion of a significantly larger number of data points increases the robustness of the predictive coefficients within the model's equation. By training the models on the full International Fatigue Database, the resulting expressions provide a more reliable foundation for general applications, even if the absolute error is higher compared to models trained on smaller, more homogeneous experimental datasets.

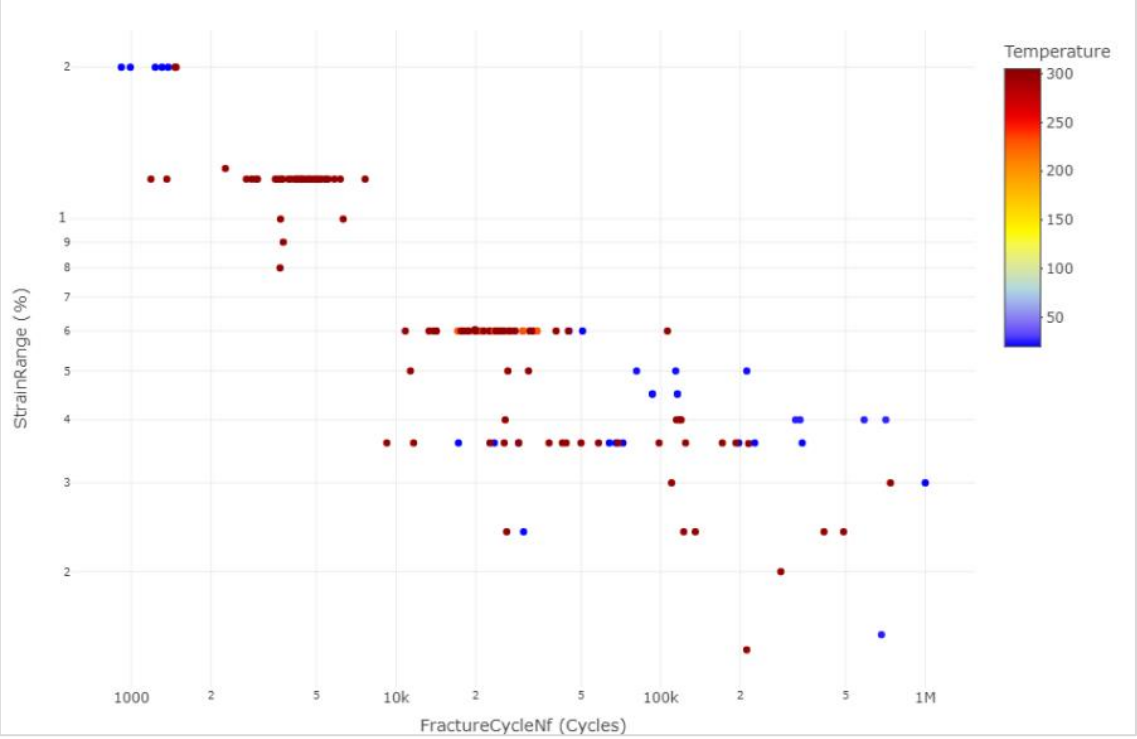

Figure 6.13. Data points in air from INCEFA-PLUS and INCEFA-SCALE data (Strain Range (%) – N (Cycles)).

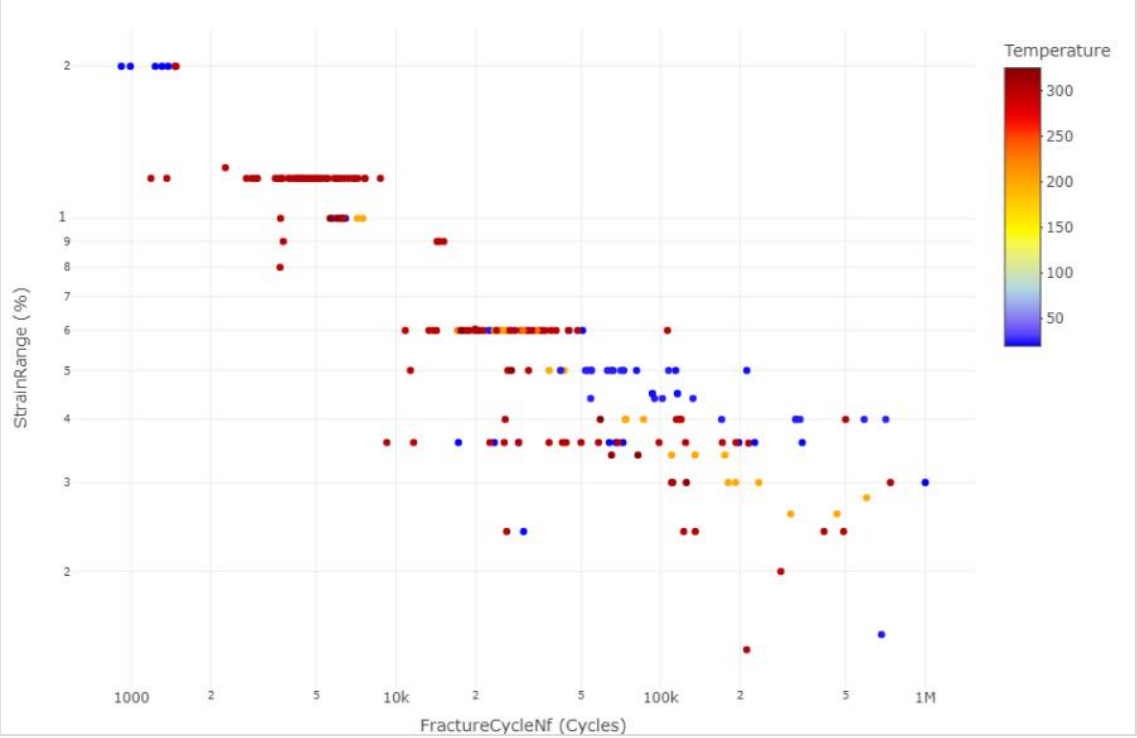

Figure 6.14. Data points in air from INCEFA-PLUS, INCEFA-SCALE and third-party data (Strain Range (%) – N (Cycles)).

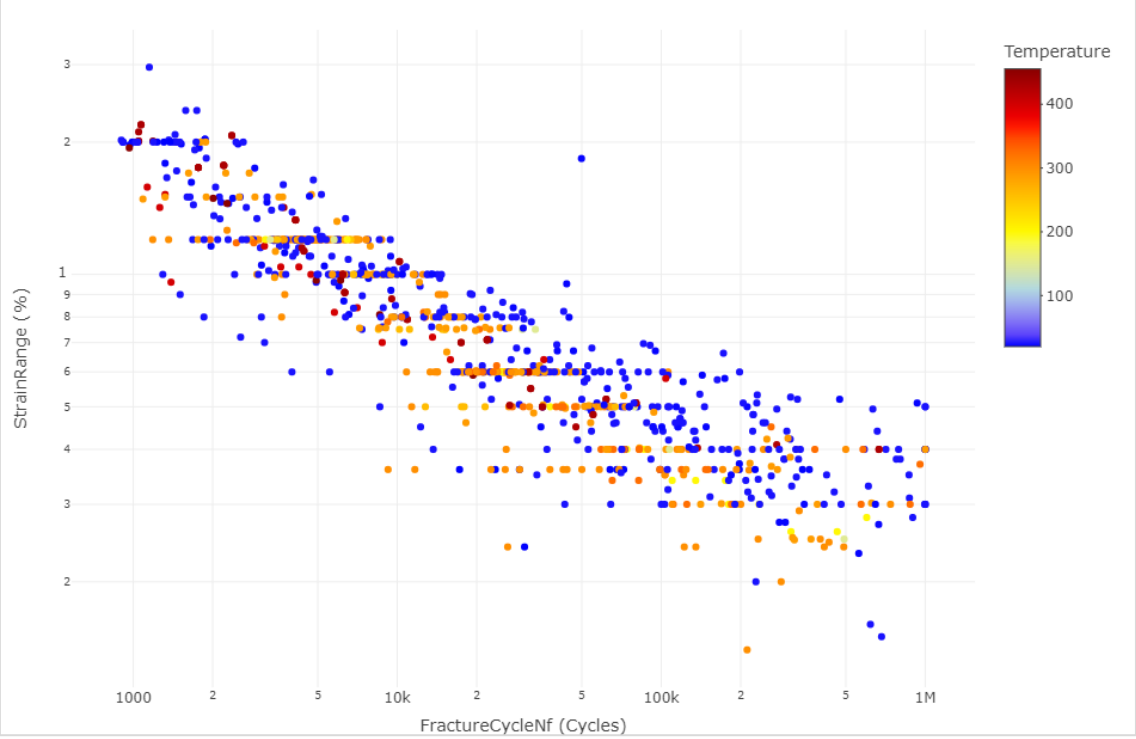

Figure 6.15. Data points in air in the IFD (Strain Range (%) – N (Cycles)).

Model #1 – Standard Linear Regression Model	
Predictor	Strain Range
Equation	$\ln(N) = 8.816 - 2.449 \cdot \ln(\varepsilon)$
MAE	0.495
Model #1 – NUREG/CR-6909, Rev.1 Expression	
Predictor	Strain Range
Equation	$\ln(N) = 8.816 - 2.449 \cdot \ln(\varepsilon)$
MAE	0.495
Model #2 – Standard Linear Regression Model	
Predictor	Strain range, Temperature
Equation	$\ln(N) = 9.383 - 2.362 \cdot \ln(\varepsilon) - 0.002 \cdot T$
MAE	0.483
Model #2 – NUREG/CR-6909, Rev.1 Expression	
Predictor	Strain range, Temperature
Equation	$\ln(N) = 9.383 - 2.362 \cdot \ln(\varepsilon) - 0.002 \cdot T$
MAE	0.483

Table 6.4. Models for INCEFA-PLUS and INCEFA-SCALE data in air.

Model #3 – Standard Linear Regression Model	
Predictor	Strain Range
Equation	$\ln(N) = 8.891 - 2.554 \cdot \ln(\varepsilon)$
MAE	0.458
Model #3 – NUREG/CR-6909, Rev.1 Expression	
Predictor	Strain Range
Equation	$\ln(N) = 8.891 - 2.554 \cdot \ln(\varepsilon)$
MAE	0.458

Model #4 – Standard Linear Regression Model	
Predictor	Strain range, Temperature
Equation	$\ln(N) = 9.331 - 2.471 \cdot \ln(\varepsilon) - 0.002 \cdot T$
MAE	0.438
Model #4 – NUREG/CR-6909, Rev.1 Expression	
Predictor	Strain range, Temperature
Equation	$\ln(N) = 9.331 - 2.471 \cdot \ln(\varepsilon) - 0.002 \cdot T$
MAE	0.438

Table 6.5. Models for INCEFA-PLUS, INCEFA-SCALE, and third-party data in air.

Model #5 – Standard Linear Regression Model	
Predictor	Strain Range
Equation	$\ln(N) = 9.067 - 3.343 \cdot \ln(\varepsilon)$
MAE	0.774
Model #5 – NUREG/CR-6909, Rev.1 Expression	
Predictor	Strain Range
Equation	$\ln(N) = 8.701 - 2.828 \cdot \ln(\varepsilon + 0.095)$
MAE	0.738
Model #6 – Standard Linear Regression Model	
Predictor	Strain range, Temperature
Equation	$\ln(N) = 9.361 - 3.333 \cdot \ln(\varepsilon) - 0.002 \cdot T$
MAE	0.751
Model #6 – NUREG/CR-6909, Rev.1 Expression	
Predictor	Strain range, Temperature
Equation	$\ln(N) = 8.985 - 2.836 \cdot \ln(\varepsilon + 0.093) - 0.002 \cdot T$
MAE	0.722

Table 6.6. Models for IFD data in air.

It should be noted that the statistical analyses performed throughout the project indicated no significant influence of specific stainless-steel grades and surface roughness on fatigue performance under air conditions.

To complement the analyses, Figure 6.16 and Figure 6.17 present a graphical comparison between the fatigue life values predicted by Model 6 (using the standard and NUREG/CR-6909, Rev. 1 expressions, respectively) and several established stainless steel design fatigue curves in air, specifically ASME (pre-2009 and 2009), RCC-M RPP2, NUREG/CR-6909, Rev.1, and the Asada design curve.

In this specific evaluation, Model 6 serves as a predictive tool that explicitly has temperature and strain range as explanatory variables. No temperature dependence for the mean curve was identified in NUREG/CR-6909, Rev.1, which relies solely on the strain range. However, subsequent analysis from several sources has identified temperature as a factor controlling the shape of the curve and the fatigue limit [6.8]. The mean curve models presented by Asada et al. [6.8] and Currie et al. [6.7] use the materials ultimate tensile strength to define the mean curve parameters and influences the shape and fatigue limit of the curve. The use of ultimate tensile strength enables these curves to account for the effect of temperature on the shape of the curve. The analysis of the datasets presented here supports the use of temperature dependent mean curves.

The resulting visualization of Model 6 demonstrates that the design curves have adequate margin over the range that the model is valid for ($\varepsilon_r > 0.4\%$).

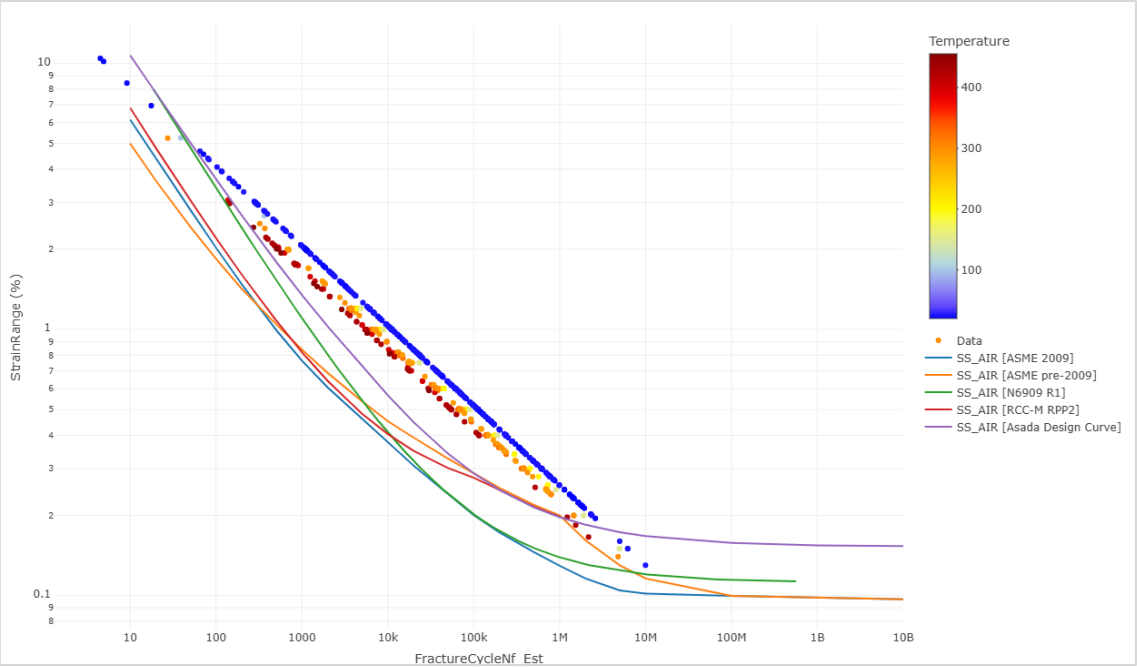

Figure 6.16. Predicted data points from Model 6 – Standard Expression compared to standard reference SS air S-N curves (Strain Range (%) – N (Cycles)).

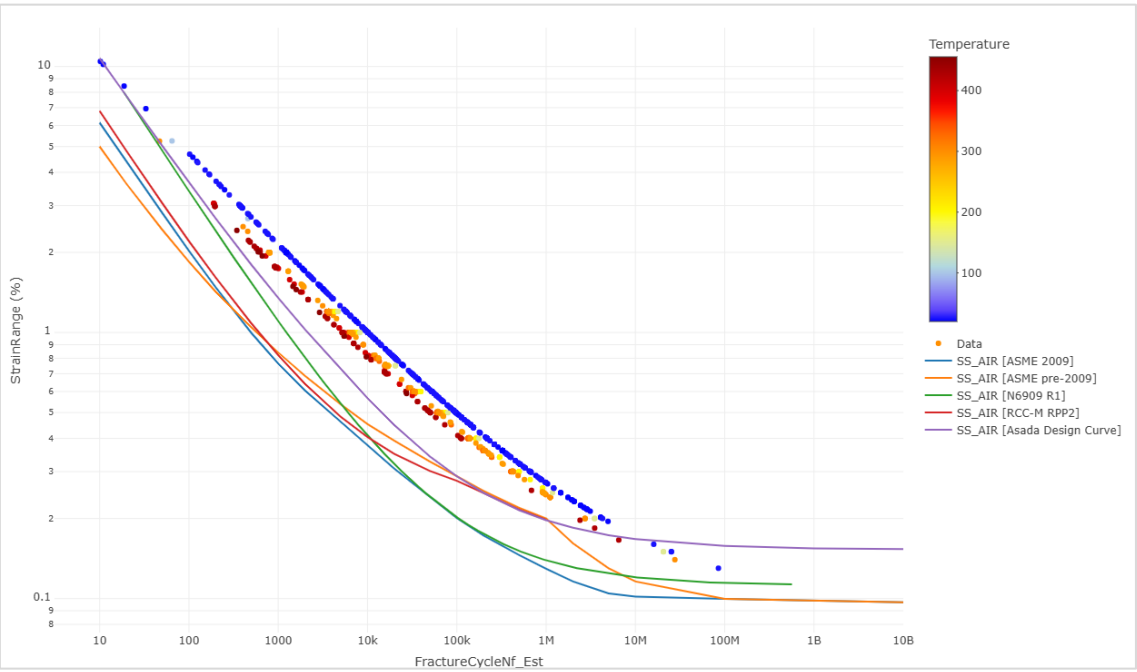

Figure 6.17. Predicted data points from Model 6 – NUREG/CR-6909, Rev.1 Expression compared to standard reference SS air S-N curves (Strain Range (%) – N (Cycles)).

6.2.3.2 MODEL FOR CONDITIONS IN PWR

Following the same methodology applied to air conditions, the statistical evaluation was extended to fatigue behavior within the Pressurized Water Reactor (PWR) environment. The analysis followed a cumulative sequence, beginning with high-quality internal project results before integrating broader international data to evaluate model stability and accuracy.

INCEFA-PLUS and INCEFA-SCALE Data Analysis: The initial phase focused exclusively on the data generated during the INCEFA-PLUS and INCEFA-SCALE experimental campaigns. Figure 6.18 presents this internal dataset, which consists of 183 data points with cycles to failure ranging from 100 to 775000. This specific cycle range was maintained throughout all subsequent analyses to ensure consistent benchmarking when incorporating external data.

As explained above, the iterative model selection process aimed to minimize the MAE and maximize the R^2. During this development, the statistical significance of each predictor was verified using p-values. Table 6.7 presents five predictive models derived from these internal data, showing the impact of progressively adding explanatory variables.

Cumulative Dataset Expansion: To enhance the robustness of the findings, the study incorporated increasingly larger datasets:

- Table 6.8 and Figure 6.19 present models expanded to include third-party data (integrating internal and external project results), reaching a total of 363 data points.
- Table 6.9 and Figure 6.20 represent the most exhaustive analysis, incorporating the NUREG/CR-6909, Rev.1 database to reach a final set of 942 data points.

Interpretation of Model Performance: Consistent with the observations in air, incorporating the full scale of the International Fatigue Database did not lead to a lower MAE compared to models trained on smaller, more homogeneous datasets. However, the use of a larger dataset significantly enhanced the robustness of the predictive coefficients.

A major technical finding of this analysis is the significance of the strain waveform. In Model 15, which utilizes the complete IFD dataset, the inclusion of the waveform variable resulted in a marked reduction of the MAE to 0.540 in the standard linear regression expression and a reduction to 0.527 in the NUREG/CR-6909, Rev.1 expression. This improvement was not as pronounced in smaller internal datasets (Models 5 or 10), suggesting that the complex influence of the strain waveform is more accurately captured when analyzed across a diverse international data pool.

Additionally, the analysis indicates that a single mean curve that accounts for temperature effects can be used generally for 300 series stainless under PWR and air conditions.

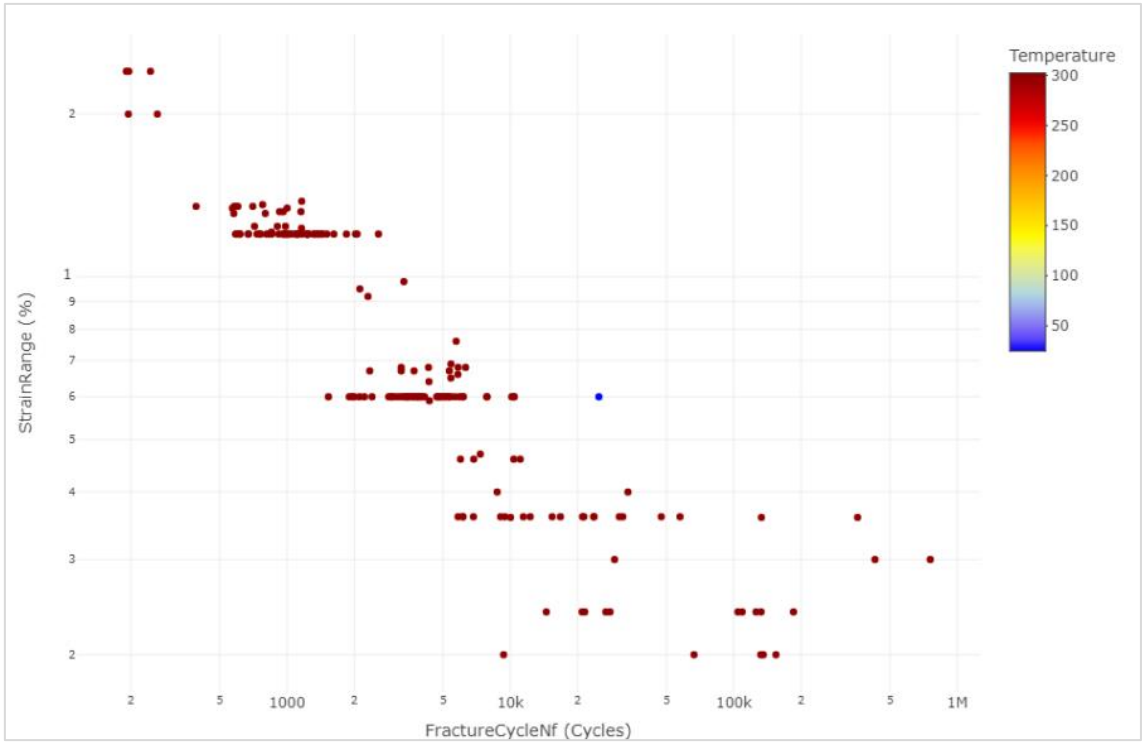

Figure 6.18. Data points in PWR environment from INCEFA-PLUS and INCEFA-SCALE data (Strain Range (%) – N (Cycles)).

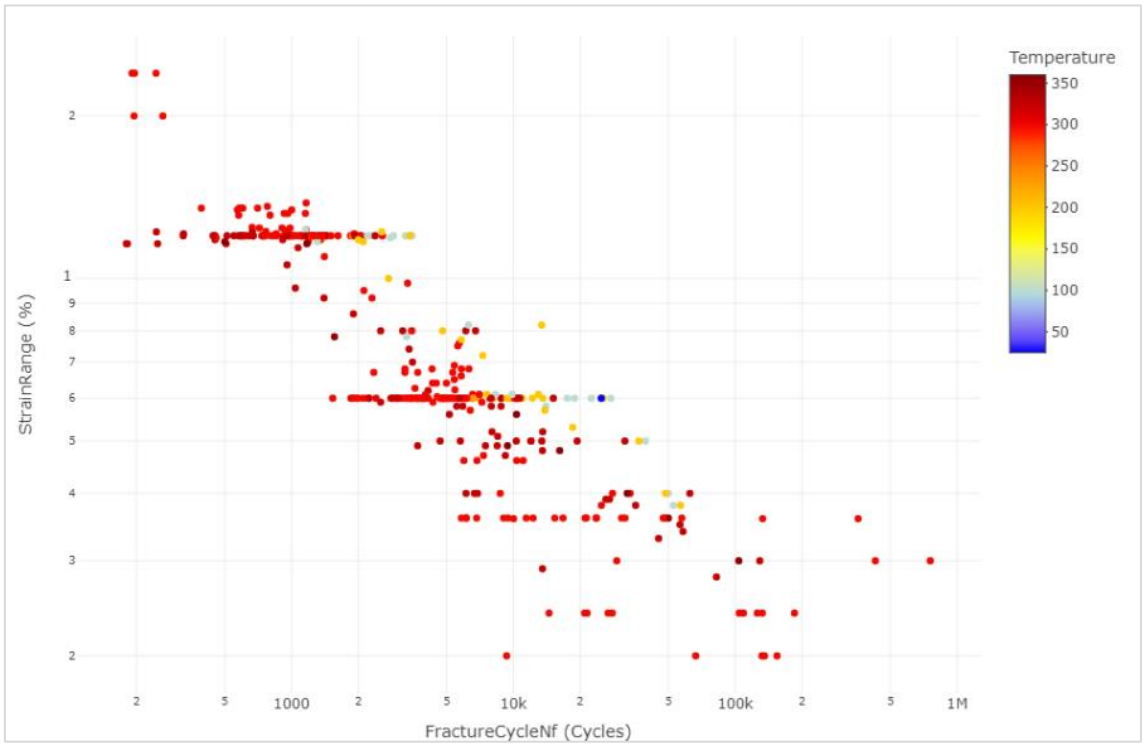

Figure 6.19. Data points in PWR environment from INCEFA-PLUS, INCEFA-SCALE, and third-party data (Strain Range (%) – N (Cycles)).

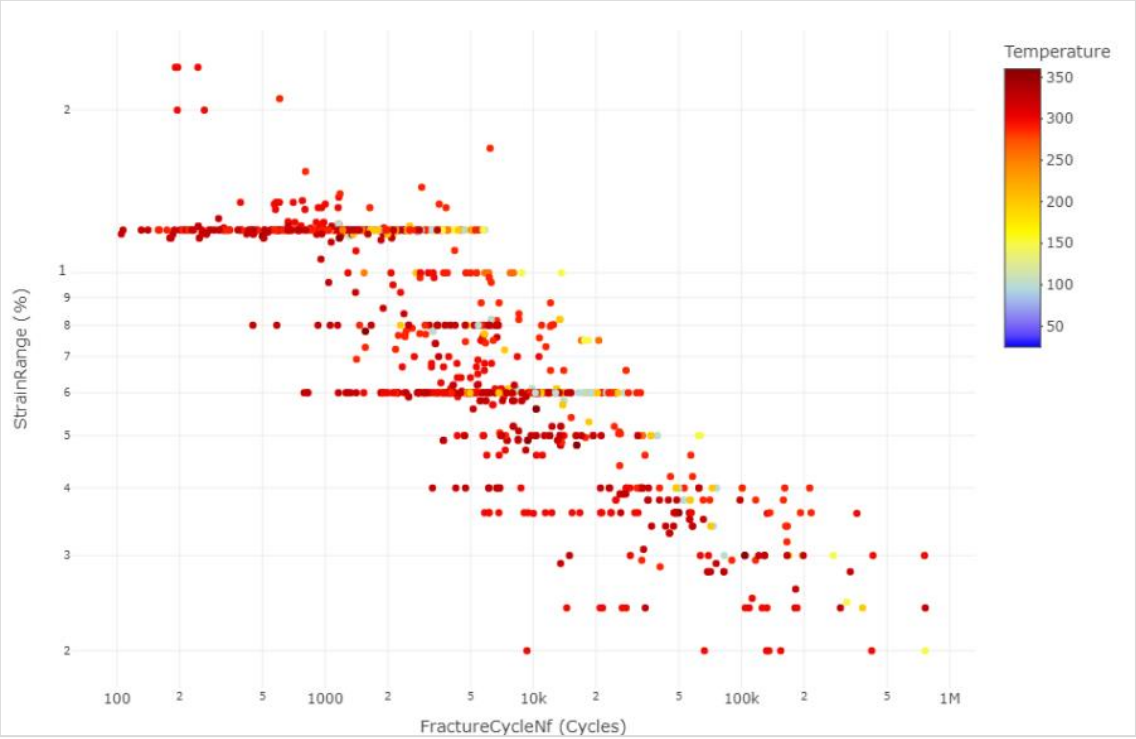

Figure 6.20. Data points in PWR environment in the IFD (Strain Range (%) – N (Cycles)).

Model #1 – Standard Linear Regression Model	
Predictor	Strain Range
Equation	$\ln(N) = 7.34 - 2.454 \cdot \ln(\varepsilon)$
MAE	0.452
Model #1 – NUREG/CR-6909, Rev.1 Expression	
Predictor	Strain Range
Equation	$\ln(N) = 7.189 - 2.174 \cdot \ln(\varepsilon + 0.063)$
MAE	0.444
Model #2 – Standard Linear Regression Model	
Predictor	Strain range, Temperature
Equation	$\ln(N) = 9.043 - 2.45 \cdot \ln(\varepsilon) - 0.006 \cdot T$
MAE	0.443
Model #2 – NUREG/CR-6909, Rev.1 Expression	
Predictor	Strain range, Temperature
Equation	$\ln(N) = 8.938 - 2.145 \cdot \ln(\varepsilon + 0.068) - 0.006 \cdot T$
MAE	0.433
Model #3 – Standard Linear Regression Model	
Predictor	Strain range, Temperature, Strain rate
Equation	$\ln(N) = 8.981 - 2.465 \cdot \ln(\varepsilon) - 0.006 \cdot T + 689.523 \cdot \varepsilon'$
MAE	0.424
Model #3 – NUREG/CR-6909, Rev.1 Expression	
Predictor	Strain range, Temperature, Strain rate
Equation	$\ln(N) = 8.864 - 2.045 \cdot \ln(\varepsilon + 0.092) - 0.007 \cdot T + 726.181 \cdot \varepsilon'$
MAE	0.410

Model #4 – Standard Linear Regression Model	
Predictor	Strain range, Temperature, Strain rate, Surface finish
Equation	$\ln(N) = 8.712 - 2.404 \cdot \ln(\varepsilon) - 0.006 \cdot T + 677.827 \cdot \varepsilon' + 0.043 \cdot SFground + 0.093 \cdot SFhoned + 0.297 \cdot SFpolished$
MAE	0.399
Model #4 – NUREG/CR-6909, Rev.1 Expression	
Predictor	Strain range, Temperature, Strain rate, Surface finish
Equation	$\ln(N) = 8.809 - 2.050 \cdot \ln(\varepsilon + 0.081) - 0.006 \cdot T + 710.018 \cdot \varepsilon' + 0.070 \cdot SFground + 0.126 \cdot SFhoned + 0.288 \cdot SFpolished$
MAE	0.392
Model #5 – Standard Linear Regression Model	
Predictor	Strain range, Temperature, Strain rate, Surface finish, Waveform
Equation	$\ln(N) = 8.639 - 2.382 \cdot \ln(\varepsilon) - 0.006 \cdot T + 652.374 \cdot \varepsilon' - 0.013 \cdot SFground + 0.047 \cdot SFhoned + 0.252 \cdot SFpolished + 0.069 \cdot Sawtooth(holdtimes) + 0.134 \cdot Triangular + 0.208 \cdot Triangular(holdtimes)$
MAE	0.401
Model #5 – NUREG/CR-6909, Rev.1 Expression	
Predictor	Strain range, Temperature, Strain rate, Surface finish, Waveform
Equation	$\ln(N) = 8.560 - 2.051 \cdot \ln(\varepsilon + 0.078) - 0.006 \cdot T + 697.639 \cdot \varepsilon' + 0.010 \cdot SFground + 0.078 \cdot SFhoned + 0.244 \cdot SFpolished + 0.080 \cdot Sawtooth(holdtimes) + 0.105 \cdot Triangular + 0.211 \cdot Triangular(holdtimes)$
MAE	0.395

Table 6.7. Models for INCEFA-PLUS and INCEFA-SCALE data in PWR environment.

Model #6 – Standard Linear Regression Model	
Predictor	Strain Range
Equation	$\ln(N) = 7.393 - 2.781 \cdot \ln(\varepsilon)$
MAE	0.562
Model #6 – NUREG/CR-6909, Rev.1 Expression	
Predictor	Strain Range
Equation	$\ln(N) = 7.240 - 2.450 \cdot \ln(\varepsilon + 0.058)$
MAE	0.558
Model #7 – Standard Linear Regression Model	
Predictor	Strain range, Temperature
Equation	$\ln(N) = 8.635 - 2.818 \cdot \ln(\varepsilon) - 0.004 \cdot T$
MAE	0.508
Model #7 – NUREG/CR-6909, Rev.1 Expression	
Predictor	Strain range, Temperature
Equation	$\ln(N) = 8.478 - 2.445 \cdot \ln(\varepsilon + 0.075) - 0.005 \cdot T$
MAE	0.500
Model #8 – Standard Linear Regression Model	
Predictor	Strain range, Temperature, Strain rate
Equation	$\ln(N) = 8.084 - 2.690 \cdot \ln(\varepsilon) - 0.003 \cdot T + 228.182 \cdot \varepsilon'$
MAE	0.45
Model #8 – NUREG/CR-6909, Rev.1 Expression	
Predictor	Strain range, Temperature, Strain rate
Equation	$\ln(N) = 7.903 - 2.250 \cdot \ln(\varepsilon + 0.091) - 0.003 \cdot T + 231.538 \cdot \varepsilon'$
MAE	0.439

Model #9 – Standard Linear Regression Model	
Predictor	Strain range, Temperature, Strain rate, Surface finish
Equation	$\ln(N) = 7.993 - 2.684 \cdot \ln(\varepsilon) - 0.003 \cdot T + 221.528 \cdot \varepsilon' + 0.044 \cdot SFground + 0.002 \cdot SFhoned + 0.112 \cdot SFpolished$
MAE	0.445
Model #9 – NUREG/CR-6909, Rev.1 Expression	
Predictor	Strain range, Temperature, Strain rate, Surface finish
Equation	$\ln(N) = 7.784 - 2.253 \cdot \ln(\varepsilon + 0.090) - 0.003 \cdot T + 226.401 \cdot \varepsilon' + 0.089 \cdot SFground + 0.044 \cdot SFhoned + 0.137 \cdot SFpolished$
MAE	0.435
Model #10 – Standard Linear Regression Model	
Predictor	Strain range, Temperature, Strain rate, Surface finish, Waveform
Equation	$\ln(N) = 7.976 - 2.647 \cdot \ln(\varepsilon) - 0.003 \cdot T + 244.730 \cdot \varepsilon' - 0.065 \cdot SFground - 0.093 \cdot SFhoned + 0.043 \cdot SFpolished + 0.135 \cdot Sawtooth + 0.228 \cdot Sawtooth(holdtimes) + 0.180 \cdot Triangular$
MAE	0.441
Model #10 – NUREG/CR-6909, Rev.1 Expression	
Predictor	Strain range, Temperature, Strain rate, Surface finish, Waveform
Equation	$\ln(N) = 7.777 - 2.237 \cdot \ln(\varepsilon + 0.087) - 0.003 \cdot T + 248.106 \cdot \varepsilon' - 0.020 \cdot SFground - 0.048 \cdot SFhoned + 0.070 \cdot SFpolished + 0.127 \cdot Sawtooth + 0.214 \cdot Sawtooth(holdtimes) + 0.200 \cdot Triangular$
MAE	0.432

Table 6.8. Models for INCEFA-PLUS, INCEFA-SCALE, and third-party data in PWR environment.

Model #11 – Standard Linear Regression Model	
Predictor	Strain Range
Equation	$\ln(N) = 7.501 - 3.337 \cdot \ln(\varepsilon)$
MAE	0.809
Model #11 – NUREG/CR-6909, Rev.1 Expression	
Predictor	Strain Range
Equation	$\ln(N) = 7.165 - 2.546 \cdot \ln(\varepsilon + 0.124)$
MAE	0.783
Model #12 – Standard Linear Regression Model	
Predictor	Strain range, Temperature
Equation	$\ln(N) = 8.979 - 3.384 \cdot \ln(\varepsilon) - 0.005 \cdot T$
MAE	0.747
Model #12 – NUREG/CR-6909, Rev.1 Expression	
Predictor	Strain range, Temperature
Equation	$\ln(N) = 8.609 - 2.620 \cdot \ln(\varepsilon + 0.118) - 0.005 \cdot T$
MAE	0.722
Model #13 – Standard Linear Regression Model	
Predictor	Strain range, Temperature, Strain rate
Equation	$\ln(N) = 8.951 - 3.332 \cdot \ln(\varepsilon) - 0.005 \cdot T + 8.440 \cdot \varepsilon'$
MAE	0.722
Model #13 – NUREG/CR-6909, Rev.1 Expression	
Predictor	Strain range, Temperature, Strain rate
Equation	$\ln(N) = 8.588 - 2.582 \cdot \ln(\varepsilon + 0.118) - 0.005 \cdot T + 8.273 \cdot \varepsilon'$
MAE	0.697

Model #14 – Standard Linear Regression Model	
Predictor	Strain range, Temperature, Strain rate, Surface finish
Equation	$\ln(N) = 9.029 - 3.337 \cdot \ln(\varepsilon) - 0.005 \cdot T + 7.906 \cdot \varepsilon' - 0.428 \cdot SFground - 0.664 \cdot SFhoned - 0.333 \cdot SFpolished$
MAE	0.707
Model #14 – NUREG/CR-6909, Rev.1 Expression	
Predictor	Strain range, Temperature, Strain rate, Surface finish
Equation	$\ln(N) = 8.668 - 2.597 \cdot \ln(\varepsilon + 0.116) - 0.005 \cdot T + 7.765 \cdot \varepsilon' - 0.406 \cdot SFground - 0.634 \cdot SFhoned - 0.320 \cdot SFpolished$
MAE	0.685
Model #15 – Standard Linear Regression Model	
Predictor	Strain range, Temperature, Strain rate, Surface finish, Waveform
Equation	$\ln(N) = 8.341 - 2.816 \cdot \ln(\varepsilon) - 0.004 \cdot T \pm 2.080 \cdot \varepsilon' + 0.086 \cdot SFground + 0.003 \cdot SFhoned + 0.321 \cdot SFpolished - 0.091 \cdot Sawtooth(holdtimes) + 3.531 \cdot Sinusoidal \pm 0.069 \cdot Triangular \pm 0.070 \cdot Triangular(holdtimes)$
MAE	0.540
Model #15 – NUREG/CR-6909, Rev.1 Expression	
Predictor	Strain range, Temperature, Strain rate, Surface finish, Waveform
Equation	$\ln(N) = 8.096 - 2.273 \cdot \ln(\varepsilon + 0.107) - 0.004 \cdot T - 1.998 \cdot \varepsilon' + 0.155 \cdot SFground + 0.072 \cdot SFhoned + 0.367 \cdot SFpolished - 0.107 \cdot Sawtooth(holdtimes) + 3.497 \cdot Sinusoidal - 0.096 \cdot Triangular - 0.048 \cdot Triangular(holdtimes)$
MAE	0.527

Table 6.9. Models for IFD data in PWR environment.

Benchmarking: To conclude the analysis, Figure 6.21 and Figure 6.22 present a graphical comparison between the predicted fatigue life values from Model 15 (using the standard and NUREG/CR-6909, Rev.1 expressions, respectively) and several established stainless steel fatigue curves developed for air environments.

This comparison provides a useful illustration of the development of design curves and how environmental effects of water environments have been accounted for over the iterations of the methods. The design curves prior to and including ASME 2009 were generally considered to be bounding of environmental effects. However, this was challenged and Paragraph NB-3121 of ASME Section III was added from 1971 onwards stating that the design fatigue curves did not include tests in the presence of corrosive environments [6.13]. The design curves then evolved to be specifically air fatigue design curves and deliberately did not consider water environmental effects (NUREG/CR-6909, Rev.1, RCCM, and Asada). The methods for accounting for the effect of corrosive water environments was developed to be applied to those air design fatigue curves separately as part of a fatigue analysis [6.1].

The comparison shows that the early fatigue design curves, most notably ASME 2009, effectively envelop the predicted environmental data. This suggests that the design factors traditionally used to account for data scatter, specimen size, ambient conditions and surface finish in air were, in some cases, large enough to encompass environmental effects, albeit leading to excessive conservatism in high-strain regions. The design curves after this were specifically created to have a separate environmental effect applied to them and that is why the PWR data as it stands is not bounded by the design curves below.

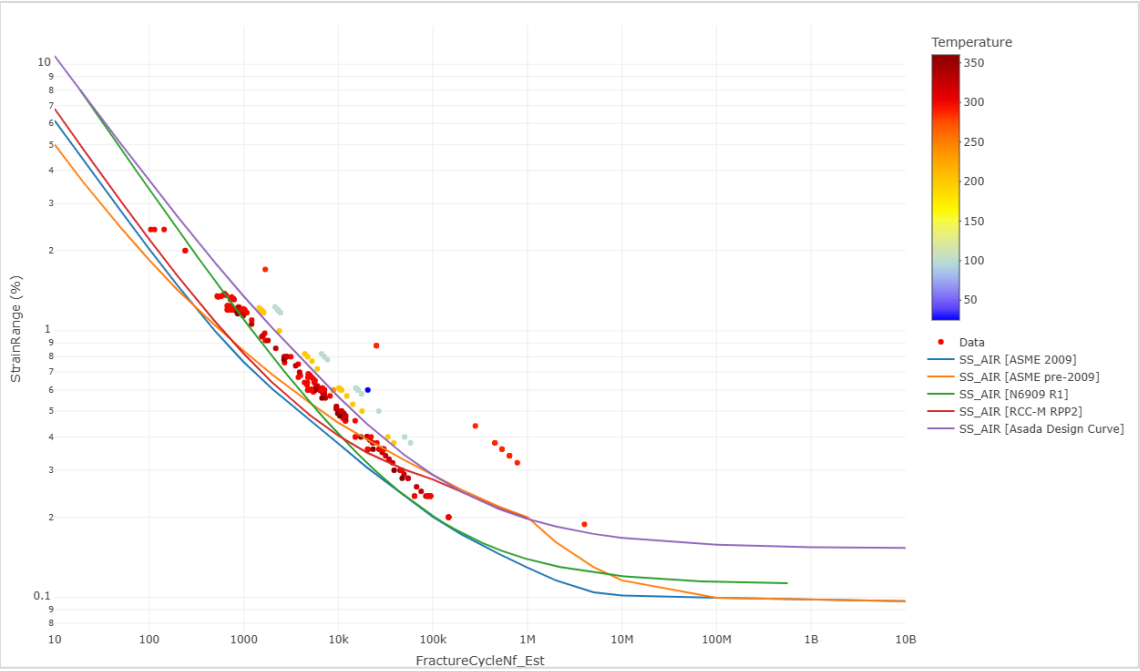

Figure 6.21. Predicted data points from Model 15 – Standard Linear Regression compared to standard reference air SS S-N curves (Strain Range (%) – N (Cycles)).

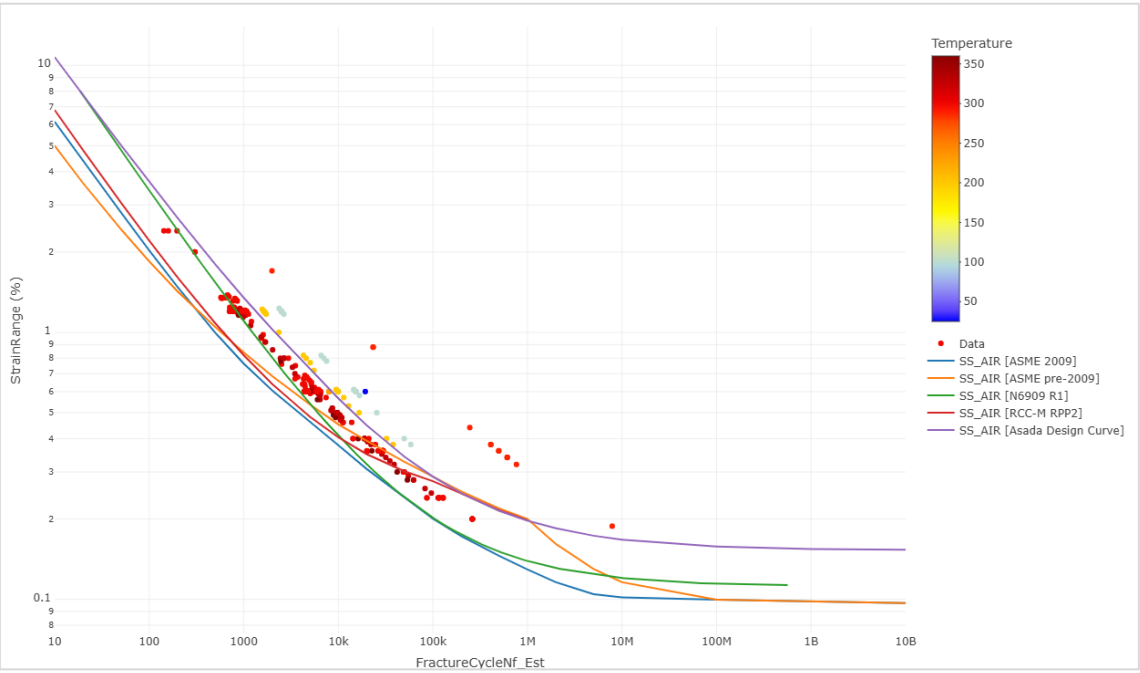

Figure 6.22. Predicted data points from Model 15 – NUREG/CR-6909, Rev.1 Expression compared to standard reference air SS S-N curves (Strain Range (%) – N (Cycles)).

6.2.3.3 DISCUSSION

The evaluation utilized progressively enriched datasets to develop robust predictive fatigue models, beginning with high-quality results from the INCEFA-PLUS and INCEFA-SCALE projects and extending to the comprehensive IFD. The results demonstrate that while incorporating additional data significantly improves the robustness of the predictive coefficients, it does not always lead to a reduction in the MAE. This is attributed to the increased variability inherent in

large-scale, heterogeneous international repositories compared to smaller, more homogeneous experimental campaigns.

In air environments, temperature consistently emerged as the sole predictive variable that significantly enhances model accuracy beyond the mandatory strain range. Statistical analyses confirmed that specific material grades and surface roughness had no measurable influence on fatigue performance under these conditions. Graphical comparison of the most refined model developed for air conditions against established stainless steel S-N curves revealed that nearly every predicted point exceeded the corresponding number of cycles indicated by the reference curves, highlighting their inherent conservatism.

For PWR environments, the inclusion of the strain waveform as a predictive variable in the most comprehensive model significantly improved predictive accuracy. This finding underscores the critical role of waveform effects in fatigue behavior, validating a primary research pillar of the INCEFA-SCALE Project. Notably, and in contrast to the results obtained in air, surface roughness emerged as a significant explanatory variable in the PWR models, indicating that surface finish plays a more substantial role in environmentally assisted fatigue. This was identified in an analysis presented in the INCEFA-PLUS reference book [6.14] that indicated there was a small effect of surface finish in air and a greater one in water. Depending on the dataset used and how the data was treated the difference in surface finish effect between the environments was not always significant. However, analysis of the targeted INCEFA-PLUS dataset did indicate that there was a general surface finish effect. Furthermore, statistical evaluations indicated that water chemistry parameters did not show a measurable influence on the resulting predictive expressions. Like the air environment findings, material grade showed no significant influence on fatigue behavior under PWR conditions.

The benchmarking of the most accurate PWR-based model against air-based design curves serves as an evaluation of how fatigue design curves have changed over the years and the definition of their use in methods better defined. The results reveal that certain air-based curves (most notably ASME 2009) effectively envelop the predicted environmental data. This indicates that the sub-factors traditionally applied during the construction of air design curves (intended to account for data scatter, specimen size, ambient conditions and surface finish) can be sufficient to encompass environmental effects. However, this often results in excessive conservatism, particularly in the high strain range. As the intent of the original adjustment factors became clear and did not include corrosive environments, modern design curves have been developed with adjustment factors that have a much clearer technical basis. These curves are intended for use with a separate environmental factor in an assessment to account for the corrosive environments in plant. This creates a fatigue assessment with substantially clearer descriptions of margin [6.7,6.8].

The integration of internal data with international contributions continues to strengthen the IFD's dual role as a data repository and a platform for advanced fatigue analysis. With its evolving functionalities, the IFD represents a critical step toward addressing gaps in understanding environmental fatigue effects on nuclear components and supporting the development of more robust predictive models

6.3 CONCLUSIONS

The purpose of this Chapter was to present the fatigue data foundations, database development efforts, and predictive modelling approaches used to evaluate the fatigue behaviour of austenitic stainless steels in air and PWR environments.

The chapter described the evolution of fatigue datasets from the NUREG/CR-6909, Rev.1 [6.1] compilation to the expanded International Fatigue Database, incorporating recent data from the INCEFA-PLUS and INCEFA-SCALE projects alongside international contributors. Through systematic data analysis and regression modelling, key variables influencing fatigue life were identified, specifically the dominant role of temperature in air and the additional significance of strain waveform and surface roughness under PWR conditions.

The results demonstrate that larger and more diverse datasets improve the statistical robustness of predictive models and can enable the improvement of design methods. Overall, this Chapter establishes a comprehensive, data-driven basis for refining fatigue design methodologies. It supports the requirement for environment-specific fatigue assessment criteria and advocates for the refinement of design sub-factors or the appropriate application of environmental factors to reduce unnecessary conservatism while maintaining the highest standards of structural safety.

REFERENCES

[6.1] O.K. Chopra, G.L. Stevens, NUREG/CR-6909,Rev.1; Effect of LWR Water Environments on the Fatigue Life of Reactor Materials. Final Report, 2018.

[6.2] T. Austin, K. Bei, T. Efthymiadis, E. Koumoulos, Lessons Learnt from Engineering Science Projects Participating in the Horizon 2020 Open Research Data Pilot, Data. 6 (2021) 96. doi:10.3390/data6090096.

[6.3] Joint Research Center - European Commission, ODIN Portal - MatDB, (2025). https://odin.jrc.ec.europa.eu/alcor/.

[6.4] JRC FAIR data guidelines, Publications Office of the European Union, 2025. doi:doi/10.2760/5646214.

[6.5] RDA FAIR Data Maturity Working Group, FAIR Data Maturity Model. Specification and Guidelines, (2020) 47. doi:10.15497/rda00045.

[6.6] A. Mclennan, R. Tregoning, K. Mottershead, International Fatigue Database in Support of Nuclear Energy Safety, in: Vol. 1 Codes Stand., American Society of Mechanical Engineers, 2025. doi:10.1115/PVP2025-155276.

[6.7] C. Currie, A. Morley, A. Mclennan, Suitably Accounting for Mean Stress Effects in Pseudo-Stress-Based Design Fatigue Curves, in: Vol. 1 Codes Stand., American Society of Mechanical Engineers, 2025. doi:10.1115/PVP2025-154711.

[6.8] S. Asada, T. Nakamura, M. Kamaya, Y. Takahashi, Technical Revisions of Jsme Environmental Fatigue Evaluation Method, Am. Soc. Mech. Eng. Press. Vessel. Pip. Div. PVP. 1 (2023). doi:10.1115/PVP2023-102692.

[6.9] M. Bruchhausen, G. Dundulis, A. McLennan, S. Arrieta, T. Austin, R. Cicero, W.-J. Chitty, L. Doremus, M. Ernestova, A. Grybenas, C. Huotilainen, J. Mann, K. Mottershead, R. Novotny, F.J. Perosanz, N. Platts, J.-C. le Roux, P. Spätig, C. Torre Celeizábal, M. Twite, M. Vankeerberghen, Characterization of Austenitic Stainless Steels with Regard to

Environmentally Assisted Fatigue in Simulated Light Water Reactor Conditions, Metals (Basel). 11 (2021) 307. doi:10.3390/met11020307.

[6.10] T.P. Métais, G. Stevens, G. Blatman, J.C. Le Roux, R.L. Tregoning, EDF/NRC High-Cycle Fatigue Database Proposal, in: Vol. 1A Codes Stand., American Society of Mechanical Engineers, 2015. doi:10.1115/PVP2015-45146.

[6.11] A. McLennan, International Fatigue Database in Support of Nuclear Energy Safety, version 1.0, (2024). doi:10.5290/70.

[6.12] Innomerics, Data Mining Tool, (2025). https://incefascale.innomerics.com/dataminingtool/.

[6.13] US-NRC, Regulatory Guide 1.207,Rev.1; Guidelines for evaluating the effects of Light-Water Reactor Water Environments in Fatigue Analyses of Metal Components, 2018.

[6.14] INCEFA-PLUS Consortium, S. Arrieta, T. Austin, M. Bruchhausen, W.-J. Chitty, R. Cicero, S. Cicero, S. Cuvilliez, L. De Baglion, G. Dundulis, C. Gourdin, C. Huotilainen, J.-C. Le Roux, J. Mann, W. Mayinger, A. McLennan, T. Métais, E. Miroslava, K. Mottershead, R. Novotny, F.J. Perosanz López, N. Platts, I. Procopio, N. Prompt, P. Spätig, M. Twite, M. Vankeerberghen, INCEFA-PLUS findings on Environmental Fatigue, INCEFA-PLUS Project, 2020. doi:10.5281/zenodo.4243979.

This page intentionally left blank.

CHAPTER 7 OTHER MODELLING INCEFA-SCALE ACTIONS

This Chapter describes advanced numerical and analytical methodologies used to reproduce material behavior and predict crack growth across various geometries, including Peridynamics, the Theory of Critical Distances, and EPRI-led component-scale research, by Stéphan Courtin, Gintautas Dundulis, Sergio Arrieta, and Thomas Damiani.

7.1 FATIGUE BEHAVIOUR MODELLING

This Section describes work carried out to model the stress or strain behaviour of the specimens under the unique loading combinations or geometries applied during the testing within the project. The section includes work from various different laboratories across the consortium including KTU, PSI, Framatome (France), CEA, and EDF. All of the work was aimed at better understanding the material behaviour on-test, or using the test data to improve and refine existing models.

7.1.1 KTU MODELLING OF LOW CYCLE FATIGUE BEHAVIOUR

The objective here was to propose a numerical simulation methodology, based on the finite element (FE) method, for investigating the low cycle fatigue behaviour of AISI 316L steel under various loading conditions and temperatures. The validation of the numerical determination methodology was carried out by comparing the stress versus cycles values obtained by the simulation with the values determined experimentally.

7.1.1.1 METHODOLOGY USING CHABOCHE MODEL

The nonlinear combined isotropic/kinematic hardening was used to model the mechanical behaviour of grade AISI 316L steel subjected to cyclic loading. The Chaboche kinematic hardening model is applied to define the kinematic hardening component [7.1].

This approach is based on the total strain rate $\dot{\mathcal{E}}^{\mathrm{tot}}$ which consists of the elastic $\dot{\mathcal{E}}^{\mathrm{el}}$ and plastic $\dot{\mathcal{E}}^{\mathrm{pl}}$ components:

$$\dot{\mathcal{E}}^{tot} = \dot{\mathcal{E}}^{el} + \dot{\mathcal{E}}^{pl} \qquad \text{eq. 7.1}$$

The elastic response can be determined as follows:

$$\dot{\mathcal{E}}^{el} = [D^{el}]^{-1} : \sigma \qquad \text{eq. 7.2}$$

where D^{el} is the elasticity tensor, and σ is the total stress tensor.

The plastic component is determined as follows:

$$\dot{\mathcal{E}}^{pl} = \dot{\bar{\mathcal{E}}}^{pl} \frac{\partial F}{\partial \sigma} \qquad \text{eq. 7.3}$$

where $\dot{\mathcal{E}}^{\mathrm{pl}}$ the rate of plastic flow, $\dot{\bar{\mathcal{E}}}^{\mathrm{pl}}$ is the equivalent plastic strain rate that is expressed as follows:

$$\dot{\bar{\mathcal{E}}}^{pl} = \sqrt{\frac{3}{2}\dot{\mathcal{E}}^{pl} : \dot{\mathcal{E}}^{pl}} \quad \text{eq. 7.4}$$

F is the equivalent von Mises stress:

$$F = f(\sigma - \alpha) = \sqrt{\frac{3}{2}(\sigma^{dev} - \alpha^{dev}) : (\sigma^{dev} - \alpha^{dev})} \quad \text{eq. 7.5}$$

where α the overall backstress, σ^{dev} is the deviatoric part of the stress tensor which is written as follows:

$$\sigma^{dev} = \sigma - p\mathrm{I} \quad \text{eq. 7.6}$$

where p is the equivalent pressure stress, and I is the identity tensor.

α^{dev} is the deviatoric part of overall backstress, which is expressed as follows:

$$\alpha = \sum_{k=1}^{N} \alpha_k \quad \text{eq. 7.7}$$

where α_k is the k-th backstress, and N is the total number of backstresses.

The backstress α consists of multiple backstress components that are expressed as follows:

$$\dot{\alpha}_k = C_k \frac{1}{\sigma^0}(\sigma - \alpha)\dot{\bar{\mathcal{E}}}^{pl} - \gamma_k \alpha_k \dot{\bar{\mathcal{E}}}^{pl} + \frac{1}{C_k}\alpha_k \dot{C}_k \quad \text{eq. 7.8}$$

where C_k represents the initial kinematic hardening moduli, γ_k expresses the rate at which the kinematic hardening moduli decrease depending on plastic deformation, and σ^0 is the evolution of the yield surface size. C_k and γ_k can be calibrated using the experimental stress-strain results (Figure 7.1).

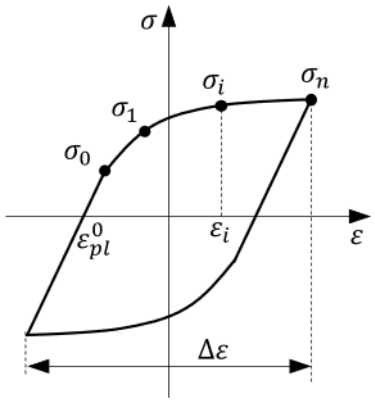

Figure 7.1. Experimental stress-strain data for a stabilized cycle.

Each set of data pairs (σ_i, ε_j^{pl}) are specified with the strain axis shifted to ε_{pl}^0 as follows:

$$\mathcal{E}_i^{pl} = \mathcal{E}_i - \frac{\sigma_i}{E} - \mathcal{E}_{pl}^0 \quad \text{eq. 7.9}$$

where the first data pair will be (σ_1, 0) as the first plastic strain point is $\varepsilon_1^{pl} = 0$. For each data pair (σ_i, ε_j^{pl}) that are determined experimentally, the overall back stress α_i is obtained as follows:

$$\alpha_i = \sigma_i - \frac{\sigma_1 + \sigma_n}{2}$$ eq. 7.10

where $(\sigma_1 + \sigma_n)/2$ is the stabilized size of the yield surface. Integration of the backstress evolution laws over this uniaxial strain cycle, with an exact match for the first data pair (σ_1, 0), leads to the following expressions:

$$\alpha_k = \frac{C_k}{\gamma_k}\left(1 - e^{-\gamma_k \varepsilon^{pl}}\right) + \alpha_{k,1} e^{-\gamma_k \varepsilon^{pl}}$$ eq. 7.11

where $\alpha_{k,1}$ is the initial value of the k-th backstress at the first data point.

The isotropic hardening component can be defined by specifying the equivalent stress defining the size of the yield surface as a function of the equivalent plastic strain.

The isotropic hardening behaviour of the model determines the evolution of the yield surface size σ^0 as a function of the equivalent plastic strain $\bar{\varepsilon}^{pl}$. The data pairs (σ_0, $\bar{\varepsilon}^{pl}$) that define this function are obtained from the experimental data (Figure 7.2). Since the Young's Modulus of the material is large in comparison to the hardening modulus of the material, the following approximation can be made:

$$\Delta\mathcal{E}^{pl} \approx \Delta\mathcal{E} - \frac{2\sigma_1^t}{E}$$ eq. 7.12

where E is the Young's Modulus.

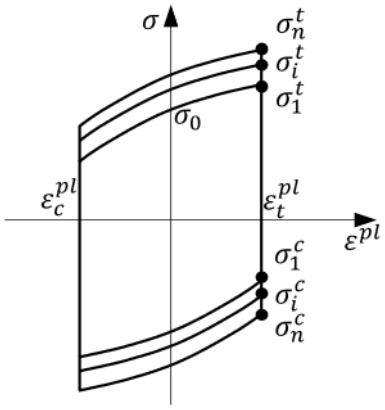

Figure 7.2. Schematic diagram of the experimental data of the stress-strain cyclic response.

For each i-cycle, the equivalent stress that defines the size of the yield surface is calculated by isolating the kinematic component from the yield stress:

$$\sigma_i^0 = \sigma_i^t - \alpha_i$$ eq. 7.13

where $\alpha_i = (\sigma_1^t + \sigma_1^c)/2$. As roughly the same backstress is expected in each cycle at a particular strain level, it can be assumed that $\alpha_i \approx (\sigma_1^t + \sigma_1^c)/2$. The equivalent plastic strain corresponding to σ_i^0 can is calculated as follows:

$$\bar{\mathcal{E}}_c^{pl} = \frac{1}{2}(4i - 3)\Delta\mathcal{E}^{pl}$$ eq. 7.14

ABAQUS allows to define the isotropic component by directly specifying the size of the yield surface as a tabular function of the equivalent plastic strain.

The evolution of the yield surface size can also be defined using the following exponential law:

$$\sigma^0 = \sigma_0 + \mathcal{Q}_\infty \left(1 - e^{-b\bar{\varepsilon}^{pl}}\right) \quad \text{eq. 7.15}$$

where σ_0 is the yield stress at zero plastic strain, $\mathcal{Q}_\infty$ is the maximum variation in the size of the yield surface, and b is the rate at which the size of the yield surface changes as plastic straining develops.

The rate of evolution of the yield surface size strongly depends on the strain range. Under complex amplitude loading conditions, the isotropic hardening properties vary significantly across different strain ranges. To address this issue, a USDFLD subroutine was developed to incorporate the dependence of isotropic hardening properties on different strain ranges. The flowchart of this subroutine is presented in Figure 7.3. During the solving process, the material properties are updated based on the value defined in the FIELD (1) variable in each time increment.

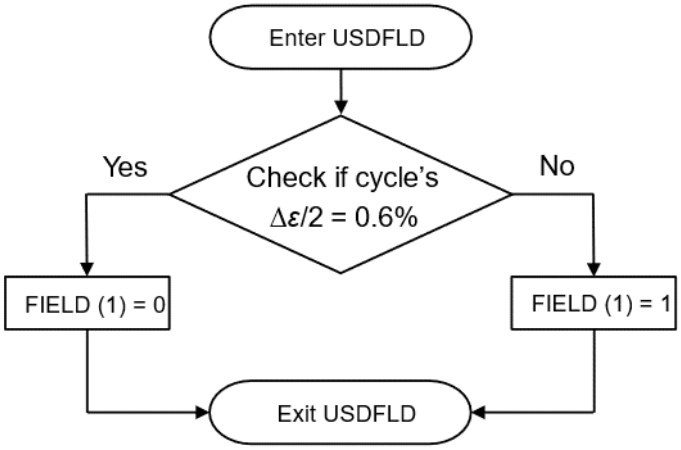

Figure 7.3. Flowchart of the USDFLD subroutine for varying material parameters.

Numerical simulations were conducted on a single finite element under tensile loading conditions.

7.1.1.2 METHODOLOGY USING ARMSTRONG-FREDERICK MODEL

The Armstrong–Frederick kinematic hardening model was employed to define the kinematic hardening behaviour of the material. The Armstrong and Frederick kinematic hardening model suits the scheme of the presented research as this model is able to predict the plasticity for strain-controlled cyclic loading with zero mean stress. The simulation results were validated by comparing them with the results of the experimental test [7.2]. The software LS-Dyna was used for LCF modelling. To model the material for numerical simulation, isotropic hardening along with kinematic hardening was employed. LS-Dyna has a predefined material model titled MAT_DAMAGE_3. This material model consists of kinematic hardening combined with the isotropic hardening for modelling low cycle fatigue. The isotropic hardening applied to the numerical model was calculated on the experimental results recorded from the low cycle fatigue test.

The Armstrong–Frederick kinematic hardening model is broadly employed for the simulation of the hardening behaviour of the steel. The advantage of this model is that the total backstress of the stress–strain curve is divided into fewer parts and each part has a limited surface.

The MAT_DAMAGE_3 material model in LS-Dyna uses the Armstrong–Frederick kinematic hardening model [7.2].

The Armstrong–Frederick kinematic hardening model is defined in LS-Dyna as follows:

$$\dot{\alpha}_j = \frac{2}{3} C_j \dot{\varepsilon}^{pl} - \gamma_j \alpha_j \dot{\bar{\varepsilon}}^{pl} \qquad \text{eq. 7.16}$$

where C is the coefficient of kinematic hardening (MPa), γ the exponent for kinematic ardening, $\dot{\varepsilon}^{pl}$ the plastic strain, $\dot{\bar{\varepsilon}}^{pl}$ the accumulated plastic deformation, and α_j the backstress.

The kinematic hardening parameters were estimated according to eq. 7.17. Three significant points on the tension-loading side of the stress–strain hysteresis loop of the stabilised cycle 171000 and cycle 595 were selected for the 0.18% and 0.6% strain models, respectively.

$$\alpha_{max} = \sum_{j=1}^{3} \left[\frac{2}{3} C_j \dot{\varepsilon}^{pl} - \gamma_j \alpha_j \dot{\bar{\varepsilon}}^{pl} \right] \qquad \text{eq. 7.17}$$

where α_{max} is the maximum cycle stress (MPa).

The kinematic hardening parameters and the variable isotropic hardening parameters were calibrated using the experimental data.

7.1.1.3 RESULTS

Numerical simulations of grade AISI 316L steel subjected to cyclic loading were carried out using the developed computational models and compared to the test data, with the results reported below. Here the results are for simulations using the symmetric and more complex variable amplitude loading waveforms applied on the uniaxial test programme.

7.1.1.3.1 RESULTS FOR CHABOCHE MODEL UNDER SYMMETRIC LOADING CONDITIONS

A Young's Modulus of 195 GPa and a Poisson's ratio of 0.3 were assigned to the steel at room temperature. In the case of symmetric loading, calibration of the material parameters of the kinematic hardening component was carried out using the stabilised cycle data. The calibration resulted in the kinematic hardening parameters that are provided in Table 7.1.

Δε/2 (%)	**C_1 (MPa)**	**γ_1**	**C_2 (MPa)**	**γ_2**	**C_3 (MPa)**	**γ_3**
0.18%	53647	0	135435	3622.9	1032190	21970

Table 7.1. Kinematic hardening parameters of 316L stainless steel at room temperature.

The evolution of the size of the yield surface as a function of the accumulated effective plastic strain obtained from the experimental data is shown in Figure 7.4.

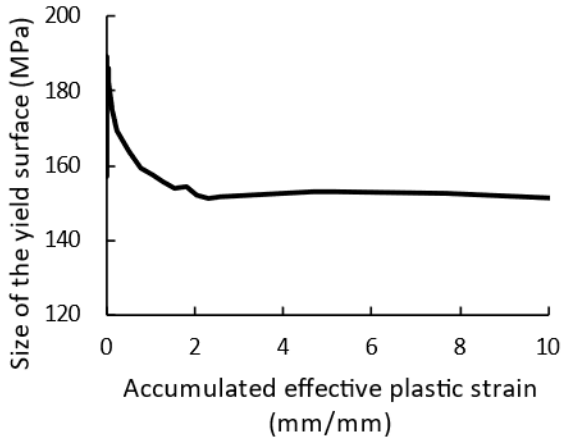

Figure 7.4. Evolution of the size of the yield surface vs. the accumulated effective plastic strain.

Calibration of the parameters of the isotropic hardening component for the exponential law resulted in the values presented in Table 7.2.

Δε/2 (%)	σ^0 (MPa)	Q_∞	b
0.18%	122.231	-33.8183	1.98271

Table 7.2. Isotropic hardening parameters of 316L stainless steel at room temperature.

Figure 7.5 shows the maximum stress depending on the number of cycles, when the isotropic hardening component is defined by the exponential law. The results have demonstrated that grade AISI 316L steel exhibits the cyclic softening behaviour in cyclic loading under symmetric loading conditions with ε_{max} = 0.18%. When the isotropic hardening component is defined by specifying the size of the yield surface, the maximum stress in the first cycles were slightly closer to the experimental data (Figure 7.6). The differences in the results obtained using these two different methods for defining the isotropic component were not very significant.

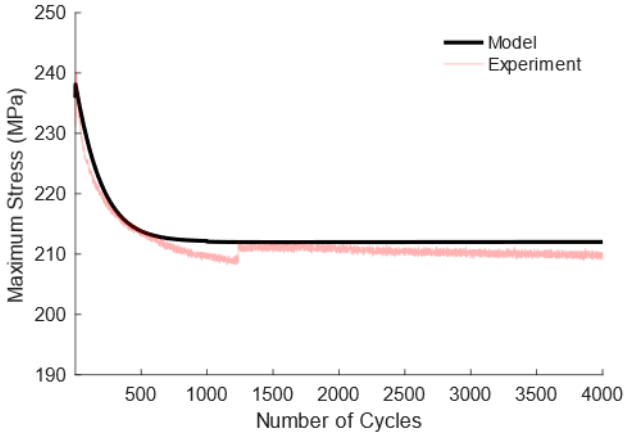

Figure 7.5. Maximum stress depending on the number of cycles at R = -1, ε_{max} = 0.18%, when the isotropic hardening component is defined by the exponential law.

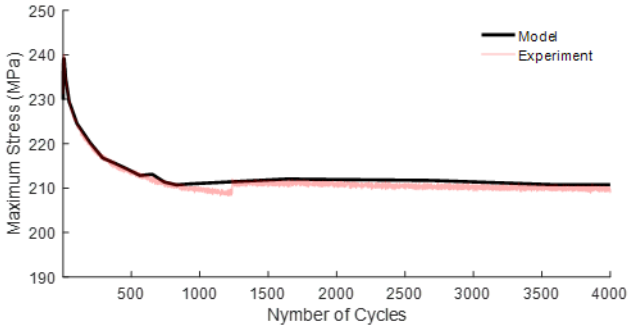

Figure 7.6. Maximum stress depending on the number of cycles at R = -1, ε_{max} = 0.18%, when the isotropic hardening component is defined by specifying the size of the yield surface.

Figure 7.7 shows the hysteresis loops of the experimental and modelling results obtained at symmetric loading conditions with ε_{max} = 0.18% under various numbers of cycles. In this case, a good agreement between the modelling and experimental results was observed.

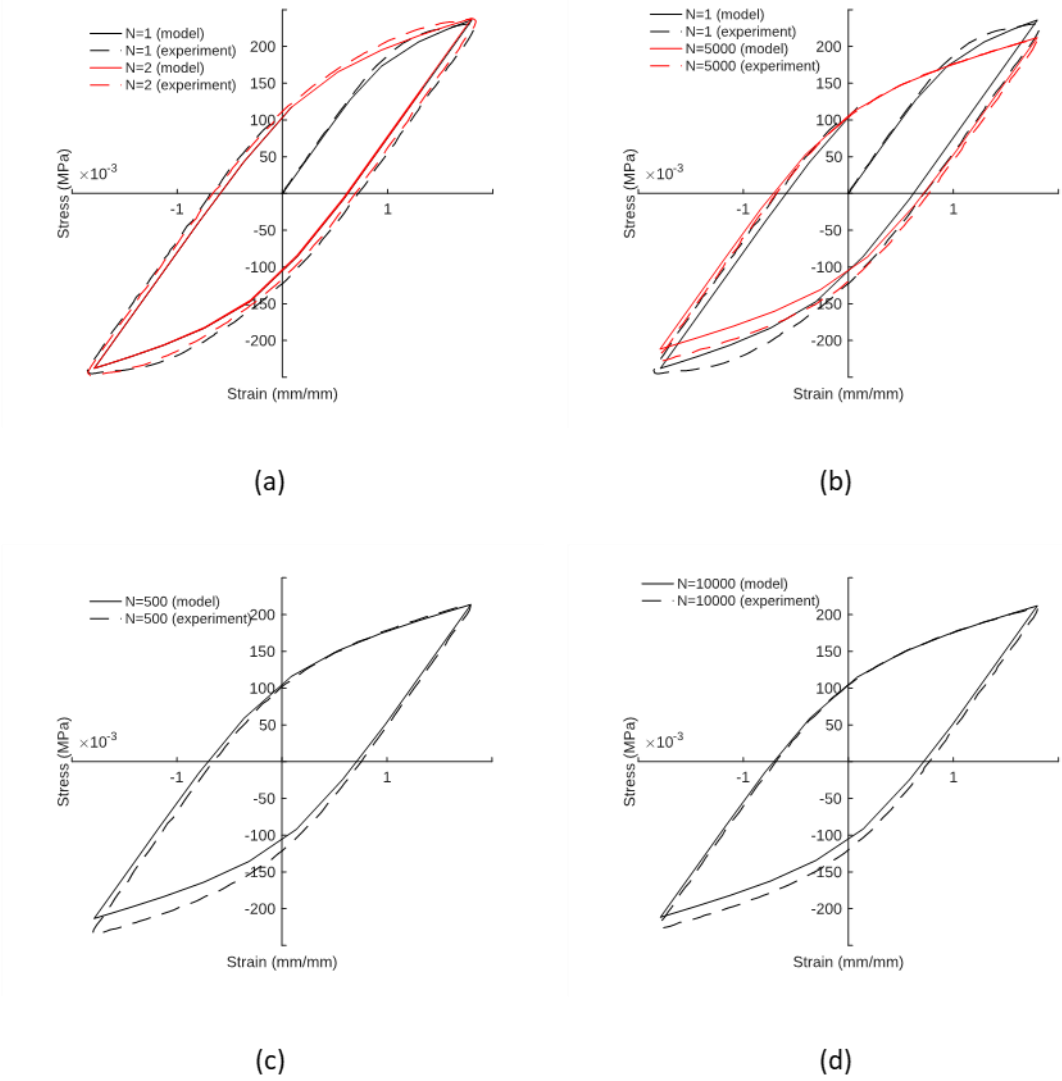

Figure 7.7. Hysteresis loops of the experimental and modelling results at R = -1, ε_{max} = 0.18%: (a) in the 1st and 2nd cycles; (b) in the 1st and 5000th cycles; (c) in the 500th cycle; (d) in the 10000th cycle.

7.1.1.3.2 RESULTS FOR CHABOCHE MODEL UNDER COMPLEX AMPLITUDE LOADING

Numerical simulations of grade AISI 316L steel subjected to cyclic POL (Periodic Overload) and PUL (Periodic Underload) loading conditions were carried out taking into account the isotropic hardening properties varying with respect to different strain ranges. The model in which both the isotropic and kinematic hardening parameters were varied did not yield better results. Therefore, only the results from the model with varying isotropic parameters were analysed. The modelling was carried out with a single element subjected to tension-compression cycles.

A Young's Modulus of 195 GPa and a Poisson's ratio of 0.3 were assigned to the steel at room temperature, while values of 160 GPa and 0.3 were used at 300 °C. The kinematic hardening parameters and the variable isotropic hardening parameters were calibrated using the experimental data. The calibrated kinematic hardening parameters that were used for the modelling of the cyclic behaviour of AISI 316L steel subjected to complex loadings at room temperature are shown in Table 7.3, and at 300 °C in Table 7.5. The isotropic parameters that were used for the modelling at room temperature are shown in Table 7.4, and at 300 °C in Table 7.6.

	C_1 (MPa)	γ_1	C_2 (MPa)	γ_2	C_3 (MPa)	γ_3
POL (0.6%/0.18%)	55179	1718	23814	1655.9	13659	144.54
PUL (0.6%/0.18%)	132473	20135	48783	1063.7	19079	139.39

Table 7.3. Kinematic hardening parameters of 316L stainless steel at room temperature.

Δε/2 (%)	**σ^0 (MPa)**	Q_∞	**b**
POL, 0.6%	164.70	44.70	0.42508
POL, 18%	172.58	-18.64	0.21053
PUL, 0.6%	170.70	31.20	0.38179
PUL, 18%	152.10	25.26	0.22174

Table 7.4. Isotropic hardening parameters of 316L stainless steel at room temperature.

	C_1 (MPa)	γ_1	C_2 (MPa)	γ_2	C_3 (MPa)	γ_3
POL (0.6%/0.18%)	3580.9	28.408	97497	1464.0	310000	18864
PUL (0.6%/0.18%)	1.82818	7210	56802	781.64	3456.1	101.78

Table 7.5. Kinematic hardening parameters of 316L stainless steel at 300 °C.

Δε/2 (%)	**σ^0 (MPa)**	Q_∞	**b**
POL, 0.6%	68.02	97.21	0.12840
POL, 18%	77.50	384.35	0.00004
PUL, 0.6%	70.90	96.43	0.09810
PUL, 18%	87.13	7.522	0.06769

Table 7.6. Isotropic hardening parameters of 316L stainless steel at 300 °C.

Figure 7.8 shows the variation of maximum stress with the number of cycles under complex loading conditions (POL 0.6% with a 0.18% baseline) obtained using the model with constant material parameters. The results show that the model with constant material parameters fails to capture the observed behaviour, where the maximum stress initially increases for cycles with a 0.6% strain amplitude, while it decreases for those with a 0.18% amplitude.

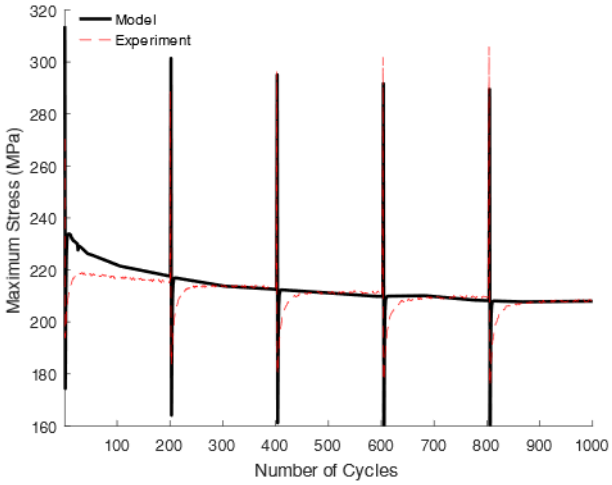

Figure 7.8. Maximum stress depending on the number of cycles (POL 0.6% with 0.18% baseline, room temperature) obtained using the model with constant material parameters.

Figure 7.9 shows the variation of maximum stress with the number of cycles under complex loading conditions (POL 0.6% with a 0.18% baseline), obtained using the model that accounts for isotropic hardening properties varying across different strain ranges. The results were in a good agreement with the experimental data.

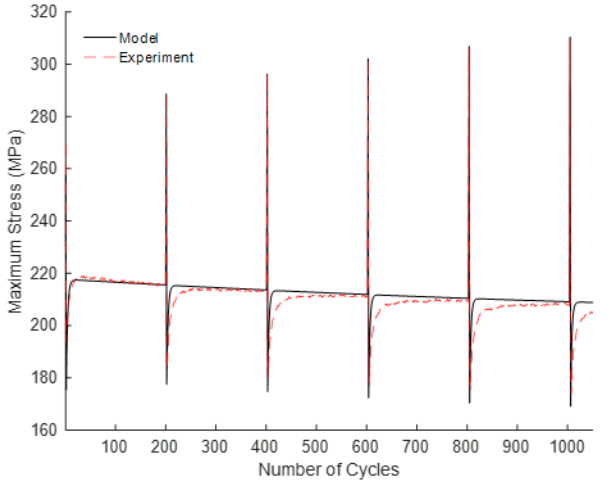

Figure 7.9. Maximum stress depending on the number of cycles (POL 0.6% with 0.18% baseline, room temperature) obtained using considering the isotropic hardening properties varying with respect to different strain ranges.

However, the minimum stress values for the 0.18% amplitude deviated more from the experimental data as the Chaboche model has some limitations when it comes to accurately capturing behaviour under non-zero mean stresses, particularly in complex loading conditions. Figure 7.10 shows the maximum and minimum stress depending on the number of cycles in the case of complex loading (POL 0.6% with 0.18% baseline).

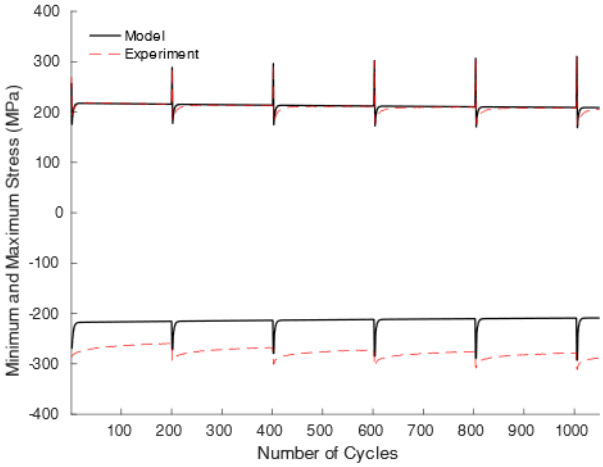

Figure 7.10. Maximum and minimum stress depending on the number of cycles (POL 0.6% with 0.18% baseline, room temperature).

Figure 7.11 shows the hysteresis loops of the experimental and modelling results obtained for the complex loadings (POL, 0.6% with 0.18% baseline).

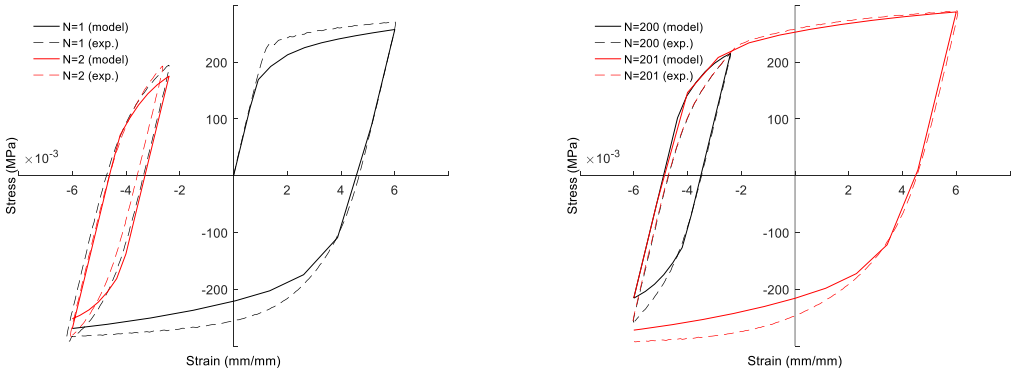

(a)

(b)

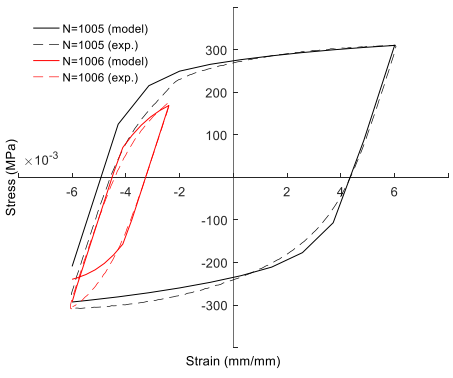

(c)

Figure 7.11. Hysteresis loops of the experimental and modelling results, POL (0.6% with 0.18% baseline, room temperature): (a) in the 1st and 2nd cycles; (b) in the 200th and 201st cycles; (c) in the 1005th and 1006th cycles.

The model captured the shape of the hysteresis loops at a 0.6% amplitude well; however, at the 0.18% baseline amplitude, the simulated loop was nearly symmetric. In contrast, the experimental loop at this amplitude was non-symmetric, exhibiting a negative mean stress.

Figure 7.12 shows the maximum and minimum stress depending on the number of cycles in the case of complex loading (PUL 0.6% with 0.18% baseline). In this case, the minimum stresses were in good agreement with the experimental data, while the maximum stresses were deviated more. It could be related to the fact that the mean stress observed in the experiment was positive for the PUL case and negative for the POL case.

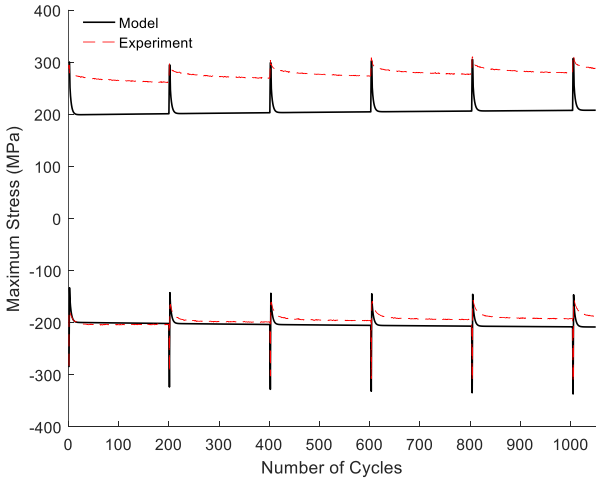

Figure 7.12. Maximum and minimum stress depending on the number of cycles (PUL 0.6% with 0.18% baseline, room temperature).

Figure 7.13 shows the hysteresis loops of the experimental and modelling results obtained for the complex loadings (PUL, 0.6% with 0.18% baseline). Similarly like in the POL case, the shapes of the hysteresis loops matched the shapes recoded in the experiment better in the lower range of the number of cycles. As in the POL case, the model captured the shape of the hysteresis loops at a 0.6% amplitude well under PUL loading conditions; however, the simulated loop at the 0.18% baseline amplitude was nearly symmetric. In contrast, the experimental loop at this amplitude was non-symmetric, exhibiting a positive mean stress.

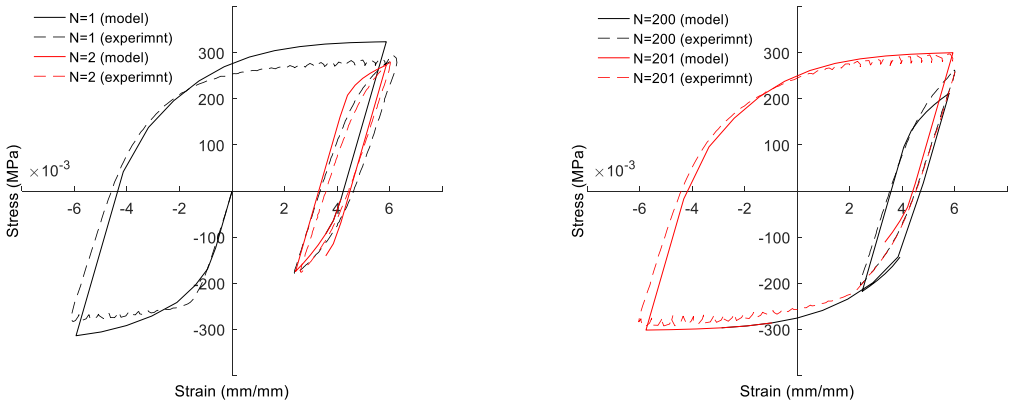

(a) (b)

Figure 7.13. Hysteresis loops of the experimental and modelling results, PUL (0.6% with 0.18% baseline, room temperature): (a) in the 1st and 2nd cycles; (b) in the 200th and 201st cycles.

Figure 7.14 illustrates the evolution of the maximum stress as a function of the number of cycles under complex loading conditions (PUL 0.6% with a 0.18% baseline) at 300 °C. Figure 7.15 presents the evolution of both maximum and minimum stresses as functions of the number of cycles under complex loading conditions (PUL 0.6% with a 0.18% baseline) at 300 °C. Similar to the results at room temperature, the maximum stress was predicted more accurately than the minimum stress for the POL loading condition.

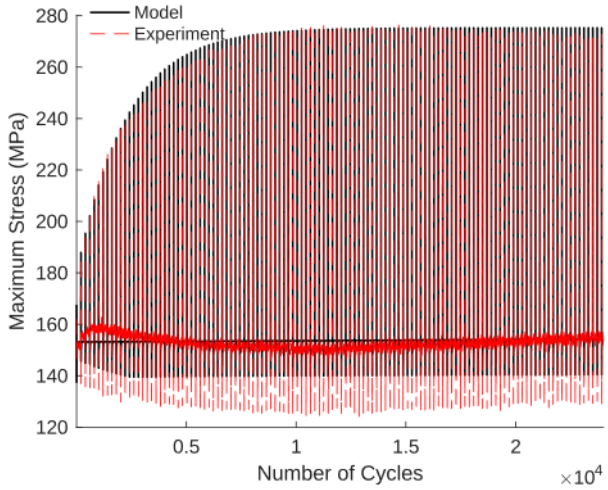

Figure 7.14. Maximum stress depending on the number of cycles (PUL 0.6% with 0.18% baseline at 300 °C).

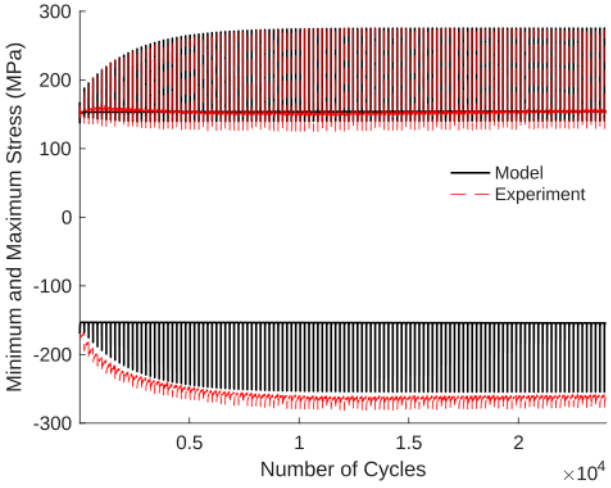

Figure 7.15. Maximum and minimum stress depending on the number of cycles (PUL 0.6% with 0.18% baseline at 300 °C).

Figure 7.16 presents the hysteresis loops from both the experimental and simulated results for the complex loading condition (POL, 0.6% with a 0.18% baseline) at 300 °C. The results exhibited similar trends to those observed in the POL case at room temperature.

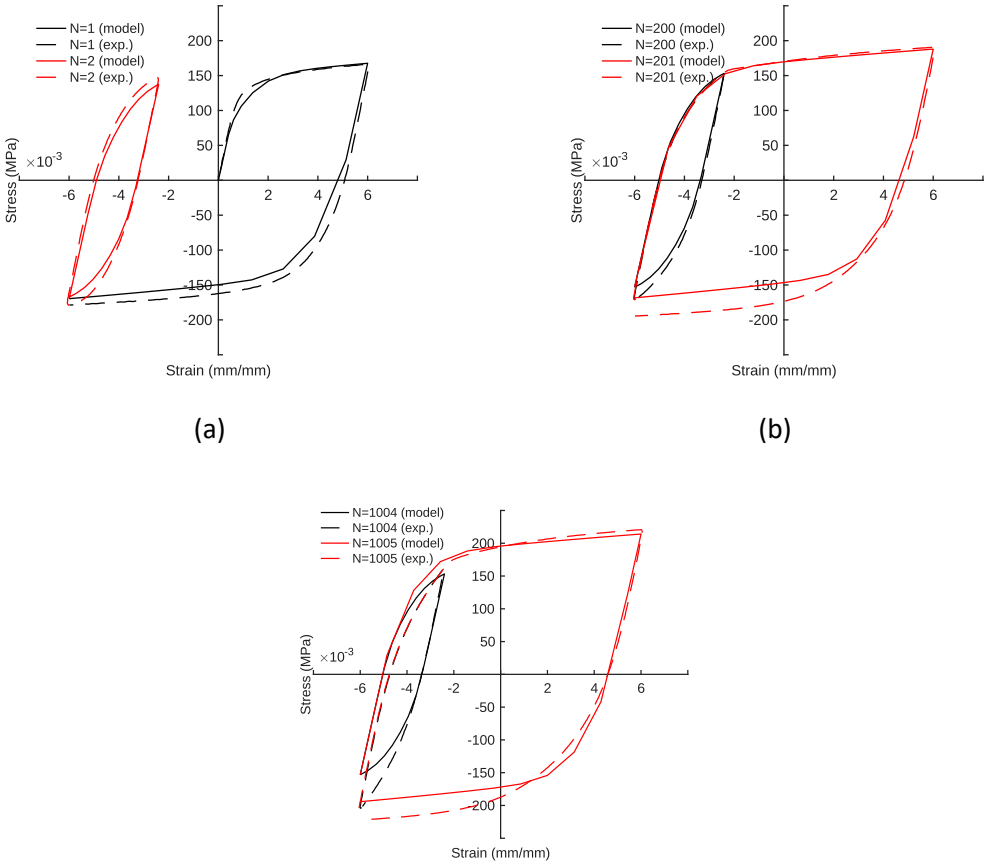

Figure 7.16. Hysteresis loops of the experimental and modelling results, POL (0.6% with 0.18% baseline at 300 °C): (a) in the 1st and 2nd cycles; (b) in the 200th and 201st cycles; (c) in the 1004th and 1005th cycles.

Minimum stress depending on the number of cycles (PUL 0.6% with 0.18% baseline at 300 °C) is shown in Figure 7.17.

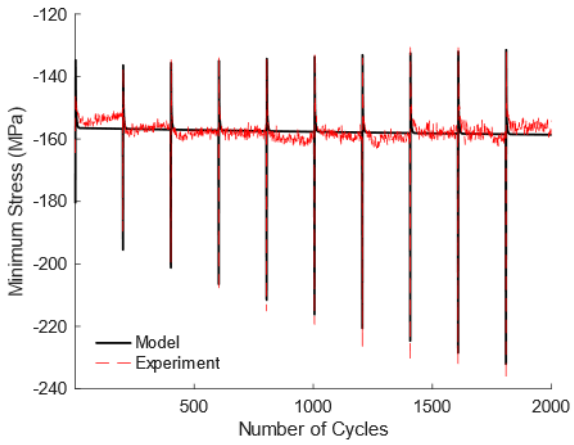

Figure 7.17. Minimum stress depending on the number of cycles (PUL 0.6% with 0.18% baseline at 300 °C).

Figure 7.18 demonstrates the evolution of maximum and minimum stresses as functions of the number of cycles under PUL loading (0.6% with a 0.18% baseline) at 300 °C. In this case, the minimum stresses show good agreement with the experimental data, while the maximum stresses deviate more noticeably.

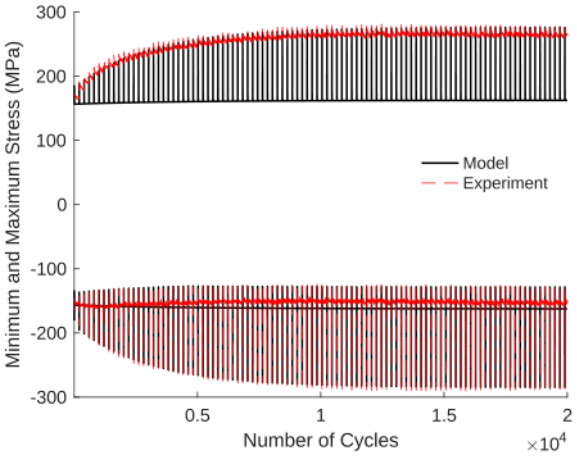

Figure 7.18. Maximum and minimum stress depending on the number of cycles (PUL 0.6% with 0.18% baseline at 300 °C).

Figure 7.19 presents the hysteresis loops from both the experimental and simulated results for the complex loading condition (PUL, 0.6% with a 0.18% baseline) at 300 °C. The results exhibit similar trends to those observed in the PUL case at room temperature.

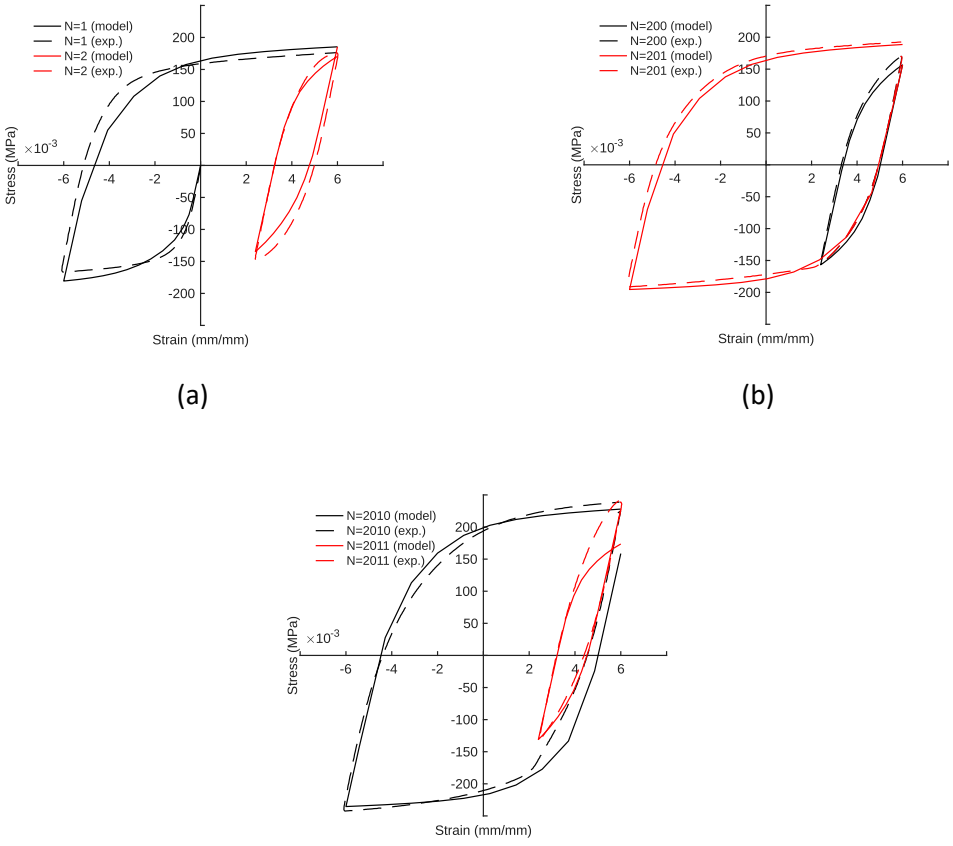

Figure 7.19. Hysteresis loops of the experimental and modelling results, PUL (0.6% with 0.18% baseline at 300 °C): (a) in the 1st and 2nd cycles; (b) in the 200th and 201st cycles; (c) in the 2010th and 2011th cycles.

7.1.1.3.3 CONCLUSIONS FOR CHABOCHE MODEL

A computational model for the investigation of the low cycle fatigue behaviour of grade 316L steel based on the Finite Element Model (FEM) was developed. Numerical simulations were carried out under symmetrical and complex POL and PUL loadings. The isotropic hardening properties varying with respect to different strain ranges were implemented in the model for POL and PUL loadings.

The results demonstrated a good agreement between the modelling and experimental results obtained at symmetric loading conditions with ε_{max} = 0.18%.

The variation of maximum stress with the number of cycles under complex loading (POL 0.6% with a 0.18% baseline) showed good agreement with the experimental data. However, the minimum stress values deviated more noticeably, as the Chaboche model has certain limitations in accurately capturing the material response under non-zero mean stresses, particularly in complex loading conditions.

For the PUL 0.6% with a 0.18% baseline case, the minimum stresses were in good agreement with the experimental data, while the maximum stresses exhibited larger deviations. This difference may be attributed to the mean stress behaviour observed in the experiments, which was positive for the PUL loading and negative for the POL loading.

7.1.1.3.4 RESULTS USING ARMSTRONG-FREDERICK MODEL FOR SYMMETRIC LOADING CONDITIONS

The simulation was performed by employing the explicit solver in Ls-Dyna R13.1.0 software. The results of the numerical simulation were plotted as the stress-versus-strain hysteresis loop in Figure 7.20, and the maximum stress for the cycle versus the number of cycles in Figure 7.21, along with the experimental results [7.2].

To check the validity of the numerical model prepared by applying isotropic hardening along with kinematic hardening to model the material for the total number of loading cycles up to the failure, the results obtained from the numerical simulation were compared with the experimental results. For the same purpose, a curve was plotted for the maximum stress versus the corresponding number of cycles, which is presented in Figure 7.22.

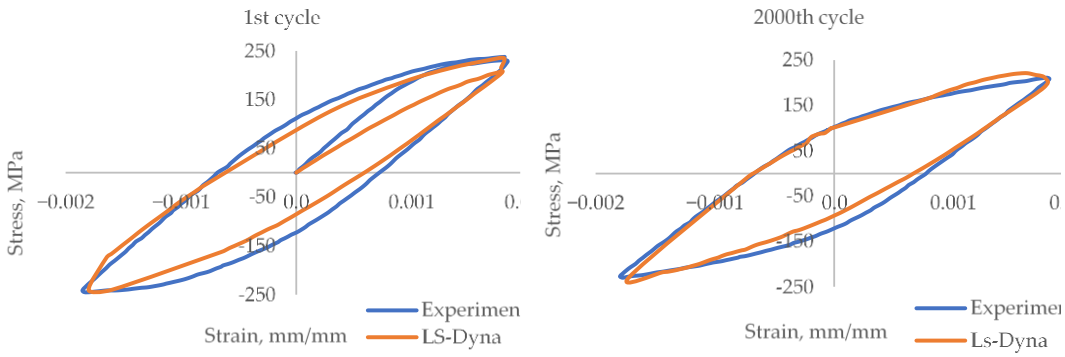

(a) (b)

Figure 7.20. A comparison of the stress-versus-strain hysteresis for the 0.18% strain model (a) for the 1st cycle; (b) for the 2000th cycle.

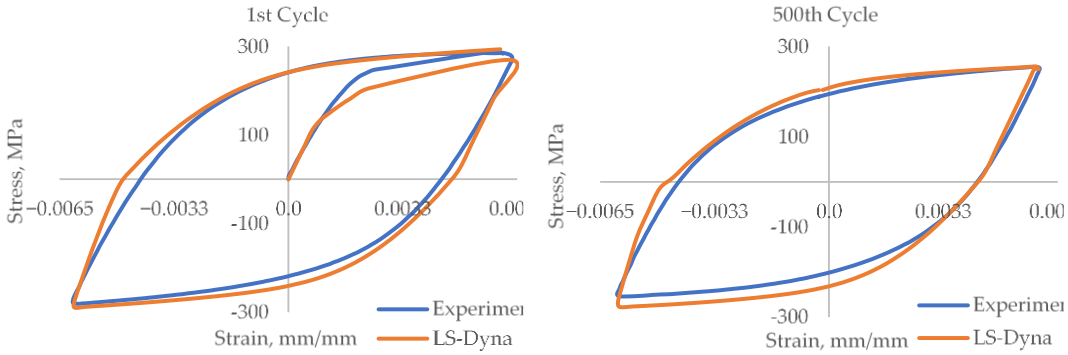

Figure 7.21. A comparison of the stress-versus-strain hysteresis for the 0.6% strain model (a) for the 1st cycle; (b) for the 500th cycle.

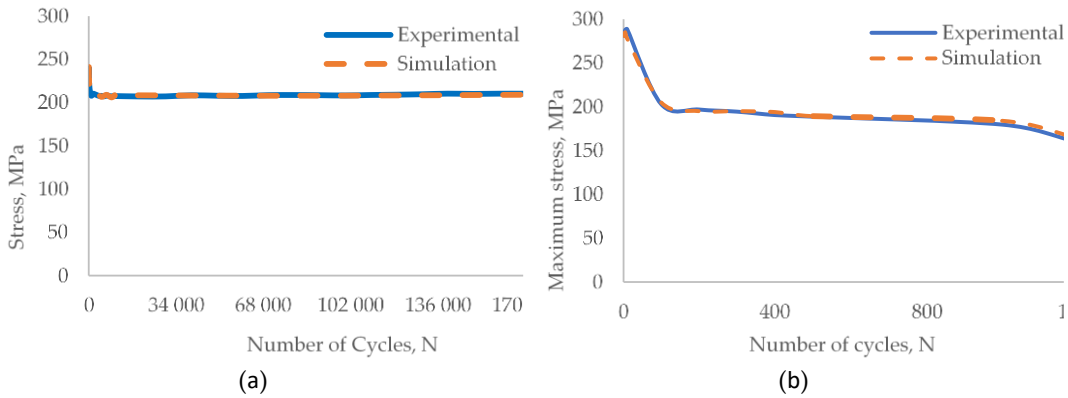

Figure 7.22. A comparison between the experimental and simulation stress-versus-number-of-cycle results of (a) 0.18% strain and (b) 0.6% strain.

The simulation results agreed well with the experimental results. For the initial few cycles, the maximum stress value deviates from the experimental results. For the 0.18% strain amplitude model, the maximum stress deviates by 1.58% between the 1st and the 100th cycle and by 0.5% between the 101st and the 170000th cycle. In the case of the 0.6% strain amplitude model, the deviation was 3.7% for cycles between the 1st and the 60th and 1% from the 61st to the 1192nd cycles. The proposed numerical simulation model captures the cyclic hardening for initial cycles followed by the cyclic softening behaviour that is similar to the experimental results (see Figure 7.23). The proposed model can be used for the approximate prediction of the fatigue life of the component exposed to similar loading conditions.

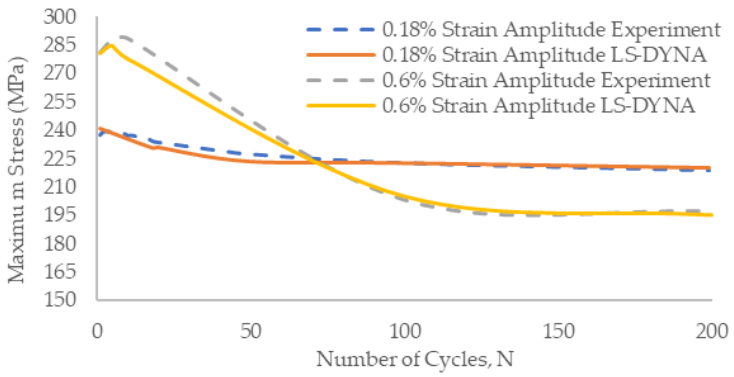

Figure 7.23. A comparison between experimental and simulation stress-versus-number-of-cycle results for the initial 200 cycles.

7.1.1.3.5 EFFECTS OF STRAIN AMPLITUDE AND TEMPERATURE ON KINEMATIC HARDENING PARAMETER RESULTS FOR COMPLEX AMPLITUDE LOADING

To perform a numerical simulation of low cycle fatigue behaviour it is very important to model the elastoplastic behaviour of the material and for this, the proper estimation of the kinematic hardening parameters is a very critical part. The numerical investigation of the low cycle fatigue behaviour was carried out on the solid and hollow specimens with different strain amplitude and temperature. The simulation results were compared with the experimental data, and the agreement of these results was acceptable. On the basis of the results, preliminary equations for the estimation of kinematic hardening parameters are proposed, and the estimated parameters through these equations gave simulation results to the experimental results [7.3].

To simplify the process of calibration of kinematic hardening parameters, preliminary equations for the estimation of kinematic hardening parameters are proposed. Based on the calibrated values of the kinematic hardening parameters, some preliminary relations by taking into account the operating temperature and strain amplitude, eq. 7.18 to eq. 7.23 are formulated for the estimation of the kinematic hardening parameters.

$$C_1 = -0.0122\sigma_{YS} - 8.8551\Delta\varepsilon^2 + 10.5727\Delta\varepsilon + 1.2496T \quad \text{eq. 7.18}$$

$$\gamma_1 = -264.3294\Delta\varepsilon^2 + 715.8896\Delta\varepsilon + 48.1017T \quad \text{eq. 7.19}$$

$$C_2 = 0.1158\sigma_{YS} + 0.0805\Delta\varepsilon^2 - 26.2504\Delta\varepsilon + 1.4235T \quad \text{eq. 7.20}$$

$$\gamma_2 = 9263.575\Delta\varepsilon^2 + 695.3537\Delta\varepsilon + 21.2144T \quad \text{eq. 7.21}$$

$$C_3 = 0.4333\sigma_{YS} + 12.3301\Delta\varepsilon^2 + 10986.4059\Delta\varepsilon + 3.2122T \quad \text{eq. 7.22}$$

$$\gamma_3 = 10324634.68\Delta\varepsilon^2 + 5012.0759\Delta\varepsilon + 37.6428T \quad \text{eq. 7.23}$$

where:

σ_{YS}: Yield stress of the material (MPa).

$\Delta\varepsilon$: Strain amplitude (%).

$$\mathrm{T} = \frac{\text{Operating Temperature (°C)}}{20\ (°\mathrm{C})}$$

To validate the formulated preliminary equations, kinematic hardening parameters are estimated with eq. 7.18 to eq. 7.23 and used them for the simulation.

The numerical simulation results are validated by plotting the results in the form of stress versus strain curves and stress versus number of cycle curves against the experimental results plotted for the same curve. Figure 7.24.a and Figure 7.24.b present the stress versus strain curve for the solid specimen 0.5% strain amplitude LCF test and the 1.0% strain amplitude LCF test, respectively.

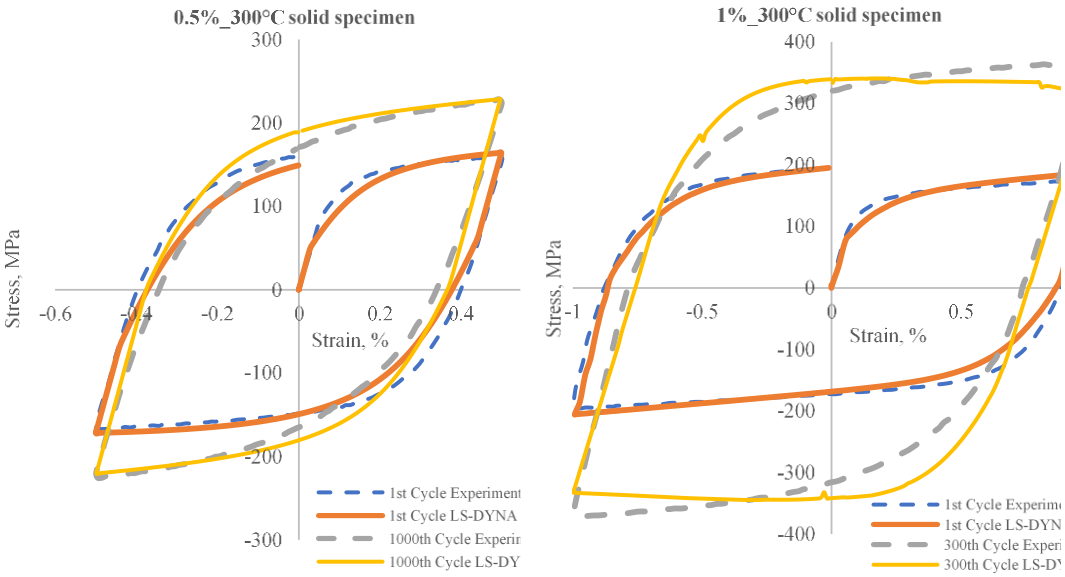

(a) (b)

Figure 7.24. Stress versus strain curve for (a) 0.5% and (b) 1% strain amplitude solid specimen.

The maximum stress versus number of cycles curves are also plotted for all the schemes, Figure 7.25.a and Figure 7.25.b present the results for the solid specimen 0.5% strain amplitude LCF test and the 1.0% strain amplitude LCF test, respectively. The experimental and simulation results showed very close agreement especially for the results at 20 °C for both 0.5% and 1.0% strain amplitude tests; there were some deviations in the stress value at the failure of the specimen. On the other hand, the simulation results at 300 °C for 0.5% strain amplitude showed close results to that of the experimental results, for initial cycles, after that until cycle 1000 cycles deviations were observed, and then the results were close until failure.

The maximum stress versus number of cycles curves and the maximum stress versus number of cycles curves are plotted for all the schemes, Figure 7.26.a and Figure 7.26.b presents the results for hollow specimen 0.3% strain amplitude LCF test respectively. The simulation results showed acceptable results to that of the experimental results.

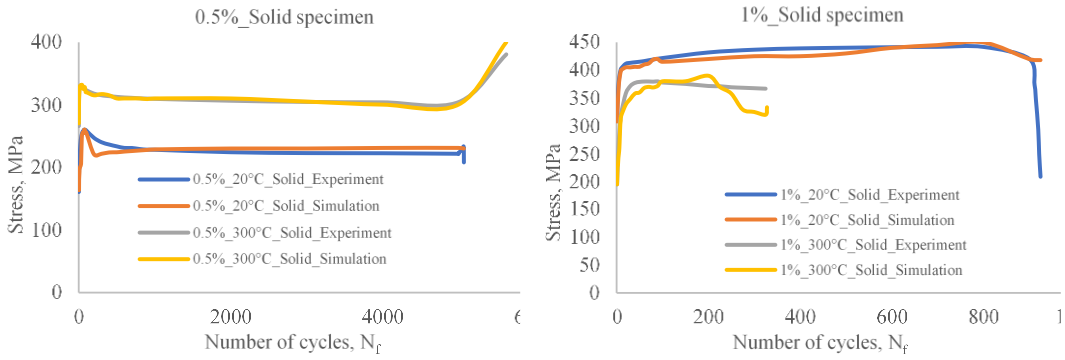

(a) (b)

Figure 7.25. Maximum stress vs. number of cycles for the experimental and simulation results of the solid specimen.

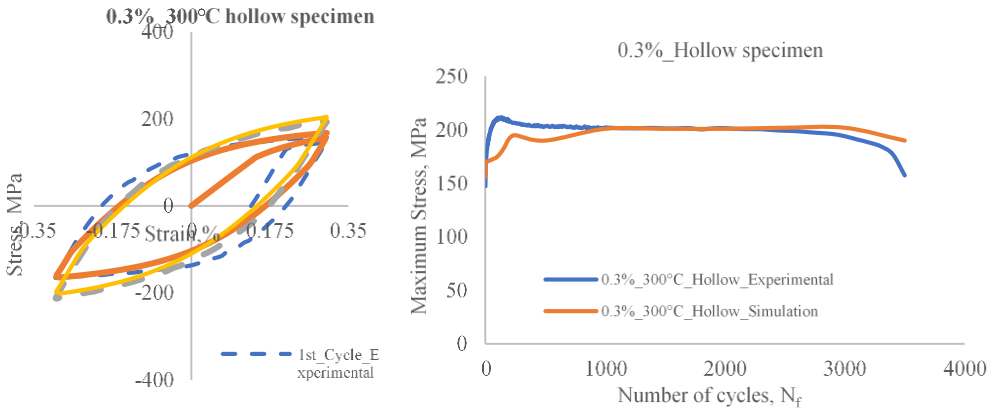

(a) (b)

Figure 7.26. (a) Stress versus strain curve and (b) maximum stress vs. number of cycles of the hollow specimen for hollow specimen with 0.3% strain amplitude.

7.1.1.3.6 CONCLUSIONS FOR ARMSTRONG-FREDERICK MODEL

On the basis of these results, preliminary equations were formulated for the prediction of the kinematic hardening parameters based on the stain amplitude and operating temperature. These preliminary equations were used to estimate the kinematic hardening parameters for the 1.0% strain amplitude at 300 °C and the 0.3% strain amplitude of the hollow specimen at 300 °C. These parameters were employed for simulation and validation to compare the results with the experimental results. The stress-strain hysteresis loop of simulation results was very close to the experimental results, the maximum stress of the cycles matched well. For the maximum stress versus number of cycles curve, the simulation results deviate by 22% with the experimental results for the initial cycles, and the curve got better and close to the experimental results as the number of cycles increases, and at the end of the simulation the results deviated by 10% for the last cycle.

7.1.2 PSI MODELLING FOR HOLLOW SPECIMENS

Finite element simulations were launched to investigate the stress state and its evolution with cyclic plasticity on the internal surface of hollow specimens.

Due to the internal pressure, there is a triaxial stress state on the internal surface where the crack initiates and the role of this stress state on the entire fatigue life needs to be clarified. In particular, the amplitude of the hoop stress depends on the internal pressure but also on the outer and inner diameters of the specimen. Typically, when calculated in the frame of elasticity theory and for a specimen with an outer diameter of 10 mm and inner one of 5 mm, the hoop stress on the internal surface is about 30 MPa when the internal pressure is 200 bar.

The possible effects of the specimen geometry (hollow versus solid bars) and on the hoop stress on the fatigue life remains poorly documented and subject to debate. Furthermore, under uniaxial cyclic solicitation, it is expected that a certain amount of ratcheting occurs for the hoop and radial strain, which are likely to affect the initiation life.

As a first step, FE simulation of the cyclic behavior at the beginning of the fatigue to estimate the amount of ratcheting one may expect. A model was built with ABAQUS based on the

standard specimen geometry used at Paul Scherrer Institute and shown in Figure 7.27. For the time being, the model was run to calculate the stress state on the internal surface at the middle of hollow specimens for different loading cases, comprising unpressurized, pressurized at 100 and 200 bar and for two different strain amplitudes, namely 0.3% and 0.6%.

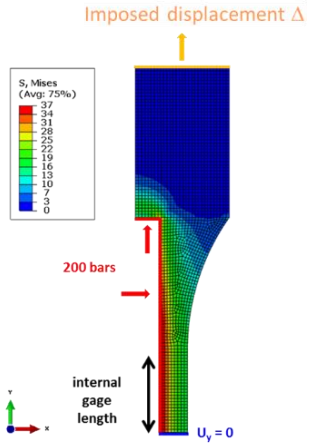

Figure 7.27. FE model of the hollow specimen.

The model considered is based on a combination of isotropic/cyclic and kinematic hardenings provided by ABAQUS. The isotropic hardening component is given in the form of tabular data, where the size of the yield surface at the end of the i^{th} cycle number is given by:

$$\sigma_{y,i} = \left(\frac{\sigma_{t,i} - \sigma_{c,i}}{2}\right) \qquad \text{eq. 7.24}$$

where $\sigma_{t,i}$ and $\sigma_{c,i}$ are respectively the maximum tensile stress and the yield stress in compression during the i^{th} cycle. While $\sigma_{t,i}$ is unambiguously defined, $\sigma_{c,i}$, is intrinsically ill-defined. Here, it was arbitrarily chosen at a compressive plastic strain of 0.05% (see Figure 7.28).

The isotropic hardening is then given by the increase of $\sigma_{y,i}$ divided by the increase of the plastic strain at each cycle. The back stress $\sigma_{b,i}$ is naturally defined as:

$$\sigma_{b,i} = \left(\frac{\sigma_{t,i} + \sigma_{c,i}}{2}\right) \qquad \text{eq. 7.25}$$

characterizes the shift of the yield surface.

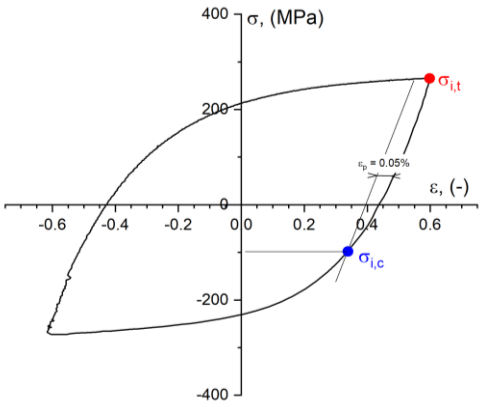

Figure 7.28. Hysteresis with the definition of $\sigma_{t,i}$ and $\sigma_{c,i}$ used to calculate the size of the yield function and the back stress.

In Figure 7.29, we plot the evolution of the yield stress ($\sigma_{y,i}$) function as well as the back stress against the equivalent plastic strain $\varepsilon_{p,eq}$, which is fitted using two back stresses as:

$$\sigma_b(\epsilon_{p,eq}) = \left(\frac{C_1}{\gamma_1}\right) * \left(1 - \exp\left(-\gamma_1 \epsilon_{p,eq}\right)\right) + \left(\frac{C_2}{\gamma_2}\right) * \left(1 - \exp\left(-\gamma_2 \epsilon_{p,eq}\right)\right) \quad \text{eq. 7.26}$$

with C_1 = 248142, γ_1 = 3031, C_2 = 561.2 and γ_2 = 30.9.

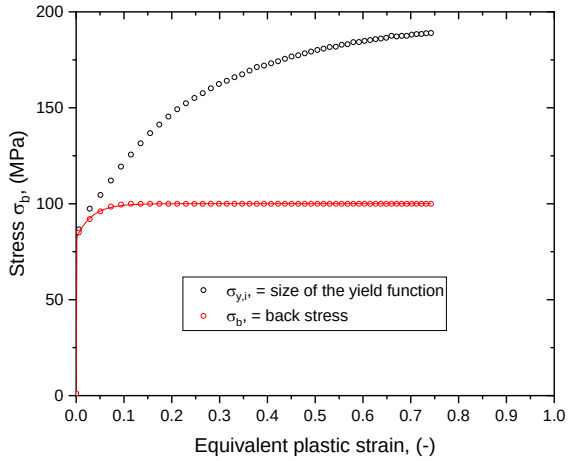

Figure 7.29. $\sigma_{y,i}$ and σ_b versus the equivalent plastic strain; each point corresponds to one cycle.

These four constants are used as input in ABAQUS to characterize the kinematic hardening. As an example, the calculated σ_{max} and σ_{min} versus the cycle number are plotted in Figure 7.30 in the case of an unpressurized hollow specimen cyclically simulated with a strain amplitude of 0.6%. We emphasize that the imposed displacement D of the specimen head had to be adjusted iteratively until the desired strain amplitude was calculated at the contact point between the extensometer blade and the specimen (see Figure 7.27). Once D is properly calibrated, a simulation was run over the first 50 cycles. In Figure 7.30, one can see that the maximum stress and minimum stress are in relatively good agreement with the experimental data, validating the back stress used in the simulations that was further considered in the other simulations. In fact, the model underestimates the experimental data by about 10 MPa.

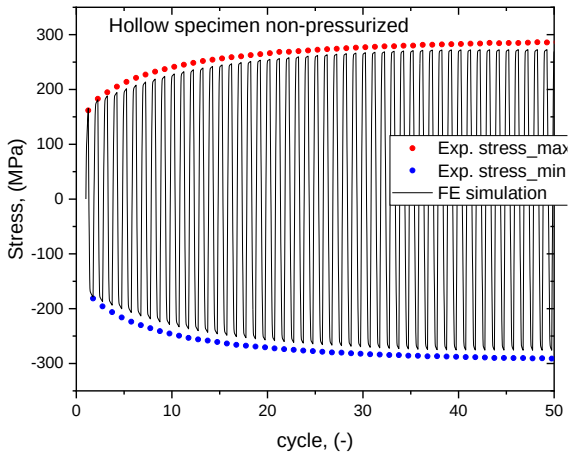

Figure 7.30. Comparison of the measure σ_{max} and σ_{min} with the calculated ones.

Since the effect of two different internal pressures (100 and 200 bar) and of the two different strain amplitudes (0.3% and 0.6%) were studied, we simplified the model by simulating an infinite hollow specimen to avoid the calibration of the displacement head D to impose for each simulated condition to reach the correct strain amplitude as measured by the extensometer. We focused in particular in the amount of ratcheting that one expects to occur on the internal surface of the specimens at the very beginning of the fatigue life.

In Figure 7.31, the variation with the cycle number is shown. It can be clearly observed that both the strain and the internal pressure have a strong influence on the ratcheting of the hoop stress, which according to the simulation is far from being negligible and may impact the fatigue life to some extent. One word of caution is needed regarding the development of the back stresses that might be different on the pressurized specimen from the uniaxially loaded specimen; in other words, the function $\sigma_b(\varepsilon_p)$ might have a dependence on the type of loading. However, the occurrence of ratcheting in the radial and hoop direction seems undisputed but to which extent it continues or stabilizes after a certain number of cycles needs to be established. This conclusion has led the consortium to define a program on hollow specimens to vary the stress state through the internal pressure and the geometry of the specimens in PWR and reference environments (pure deoxygenated water and room temperature air).

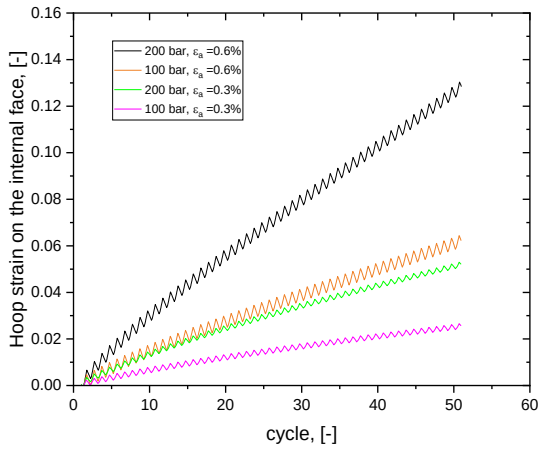

Figure 7.31. Evolution of the hoop stress for four different configurations of a pressurized tube over the first 50 cycles.

7.1.3 FRAMATOME FRANCE MODELLING FOR NOTCHED SPECIMENS

Despite that fatigue testing is traditionally realized with strain control, some modification has to be adopted for the notched specimen configuration. As the strain measurement at the bottom of the notch required complex instrumentation, it was decided to pilot the test in load control. Additionally, an extensometer will be used to measure the elongation in the vicinity of the notched (see Figure 7.32).

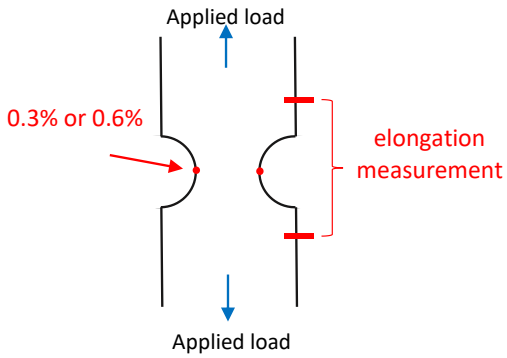

Figure 7.32. Elongation measurement in the notched specimen.

Before testing, to define the load level and the equivalent strain range in the bottom of the notch, some elastoplastic calculations were required, for each geometry tested in the various laboratories.

This analysis was focused on the stabilized state and two models were used:

- A non-linear kinematic model with 2 centres.
- A 1/4 cycle model with the cyclic curve [7.4].

The two models were calibrated to reproduce the uniaxial experimental data at the stabilized state [7.5] (see Figure 7.33). The results of the two models were compared in Figure 7.34 and we observed a global consistency. In this configuration, the ¼ cycle model presented the advantage to give information for different load levels from one calculation where the complex model required one calculation per load level.

With the ¼ cycle model, we determined the evolution of the applied load as a function of the maximal equivalent strain with one calculation. Thanks to these curves, it was easy to determine the load to apply for each test following a criterion on the maximal strain range (see Figure 7.35).

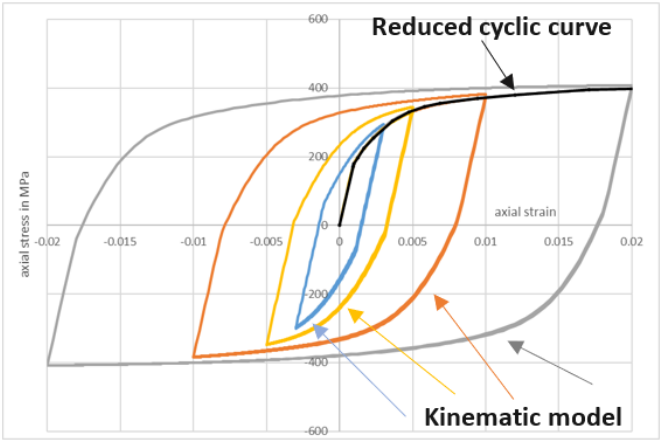

Figure 7.33. Adjustment of the FE model.

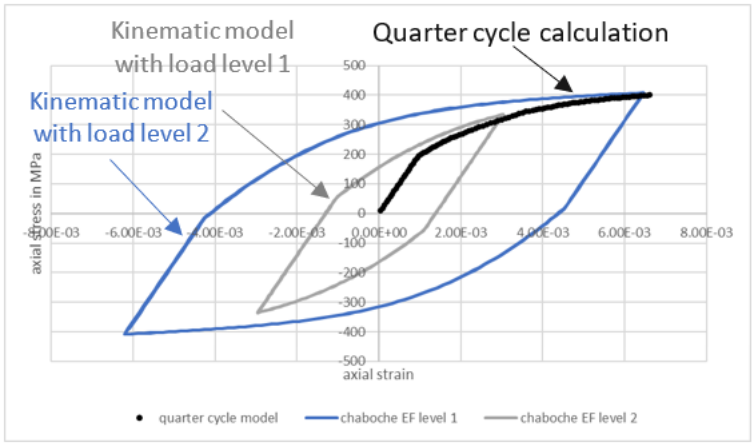

Figure 7.34. Comparison between the two models.

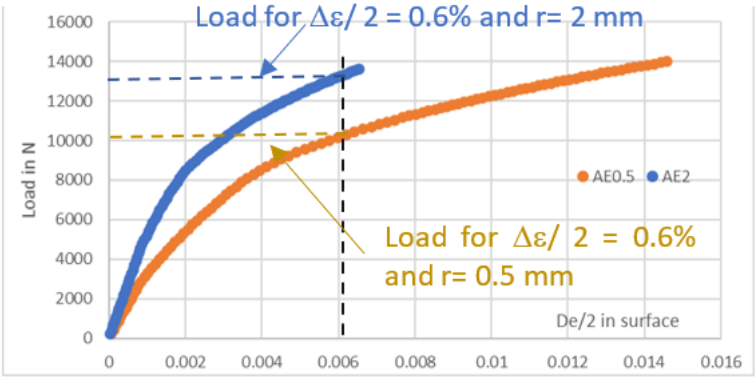

Figure 7.35. Evolution of the load as a function of the maximal equivalent strain.

After the preliminary tests on notched specimens, with constant amplitude loading and stepped loading conditions, some analyses were performed to explain the differences between experimental and numerical results.

First, according to the experimental loops, we proposed the definition of a lower and a higher bound of the cyclic curve (see Figure 7.36). Two curves were then proposed corresponding to a scattering ±10 MPa for $\Delta\varepsilon/2$ = 0.5%, to catch the higher and lower experimental loop. A scattering on behaviour could explain a part of the difference between Finite Element Analysis (FEA) and experimental results.

Then, it could be observed on the comparisons between numerical and experimental loops that FE results stayed symmetric and did not catch the “ratcheting/translating” effect experimentally obtained. So, an offset was artificially added to make the comparison possible.

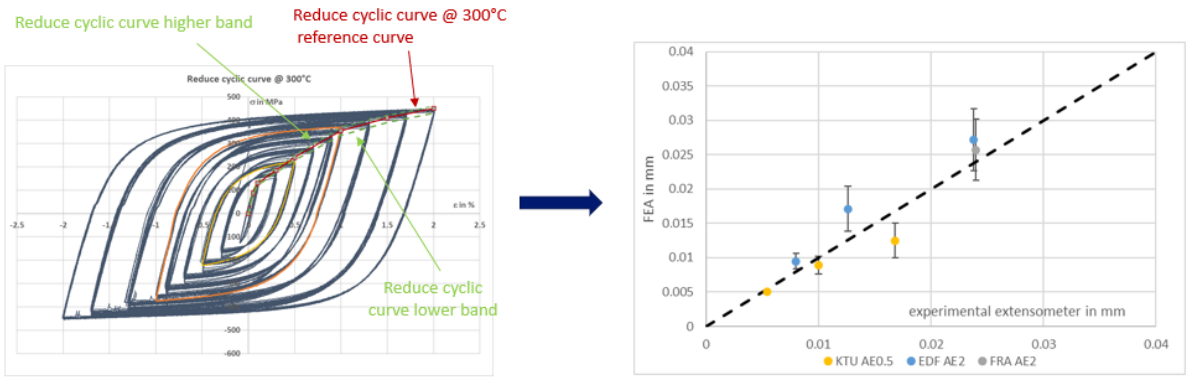

Figure 7.36. Analyses on the behaviour scattering.

For the first notched specimen tested in stepped loading conditions by EDF, the main results are as follows (see Figure 7.37):

- For the 1st step, the slope of the elastic part is a little bit underestimated and requires an adjustment of the value chosen for the Young's Modulus. E = 176 GPa, like in the RCC-M code, is proposed.
- The 2nd step is correctly modelled.
- The level of plasticity in the 3rd step is underestimated.

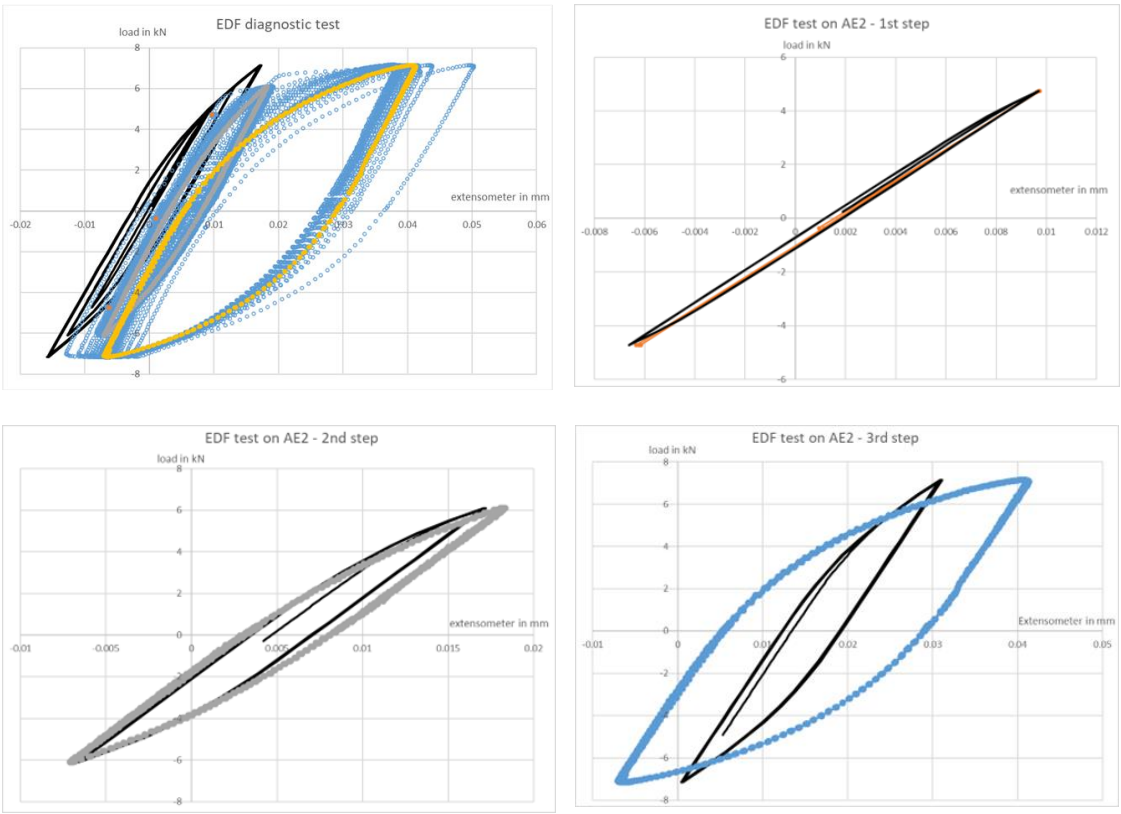

Figure 7.37. Analyses on the first notched specimen tested in stepped loading conditions by EDF.

For the first notched specimen tested in stepped loading conditions by KTU, the main results are as follows (see Figure 7.38):

- For the 1st step, the slope of the elastic part, with the adjustment on the Young's Modulus value, agrees with the experimental results.
- The levels of plasticity in the 2nd and 3rd steps are underestimated, and improvements in the identification of the Chaboche parameters in the relevant range of $\Delta\varepsilon/2$ between 0 and 0.6%, are required.

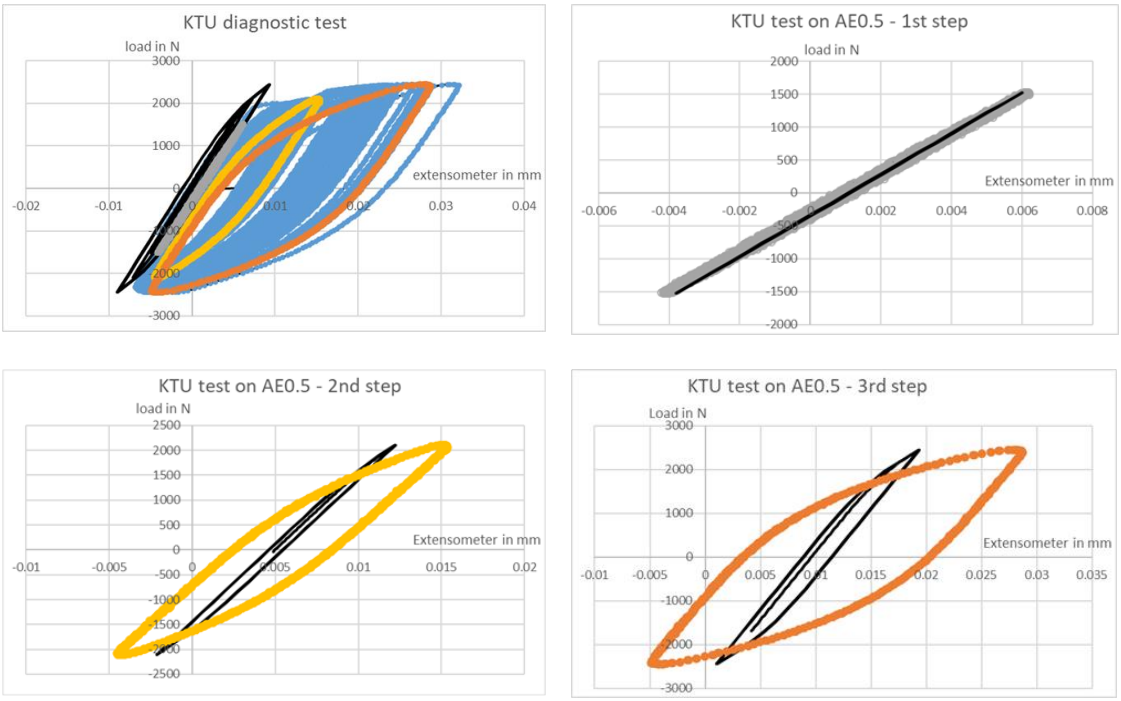

Figure 7.38. Analyses on the first notched specimen tested in stepped loading conditions by KTU.

7.1.4 CEA MODELLING FOR NOTCHED SPECIMENS

7.1.4.1 MATERIAL MODELLING

The material used in INCEFA-SCALE Project is a 316L austenitic stainless steel provided by EDF. Its complex behaviour under cycling loading can be represented with a Chaboche type model.

The Chaboche constitutive model implemented in Cast3M is similar to that used in Zhang PhD (see [7.5] and Figure 7.39) except for the non-linear isotropic hardening. Cast3M model does not account for history effect, so the following equation:

$$\dot{R} = b(Q - R)\dot{p} \qquad \text{eq. 7.27}$$

becoming:

$$dR = b(R_m - R)dp \qquad \text{eq. 7.28}$$

with an additional R_m parameter for isotropic hardening.

The Chaboche model used is then an elastic-plastic model with both non-linear kinematic (2 back stresses X1 and X2) and non-linear isotropic hardenings. The parameters for kinematic hardening are different from EDF Code_Aster model to Cast3M one. The relation is then:

Ai (Cast3M) = Ci / γi (Code_Aster) and Ci (Cast3M) = γi (Code_Aster)

a)

Strain partition	$\varepsilon = \varepsilon^e + \varepsilon^p$
Hooke's law	$\sigma = \frac{Ev}{(1+v)(1-2v)} tr(\varepsilon^e) I + \frac{E}{(1+v)} \varepsilon^e$
Field threshold	$f(\sigma, X, p) = J_2(\sigma - X) - (R(p) + R_0) \leqslant 0$ with $J_2(\sigma - X) = \sqrt{\frac{3}{2}(\tilde{\sigma} - X) : (\tilde{\sigma} - X)}$ and $\tilde{\sigma} = \sigma - \frac{1}{3} tr(\sigma) I$
Plastic flow	$\dot{\varepsilon}^p = \dot{\lambda} \frac{\partial f}{\partial \sigma} = \frac{3}{2} \dot{\lambda} \frac{\tilde{\sigma} - X}{J_2(\sigma - X)}$ $f = 0$
Non-linear kinematic hardening	$X = \sum(X_i)$ $\dot{X}_i = \frac{2}{3} C_i(p) \dot{\varepsilon}^p - \gamma_i X_i \dot{p}$ with $C_i(p) = C_i^{\infty}(1 + (k-1)) e^{-wp}$ $\gamma_i(p) = \gamma_i^0 (a_{\infty} + (1 - a_{\infty})) e^{-bp}$ and $\dot{p} = \sqrt{\frac{2}{3} \dot{\varepsilon}^p : \dot{\varepsilon}^p}$ where i represents each kinematic hardening
Non-linear isotropic hardening	$\dot{R} = b(Q - R)\dot{p}$ $Q(q) = Q_0 + (Q_m - Q_0)(1 - e^{-2\mu q})$ $F = \frac{2}{3} J_2(\varepsilon^p - \xi) - q \leqslant 0$ $d\xi = \frac{1 - \eta}{\eta} dq n^*$ n^* corresponds to the normal direction of surface F

b)

	Parameters	20°C	150°C	300°C
Elasticity	E (MPa)	190000	170000	160000
	ν	0.3	0.3	0.3
Kinematic Hardening	C_1(MPa)	90000	117907	170000
	γ_1	630	1200	1500
	C_2(MPa)	9000	17000	25000
	γ_2	100	150	200
Isotropic Hardening	R_0(MPa)	180	125	110
	b	5	5	10
History Effect	μ	12	16	16
	η	1	1	1
	Q_0(MPa)	620	270	250
	Q_m(MPa)	-100	-50	-50

Figure 7.39. (a) Chaboche model used in [7.5] and (b) the parameters calibrated for the 316L stainless steel.

The model has been calibrated using the experimental data provided by EDF, which are uniaxial fatigue tests performed at 300 °C and 20 °C at two different strain levels: ±0.5% and ±1.0%.

Finite elements simulations of the uniaxial tensile tests have been performed with Cast3M using an axisymmetric model.

T = 300 °C:

Different parameter sets have been calibrated (see Figure 7.40 to Figure 7.43, and Table 7.7). As the material behaviour is very different for both strain levels (±0.5% and ±1.0%), it is impossible to find parameters that fit both. Therefore, the calibration focuses on the ±0.5% strain data, which is acceptable as we intend to simulate the notch specimen tested between strain levels of ±0.2% and ±0.6%.

- **Parameter set 1:** models the stabilised stress state at the maximum stress level (N ≈ 100). b = 1 allows to reach a stabilised stress state at cycle N = 2.
- **Parameter set 2:** models the stabilised stress state at half-life (N ≈ 2500). b = 1 allows to reach a stabilised stress state at cycle N = 2. These parameters can only be used to simulate low strain levels close to ±0.5% strain because they do not accurately represent the material behaviour at higher strain levels.
- **Parameter set 3**: models the stress softening between the cycles at the maximum stress and the cycles at half-life on ±0.5% strain data.
- **Parameter set 4**: models the stress hardening up to the maximum stress level on ±0.5% strain data.

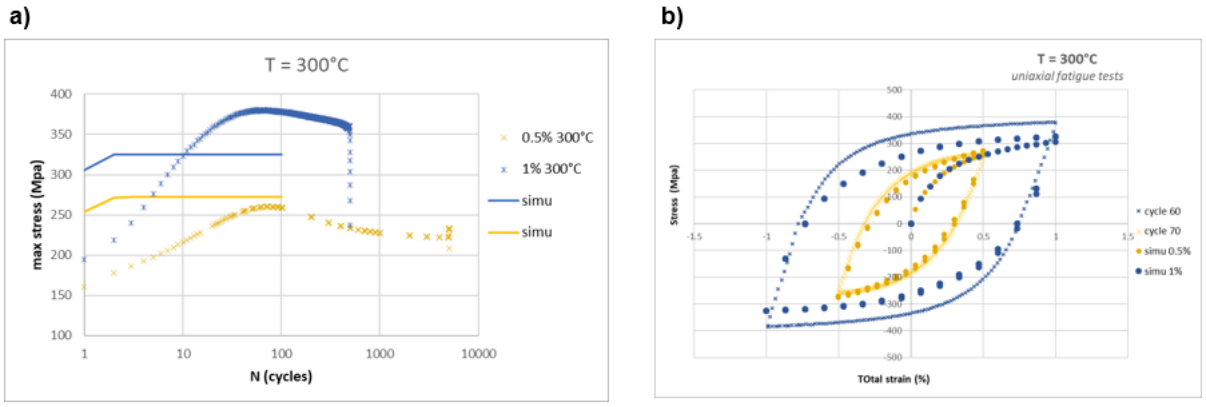

Figure 7.40. Chaboche model – parameter set 1 (maximum stress).

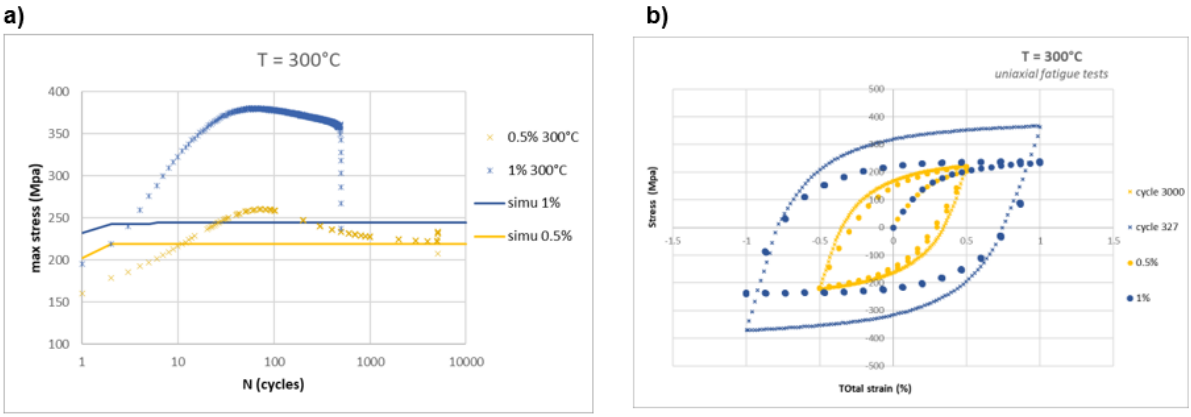

Figure 7.41. Chaboche model at 300 °C – parameter set 2 (half-life).

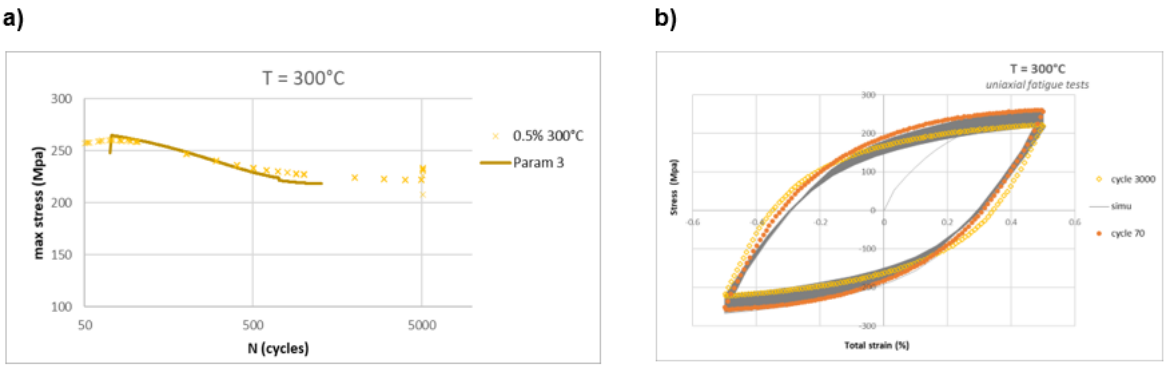

Figure 7.42. Chaboche model at 300 °C – parameter set 3 (stress softening between max stress and half-life).

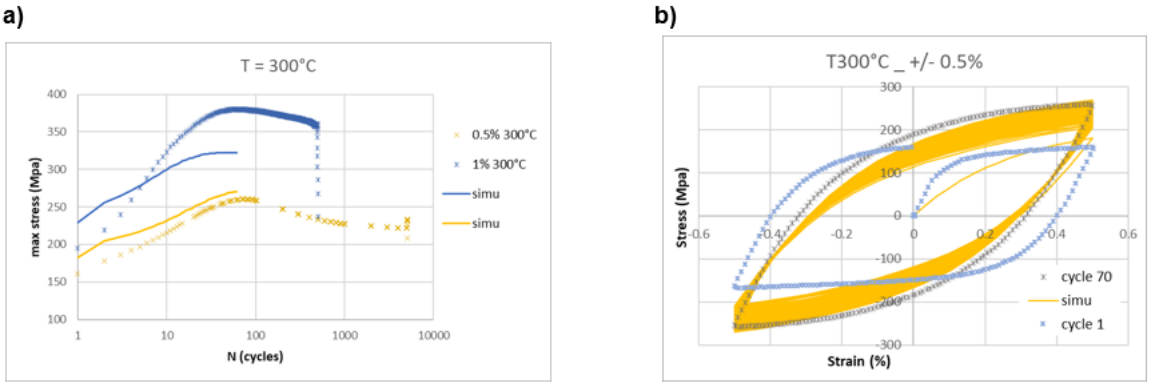

Figure 7.43. Chaboche model at 300 °C – parameter set 4 (stress hardening up to max stress).

a) Parameter set 1

E (Gpa)	nu		Corresponding EDF parameters	
160	0.3			
A1 (Pa) = C1 /	C1 = γ1		C1	γ1
9.00E+07	1000		9.00E+10	1000
A2 (Pa) = C2 /	C2 = γ2		C2	γ2
1.60E+08	214		3.42E+10	214
Psi	Omega			
1	0			
R0 (Pa)	RM (Pa)	b		
8.00E+08	8.00E+08	1		

b) Parameter set 2

E (Gpa)	nu		Corresponding EDF parameters	
160	0.3			
A1 (Pa) = C1 /	C1 = γ1		C1	γ1
1.14E+08	1200		1.36E+11	1200
A2 (Pa) = C2 /	C2 = γ2		C2	γ2
1.20E+08	303.194		3.64E+10	303.194
Psi	Omega			
1	0			
R0 (Pa)	RM (Pa)	b		
5.00E+06	5.00E+06	1		

c) Parameter set 3

E (Gpa)	nu		Corresponding EDF parameters	
160	0.3			
A1 (Pa) = C1 /	C1 = γ1		C1	γ1
1.14E+08	1600		1.82E+11	1600
A2 (Pa) = C2 /	C2 = γ2		C2	γ2
1.07E+08	303.194		3.24E+10	303.194
Psi	Omega			
1	0			
R0 (Pa)	RM (Pa)	b		
5.50E+07	5.00E+06	0.25		

d) Parameter set 4

E (Gpa)	nu			
180	0.3			
A1 (Pa) = C1 /	C1 = γ1		C1	γ1
8.70E+07	1000		8.70E+10	1000
A2 (Pa) = C2 /	C2 = γ2		C2	γ2
1.61E+08	212		3.41E+10	212
Psi	Omega			
1	0			
R0 (Pa)	RM (Pa)	b		
5.00E+06	8.00E+07	4		

Table 7.7. Chaboche parameter at 300 °C (a) set 1; (b) set 2; (c) set3; and (d) set 4.

This model can represent a stabilised state of stress or stress hardening or stress softening independently only but not several phenomena at the same time. It does not account for ratcheting.

T = 20 °C:

Different parameter sets have been calibrated (see Figure 7.44 and Figure 7.45, and Table 7.8):

- **Parameter set 1:** models the stress hardening up to the maximum stress level on both strain levels (±0.5% and ±1.0%).
- **Parameter set 2:** models the stabilised stress state at half-life (N ≈ 2000). b = 1 allows to reach a stabilised stress state at cycle N = 2.

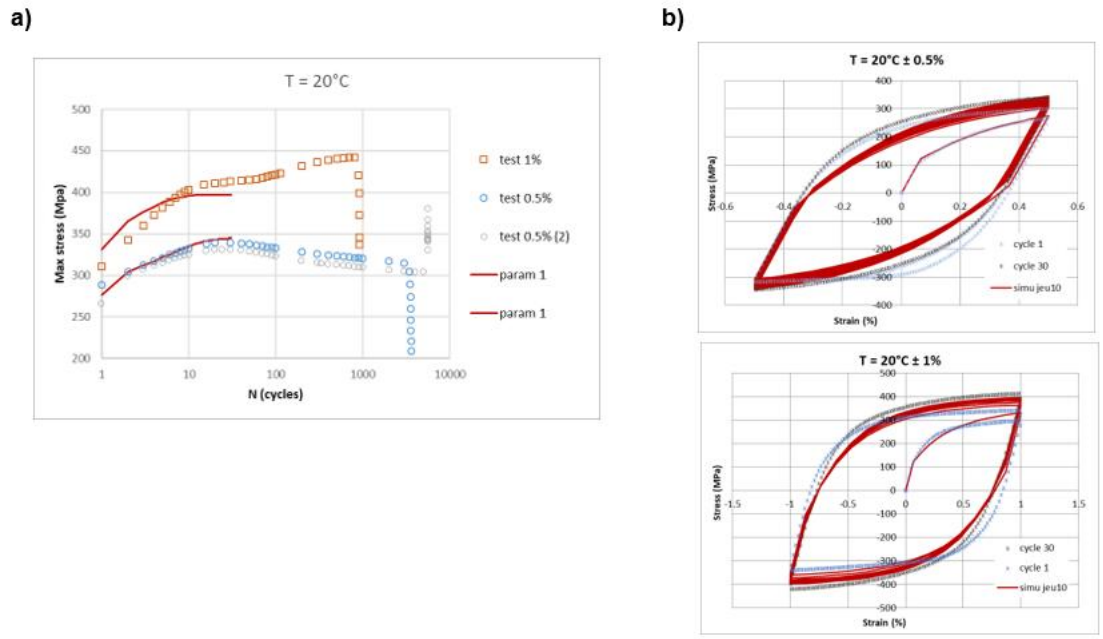

Figure 7.44. Chaboche model at 20 °C – parameter set 1 (stress hardening up to max stress).

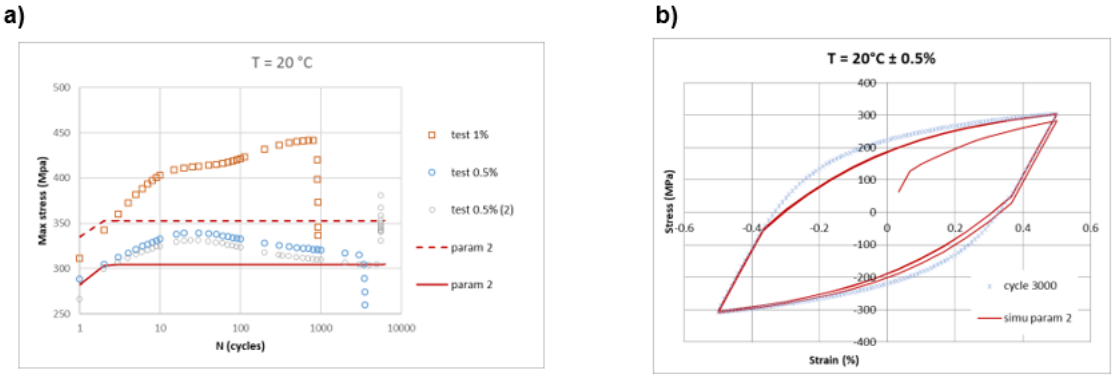

Figure 7.45. Chaboche model at 20 °C – parameter set 2 (half-life).

a) Parameter set 1

E (Gpa)	nu			
190	0.3			
A1 (Pa) = C1 /	C1 = γ1		C1	γ1
8.77E+07	600		5.26E+10	600
A2 (Pa) = C2 /	C2 = γ2		C2	γ2
1.41E+08	202.99		2.87E+10	202.99
Psi	Omega			
1	0			
R0 (Pa)	RM (Pa)	b		
1.20E+08	1.75E+08	13		

b) Parameter set 2

E (Gpa)	nu	
190	0.3	
A1 (Pa) = C1 / γ1	C1 = γ1	
8.77E+07	600	
A2 (Pa) = C2 / γ2	C2 = γ2	
1.41E+08	202.99	
Psi	Omega	
1	0	
R0 (Pa)	RM (Pa)	b
1.30E+08	1.30E+08	1

Table 7.8. Chaboche parameter at 20 °C (a) set 1 and (b) set 2.

7.1.4.2 TESTS ON NOTCHED SPECIMENS

FE model:

Mesh: 2D axisymmetric conditions for all meshes, quadratic elements.

Material: Chaboche model calibrated at 300 °C, different parameter sets are then compared.

Test design:

Two specimen geometries are modelled to compare the results to Framatome simulations:

- FRF specimen: D = 9.0 mm, d = 7.0 mm, R = 0.5 mm and extensometer gage length = 12.0 mm.
- EDF specimen: D = 8.0 mm, d = 6.22 mm, R = 0.5 mm and extensometer gage length = 12.5 mm.

An optimisation algorithm is used to define the maximum load required to reach the strain level defined for the test: 0.6% or 0.3%. The strain level is calculated according to the equivalent von Mises strain at the notch tip location.

These design simulations are performed using either Chaboche model parameter set 1 or 2 calibrated at 300 °C. A minimum of 3 cycles is simulated in order to reach the stabilisation of the stress before extracting the extensometer value at the notch tip.

Comparisons to Framatome simulations are rough, as we do not have any numerical results from Framatome, only the graphs shown on the following figures (see Figure 7.46 to Figure 7.48).

Comparison to Framatome simulation on FRF specimens:

FRF specimen is loaded up to an equivalent von Mises strain level of ±0.6%, with the material parameter set 1 (calibrated at max stress).

- Good agreement on the predicted maximum load level and corresponding extensometer value. The equivalent maximum von Mises strain fields are similar. The strain evolution from the notch tip and through the specimen thickness (along the yellow axis) is similar on both simulations whereas the strain level along the specimen axis (along the black axis) is higher on the CEA simulation. On should be noted that different mesh refinements have been compared and the strain evolution remains the same on CEA simulations.

The same FRF specimen is then loaded up an equivalent von Mises strain level of ±0.3%, with the same material parameter set 1.

- The agreement is good on the predicted maximum load levels. The corresponding extensometer value is higher on CEA simulations.

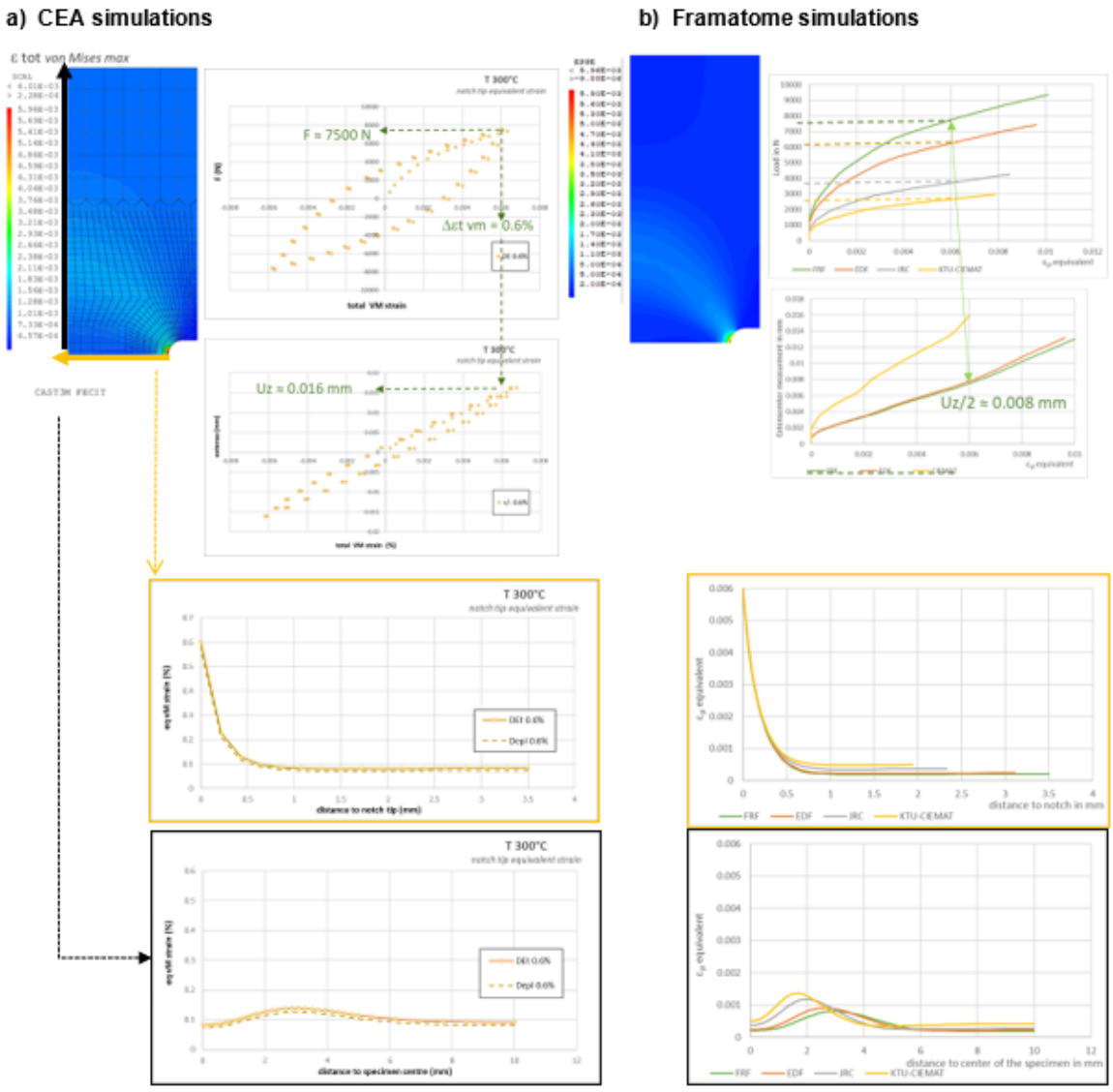

Figure 7.46. Chaboche parameter set 1 (max stress) at 300 °C – Specimen FRF D = 9.0 mm, R = 0.5 mm – max equivalent von Mises strain = 0.6%.

Comparison to Framatome simulation on EDF specimens:

EDF specimen is loaded up to an equivalent von Mises strain level of ±0.6%, with the material parameter set 1 (calibrated at max stress).

- Good agreement on the predicted maximum load.

Concluding remark about the comparison: on lower loading levels (lower strain level) the difference between CEA and Framatome extensometer values is higher.

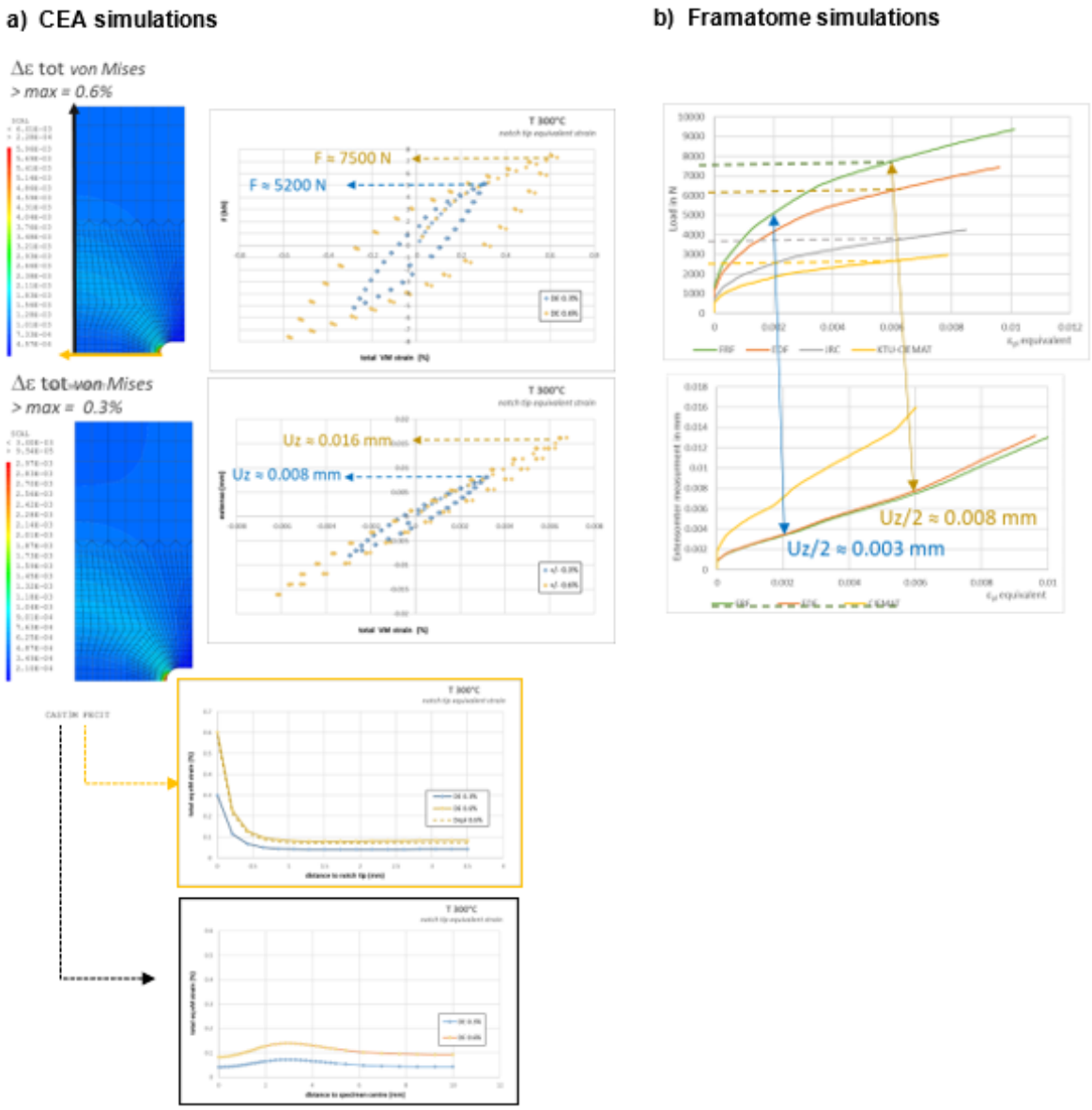

Figure 7.47. Chaboche parameter set 1 (max stress) at 300 °C – Specimen FRF D = 9.0 mm, R = 0.5 mm – max equivalent von Mises strain = 0.6% and 0.3%.

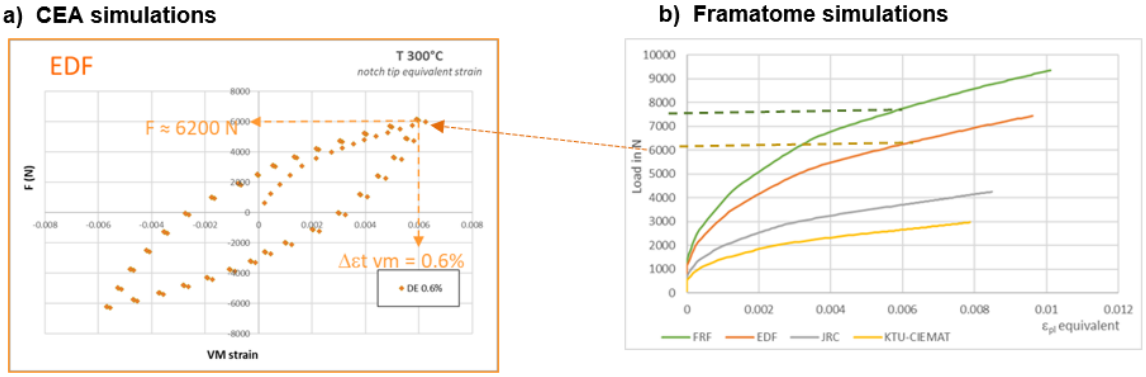

Figure 7.48. Chaboche parameter set 1 (max stress) at 300 °C – Specimen EDF D = 8.0 mm, R = 0.5 mm – max equivalent von Mises strain = 0.6%.

Effect of the material parameters:

On FRF specimen, we intend to compare the effect of parameter set 1 (calibrated at max stress) and set 2 (calibrated at half-life) on the predicted load and the extensometer value, for both strain levels ±0.3% and ±0.6% (see Figure 7.49).

- Large predicted load variation (for the same strain level) due to the Chaboche parameter set used. It is though important to recalibrate the model on the first experimental tests.

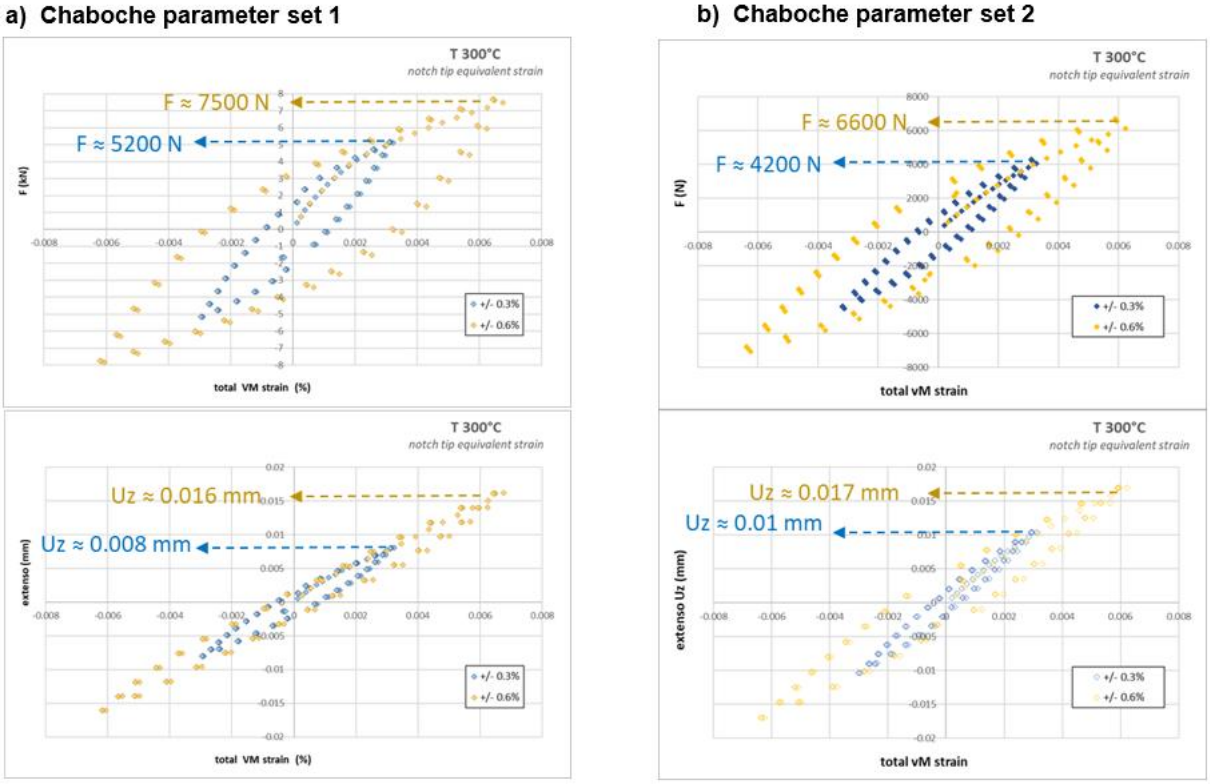

Figure 7.49. Chaboche parameter set 1 (max stress) and set 2 (half-life) at 300 °C. Specimen FRF D = 9.0 mm, R = 0.5 mm – max equivalent von Mises strain = 0.6% and 0.3%.

Test analysis:

The three tests of Table 7.9 have been simulated using either Chaboche model parameter set 1 or set 2 calibrated at 300 °C. The specimen is loaded up and down to a constant load amplitude (corresponding to the experimental one). A minimum of 3 cycles are simulated to reach the stabilised stress state.

Lab	Type of test	Step	Number of cycle for the step	D (mm)	d (mm)	Notch radius r (mm)	Targeted strain at the notch root ε (%)	R	F (N)	Waveform	Frequency (Hz)	Temperature (°C)	Extensometer gage length (mm)	Extensometer amplitude measurement (mm)	FEA calculations (Framatome)	Difference experimental/FEA (%)
FRF	Constant amplitude test	-	-	9	7,00	2	0,6	-1	8908	Triangular	1	300	12	0,0240	0,0257	6,5
EDF	Stepped test	1	10455	8	6,22	2	0,2	-1	4737	Triangular	1	300	12,5	0,0080	0,0095	15,7
		2	2146	8	6,22	2	0,4	-1	6108	Triangular	1	300	12,5	0,0126	0,0171	26,5
		3	Until failure	8	6,22	2	0,6	-1	7147	Triangular	1	300	12,5	0,0238	0,0272	12,4
KTU	Stepped test	1	10455	5	3,89	0,5	0,2	-1	1521	Triangular	1	300	10	0,0054	0,0051	-6,1
		2	1610	5	3,89	0,5	0,4	-1	2107	Triangular	1	300	10	0,0100	0,0089	-12,4
		3	Until failure	5	3,89	0,5	0,6	-1	2447	Triangular	1	300	10	0,0168	0,0125	-34,2

Table 7.9. Tests on notched specimens.

Test FRFAIR-11:

Simulation with parameter set 2 seems to better agree with the experiment (see Figure 7.50), but one should note that the experimental extensometer value has not been initialised properly, so we can only compare simulated and experimental extensometer amplitude. The simulated amplitude value is 0.0259 mm (with parameter set 2) whereas the experimental one is 0.0240 mm, which is close.

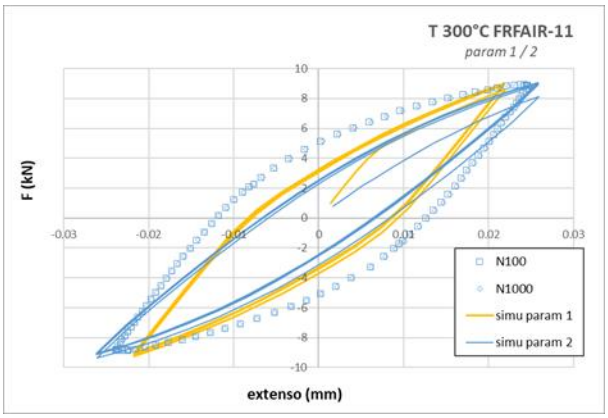

Figure 7.50. Test FRFAIR-11: specimen D = 9.0 mm, R = 2.0 mm – strain level = ±0.6%. Comparison of Chaboche parameter set 1 (max stress) and set 2 (half-life) at 300 °C.

Test EDFAIR-9:

On the lowest loading level (F = ±4737, N ≈ ±0.2%), the simulation with parameter set 1 seems to better agree with the experiment (see Figure 7.51), but only on the maximum extensometer value. In both simulations, the model does not account for the non-symmetrical behaviour.

The three loading levels are then simulated, including 5 cycles per loading level, and only with the parameter set 1 (see Figure 7.52). The maximum extensometer value is well predicted by the simulation for the first two loading levels (F = ±4737, N ≈ ±0.2% and F = ±6108, N ≈ ±0.4%). The simulated load-extensometer loops remain non-symmetrical and the model does not represent the high strain increase on the last loading level (F = ±7147, N ≈ ±0.6%).

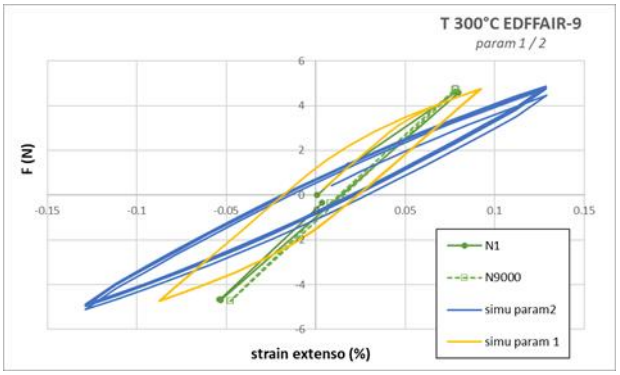

Figure 7.51. Test EDFAIR-9: specimen D = 8.0 mm, R = 2.0 mm – strain level = ±0.2%. Comparison of Chaboche parameter set 1 (max stress) and set 2 (half-life) at 300 °C.

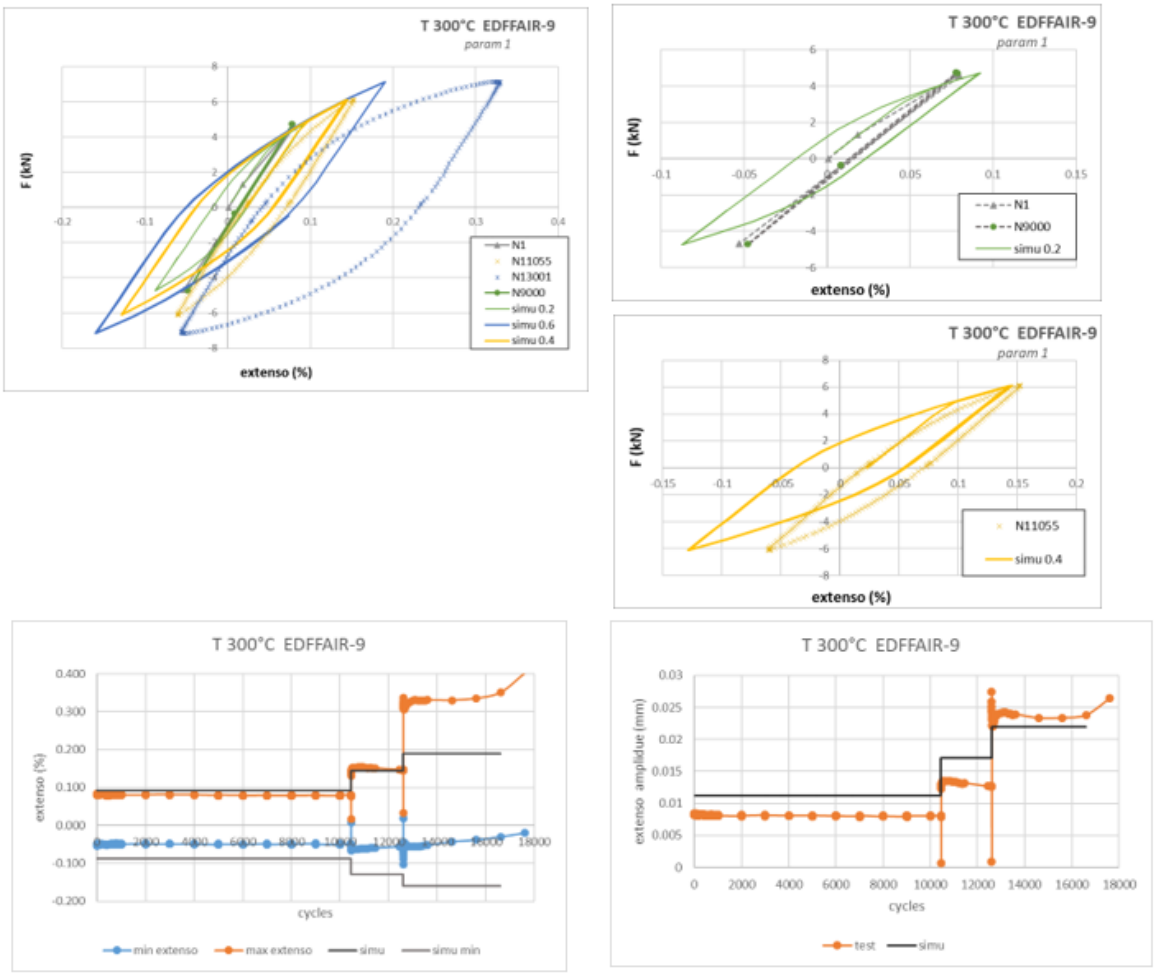

Figure 7.52. Test EDFAIR-9: specimen D = 8.0 mm, R = 2.0 mm – strain levels = ±0.2%, 0.4%, and 0.6%. Chaboche parameter set 1 (max stress) at 300 °C.

Test KTUAIR-13:

On the lowest loading level (F = ±1521, N ≈ ±0.2%), the simulation with parameter set 1 better agrees with the experiment than parameter set 2 and gives closest results on the whole cycle, unlike on EDFAIR-9 (see Figure 7.53).

Parameter set 3 is fine on extensometer maximum value: it remains constant during the 400 cycles that have been simulated. But it is less accurate than parameter set 1.

Nevertheless, when the three loading levels are simulated, with the parameter set 1, the results at the two higher loading levels are far away from the experimental extensometer values on this test (see Figure 7.54). Neither parameter set 3 reproduces the strain increase between different loading levels.

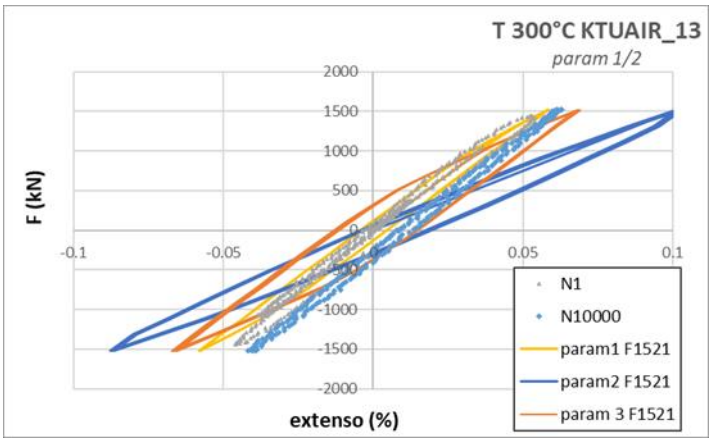

Figure 7.53. Test KTUAIR-13: specimen D = 5.0 mm, R = 0.5 mm – strain level = ±0.2%. Comparison of Chaboche parameter set 1 (max stress), set 2 (half-life), and set 3 (stress softening) at 300 °C.

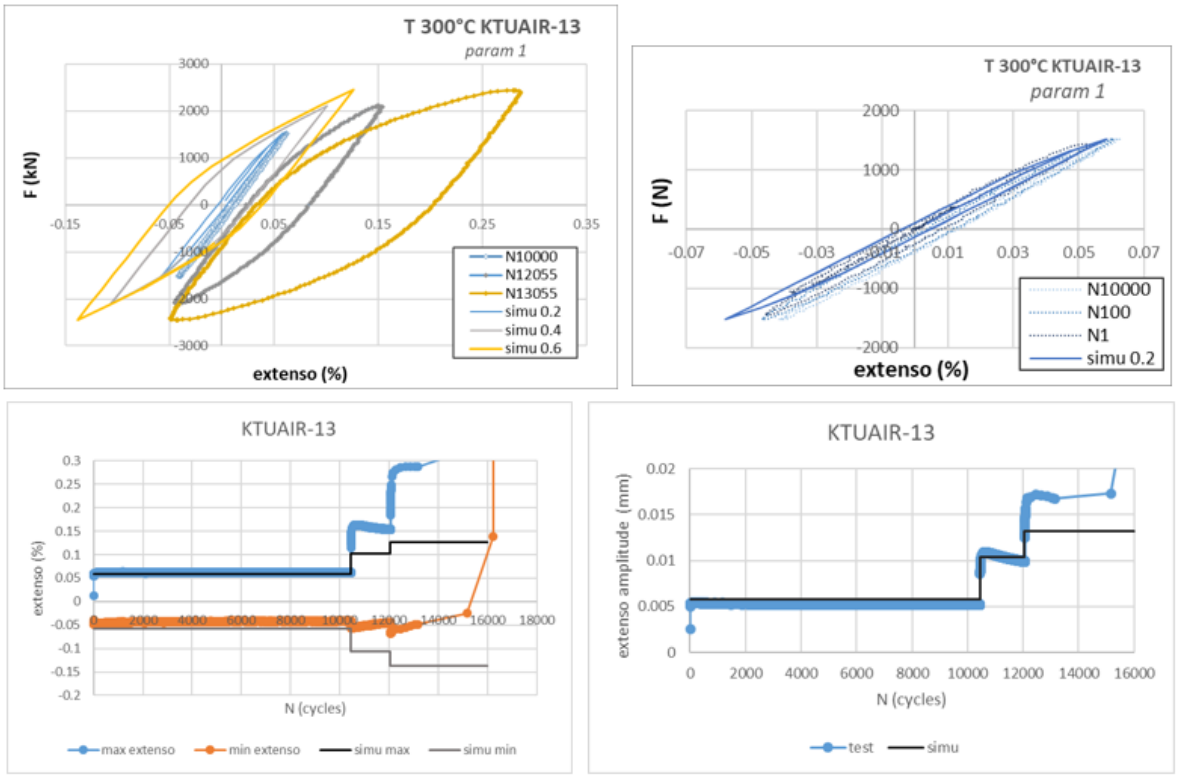

Figure 7.54. Test KTUAIR-13: specimen D = 5.0 mm, R = 0.5 mm – strain levels = ±0.2%, 0.4%, and 0.6%. Comparison of Chaboche parameter set 1 (max stress) at 300 °C.

<u>Conclusions on the 3 tests:</u>

Comparison of applied load and applied displacement (optimised value to fit the experimental load) simulations shows a slight difference on the extensometer value (see Table 7.10).

Parameter set 1 definitely gives the closest results to the experiments except on test FRFAIR-11, but this test should not be taken into account because of the experimental extensometer initialisation issue.

Lab	Step	F (N)	Extensometer amplitude measurement (mm)	Simulated Extensometer amplitude (mm)
FRF	-	8908	0,0240	0.0259
EDF	1	4737	0,0080	0.0112
	2	6108	0,0126	0.0171
	3	7147	0,0238	0.0220
KTU	1	1521	0,0054	0.0058
	2	2107	0,0100	0.0104
	3	2447	0,0168	0.0132

Table 7.10. Comparison of experimental end simulated extensometer amplitude values on notch specimens (tests EDF and KTU simulated with parameter set 1 and FRF with parameter set 2).

7.1.5 EDF MODELLING FOR NOTCHED SPECIMENS

Further analyses have been carried out to quantify the effect of the FEA strain/load calibration for notched specimens. First another elastic-plastic reduced cyclic curve has been considered to perform 1/4 cycle modelling for load definition (see Figure 7.55). Note that the initial one used for load definition by Framatome France, was more representative of the maximal hardening observed in the experimental data whereas the new curve considered in this paragraph, is closer to half-life experimental data.

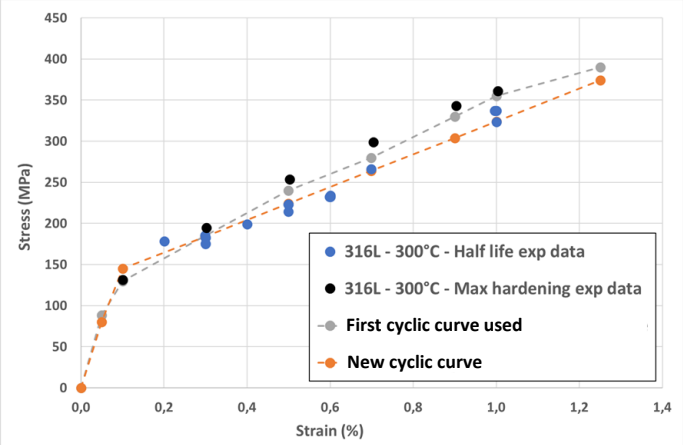

Figure 7.55. Elastic-plastic reduced cyclic curves considered for 1/4 cycle modelling.

The comparisons on the extensometer amplitudes, for several tests conditions and specimen geometries, showed the following results:

- Differences in the range [-16%; +8%] between the uses of the initial curve and of the new one.
- Differences in the range [-37%; +18%] between the use of the new curve and the experimental data, whereas the use of the initial one leaded to differences in the range [-26%; +36%].

Finally, no clear conclusion could be drawn about the most relevant cyclic curve to represent experimental data. Note that the latter also include some uncertainties that makes these comparisons difficult.

For the prediction of the maximal strain at the notch root, the differences between the uses of the initial curve and of the new one, were in the range [-14%; 0%], this indicating that the initial calibration might have underestimated the strain loading in the tests.

To go further, non-linear kinematic and isotropic hardening modelling has been also performed, but similar significant differences, in the range [-25%; +34%], between numerical results and experimental data were observed for extensometer amplitudes. The possible underestimation of the strain amplitude at the notch tip was also confirmed since the differences between the modelling results and the experimental targets were in the range [-18%; +5%].

Note that this non-linear kinematic and isotropic hardening modelling consisted in an optimization of the Chaboche model parameters identified by Zhang [7.5], for the considered strain amplitudes, lower than 1% (see Table 7.11 and Figure 7.56).

	Parameters	Zhang	Optimization
Elasticity	E [GPa]	160	160
	ν	0.3	0.3
Kinematic Hardening	C_1 [MPa]	170000	165245
	γ_1	1500	1985
	C_2 [MPa]	25000	20257
	γ_2	200	211
Isotropic Hardening	R_0 [MPa]	110	81
	b	10	4.5

Table 7.11. Optimization of the Chaboche model identified by Zhang [7.5].

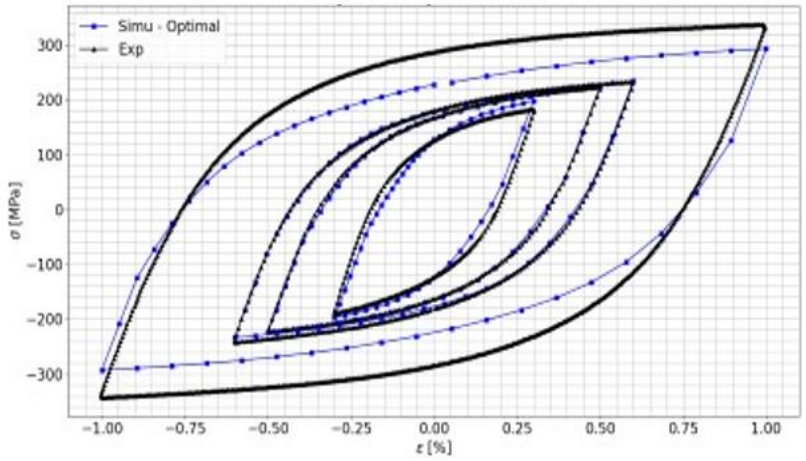

Figure 7.56. Stress-strain hysteris loops with the optimization.

7.1.6 CONCLUSIONS ON FATIGUE BEHAVIOUR MODELLING

The purpose of this Section was to describe the attempts carried out by various INCEFA-SCALE partners to model the cyclic behaviour of the 316L austenitic stainless steel used in the project. Different strategies are highlighted depending on the objectives of the analyses. Modelling is generally in agreement with experimental data, but certain difficulties are also mentioned, and further developments could be welcome.

7.2 FATIGUE DAMAGE AND CRACK GROWTH FINITE ELEMENT ANALYSIS ON SOLID SPECIMENS

7.2.1 KTU MODELLING OF FATIGUE DAMAGE

The objective was to propose a numerical simulation methodology, based on the finite element method, for fatigue damage and crack growth during low cycle fatigue behaviour of AISI 316L steel under various loading conditions and temperatures. The validation of the numerical determination methodology was carried out by comparing the crack growth values obtained by the simulation with the values determined experimentally.

7.2.1.1 THEORETICAL BACKGROUND OF THE FATIGUE DAMAGE MODELLING

Progressive damage and failure based on the continuum damage mechanics approach [7.6] can be applied for the modelling of fatigue damage. The damage initiation criterion is a phenomenological model used to predict the onset of damage due to stress reversals and the accumulation of inelastic strain in a low cycle fatigue analysis. It is characterised by the accumulated inelastic hysteresis energy per cycle, Δw_{sta}, in a material point when the structure response is stabilised in the cycle. In this case, the damage initiation is based on the accumulated inelastic strain energy density of the stabilised hysteresis loop for damage initiation using the following equation:

$$N_0 = c_1 \Delta w_{sta}{}^{c_2} \qquad \text{eq. 7.29}$$

where c_1 and c_2 are the damage initiation material parameters that can be determined from a dependence of N_0 on Δw_{sta} as shown in Figure 7.57.

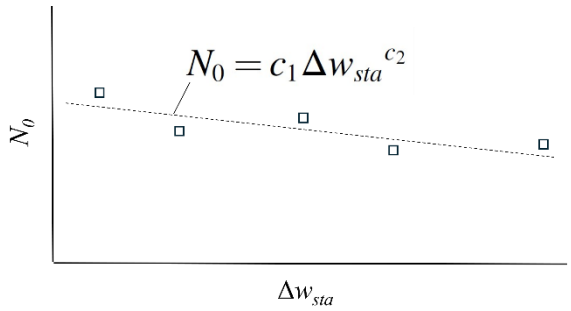

Figure 7.57. N_0 as function of Δw_{sta} (used for the determination of damage initiation parameters c_1 and c_2).

The number of cycled for damage initiation N_0 and damage evolution ΔN can be obtained from a cyclic stress curve (Figure 7.58). N_{sta} is the number of cycles to the stabilised state, N_i is the number of cycles for damage initiation, and N_f is the number of cycles to final failure.

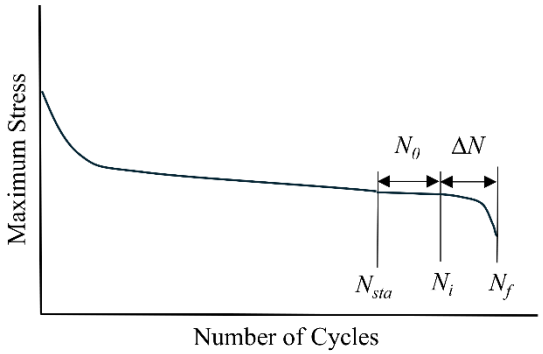

Figure 7.58. Maximum stress as function of the number of cycles (used for the determination of the number of cycles for damage initiation N_0 and damage evolution ΔN).

The damage evolution can be based on the average inelastic hysteresis strain energy density Δw_{avg}:

$$\frac{\Delta D}{\Delta N} = \frac{c_3 \cdot \Delta w_{avg}{}^{c_4}}{L} \qquad \text{eq. 7.30}$$

where L is the characteristic element length and c_3 and c_4 are damage evolution material parameters, respectively. These parameters can be calibrated from a plot shown in Figure 7.81.

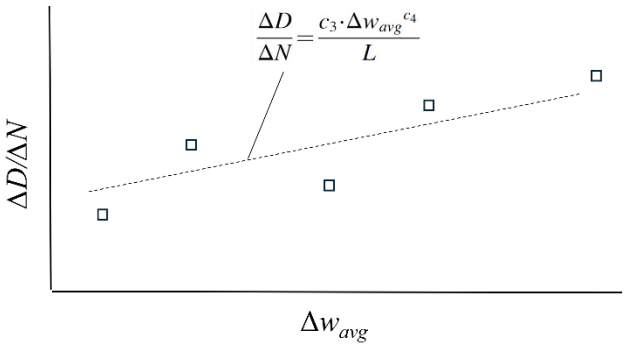

Figure 7.59. Dependence of ΔD/ΔN on Δw_{avg}.

For damage in ductile materials, the degradation of the elastic stiffness can be modelled using the scalar damage variable D. At any given loading cycle during the analysis, the stress tensor in the material is given by the scalar damage equation:

$$\sigma = (1 - D)\bar{\sigma} \qquad \text{eq. 7.31}$$

$\bar{\sigma}$ is the effective (or undamaged) stress tensor that would exist in the material in the absence of damage computed in the current increment.

7.2.1.2 FATIGUE DAMAGE MODELLING USING ABAQUS

Fatigue damage modelling investigations were carried out using a direct cyclic step in ABAQUS. This step is designed to predict the stabilised response of a structure subjected to cyclic loading, without having to simulate every cycle explicitly. A combined kinematic-isotropic material model was applied for the modelling. The material parameters defining the kinematic and isotropic components for a 0.18% strain amplitude cyclic load are provided in Section 7.1.1.3.1.

The damage constants were based on the literature with some adjustments to fit the experimental data better. The damage constants that were adopted in the modelling are provided in Table 7.12.

c_1	c_2	c_3	c_3
2153.5	-1.732	7.201e-5	0.391

Table 7.12. Damage constants.

Figure 7.60 shows a damaged specimen after 250000 cycles that was subjected to a symmetric cycling loading of a 0.18% strain amplitude.

This approach can be used to predict the life of components. However, this model was unable to capture the growth behaviour.

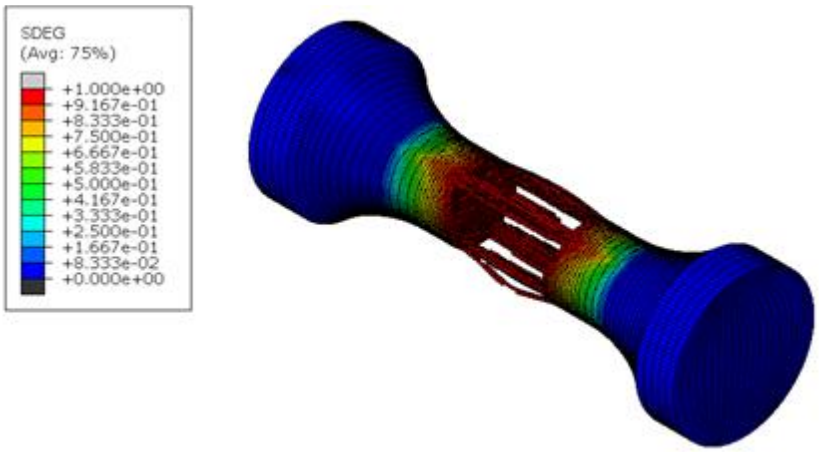

Figure 7.60. Damaged specimen.

7.2.1.3 CRACK PROPAGATION MODELLING APPROACH

The onset and fatigue crack growth are both characterized by means of Paris' law, which relates either the onset or the rate of growth of a fatigue crack to the relative fracture energy release rate (Figure 7.61).

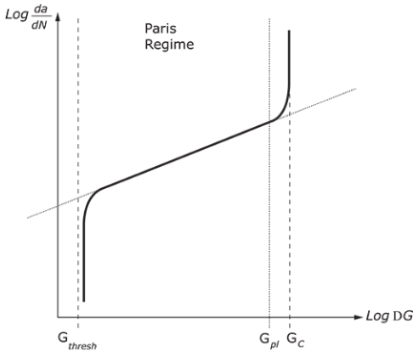

Figure 7.61. Mixed mode fatigue crack growth governed by Paris' law.

Paris' law can also be expressed in terms of the equivalent relative stress intensity factor:

$$\frac{da}{dN} = C(\Delta K_I)^n \qquad \text{eq. 7.32}$$

where:

$$\Delta K_{\mathrm{I}} = K_{\mathrm{I}}{}^{\max} - K_{\mathrm{I}}{}^{\min} \quad \text{eq. 7.33}$$

$$R = \frac{K_{\mathrm{I}}{}^{\max}}{K_{\mathrm{I}}{}^{\min}} \quad \text{eq. 7.34}$$

The n and C parameters for the modelling were selected on the basis of the fatigue crack growth data for austenitic stainless steel in an air environment as given in ASME Sect. XI, Article C-3000 and literature sources [7.7,7.8], and they were modified to better fit the experimental data obtained in the INCEFA-SCALE Project.

he ANSYS SMART Crack Growth feature and ABAQUS XFEM techniques were used to simulate crack propagation. These simulations were based on the linear-elastic fracture mechanics (LEFM) that assumes small deformations and minimal yielding at the crack tip.

ANSYS SMART Crack Growth automatically tracks crack propagation based on fracture mechanics principles. One of the key advantages of the SMART feature is adaptive remeshing. As the crack propagates, the mesh is automatically refined near the crack tip to capture the high stress and strain gradients associated with crack growth.

In the ABAQUS model, a 20x5 mm two-dimensional computational domain was considered. It was meshed using CPS4R type elements with a size of 0.05 mm in the region where the crack was expected (Figure 7.62).

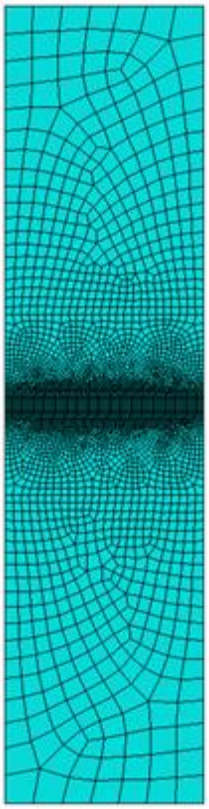

Figure 7.62. Mesh for crack propagation modelling in ABAQUS.

A 0.52 mm length wire body was used as an initial crack to define the ABAQUS XFEM crack enrichment feature, utilising the fatigue fracture criterion with a power law to describe the mixed-mode crack growth behaviour. The following parameters of Paris' law were adopted for the definition of the fatigue fracture criterion along with 60 kJ/m^2 for critical energy release rate for mode I (opening mode) fracture: C = 3.01·10^{-19} m/(Pa·m$^{1/2}$)^n and n = 3.3. The model was implemented through a direct cycle step. The nodes of the lower edge of the plate were restrained along the 1st and 2nd directions, and the upper edge was subjected to a symmetric cyclic tension-compression displacement corresponding to a strain amplitude of 0.18%.

Figure 7.63 shows a contour plot of the signed distance function (PHILSM) visualising crack propagation that was obtained using ABAQUS.

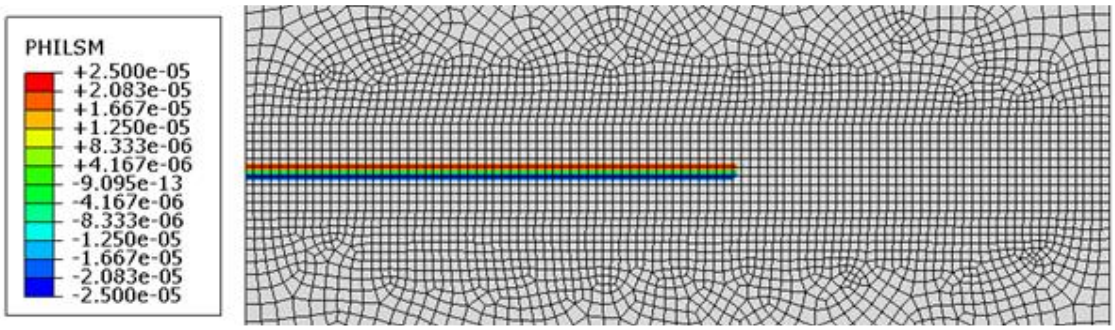

Figure 7.63. Crack propagation after 214470 cycles in the ABAQUS model.

Figure 7.64 demonstrates the crack depth on cycle curve obtained using ABAQUS that is compared with the experimental data. The model was able to capture the nature of crack propagation. The model data were in a good agreement at cycles near 200000 and above. However, the model tended to predict too rapid crack growth compared to the experimental data at lower cycles. Therefore, it still needs to be refined including additional calibrations of material parameters from more experimental data to determine correct ratios between the constants for fatigue crack growth and energy release rates of AISI 316L steel.

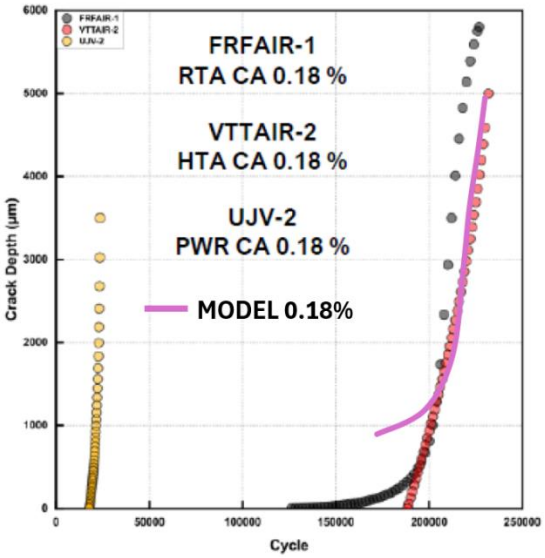

Figure 7.64. Crack depth vs. cycle curve obtained using ABAQUS compared with the experimental data.

Crack propagation modelled using the SMART Crack Growth feature is shown in Figure 7.65.

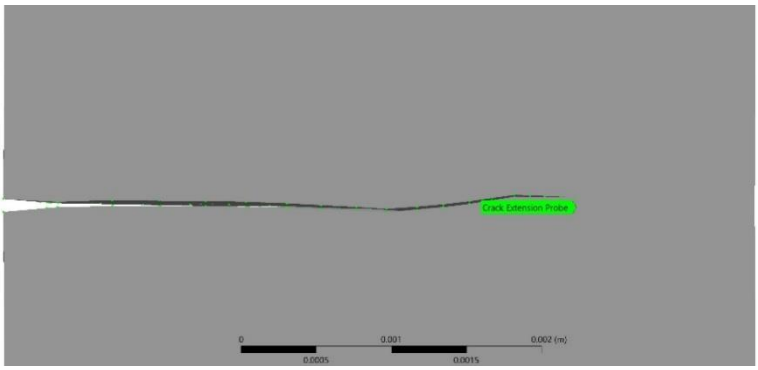

Figure 7.65. Crack propagation obtained using the SMART Crack Growth feature.

The model implemented ANSYS SMART Crack Growth feature showed a good agreement with the experimental data at a 0.18% strain amplitude at room temperature (Figure 7.66).

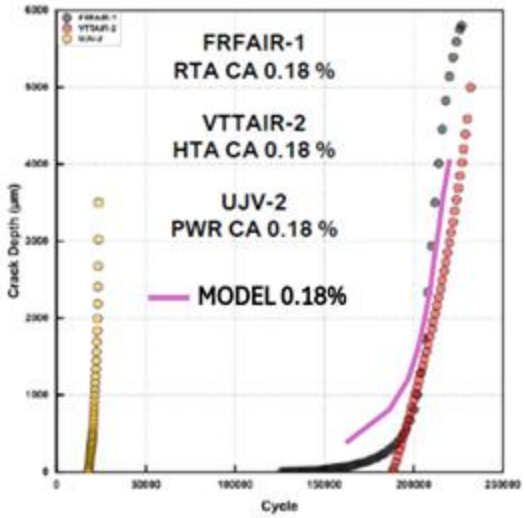

Figure 7.66. Crack depth vs. cycle curve obtained using ANSYS SMART Crack Growth compared with the experimental data.

7.2.1.4 CONCLUSIONS

Various approaches based on finite element methods for modelling damage and crack propagation were tested. The model utilising progressive damage and failure based on continuum damage mechanics can be used to predict the life of structures. However, this model is unable to capture the crack growth behaviour. To model crack propagation, computational models that utilise the ANSYS SMART Crack Growth feature and ABAQUS XFEM techniques were developed. The models were able to capture the nature of crack propagation. However, the models still need to be refined including additional calibrations of material parameters from more experimental data.

7.2.2 SIMULATION OF THE CRACK PROPAGATION USING THE CZM APPROACH

Numerical simulation of the crack propagation under low cycle fatigue loading was performed using Distributed sparse matrix direct solver of ANSYS software and contact debonding technique.

The simulation was performed for displacement controlled symmetric cyclic load ±0.18% of nominal strain and ±0.3% of nominal strain.

The modelled geometry was adopted from 5 mm diameter cylindrical test specimen. The FEM, including geometry, loads, boundary conditions, element types, etc., is described in the sections below.

LCF test results of 316L stainless steel at room temperature under strain controlled ±0.18% amplitude loading was used as a main source for the adjustment of material properties in modeling.

7.2.2.1 MATERIAL MODEL

Material model was adjusted to experimental data that were obtained from experiment test of strain controlled symmetric cyclic loading of cylindrical 5 mm diameter specimen. The load was ±0.18% for the strain gauge length 12.5 mm. The stress – plastic strain data of 300000 load cycle were fitted by power law equation and a result of such fitting was eq. 7.44 (Figure 7.67). This load cycle was chosen because exhibits a stabilised behaviour of material: no cyclic hardening or softening.

$$\varepsilon_{pl} = 497.32\sigma^{0.1279} \qquad \text{eq. 7.35}$$

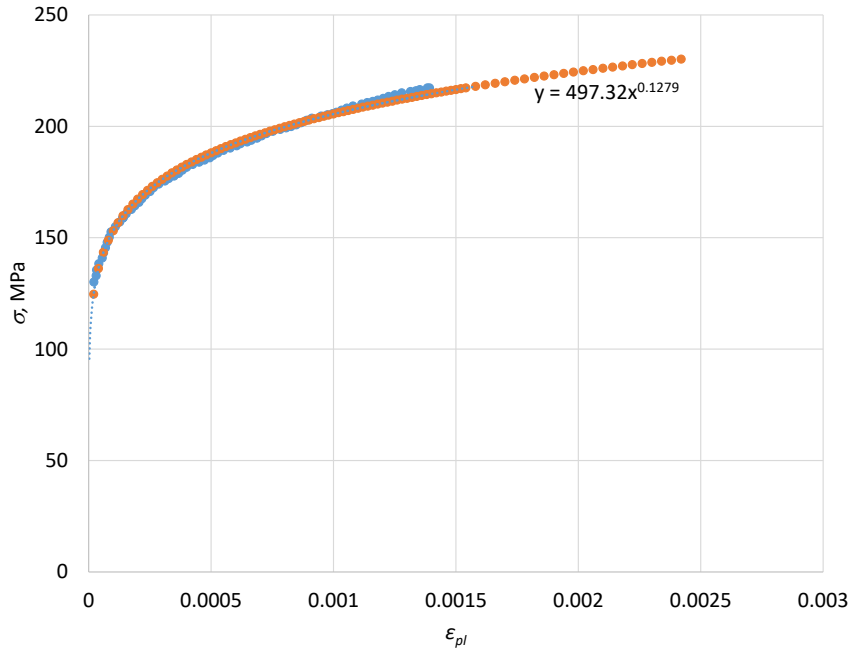

Figure 7.67. Stress - plastic strain curve for material kinematic hardening model.

To validate the material model, a FE simulation of a stress – strain hysteresis loop was performed and compared to experimental results. Kinematic hardening law of material was used and axisymmetric formulation of FEM employed (Figure 7.68).

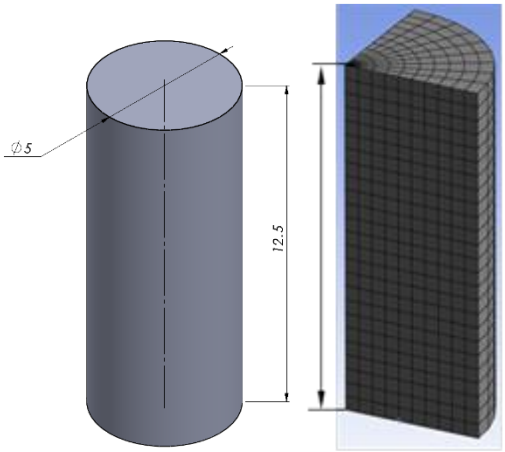

Figure 7.68. Geometry used for material model validation and FE mesh presenting 1/4 of the 2D section and 2D axisymmetric mesh – 3D segment expansion is shown for visualization purpose only.

The results are shown in Figure 7.69. The simulated stress-strain loop fits the experimental data. A little difference is observed only in a peak stress under compression. The finite element simulation shows -203 MPa under -0.18% strain; the experimental data give -225 MPa under -0.179% strain. The difference in peak compression stress is about 11%. All other simulation data are matching the experimental results with the better accuracy (Figure 7.69). Therefore, the material model is considered acceptable for the further simulations of a crack propagation.

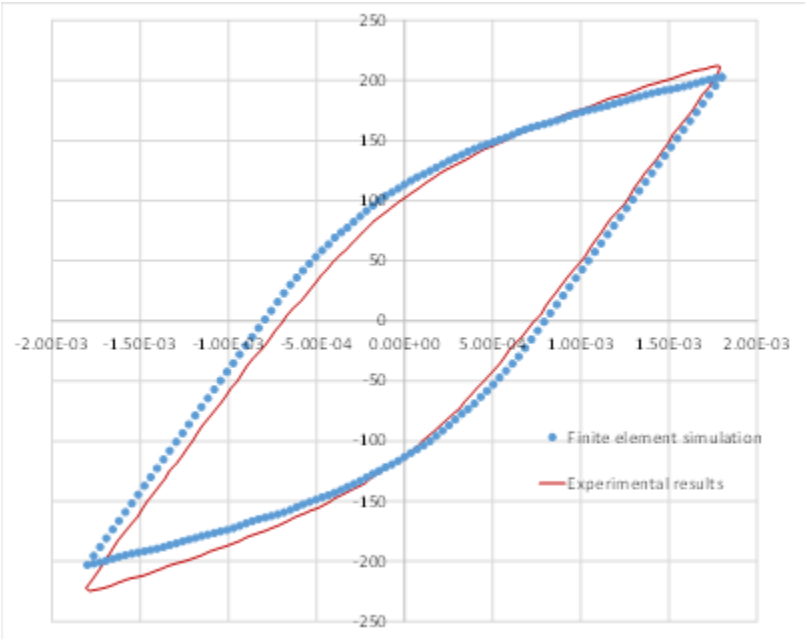

Figure 7.69. Stress-strain hysteresis loop of cyclic stabile material behaviour before crack appearance (cycle number 300000).

7.2.2.2 COHESIVE ZONE MODEL

For simulation of the crack propagation the Cohesive Zone Modelling (CZM) approach was used [7.9]. ANSYS software allows two options for this purpose: interface elements and contact elements. For interface elements, the interfacial separation is defined as the displacement jump, δ (that is, the difference of the displacements of the adjacent interface surfaces). Delamination with contact elements is referred to as debonding. The interfacial separation is defined in terms

of contact gap or penetration and tangential slip distance. In this project, the contact debonding technique was applied where normal separation between contacting surfaces is dominating. Bilinear behaviour of the debonding was used as illustrated in Figure 7.70.

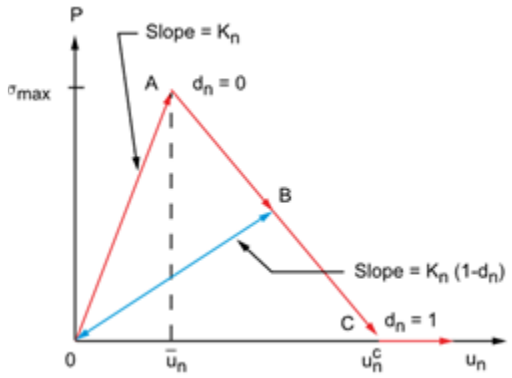

Figure 7.70. Normal contact stress and contact gap curve for bilinear cohesive zone material [7.9].

Normal contact stress:

$$\sigma = K_n u_n (1 - d_n) \quad \text{eq. 7.36}$$

$$d_n = \left(\frac{u_n - \bar{u}_n}{u_n}\right) \times \left(\frac{u_n^c}{u_n^c - \bar{u}_n}\right) if \frac{u_n}{\bar{u}_n} > 1 \; and \; d_n = 0, if \; \frac{u_n}{\bar{u}_n} \leq 1 \quad \text{eq. 7.37}$$

Here, σ is the normal contact stress (tension), K_n the normal contact stiffness, u_n the contact gap, $\bar{u}_n$ the contact gap at the maximum normal contact stress (tension), u_n^c the contact gap at the completion of debonding.

After testing various cohesive contact zone parameters, the following parameters were used for CZM:

- Maximum normal contact stress of separation σ_{max} = 500 MPa;
- contact gap at the completion of debonding u_n^c = 0.00424 mm (critical fracture energy for normal separation G = 1.06 mJ/mm^2);
- normal contact stiffness value was 10^8 N/mm^3.

7.2.2.3 FINITE ELEMENT MODEL

Several models and finite element meshing were tested to build a final model for the parametric investigation of crack propagation.

Initially applied 3D model (Figure 7.71) with imposed semi-circular symmetric crack required excessive computational resources due to element mesh size required at the cohesive zone. Because of that, the model was simplified to 2D. Two variations of 2D plane strain models were used at the final stage of CZM analysis: (a) with the initial crack and cohesive zone going through the entire remaining cross-section (Figure 7.72); and (b) initial defined size of crack and cohesive zone of defined size (Figure 7.73). Due to economy of computational time, the CZM mesh shown in Figure 7.73 was used to investigate the initial crack size influence to the crack propagation and other parametric analysis. The refined zone size was 2x2.5 mm, the element size in this zone was 0.01 mm. The higher order 2D plane strain ANSYS finite elements of square shape were used.

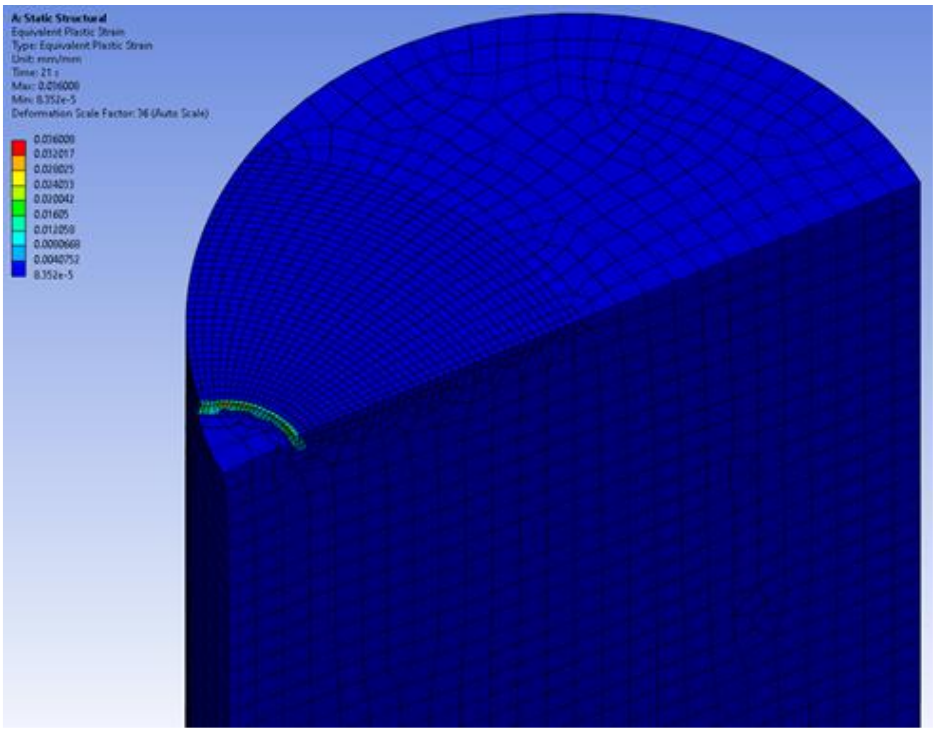

Figure 7.71. 3D finite element model with plastic strain indication at the crack tip.

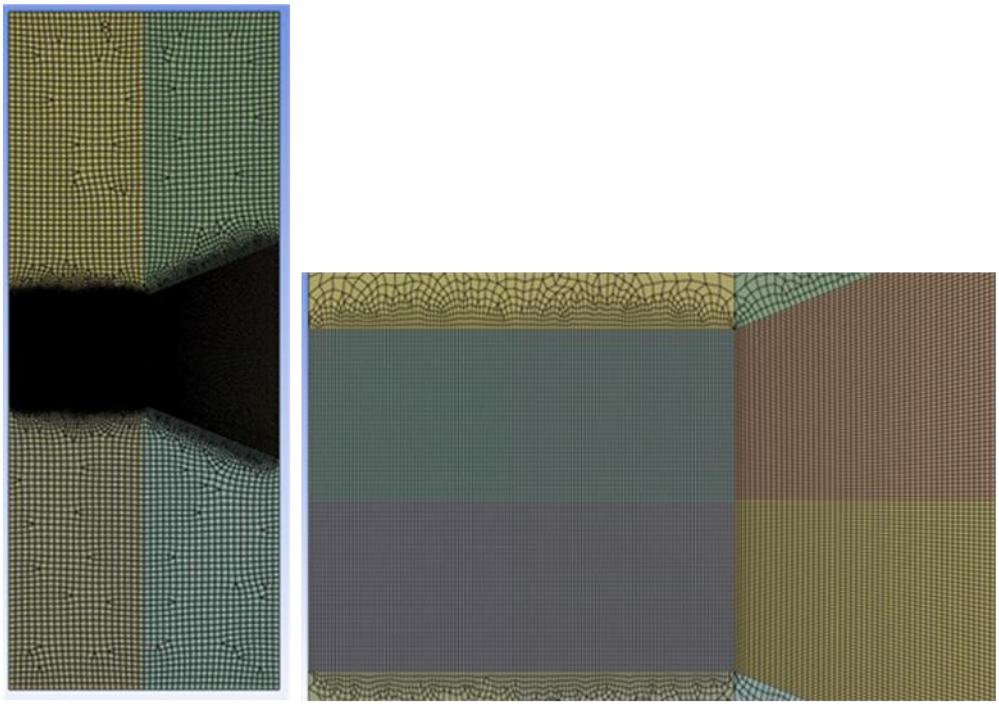

Figure 7.72. 2D plane strain FE mesh with refined cohesive zone through the entire cross-section of the model.

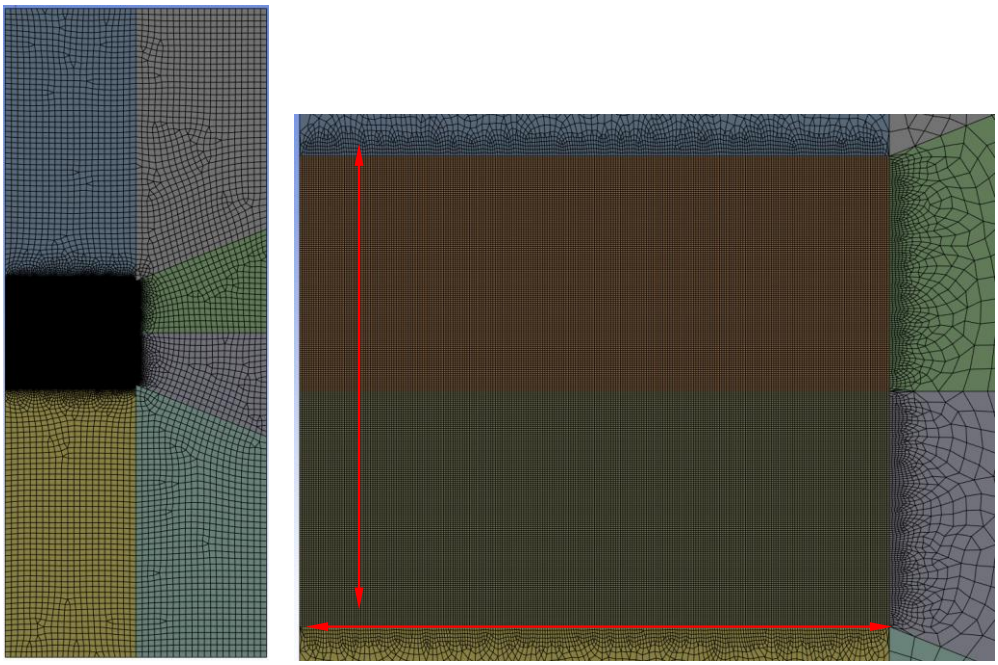

Figure 7.73. 2D plane strain FE mesh with limited cohesive zone size.

7.2.2.4 SIMULATION CONDITIONS

Displacement controlled cyclic load was imposed (Figure 7.74):

1. ±0.0225 mm (±0.18% nominal strain), and;
2. ±0.0375 mm (±0.3% nominal strain).

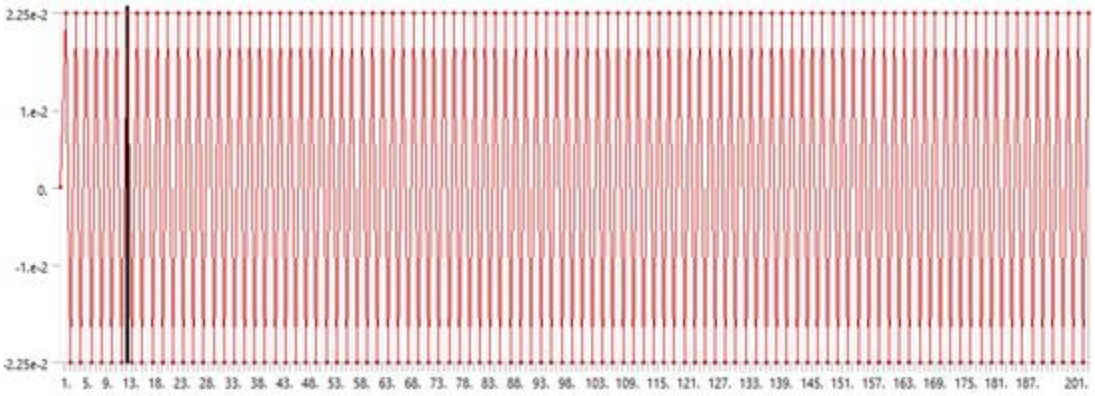

Figure 7.74. Displacement controlled cyclic load.

The displacements were applied to the upper edge of the model in vertical direction (y). The displacements of the bottom edge were restricted from motion in the y direction (see Figure 7.75).

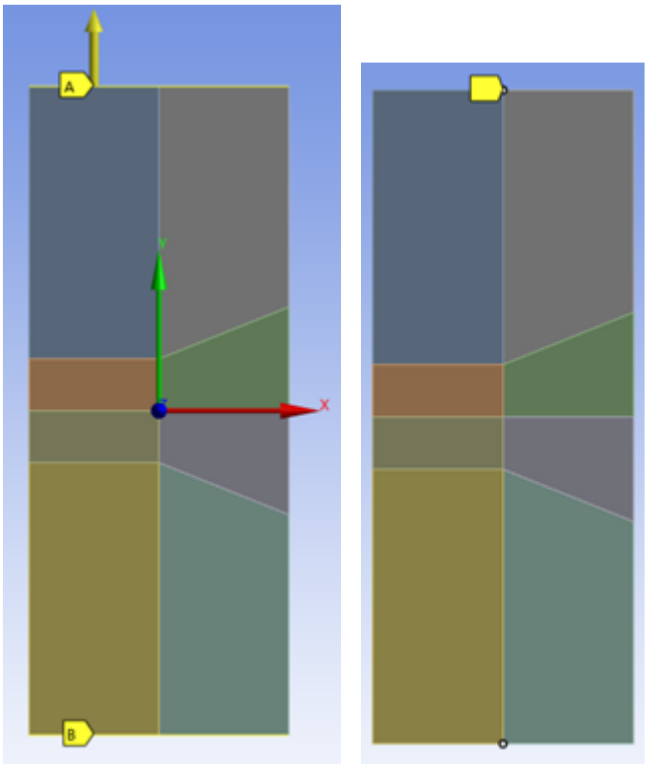

(a) (b)

Figure 7.75. Applied fixtures and load: (a) applied displacements u_y on edge A and fixed displacements $u_y = 0$ on edge B; (b) fixed displacements $u_x = 0$ of central points of these edges.

7.2.2.5 RESULTS

Parametric study of crack propagation was performed for cases of different initial crack length (0.1 mm, 0.2 mm, and 0.3 mm). The size of the cohesion contact was 0.55 mm in all cases. This limitation of the cohesion zone was applied for the computational efficiency.

Under load of ±0.0225 mm (±0.18% nominal strain) the crack propagation was not achieved over 201 load steps (100 load cycles); the initial crack was 0.1 mm and 0.2 mm. Only at an initial crack size of 0.3 mm the propagation was achieved as shown in Figure 7.76 (blue line). Under load of ±0.0375 mm (±0.3% nominal strain) and initial crack size 0.3 mm, the crack propagation was very rapid starting from the first load cycle and the crack propagated through the cohesion zone in a 15 load steps (7 cycles). Figure 7.76 shows crack propagation in a range from 0.0 to 0.4 mm.

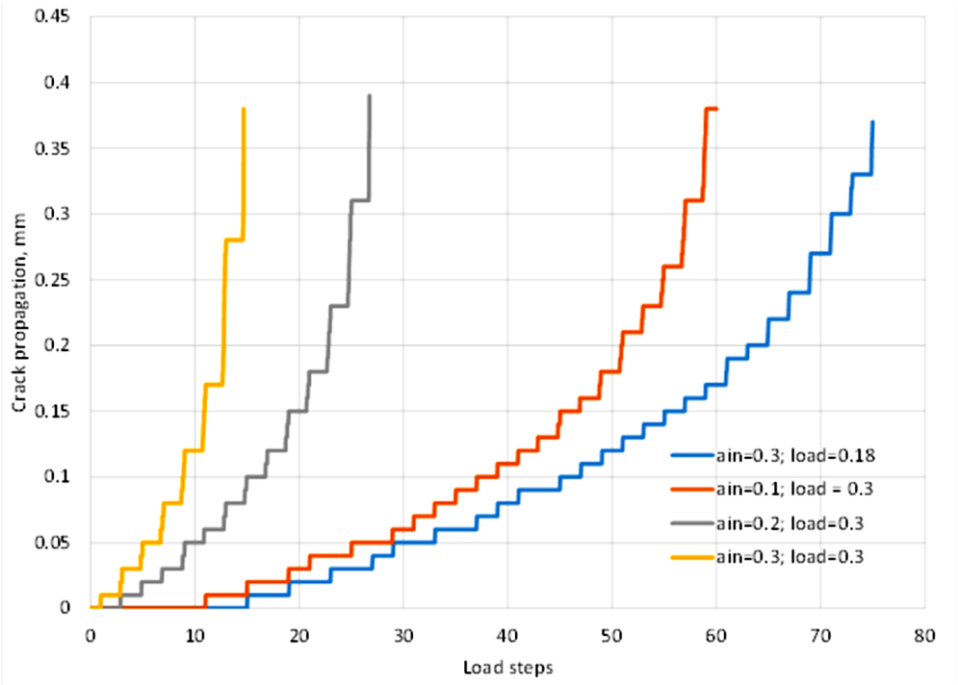

Figure 7.76. Crack propagation for cases of initial crack (a_{in}) 0.1, 0.2, and 0.3 mm under load of ±0.0375 mm imposed displacement and 0.3 mm initial crack length under load of ±0.0225 mm applied displacement.

Figure 7.77.a shows von Mises plastic strain after the firs load step, with the total crack length was 0.3 mm and load was +0.18% nominal normal strain. Figure 7.77.b presents the von Mises plastic strain after 71 load steps (35 cycles). There, the total crack length is 0.6 mm. The crack propagated 0.3 mm over 35 cycles.

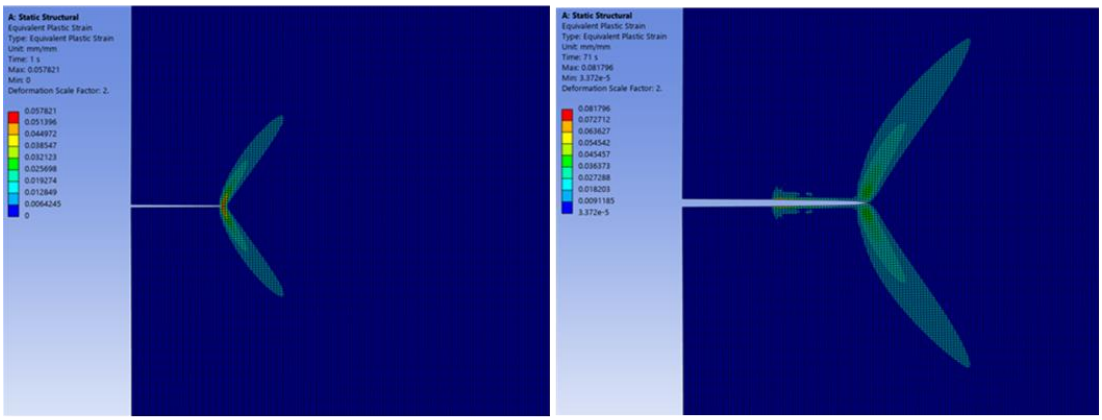

Figure 7.77. (a) Von Mises plastic strain after: a load step 1 of initial tension and (b) load step 71, after 35 cycles.

7.2.2.6 CONCLUSIONS

A finite element model was developed that allows to perform qualitative analysis investigating of influence of various parameters to the crack propagation (number of cycles, amplitude of imposed cyclic load, size of the initial crack).

The material properties used in the model were validated by comparing the cyclic stress-strain hysteresis loop calculated by model with shown by experiment under strain controlled symmetric cyclic loading ±0.18% of the nominal normal strain. The cyclic stress-strain data showed a good coincidence.

The CZM model of crack propagation was not validated and can be used only for the qualitative analysis. Due to long computational time, only 2D plane strain finite element model was used (instead of 3D model). Because of that, results of this model may have had some deviation from the experiment. There was also a lack of experimental data of the crack propagation when 5 mm diameter specimen was used.

The improvement of the CZM model may be achieved by collecting more experimental data on the crack propagation and also on material behaviour under cyclic load. Customization of the CZM modelling technique that is provided by commercial ANSYS software may also be needed to achieve better agreement with experimental data.

7.3 PERIDYNAMICS THEORY

The fatigue process can be described by using the atomistic approach based kinetic theory of fracture (KTF), which includes the process temperature, maximum and minimum stress, and the loading frequency in its differential fatigue damage equation. The kinetic theory of fracture and peridynamics (KTF-PD) theory and application is explained in manuscript [7.10]. Standard 316L stainless steel specimens are tested, and then the KTF-PD fatigue simulation is run in this study.

7.3.1 METHODOLOGY USING THE KINETIC THEORY OF FRACTURE AND PERIDYNAMICS

Peridynamics (PD) is alternative theory to classical continuum mechanics (CCM) due to its integral formulation. PD equations of motion do not contain spatial derivatives in contrast to the CCM equations, which are formulated by using partial displacement derivatives. Because of this, the PD is very attractive and have advantages against conventional finite element formulations when modelling discontinuous problems, such as crack growth; nevertheless, the PD theory can also be applied for continuous displacement fields. PD theory assumes that each material point x interacts with another material points (such as x') through PD bonds in predefined interaction range, called PD horizon H_x (Figure 7.78). PD horizon H_x in most 3D models is a sphere which radius is about three PD grid spacings Δx, e.g., $\delta \approx 3\Delta x$ (Figure 7.78). The PD grid spacing Δx is the same in the whole computational model as it is opposed to FE mesh refinements at stress concentrations.

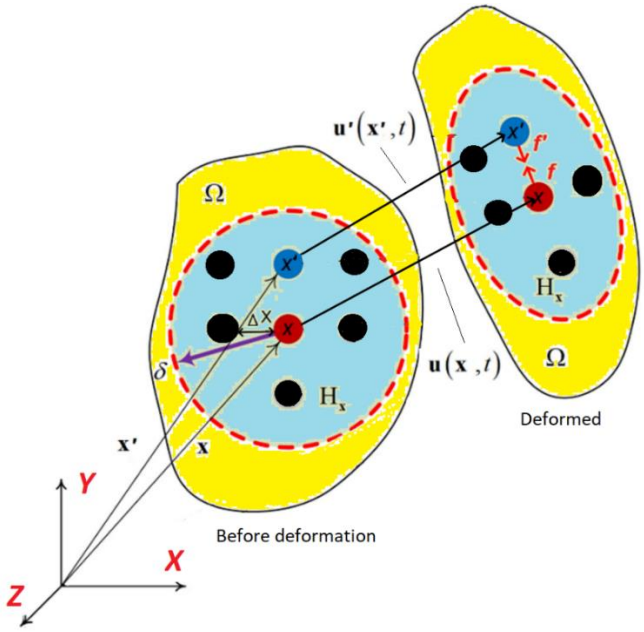

Figure 7.78. Schematics of the simplest PD case (bond-based).

This leads to following equation of motion which describes the simplest case of the PD theory (bond based, BBPD) [7.11].

$$\rho\ddot{u}(x,t) = \int_{H_x} f(u'(x,t) - u(x,t), x' - x, x)\, dV_x + b(x,t) \qquad \text{eq. 7.38}$$

where x, u and x', u' are vectors defining points x and x' positions and displacements (Figure 7.78), b(x, t) – body force vector, f – the PD bond force vector, ρ is the density of the material and V_x –material point x volume. The aforementioned PD formulation (eq. 7.38 and Figure 7.78) results that body Poisson's ratio is equal only to 0.25 for 3D model. In order to improve modelling accuracy when material Poisson's ratio is not equal to 0.25, for example, composite material, modelling plastic deformations in metals, ordinary and non-ordinary state based PD theories were created (OSBPD and NSBPD) [7.12]. Volumetric PD horizon dilatation term in state-based PD enables to circumvent fixed material Poisson's ratio problem. Nevertheless, SBPD computational time is significantly longer than BBPD, also SBPD complexity makes the model implantation in commercial software not possible because there is still no existing equivalent finite elements [7.13]. In contrast, BBPD can be implement both ways by using in-house computational code or into existing finite element software. For example, Zhang et. al. [7.14] present fatigue analysis using BBPD code in ANSYS by using existing ANSYS finite elements. Based on simplicity, computational time and implantation possibilities, the BBPD fatigue model implemented in MATLAB is used in this project. The BBPD code can also be further modified and successfully used in commercial finite element packages, such as ANSYS, LS-Dyna.

The PD horizon is still macro scale size; thus, the PD theory is not molecular or atomistic approach. Nevertheless, PD formulation results PD horizon size dependent material quantities, namely PD bond force f and PD bond stretch s which are not equal to CCM quantities, e.g., PD bond stretch is not equal to body strain. PD Bond, connecting points x and x', experience stretch which is equal to:

$$s_{xx\prime} = \frac{(|x' - x + u' - u| - |x' - x|)}{|x' - x|} \quad \text{eq. 7.39}$$

Each PD bond has its stiffness which depends on material elastic modulus E, Poisson's ratio (for SBPD only) and PD horizon size δ. Or the case of 3D BBPD model further used in this project, PD bond stiffness can be found by following equation:

$$c = \frac{12E}{\pi\delta^4} \quad \text{eq. 7.40}$$

Once PD bond is deformed and experience stretch, the PD bond force (f) value for BBPD can be found proportional to stretch value, as f = cs. For SBPD bond forces are calculated by using more complex equations [7.12]. Material plasticity can be evaluated by changing the PD bond stiffness c value after the stretch of the PD bond equivalent to proportional or yield limit deformation is reached.

Integral based peridynamic differential operator (PDDO) is used to compute strains and stresses at the PD point x [7.15,7.16]:

$$F_x = \left[\int_{H_x} \omega(x' - x)((x' - x + u' - u)\otimes(x' - x))dV_{x'-x}\right] \cdot \left(\int_{H_x} \omega(x' - x)((x' - x)\otimes(x' - x))dV_{x'-x}\right)^{-1} \quad \text{eq. 7.41}$$

Each PD horizon H_x point x' has not the same effect to the PD point x strain; thus, bond length depended inflection function ω(x' - x) is necessary [7.17,7.18]. For 3D PD models it is accurate enough to assume that the PD bond x' - x length has linear effect to the PD point x strain.

When the PD bond stretch exceeds critical stretch value (s_c), static failure of that bond is considered. Critical stretch of material is horizon size δ dependent variable and can be derived from material fracture toughness and elastic characteristics (shear μ = E/(2(1 + ν)) and bulk κ= E/(3(1 - 2ν)) modulus of material) as it was described by Madenci and Oterkus [7.11]:

$$s_c = \begin{cases} \sqrt{\dfrac{G_C}{\left(3\mu + \left(\frac{3}{4}\right)^4\left(\kappa - \frac{5}{3}\mu\right)\right)\delta}}, & \text{3D} \\ \sqrt{\dfrac{G_C}{\left(\frac{6}{\pi}\mu + \frac{16}{9\pi^2}(\kappa - 2\mu)\right)\delta}}, & \text{2D} \end{cases} \quad \text{eq. 7.42}$$

Cyclic loading PD simulation consists of set of static cycle simulations, but cyclic PD bond failure criteria must be included. It is possible to reduce critical stretch s_c value when number of cycles is increasing [7.19], but such approach cannot be applied for fatigue crack initiation process. Silling and Askari [7.20] proposed PD bond "remaining life" concept, when additional each PD bond variable, which depends on that bond loading and number cycles is used. At the start of the PD simulation, PD bond remaining life q(x, x' - x, 0) = 1 and cyclic PD bond failure is considered after N number cycles when q(x, x' - x, N) ≤ 0. Thus, each PD bond both static and cyclic failure is evaluated in scalar valued function μ(x' - x):

$$\mu(\boldsymbol{x}' - \boldsymbol{x}) = \begin{cases} 1, \text{if } s_{x'x} < s_c \ \& \ q_{x'x} > 0 \\ 0, \text{if } s_{x'x} \geq s_c \mid q_{x'x} \leq 0 \end{cases} \quad \text{eq. 7.43}$$

when PD bond failure is considered for bonds which μ = 0. Then failed PD bonds has no effect to the rest PD model, because function μ is included in PD bond forces calculation.

$$f = \mu cs \frac{x' - x + u' - u}{|x' - x + u' - u|} \quad \text{eq. 7.44}$$

The PD damage term at PD point x is expressed as a ratio of failed PD bonds to total PD bonds in the point x horizon H_x:

$$\varphi_x = \frac{\text{number of failed PD bonds at } H_x}{\text{total number of PD bonds at } H_x} \quad \text{eq. 7.45}$$

7.3.2 KINETIC THEORY OF FRACTURE

Damage, caused by cyclic loading, is measured by variable n (n = 0 no damage, n = 1 full damage) which is calculated from the process differential equation:

$$\frac{dn}{dt} = (n_0 - n)^{\lambda} K_b \quad \text{eq. 7.46}$$

where n_0 is the initial constant, λ the shape parameter (λ = 9 suggested and used in studies [7.14,7.21]), and K_b the fatigue crack formation and growth rate parameter, derived from durability equation [7.22]:

$$\tau = \tau_0 e^{-\frac{U - \gamma\sigma}{kT}} \quad \text{eq. 7.47}$$

Here τ is the failure time, τ_0 = 10-13 s, atoms oscillation period in solid body. Although PD model is not atom scale model, eq. 7.47 still can be adopted for macro scale PD model. Then parameter K_b becomes PD bond breakage rate parameter and can be calculated from Planks law:

$$K_{bxx\prime} = \frac{kT}{h} e^{-\frac{U - \gamma\sigma_{xx\prime}}{kT}} \quad \text{eq. 7.48}$$

where h and k are the Plank and Boltzmann constants, T the process temperature, U and γ the process activation energy and the activation volume (U and γ can be calibrated from material S-N curve), and $\sigma_{xx'}$ the PD bond stress (average PD point's x and x' stress $\sigma_{xx'} = (\sigma_x + \sigma_{x'})/2$).

If maximum PD bond stress occurs at the time t and minimum at the time t_1 and stress ratio R: $\sigma_{min} = R\sigma_{max}$, loading frequency f: $\Delta t = N/f'$, after the integration of eq. 7.47 it is possible to derive PD-KTF fatigue damage equation for each PD bond x' – x [7.14]:

$$n_{xx'}(N, \sigma_{\max}, R, T, f) = n_{0xx'} - \left\{ (n_{0xx'} - n_{Ixx'})^{1-\lambda} - (1 - \lambda) \frac{(kT)^2}{h} \frac{N}{\gamma f \sigma_{\max\_xx\prime}(1-R)} e^{-\frac{U}{kT}} \left[e^{\frac{\gamma\sigma_{\max\_xx\prime}}{kT}} - e^{\frac{\gamma R\sigma_{\max\_xx\prime}}{kT}} \right] \right\}^{\frac{1}{1-\lambda}}; \text{if } \lambda \neq 1 \quad \text{eq. 7.49}$$

where $n_{Ixx'}$ is the initial cyclic damage of the PD bond x' – x (if N = 1, $n_{Ixx'} = 0$). Initial constant n_0 is calculated from process initial and end conditions [7.23] and if λ = 9, then n_0 = 1.771. Finally, the PD bond "remaining life" can be calculated from fatigue damage by following equation:

$$q_{xx'} = 1 - n_{xx'} \qquad \text{eq. 7.50}$$

KTF eq. 7.49 better describes fatigue damage process including temperature, stress ratio, stress value, loading frequency variables than only empirical coefficient based Paris' law [7.24] approach.

It is possible to notice that once calibrated for symmetric cyclic loading at room temperature (RT), KTF fatigue damage eq. 7.49 results incorrect fatigue life when R → 1 as it is shown Figure 7.79.

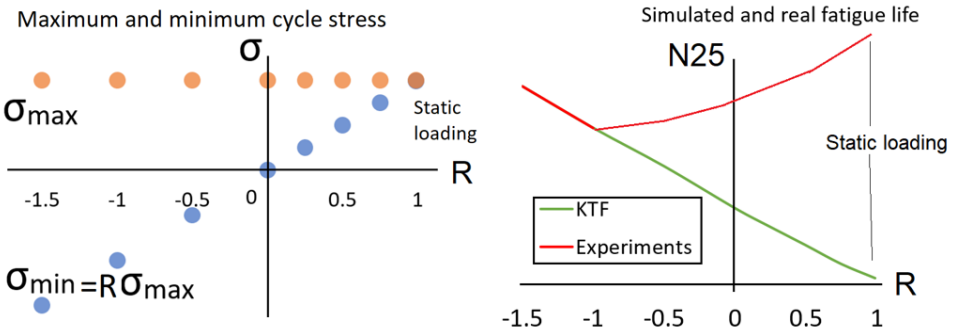

Figure 7.79. Schematics of the simplest PD case (bond-based).

Modified version of eq. 7.49 is used by Fertig et. al. [7.16, 7.17] for polymer composite. Process temperature T = T* + $\psi\sigma_a^2/\Delta t$ is sum of initial temperature T* and temperature increment $\psi\sigma_a^2/\Delta t$ caused by cyclic energy losses proportional to cycle stress amplitude square. Similarly, as for composite, in this project the term kT in eq. 7.49 for 316L steel is modified as kT + ψA, where A is cycle hysteresis loop area, and ψ the proportional constant. To evaluate the testing environment temperature, additional term αΔT is included, where α is the temperature proportional constant, ΔT the temperature increment when the base temperature is room temperature. Finally, extended eq. 7.49 results the following equation:

$$\begin{aligned} & n_{xx'}(N, \sigma_{\max}, R, T, f) \\ & = n_{0xx'} \\ & - \Bigg\{ (n_{0xx'} - n_{Ixx'})^{1-\lambda} \\ & - (1 - 11\lambda) \frac{(kT\alpha\Delta T + \psi A)^2}{h} \frac{N}{\gamma f \sigma_{\max'_{xx}} \ (1-R)} e^{-\frac{U}{kT\alpha\Delta T + \psi A}} \left[e^{\frac{\gamma \sigma_{\max'_{xx}}}{kT\alpha\Delta T + \psi A}} \right. \\ & \left. - e^{\frac{\gamma R \sigma_{\max'_{xx}}}{kT\alpha\Delta T + \psi A}} \right] \Bigg\}^{\frac{1}{1-\lambda}} \ ; \text{ if } \lambda \neq 1 \end{aligned} \qquad \text{eq. 7.51}$$

7.3.3 PD-KTH MODEL NUMERICAL IMPLEMENTATION ASPECTS

Numerical spatial and time integrations are applied to solve the PD equation of motion eq. 7.38 in PD numerical models. Because number of PD points is finite, body discretization results divided PD points at the PD horizon boundaries (Figure 7.80.a) and not full PD horizons at the body boundaries (Figure 7.80.b).

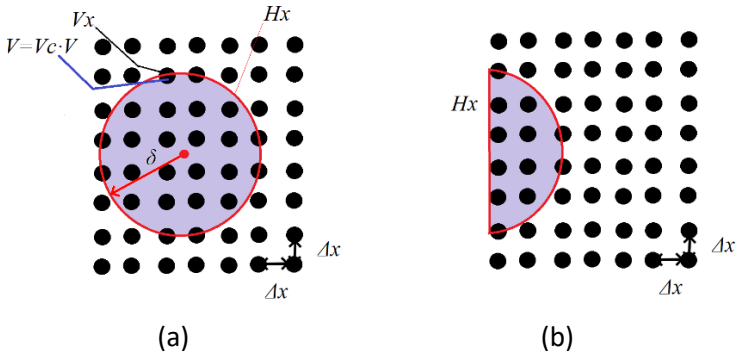

Figure 7.80. Numerical PD theory implementation issues: (a) not full PD points at the PD Horizon boundaries; (b) not full PD horizon at the boundaries of the body.

PD point volume correction can be applied by multiplying PD points in the PD horizon by coefficients which define their volumetric part in the PD horizon. Surface correction can be done similar way by stiffening the rest of the PD bonds in truncated PD horizon, also alternative methods detailly described in [7.11] exist. It is important to pay attention that PD surface effect cannot be completely vanished, only it can be reduced up to 90%. For the case of fatigue simulation, remaining PD surface effect is advantage, because body stiffness at the boundaries is reduced and then fatigue crack initiates at the surface of the body as natural phenomena.

Explicit and implicit time integration algorithms can be used to integrate discrete form of the PD equation of motion [7.27]. Explicit integration is simpler, although stability must be ensured by selecting proper time step calculated according to the PD model discretization and material parameters [7.11]. PD equation of motion is dynamic equation, thus for static (quasi-static) solution, fixed material damping has to included.

Cyclic loading numerical model is actually set of static analysis at maximum positive loading. Once cyclic failure of any PD bond is achieved N cycles, static simulation with removed failed PD bonds is repeated and number of cycles incremented till another PD bond failure. Fatigue crack initiation and growth phases should be included in the PD simulation. Material S-N curve is used to calibrate process activation energy U and activation volume γ, then U and γ (eq. 7.50, [7.23]) are used to define the fatigue crack initiation phase treating it as a local cyclic failure of the material. U and γ can be calibrated only for a specific stress range, thus several stress intervals and respective U and γ values are used for simulation as it is shown in Figure 7.81.a. PD point damage of $\phi_x = 0.5$ is sufficient to determine the end of fatigue crack initiation phase and start of the fatigue crack growth phase. Fatigue crack growth phase is faster process (in cycles) than the initiation phase, thus crack growth speed is increased by updating process activation energy and volume as $U = k_U \cdot U$ and $\gamma = k_\gamma \cdot \gamma$. Coefficients k_U and k_γ (Figure 7.81.b) can be found by comparing experimental and simulation crack growth plots: crack length vs. number of cycles. Fatigue simulation end criteria is the same as for experiment end criteria, for this project 25% reduction of maximum stress is used to consider the final failure.

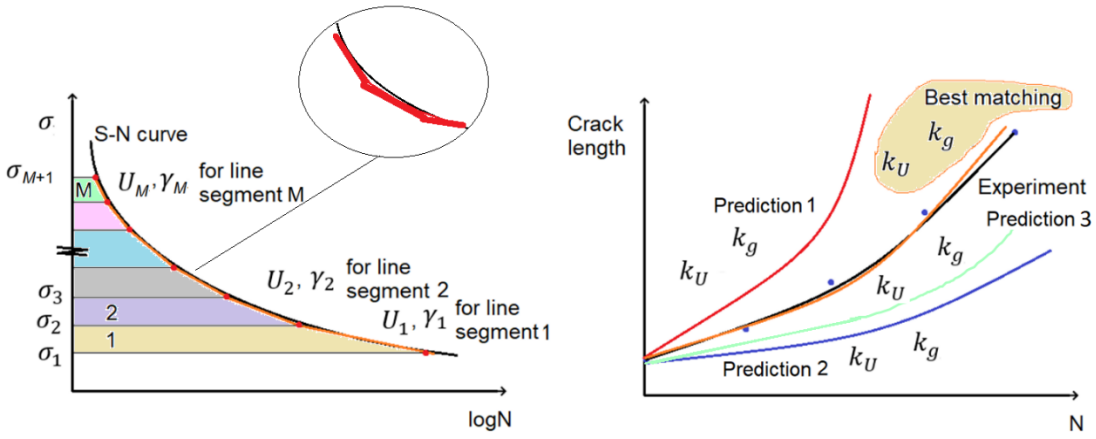

(a) (b)

Figure 7.81. PD-KTF fatigue model parameters definition: (a) activation energy U and activation volume γ calibration from S-N curve; (b) coefficients k_U and k_γ selection from experimental crack length vs. number of cycles curve.

Summarizing the previously mentioned PD-KTF fatigue model description, general scheme (based on studies [7.14,7.21]) consists of the following steps:

1. Static PD simulation to achieve maximum cycle stress;
2. Strain tensor of PD each point calculation;
3. Stress tensor of PD each point calculation;
4. Equivalent stress of PD each point calculation;
5. PD bond stress calculation: $\sigma_{xx'} = (\sigma_x + \sigma_{x'})/2$;
6. PD damage calculation. If $\phi x \leq 0.5$ – fatigue crack initiation, otherwise it is fatigue crack growth. Update U and γ as $k_U \cdot U$ and $k_\gamma \cdot \gamma$ if necessary (if fatigue crack growth phase).
7. Number of cycles N to maximum loaded PD bond failure calculation. Fatigue damage parameter n of each PD bonds calculation by using this N value. Number of cycles is incremented by N and PD bonds with $n \geq 1$ are removed.
8. Process repeats from step 1 to step 7 till final failure of the model is achieved.

Peridynamics theory and applied kinetic theory of fracture with process hysteresis loop corrections are explained in manuscript [7.10].

7.3.4 CRACK PROPAGATION MODELLING APPROACH USING PERIDYNAMICS

KTF implemented into PD model is used to simulate both crack initiation and crack growth phases in single model. Model for crack initiation phase was calibrated from material S-N curve for symmetric cyclic loading and applied modelling any type of cyclic loading, e.g., POL and PUL. KTF equation modified with cyclic loading process energy corrections (eq. 7.52, the same as in the manuscript [7.10]), is used. For comparison, conventional KTF equation is given as eq. 7.53 below.

$$n_{xx'}(N,\sigma_{\max},R,T,f) = n_{0xx'} - \left\{(n_{0xx'} - n_{Ixx'})^{1-\lambda} - (1-\lambda)\frac{(kT\alpha\Delta T+\psi A)^2}{h}\frac{N}{\gamma f \sigma_{\max\_xx'}(1-R)} e^{-\frac{U}{kT\alpha\Delta T+\psi A}}\left[e^{\frac{\gamma\sigma_{\max\_xx'}}{kT\alpha\Delta T+\psi A}} - e^{\frac{\gamma R\sigma_{\max\_xx'}}{kT\alpha\Delta T+\psi A}}\right]\right\}^{\frac{1}{1-\lambda}}; \text{ if } \lambda \neq 1 \quad \text{eq. 7.52}$$

$$n_{xx'}(N,\sigma_{\max},R,T,f) = n_{0xx'} - \left\{(n_{0xx'} - n_{Ixx'})^{1-\lambda} - (1-\lambda)\frac{(kT)^2}{h}\frac{N}{\gamma f \sigma_{\max\_xx'}(1-R)} e^{-\frac{U}{kT}}\left[e^{\frac{\gamma\sigma_{\max\_xx'}}{kT}} - e^{\frac{\gamma R\sigma_{\max\_xx'}}{kT}}\right]\right\}^{\frac{1}{1-\lambda}}; \text{if } \lambda \neq 1 \quad \text{eq. 7.53}$$

Because it was not possible to select such model parameters – activation energy U and activation volume γ, ensuring agreement to experimental results at any stress, S-N curve of material was divided into 3 stress ranges and model parameters were selected for each stress range as it is shown in Figure 7.82. Stress ranges were selected as: 1) 210/250 MPa; 2) 250/290 MPa; 3) 290/330 MPa. Hysteresis loop areas with proportional constant ψ = 50 of middle of each stress range were included into the KTF equations when selecting model parameters.

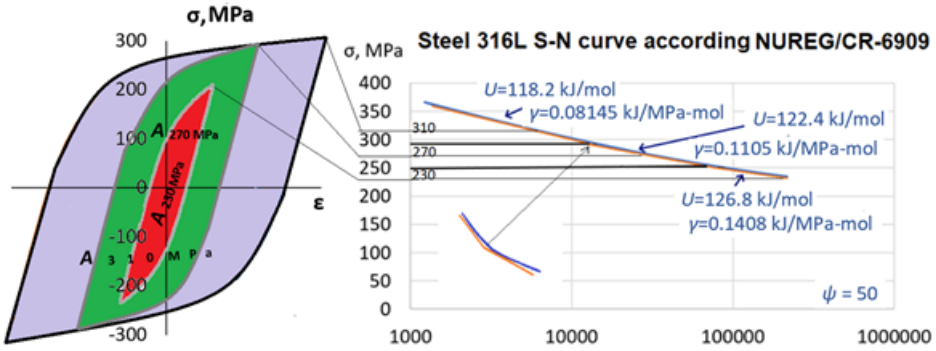

Figure 7.82. PD-KTF model calibration from S-N curve at three stress ranges.

When modelling PUL and POL loadings, hysteresis loops areas of such type loadings (areas were measured during experimental testing) are included into KTF equation. POL and PUL loading areas difference compared to symmetric cyclic loading is shown in Figure 7.83. Proportional constant ψ = 50 was established by manual selection comparing model and experimental results for different type cyclic loading.

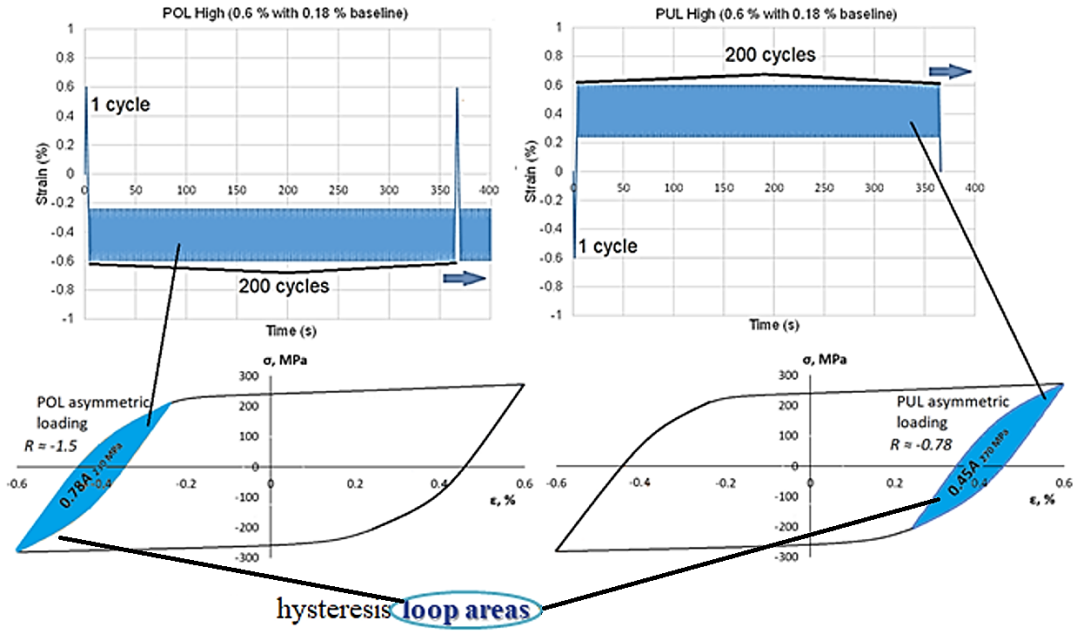

(a) (b)

Figure 7.83. Measured process hysteresis loop areas: (a) asymmetric POL loading; (b) asymmetric PUL loading.

Once fatigue crack in the model is initiated, the next phase is fatigue crack growth, which is faster than fatigue crack initiation. In order to simulate fatigue crack growth phase ensuring the same fatigue crack growth speed as in experiment, model parameters – activation energy U and activation volume γ, are updated as $k_U \cdot U$ and $k_\gamma \cdot \gamma$. Coefficients k_U and k_γ are selected comparing max stress vs. linear cycle experimental and simulated plots as it is shown in Figure 7.84.

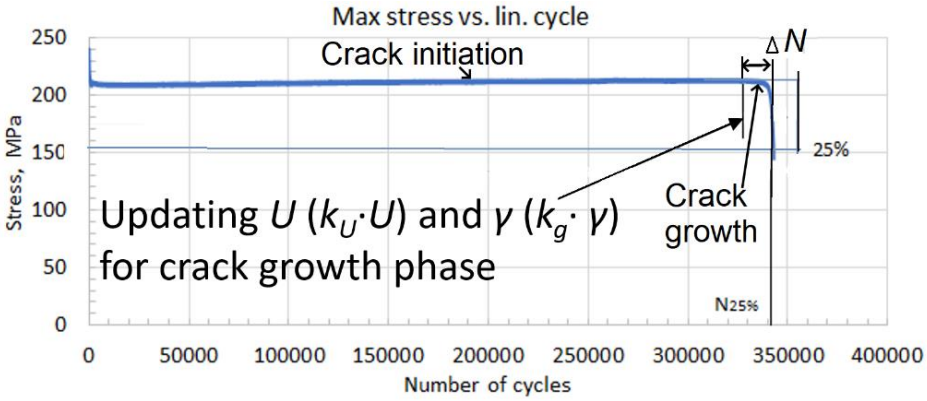

Figure 7.84. Determination of coefficients k_U and k_γ from the experimental maximum stress vs. linear cycle plot.

Selecting $k_U = 1.2$ and $k_\gamma = 1$ results the same number of cycles ΔN (Figure 7.84) in the PD model as in experiment when failure of the specimen is achieved.

Simulation and experimental results comparison of asymmetric cyclic loading, namely POL and PUL, is shown in Figure 7.85. Crack growth speed comparison in test and simulated specimen is presented in Figure 7.86.

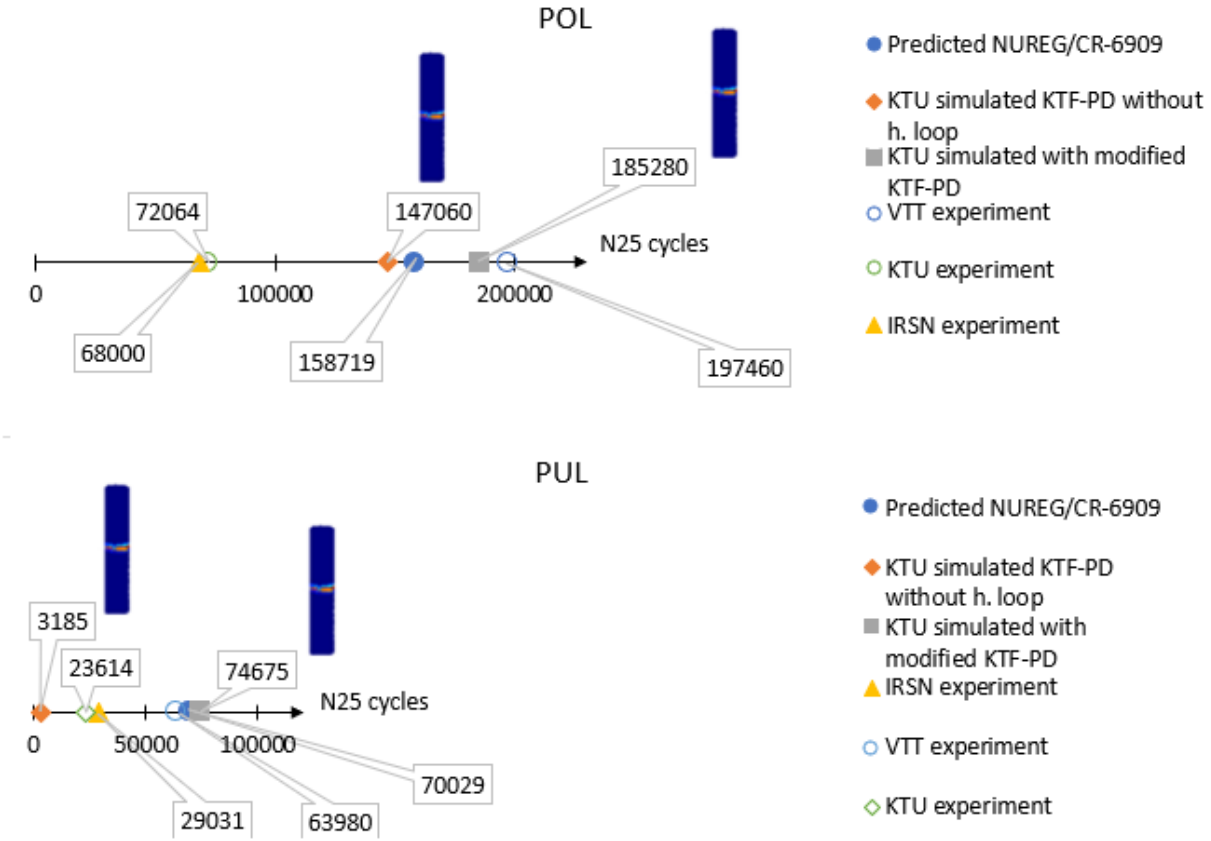

Figure 7.85. Simulation and experiment results comparison for POL and PUL cyclic loadings.

From results given in Figure 7.85, it is visible that only modified KTF predicts fatigue life correctly for both POL and PUL loading. The limitations of conventional KTF are demonstrated on PUL loading when the conventional KTF predicts more than 20 times shorter fatigue life (3185 cycles to failure vs. 74675 cycles). Modified KTF predicts fatigue life with good agreement for fatigue analysis to experimental and theoretical results (Figure 7.85, 185280 cycles vs. 158719 cycles for POL loading, 74675 cycles vs. 70029 cycles), average error of 12% compared to NUREG/CR-6909, Rev.1 curves is obtained. Only modified KTF is considered further when analysing results.

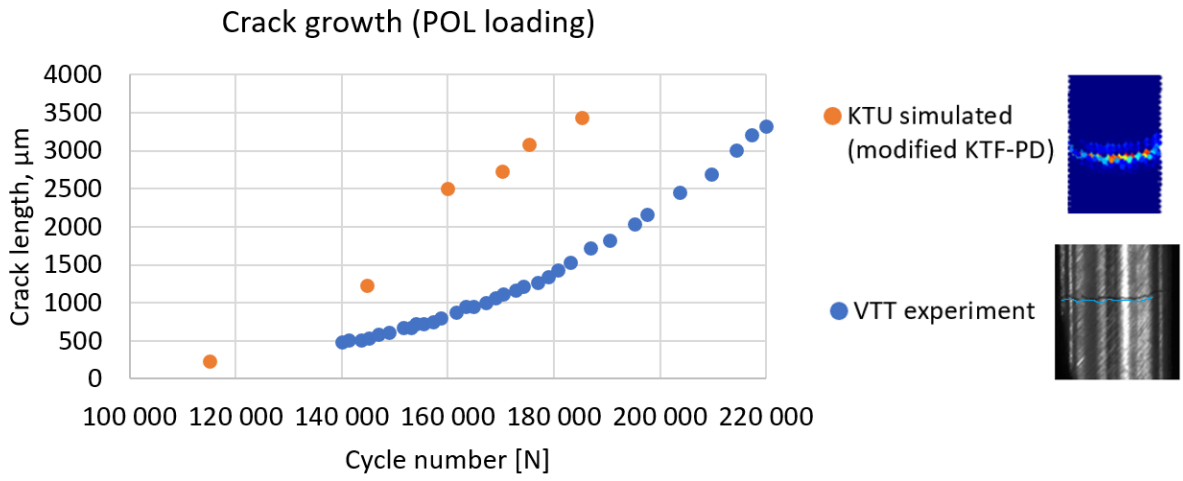

Figure 7.86. Simulated and experimental crack growth comparison for POL loading.

From comparison from Figure 7.86, it is visible that simulated and experimental crack shapes are in agreement. There are some differences between crack growth data in plot in Figure 7.86, especially due to different number of cycles to specimen failure (185000 cycles for PD simulation vs. 220000 cycles for experiment). Nevertheless, the crack length – number of cycles relation is similar for both PD simulation and experimental results. The experimental average crack growth speed computed as crack depth/number of cycles complies to experimental (differences up to 14%).

7.3.5 NUMERICAL MODELLING OF THE NOTCHED SPECIMENS

The PD fatigue model of the specimen with notch is implemented in MATLAB software by using principles of the previous PD MATLAB codes [7.28]. Notch geometry discretisation of the 0.5 mm and 2 mm radius notches in the PD model is given in Figure 7.87. Because PD is valid for computing crack initiation and growth independently on the PD grid size, very fine notch discretisation and very small PD gride size are not necessary. Finer PD grid spacing in the PD model results only more accurate crack trajectory, but it requires significantly increased computational time (model computational time increase with cubic proportionality to PD grid refinement). The current PD model is acceptable in terms of accuracy (for simulated and experimental crack growth comparison see below) and computational time of 8 hours on 16 GB RAM computer. Selected PD grid spacing is 0.29 mm (17 points per specimen diameter) and PD horizon size $\delta = 3.1\Delta x$.

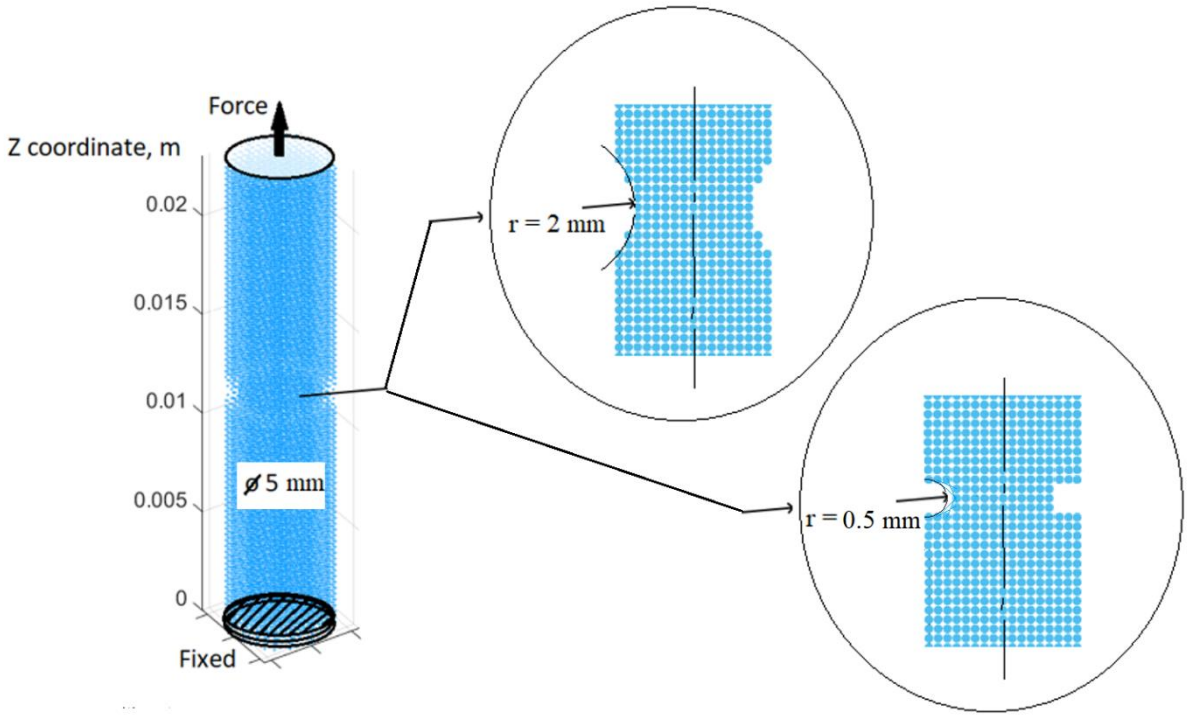

Figure 7.87. PD model of the specimen with notch (notches of 0.5 mm and 2.0 mm considered).

KTF equation (eq. 7.52), modified with cyclic loading process energy corrections (the same as in the manuscript [7.10]) is used.

The same shape parameter determining fatigue damage accumulation during the process $\lambda = 9$ is used according to experimental tests and previous simulations (also see [7.10]). Activation energy U and activation volume γ values are determined from material NUREG/CR-6909, Rev.1 S-N curve for symmetric cyclic loading. All model parameters are given in Table 7.13.

U (kJ/mol)	124.0	Stress range < 250 MPa
	115.9	Stress range 250 MPa/290 MPa
	113.4	Stress range > 290 MPa
γ (kJ/MPa-mol)	0.1390	Stress range < 250 MPa
	0.1030	Stress range 250 MPa/290 MPa
	0.0865	Stress range > 290 MPa
λ	9	
α	0.045	
ψ	50	

Table 7.13. Kinematic hardening parameters of 316L stainless steel at room temperature.

Hysteresis loop area proportional constant $\psi = 50$ and temperature proportional constant $\alpha = 0.045$ are established from previous experimental tests and modelling [7.10], and their values are the same for the specimens with notch models. Asymmetric loading effect is evaluated according to the process hysteresis loops as shown in Figure 7.88 for specimen with 0.5 mm notch and in Figure 7.89 for specimen with 2.0 mm notch.

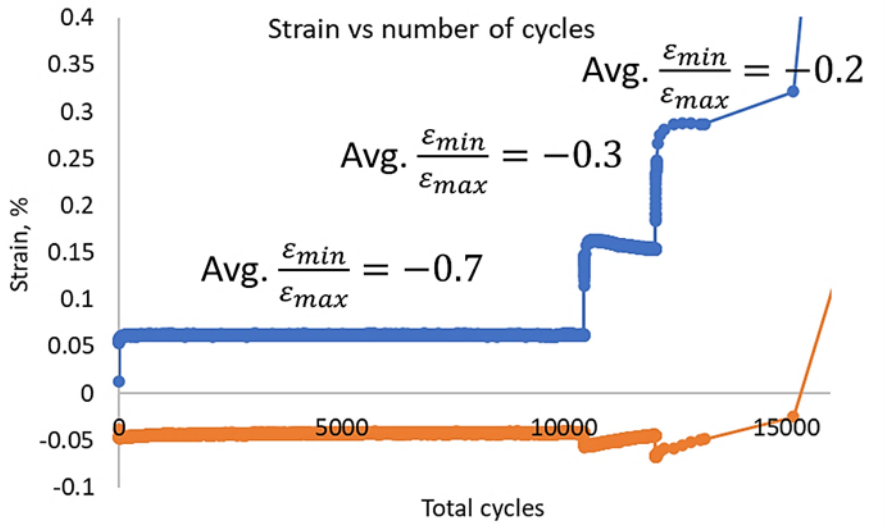

(a)

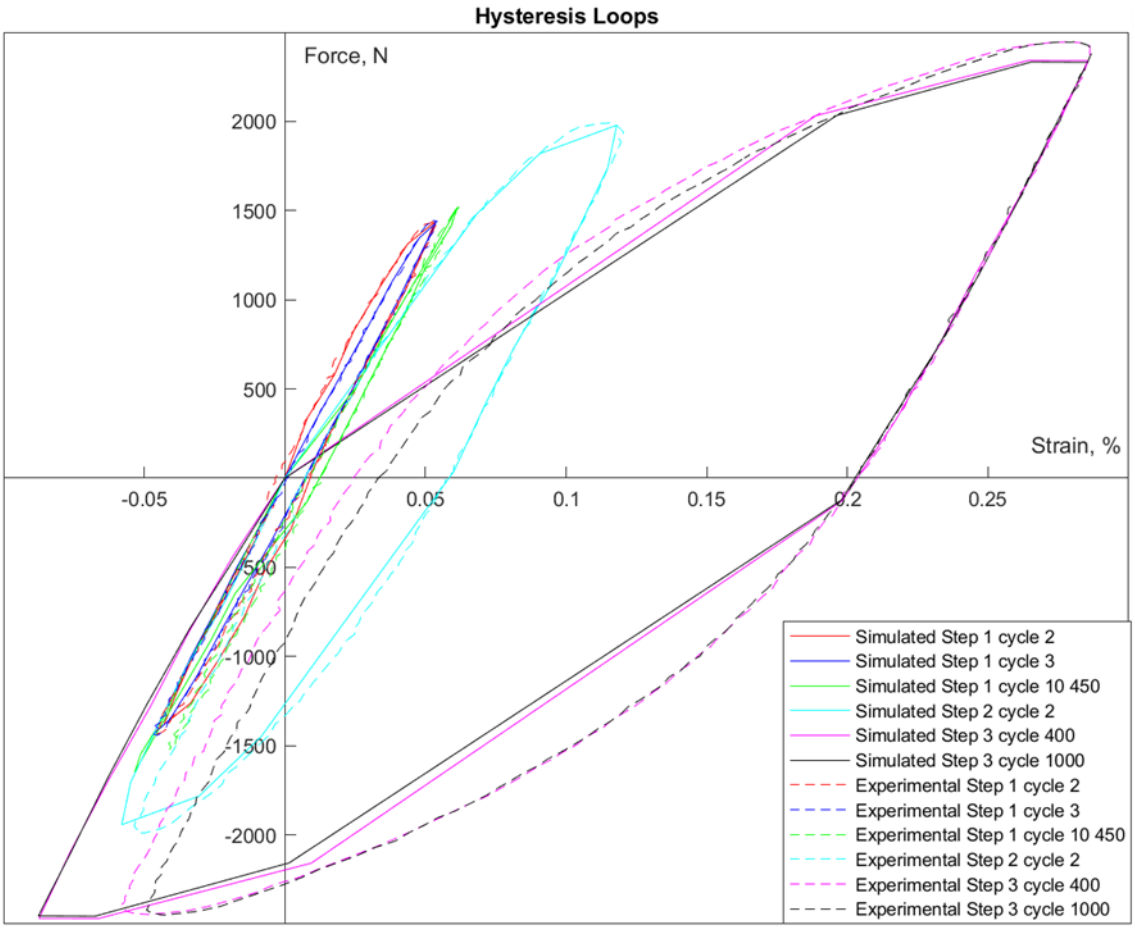

(b)

Figure 7.88. Specimen with 0.5 mm notch model parameters selection: (a) identifying stress ratio for each loading step; (b) some of experimental and simulated hysteresis loops of each loading step.

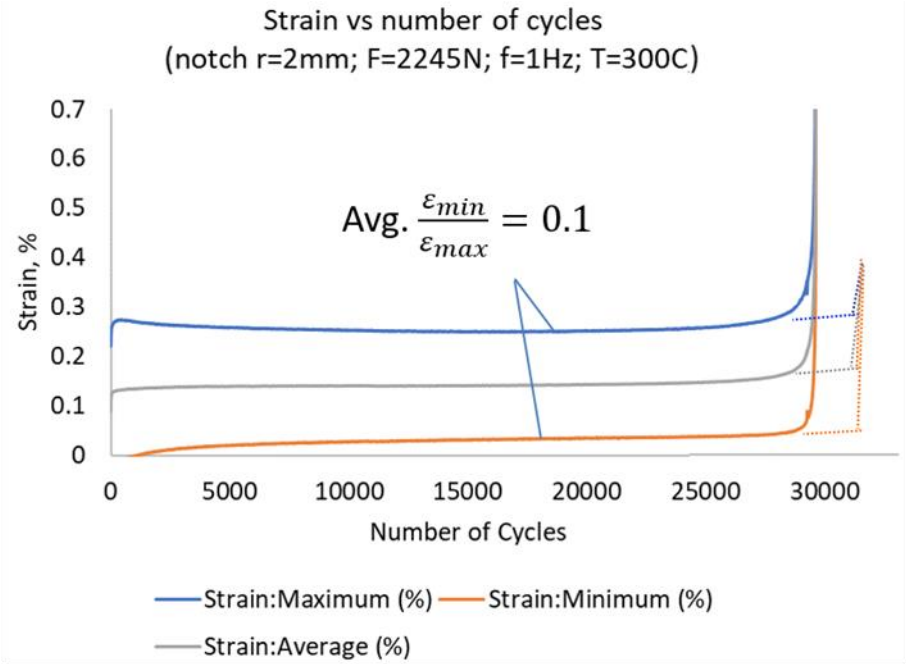

(a)

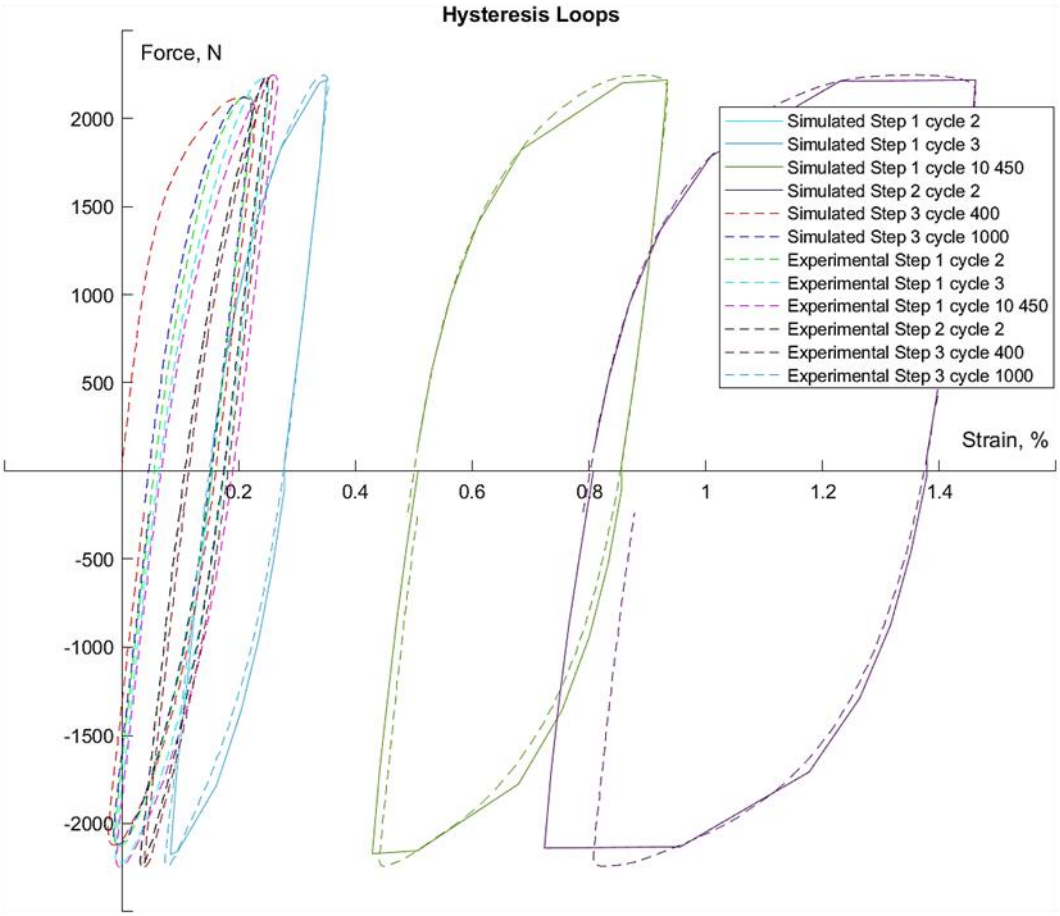

(b)

Figure 7.89. Specimen with 2.0 mm notch model parameters selection: (a) identifying loading stress ratio; (b) experimental and simulated hysteresis loops for model calibration.

For specimen with 0.5 mm notch asymmetric loadings of R = -0.7; R = -0.3; R = -0.26 stress ratios, determined from experimental strain-number of cycles plot (Figure 7.88.a), and average hysteresis loop areas from Figure 7.88.b are included into the KTF equation for each loading step. For specimen with 2 mm notch loading stress ratio of R = 0.1 is determined from process strain-number of cycles plot (Figure 7.89.a) and average hysteresis loop area is taken from experimental stress-strain curves, shown in Figure 7.89.b. When comparing experimental and simulated hysteresis loops in Figure 7.88.b – Figure 7.89.b, they are in agreement according to the shape, although some differences are visible. The reason of differences between simulated and experimental hysteresis loops is material elasto-plastic behavior approximation in PD-KTF models and material deformation behavior imperfections which are not captured in the model. Because only the maximum stress has effect on failure in the PD-KTF model, the differences between process hysteresis loops do not affect simulation accuracy and can be accepted. Modelling schematics of the specimens with 0.5 mm and 2.0 mm notches for particular loadings are given in Figure 7.90 and Figure 7.91 respectively.

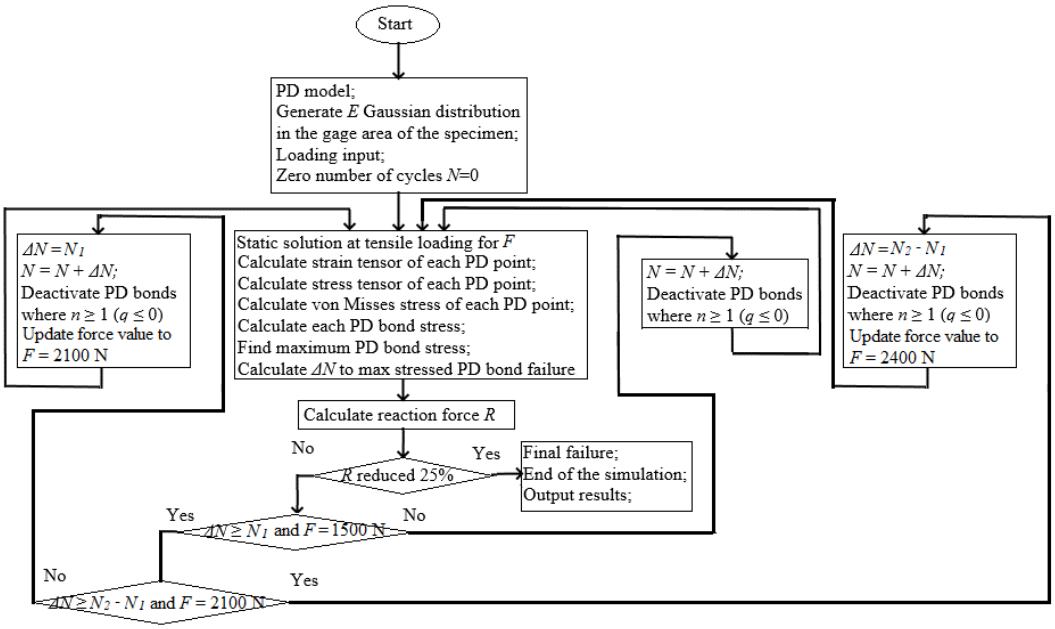

Figure 7.90. Modelling schematics for cyclic loading process with 3 loading steps (force F = 1500 N, F = 2100 N, and F = 2245 N), refers to specimen with 0.5 mm notch.

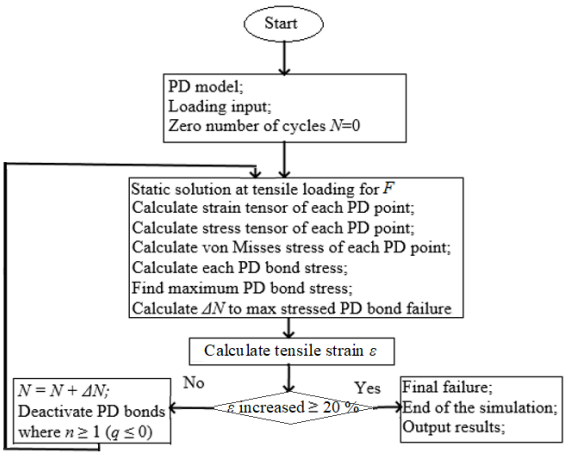

Figure 7.91. Modelling schematics for cyclic loading process of single loading step, refers to specimen with 2.0 mm notch.

Comparison of simulation and experimental results are given in Figure 7.92 (specimen with 0.5 mm notch) and Figure 7.93 (specimen with 2.0 mm notch). Plots in Figure 7.92 and Figure 7.93 show PD bond damage which values are considered as 0 – no damage, 1 – complete damage, all PD bonds of that point are broken.

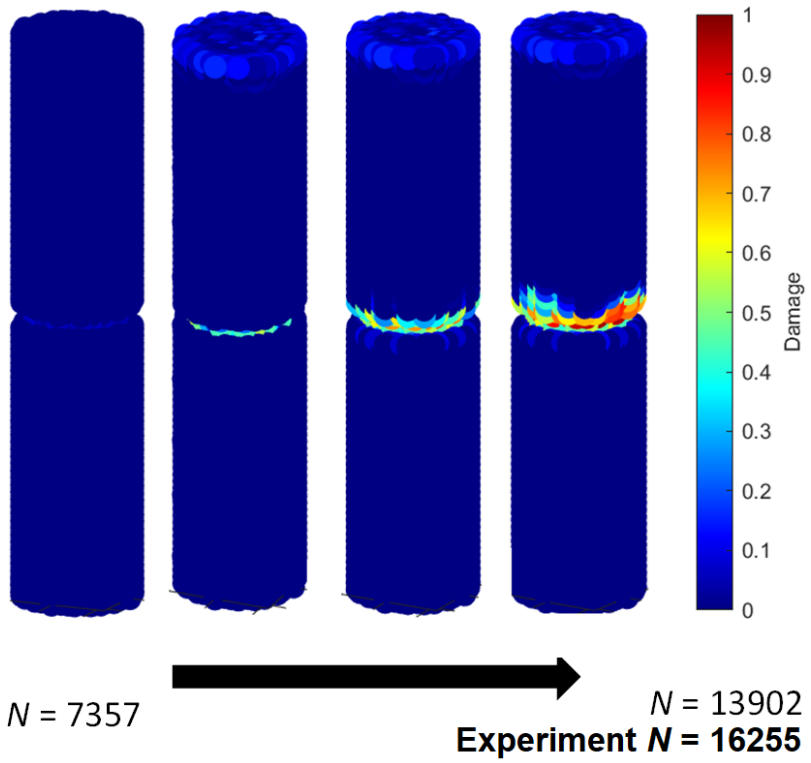

Figure 7.92. Simulated crack growth in the specimen with 0.5 mm notch.

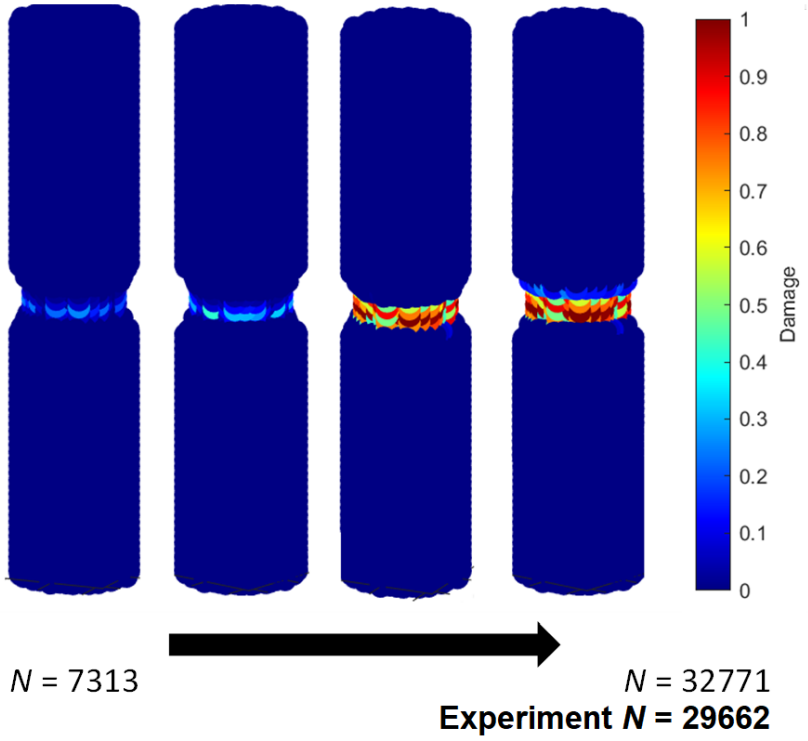

Figure 7.93. Simulated crack growth in the specimen with 2.0 mm notch.

Specimen with 0.5 mm notch simulated fatigue life is shorter 14.5% than experimental (13902 cycles vs. 16255 cycles) while specimen with 2 mm notch simulated fatigue life is longer than experimental by similar size error (32771 cycles vs. 29662). Average accuracy of the PD-KTF simulation for specimens with notch is about 12% compared to experiment. Nevertheless, it should be possible to improve simulation accuracy by adjusting model parameters, especially ψ and α, which are considered further tasks.

Strains on the specimen with 2.0 mm notch surface during experimental testing were also measured using Digital Image Correlation (DIC) from Correlated Solution with cameras Basler acA4112-20µm. Simulated and measured strains and crack growth at notch comparison is given in Figure 7.94. Comparison of specimen with 2.0 mm notch failure and simulated failure, visible in simulated displacement fields in tensile direction, is given in Figure 7.95.

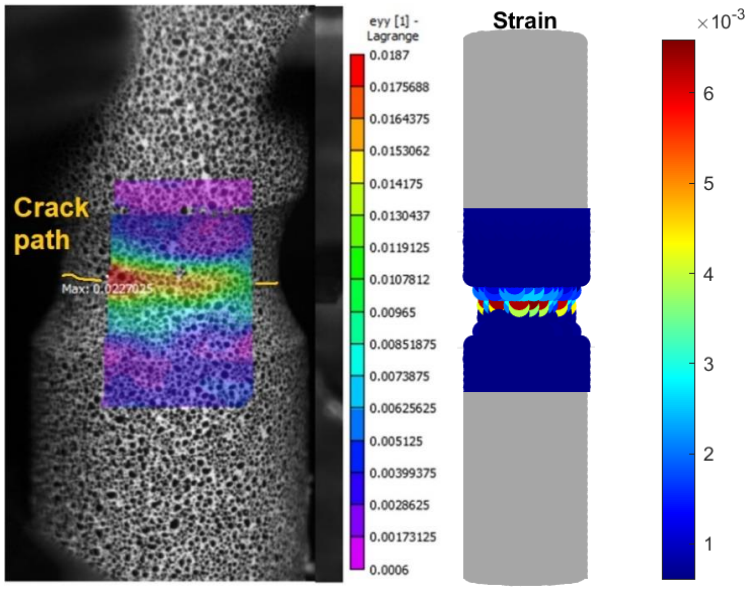

(a) (b)

Figure 7.94. Specimen with 2.0 mm notch strain comparison: (a) strains measured during experimental testing from 1 to 100 cycles; (b) PD-KTF simulated strains at 18829 cycles.

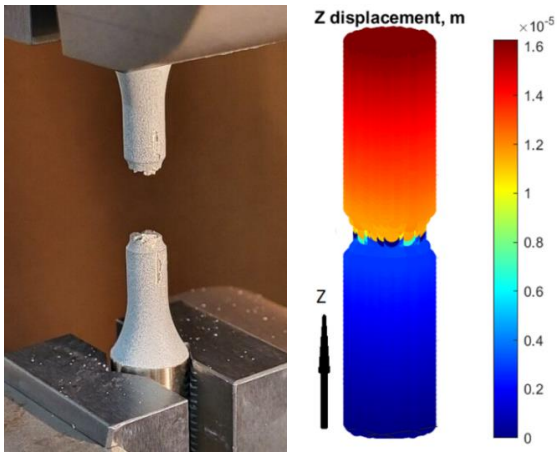

(a) (b)

Figure 7.95. Specimen with 2.0 mm notch failure comparison: (a) experimental; (b) simulated, visible in axial displacement fields.

From Figure 7.94 results it is not possible to compare strains in values, because during real fatigue process strains are more localised than in simulation and thus their values are higher. Nevertheless, the DIC measured strains field shows possible failure crack path (marked in yellow in Figure 7.94.a) which complies with strains peaks and simulated crack in the PD-KTF model. Simulated failure of the specimen, seen on tensile direction displacement plot in Figure 7.95 is the same as specimen failure during the experiment. Agreement between the simulated crack path, fatigue life and failure of the specimen in PD-KTF simulation and experiment confirms the validity of such models for fatigue life prediction and fatigue damage evaluation.

7.3.6 CONCLUSIONS

The kinetic theory of fracture implemented in peridynamic material model (peridynamic code written in MATLAB) can be used to predict fatigue life for symmetric and asymmetric cyclic loading at different temperatures with very good agreement to experimental results as it was analysed for 316L steel. Due to integral peridynamics formulation, discontinuities in material (fatigue crack in this case) are easily simulated without special additional modelling techniques. Based on this fatigue crack initiation and growth can be simulated without any predefined crack path in the model. Conventional kinetic theory of fracture predicts incorrectly shortened fatigue life for asymmetric cyclic loading with stress ratio R ≈ 0.5-1.0, thus the theory was modified including process energy losses calculated from process hysteresis loop area. Improved KTF approach once calibration for symmetric cyclic loading results acceptable results for all types of cyclic loading: symmetric, asymmetric at room and other temperatures (20 °C and 300 °C for current work). Moreover, the KTF theory in peridynamic model can be applied to accurately simulated cyclic loading problems in different geometries, namely standard test specimen according ASTM E606 [7.29] and specimen with notch.

7.4 THE THEORY OF CRITICAL DISTANCES

Critical distance approaches have been widely employed to predict fatigue and other failure modes driven by stress concentration features (notches). These methods originated applied in high-cycle fatigue with the works of Neuber [7.30] and Peterson [7.31]. Neuber's Line Method (LM) uses the average elastic stress over a distance of 2L from the notch, while Peterson's Point Method (PM) evaluates the stress at a distance of L/2. These are now unified under the Theory of Critical Distances (TCD) [7.32], which, despite its traditional reliance on linear-elastic stress analysis, has successfully been applied across a wide range of loading conditions and plasticity levels [7.33–7.35].

In contrast, the conventional approach for predicting Low Cycle Fatigue (LCF), established by Manson and Coffin [7.36,7.37], employs the strain amplitude as the primary parameter. This strain-based methodology has been successfully adapted for notched components by focusing on local strains and stresses at the notch tip [7.38,7.39].

The current study aims to bridge the concepts of TCD and Coffin-Manson by validating the hypothesis that the LCF life of notched specimens can be accurately estimated through their combined application [7.40]. This integration relies on a critical assumption: that the critical distance (L) remains constant, regardless of the notch geometry or the number of cycles to failure [7.41].

The cyclic strain-life behavior of materials subjected to fully reversed uniaxial loading (Rε = −1) is conventionally described by a combination of the Coffin-Manson relationship and the modified Basquin equation [7.42]. This methodology expresses the total strain amplitude (Δε/2) as the sum of its elastic and plastic components, relating it to the number of cycles to failure (N_f) as follows:

$$\varepsilon_a = \varepsilon_{a,e} + \varepsilon_{a,p} = \frac{\sigma'_f}{E}\left(2N_f\right)^b + \varepsilon'_f\left(2N_f\right)^c \quad \text{eq. 7.54}$$

where σ_f' is the fatigue strength coefficient, ε_f' is the fatigue ductility coefficient, b is the fatigue strength exponent (or Basquin exponent), and c is the fatigue ductility exponent (or Coffin-Manson exponent). These four material constants, which characterize the fatigue behavior, were experimentally determined using plain specimens of 316L stainless steel, common material in the frame of the INCEFA-SCALE project [7.43].

To apply the TCD to the notched specimens in the experimental program, the critical distance of the material must first be calibrated. For this purpose, a specific notched specimen, in this analysis this is the UOC-10 (Figure 7.96). It was selected and subjected to fully reversed cyclic loading (R = -1). This loading condition ensures that the strain field within the critical fatigue process zone is characterized by a strain ratio of R_ε = -1. Assuming that the critical distance is a unique material property [7.40], we can now calibrate its value. This is achieved by explicitly applying the TCD using the PM (L_{PM}), which equates the predicted life of the notched specimen (UOC-10) to its experimentally observed life, thus determining the value of L.

$$\varepsilon_{eff} = \varepsilon_a\left(r = \frac{L_{PM}}{2}, \theta = 0\right) = \frac{\sigma'_f}{E}\left(2N_f\right)^b + \varepsilon'_f\left(2N_f\right)^c \quad \text{eq. 7.55}$$

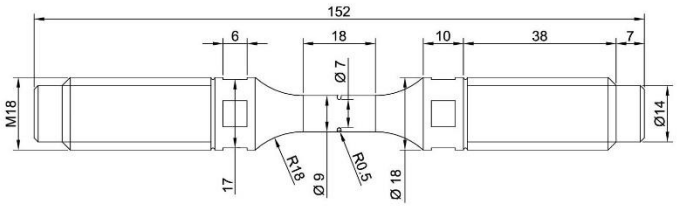

Figure 7.96. Example of fatigue notched specimen (UOC-10).

The central argument of the PM is that the fatigue life of a notched component can be directly predicted using the standard Manson-Coffin-Basquin relationship (established using unnotched specimens). This prediction hinges on defining an effective strain amplitude (ε_{eff}) at a characteristic point: a distance of $L_{PM}/2$ from the notch tip along the bisector (Figure 7.97).

The L_{PM} parameter is thus determined via a calibration procedure:

1. Using the experimentally measured number of cycles to failure (N_f) for the selected notched calibration specimen (e.g., UOC-10), the equivalent effective strain amplitude (ε_{eff}) is calculated directly from the plain-specimen Manson-Coffin-Basquin law (eq. 7.45).
2. This calculated ε_{eff} is then located on the analytical strain-distance curve (i.e., the local strain profile) along the notch bisector.
3. The physical distance corresponding to ε_{eff} on this curve directly yields the value of $L_{PM}/2$, thereby defining the critical distance, L_{PM}.

The critical distance is a unique, intrinsic material property, independent of the local stress level, notch sharpness, superimposed static stresses, and the number of cycles to failure. This implies that the size and shape of the fatigue process zone remain uninfluenced by these test parameters.

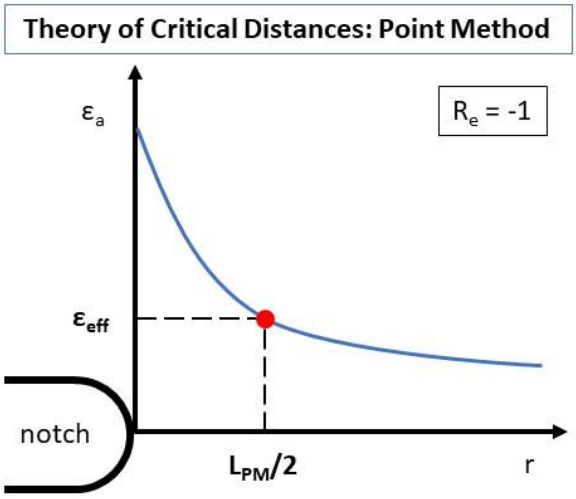

Figure 7.97. Effective strain amplitude according to the TDC-PM.

The geometrical feature chosen for this calibration significantly impacts the accuracy of the estimated L. Based on prior research utilizing the TCD [7.40,7.44,7.45], the use of the sharpest possible notch is known to achieve the most accurate results for estimating this material property. This criterion guided the selection of the calibration specimen (UOC-10) geometry.

In summary, the theoretical framework significantly simplifies fatigue life assessment: only a single calibration test is required to determine the critical distance [7.40]. This unique material property is the sole additional parameter necessary for evaluating the fatigue life of notched components, and its determination opens the door to predicting the fatigue life of critical infrastructure, such as nuclear plant components [7.46].

7.4.1 EXPERIMENTAL DETAILS

The experimental program utilized cylindrical specimens fabricated from 316L stainless steel. These components, featuring circumferential notches, were tested under fully reversed uniaxial cyclic loading (R_σ = -1).

The material fatigue parameters were determined via strain-controlled fatigue experiments on plain cylindrical specimens, conducted in accordance with ASTM E606 [7.29] as part of the INCEFA-SCALE testing campaign [7.47]. These tests were performed in air at 300 °C, a temperature typical of PWR operation, with axial strains measured throughout the duration of the testing.

The Coffin-Manson curve, obtained under fully reversed axial strain cycling, is presented in Figure 7.98. The stress amplitude (σ_a) used in this curve corresponds to the measurement taken at half the fatigue life.

The experimentally determined material constants relevant to this study are listed below:

- Young's Modulus (E): 171 GPa.
- Coffin-Manson constants:
  - Fatigue Strength Coefficient (σ_f'): 890 MPa.
  - Fatigue Strength Exponent (b): -0.138.
  - Fatigue Ductility Coefficient (ε_f'): 0.2348.
  - Fatigue Ductility Exponent (c): -0.446.

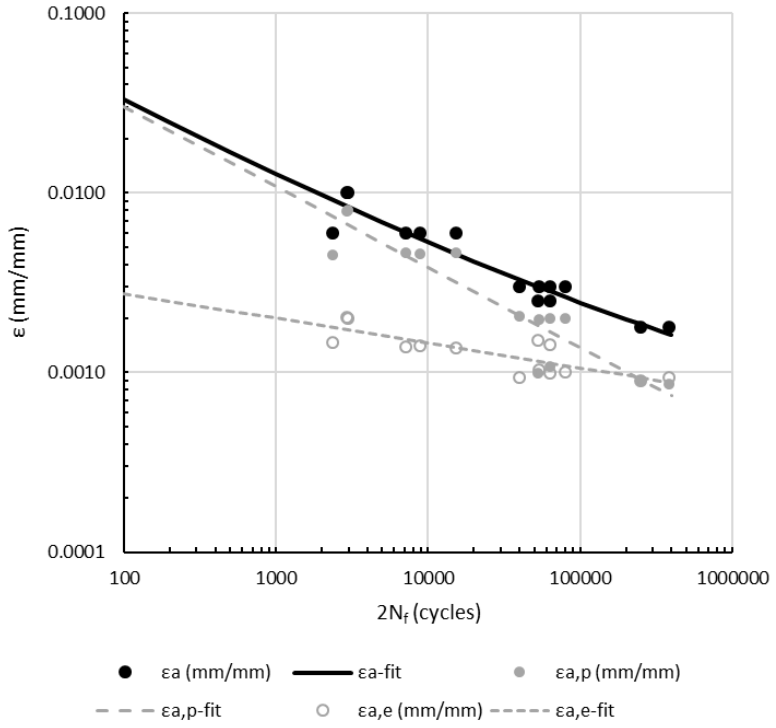

Figure 7.98. Plain specimen fatigue curve fitting.

Notched specimens for validation were tested by University of Cantabria, Framatome (France), and EDF, utilizing two distinct geometries: one set with a gross diameter of 9.0 mm and a net diameter of 7.0 mm, and a second set with a gross diameter of 8.0 mm and a net diameter of 6.2 mm. Two different notch radii (ρ, 0.5 mm and 2.0 mm) were investigated across these specimens.

All notched tests were performed under fully reversed cyclic loading (R = -1) and force-control at a frequency of 1 Hz and a temperature of 300 °C in air. The load amplitudes (ΔP) were strategically chosen based on FEM results to achieve a target strain amplitude (ε_a) at the notch tip, as detailed in Table 7.15. Fatigue life was defined by either specimen separation or a 100% increase in maximum strain.

It is important to note that while plain specimens were tested under strain control and notched specimens under force control, the methodology ensures consistency: the entire analysis is conducted through the resulting strain fields (i.e., the material response to external loading), allowing for a unified comparison. The experimental results are summarized in Table 7.15.

7.4.2 RESULTS

To characterize the fatigue process zone, elasto-plastic stress and strain fields were calculated for various notch geometries using commercial FEA software (Cast3M by Framatome and Code_Aster by EDF). The two institutions employed different modeling strategies:

Feature	FEA by Framatome [7.48]	FEA by EDF
Simulation Method	Quarter Cycle (codified in RCC-M).	Simulation of 8 cycles (to reach stabilization).
Hardening Model	Isotropic Hardening (using a "reduced cyclic curve" representative of maximum hardening).	Chaboche Non-linear Kinematic and Isotropic Hardening (representative of half-life cyclic behavior).
Calculation Type	Single calculation (quarter cycle) in load control (detailed in [7.49]).	Simulation of 8 cycles in load control.
Mesh Size (Notch Tip)	Roughly 0.05 mm.	0.01 mm.

Table 7.14. Summary FEMs by Framatome and EDF.

Despite the procedural differences, both FE methods were performed in load control and provided the essential elasto-plastic strain and stress fields required for the TCD application.

Both FE results (from Framatome and EDF, shown in Figure 7.99) were used to determine the material's critical distance via the LPM. The calibration procedure is as follow:

1. Experimental input: The number of cycles to failure (N_f) obtained from the calibration specimen (UOC-10) was introduced into the plain specimen Coffin-Manson fatigue curve (Figure 7.98) to determine the equivalent effective strain amplitude (ε_{eff}).
2. FEA input: This derived ε_{eff} value was then located on the strain-distance curves generated by the two FE models (Figure 7.99).
3. Result: The distance corresponding to ε_{eff} on each curve yielded the value of $L_{PM}/2$, allowing the final L_{PM} to be calculated.

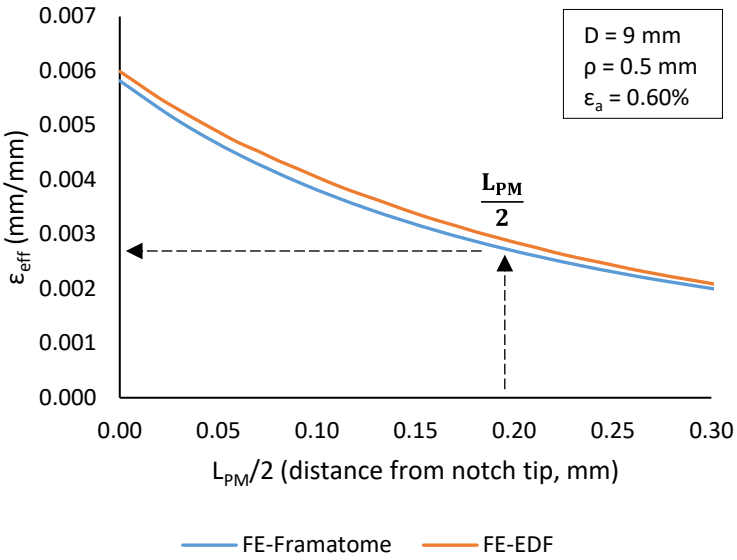

Figure 7.99. Strain fields calculated by FEAs.

Two very similar critical distance values were obtained, one for each model:

- Framatome ($L_{PM\text{-}FRF}$): 0.38 mm.
- EDF ($L_{PM\text{-}EDF}$): 0.41 mm.

The close agreement between these two values—derived from distinct elasto-plastic models—validates the consistency of the critical distance parameter.

Specimen	D (mm)	ρ (mm)	ΔP (N)	ε_a* (%)	σ_a (MPa)	N_f (cycles)	$N_{f,e\text{-}FRF}$ (cycles)	$N_{f,e\text{-}EDF}$ (cycles)
UOC-9	9.0	0.5	7304	0.64	116.8	41117	27823	26685
UOC-10*	9.0	0.5	7131	0.60	113.3	33242	33252	33244
UOC-12	9.0	2.0	6895	0.30	109.9	131234	43595	51028
UOC-11	9.0	2.0	8908	0.60	142.1	6250	6288	7828
FRFAIR-9	9.0	0.5	5167	0.30	81.6	1464172	261891	269047
FRFAIR-10	9.0	0.5	7131	0.60	112.6	22524	33252	33244
FRFAIR-12	9.0	2.0	6895	0.30	108.8	2000000	43595	51028
FRFAIR-11	9.0	2.0	8908	0.60	140.0	4840	6288	7828
EDFAIR-8	8.0	0.5	4212	0.30	83.2	709000	327442	277101
EDFAIR-7	8.0	0.5	5758	0.60	113.4	85000	35508	34737
EDFAIR-9	8.0	2.0	7147	0.60	134.6	7145	6695	7869

* Calibration specimen.

Table 7.15. Summary of experimental and estimated results.

The final validation compared the estimated fatigue life ($N_{f,e}$) against the experimental life (N_f) for the entire matrix of notched specimens (Table 7.15 and Figure 7.100). The predicted lives, calculated using the calibrated critical distance in the elasto-plastic TCD, demonstrated satisfactory accuracy, falling generally within an error factor of 3 ($1/3 \leq N_{f,e}/N_f \leq 3$). The two outliers (FRFAIR-9 and FRFAIR-12) corresponded to tests that did not induce significant plastic deformation, indicating that the elasto-plastic TCD formulation is less suited for predicting life in regimes dominated by different (likely high-cycle) fatigue micromechanisms.

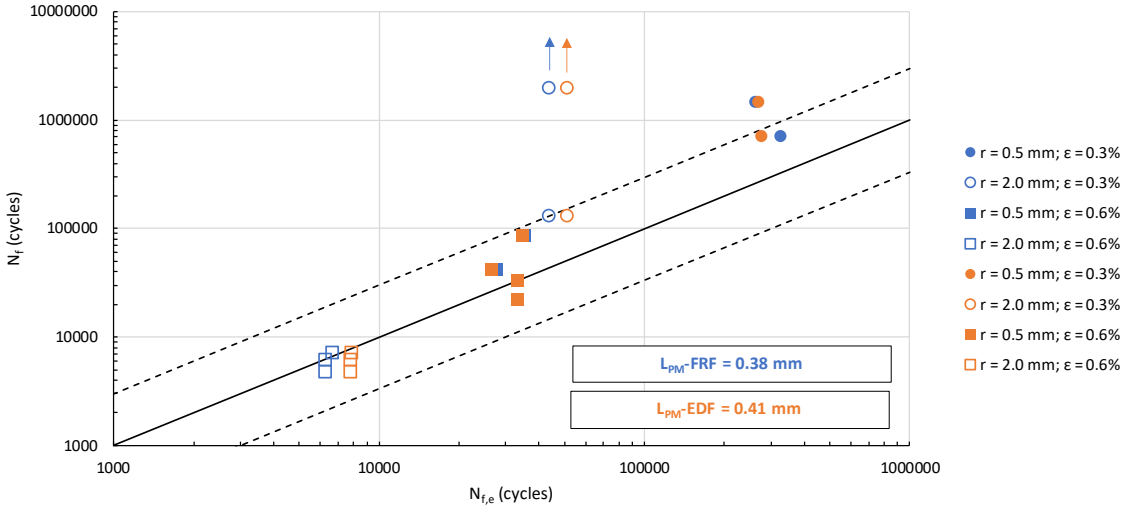

Figure 7.100. Point Method estimation of the fatigue life by using FEA: (a) by Framatome; and (b) EDF.

7.4.3 CONCLUSION

The Theory of Critical Distances, specifically its Point Method, was successfully employed to estimate the fatigue life of notched specimens in the LCF regime. A central assumption underpinning this work, that the critical distance (L_{PM}) is a unique material property independent of notch sharpness or cycles to failure, was validated by the consistency of the calibration process.

- Uniformity of calibration: Two independent elasto-plastic FEA approaches yielded highly similar critical distance values: $L_{PM\text{-}FRF}$ = 0.38 mm and $L_{PM\text{-}EDF}$ = 0.41 mm.
- Accuracy of prediction: The estimated number of cycles to failure ($N_{f,e}$) for various notched specimens showed general agreement with the experimental results.
- Future work and limitation: The study indicates that further work is necessary to improve the accuracy of predictions for specimens tested at low strain amplitudes (0.3%), suggesting potential limitations when the approach transitions toward the high-cycle fatigue regime where plastic deformation is minimal.

7.5 EPRI COMPONENT ENVIRONMENTALLY ASSISTED FATIGUE TEST MODELLING

EPRI has been involved in testing, analysis, screening, and regulatory applications of EAF for both new and operating Light Water Reactors (LWRs) since the 1990s. Research on small-scale laboratory specimens has demonstrated that fatigue testing in LWR coolant environment can significantly reduce the fatigue resistance of various materials used in nuclear steam supply system construction compared to similar testing in an air environment. Despite extensive research indicating the potential severity of EAF, there has been no operating experience from the current LWR fleet indicating fatigue failure attributed primarily to EAF.

This apparent discrepancy raises important questions about how well EAF laboratory test results apply to the real operating conditions of LWR primary plant components. Since 2008, EPRI has worked with EAF researchers, regulators, and utilities to understand this issue through various knowledge gap analyses, the latest documented in 2018 [7.1]. Many initiatives in this project stem from these analyses. Knowledge Gap 33 in [7.1] indicates that “more data using component-like features with plant-representative loading conditions are required to develop and validate methods for considering corrosion fatigue in LWR environments,” and it is considered a high-priority gap. Consequently, EPRI launched a supplemental project and issued a request for proposals aligned with the technical requirements outlined in a 2017 ASME PVP Conference paper [7.50].

The EAF Component Test Project started in 2019. The testing plan has four phases, which are shown in the Figure 7.101 below:

Phase 1 - Test Design and Prelim. FEA Modeling

- Define of component dimensions
- Define transient parameters
- Component FEA model outputs
- Predict fatigue behavior based on design assumptions

Phase 2 - Commissioning

- Test loop capability assessment
- Calibration of NDE Equipment
- Thermal and strain benchmark testing
- NDE crack size calibration
- Develop PWR-represenative water chemistry
- Align FEA with benchmark data/revise fatigue predictions

Phase 3 - Component Testing

- Testing with variable ramp rates
- EC inspection for crack initiation
- UT for crack growth monitoring
- Post-test metallographic examinations

Phase 4 - FEA Model Refinement and F_{en} comparison

- Calculate Calculate F_{en} from the test results
- Compare F_{en}

Figure 7.101. EAF component test overview.

Phase 1 of the project consisted of identifying and sourcing the material, designing the test components and test conditions, and performing initial design analysis to predict the fatigue behavior based on the design assumptions. The tested material is a dual-certified 304/304L 4 in (101.6 mm) OD 1 in (25.4 mm) wall seamless stainless steel hot-finished pipe in 12 ft (3.66 m) sections. Test components were machined from the outer diameter with a sloped transition from 1 in to 0.3 in (7.62 mm). Specimens were ID-honed to a plant representative surface roughness corresponding to ISO-1302 N7-N8.

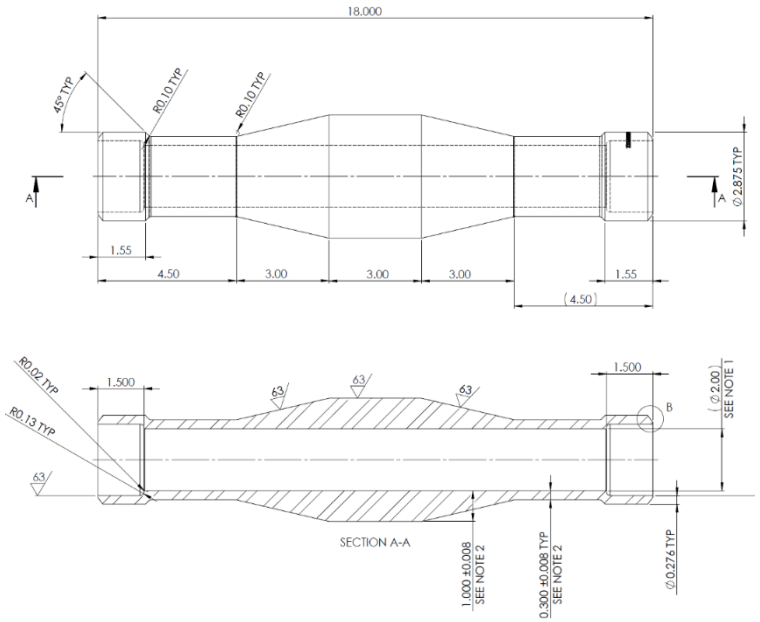

Figure 7.102. Test specimen dimensions.

The thermal transients consist of multiple thermal excursions between hot (325 °C) and cold (38 °C) steady-state conditions, with variable ramp rates ranging from 3 to 100 s. The purpose of varying the ramp rates is to enhance the calculated value of the EAF correction factor (F_{en}), while maintaining a reasonable test life. Initial design calculations based on idealized transients showed $F_{en} \approx 6$, per the equations in NUREG/CR-6909, Rev.1, for a 100 s ramp time. The transients are generated by a test loop that circulates hot and cold fluid while maintaining a pressure of 15.5 MPa (2250 psi) and mass flow rates up to 3 kg/s (73 gpm).

As part of the Phase 2 Commissioning of the test loop, two specialized specimens were developed based on the test specimen design to measure inner diameter (ID), outer diameter (OD), through-wall metal temperatures, and strains during thermal transients. These are referred to as the strain (SBS) and thermal (TBS) benchmark specimens, respectively, and are shown in Figure 7.103.

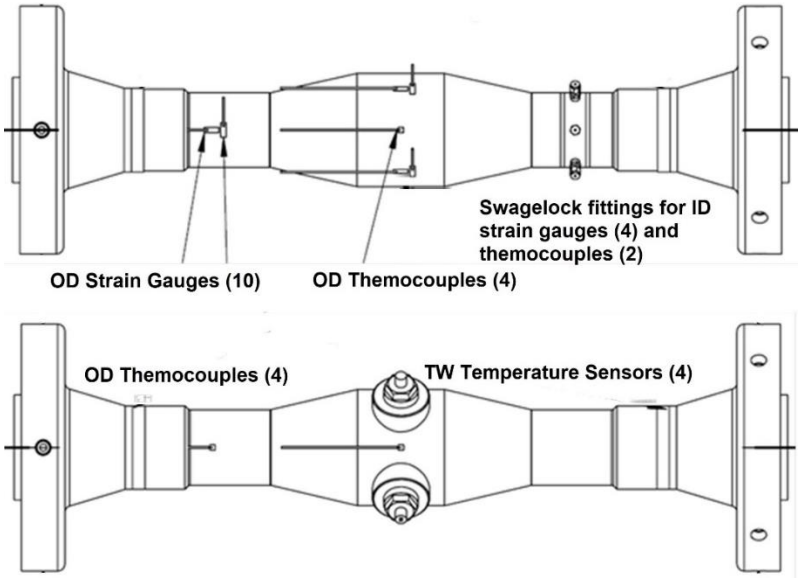

Figure 7.103. Strain (top) and thermal (bottom) benchmark specimens.

The test specimens are assembled with flanges and arranged in the test loop in an inverted U-shape configuration. The specimen arrangement and installed specimens are shown in Figure 7.104. Thermal transients were performed on these specimens in Positions 1 and 4, as shown below, and the data were collected. Comparisons of the various transients to the Phase 1 design assumptions are shown in Figure 7.105. The specifics pertaining to the Phase 2 thermal and strain benchmark testing are further detailed in [7.51].

The INCEFA-SCALE team has been given access to the benchmark test data to evaluate models and predict temperature, stress, and strain distributions, as well as fatigue. As of the writing of this report, the project is nearing the end of the Phase 2 Non-Destructive Evaluation Qualification, which is being done to calibrate the NDE equipment being used to identify crack initiation and monitor crack growth.

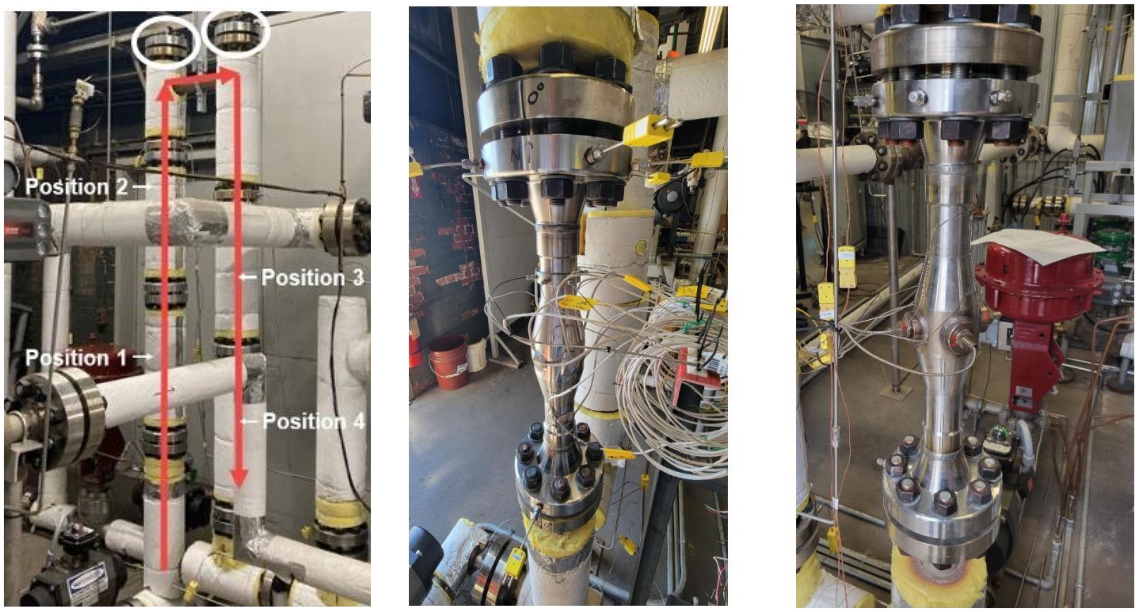

Figure 7.104. Test specimen arrangement (left); strain benchmark specimen (middle); and thermal benchmark specimen (right).

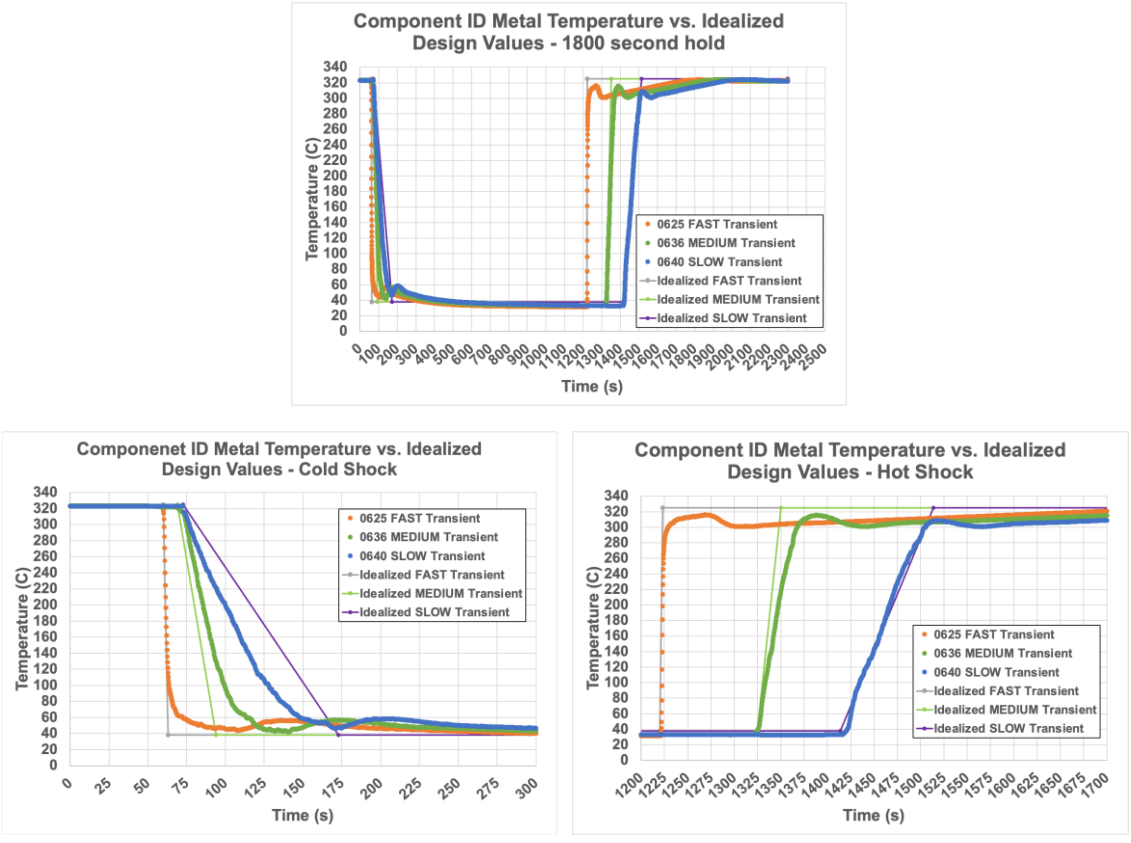

Figure 7.105. Comparison of ID Metal temperature measurement with the idealized design values. ID Metal temperatures are from below the thick section of the SBS while in position 1 and subjected to the fast, medium, and slow transients.

7.5.1 METHODOLOGY

To accurately capture the cyclic plasticity of AISI 304L steel under environmentally assisted Thermo-Mechanical Fatigue (TMF), a nonlinear constitutive model was implemented. This approach combines isotropic hardening with the Chaboche kinematic hardening model to precisely define the material's kinematic response under complex loading conditions.

This methodology is described in Section 7.1.1.1, using equations from eq. 7.1 to eq. 7.15.

7.5.2 COMPUTATIONAL MODEL

A finite element–based computational model was employed to predict the stress, strain, and temperature time histories under thermo-mechanical cyclic loading. Exploiting symmetry about all three orthogonal planes, a reduced model corresponding to one quarter of the half specimen was employed, and symmetry boundary conditions were imposed on the associated planes. The specimen was meshed using 40880 coupled temperature–displacement linear hexahedral elements (C3D8T). An element size of 1.5-5.0 mm was used depending on the local geometric features and convergence requirements. The inner surface of the specimen was subjected to cyclic temperatures ranging from 38 °C to 325 °C under a constant pressure of 15.5 MPa, while the outer surface was exposed to natural convection. The finite element mesh and applied boundary conditions are shown in Figure 7.106.

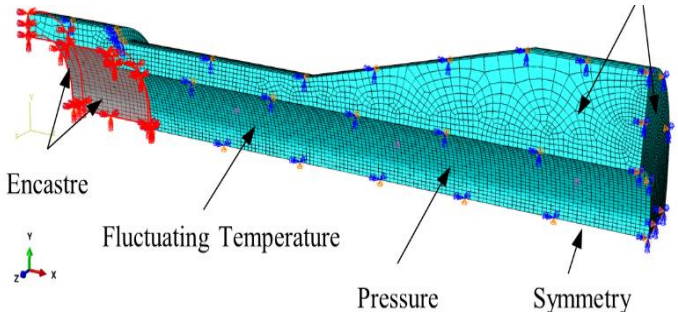

Figure 7.106. Mesh and boundary conditions.

For the computational model, AISI 304L stainless steel was assigned a thermal conductivity of 16.2 W/(m·K), a density of 7900 kg/m³, and a specific heat of 500 J/(kg·K).

Elastic properties that were used in the model are presented in Table 7.16.

Temperature (°C)	Young's Modulus, E (GPa)	Poisson's Ratio
20	195	0.3
150	175	0.3
325	162	0.3

Table 7.16. Elastic properties.

The kinematic hardening parameters are provided in Table 7.17. The kinematic hardening parameters were selected based on the data reported in reference [7.1] and subsequently modified to suit the specific conditions of the investigated case. However, further experimental

studies and systematic calibration of these parameters are required in order to more accurately capture the full range of loading conditions and material behaviour observed in the experiment.

Temperature (°C)	C_1 (MPa)	γ_1	C_2 (MPa)	γ_2
20	105000	750	12000	120
150	135000	1400	22000	180
325	185000	1650	29000	220

Table 7.17. Parameters for the Chaboche model.

The parameters of the isotropic hardening component for the exponential law resulted are presented in Table 7.18. The isotropic hardening parameters were selected based on the data reported in reference [7.1] and subsequently modified to suit the specific conditions of the investigated case. As with the kinematic hardening parameters, additional research is necessary to achieve more accurate calibration of the isotropic hardening parameters.

Temperature (°C)	σ_0 (MPa)	Q (MPa)	b
20	200	-30	1.85
150	145	-35	1.85
325	125	-44	1.85

Table 7.18. Parameters of the isotropic hardening component.

Temperature-dependent data for the coefficient of thermal expansion are presented in Table 7.19.

Temperature (°C)	Thermal expansion, α (1/K)
20	$1.73 \cdot 10^{-5}$
100	$1.78 \cdot 10^{-5}$
200	$1.84 \cdot 10^{-5}$
300	$1.91 \cdot 10^{-5}$
400	$1.99 \cdot 10^{-5}$

Table 7.19. Coefficient of thermal expansion.

7.5.3 RESULTS

A numerical simulation of the specimen subjected to thermomechanical cyclic loading was carried out using the developed computational model. Figure 7.107 shows the temperature time history, demonstrating good agreement between the modelling results and the experimental data reported in reference [7.51].

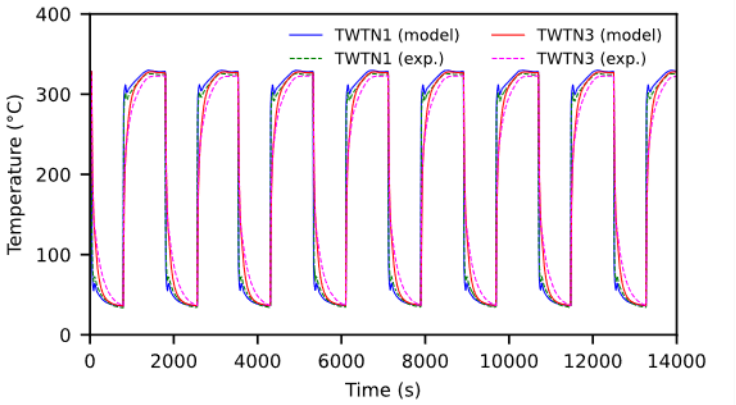

Figure 7.107. Mesh and boundary conditions.

Figure 7.108 and Figure 7.109 present the strain and stress time histories in the thin and thick sections of the specimen. The stress–strain and strain–time histories reveal pronounced ratcheting behaviour under cyclic thermomechanical loading in the thin section. Despite a nearly repeatable stress response from cycle to cycle, the strain response exhibits a progressive drift in the mean value, indicating continuous accumulation of plastic strain. The thick section shows significantly reduced ratcheting, with smaller mean strain drift and more constrained cyclic response. The obtained results demonstrate that the proposed model, employing the combined kinematic–isotropic formulation, can successfully capture the ratcheting behaviour observed in the experiments reported in [7.51].

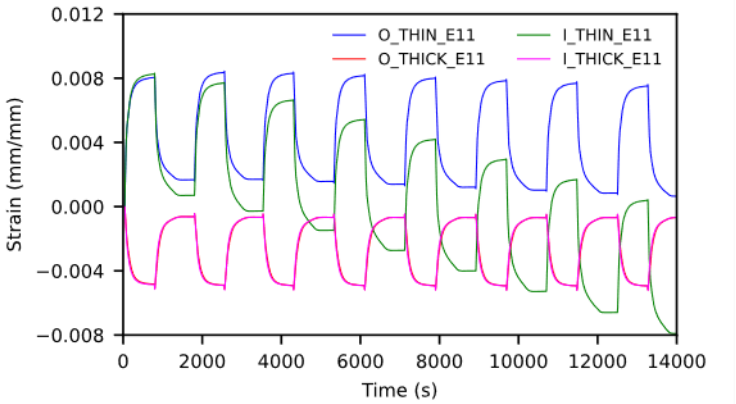

Figure 7.108. Strain time history.

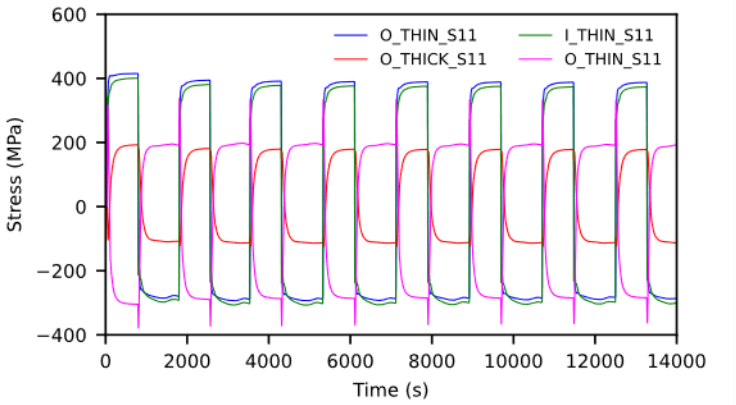

Figure 7.109. Stress time history.

Figure 7.110 demonstrates the stress–strain hysteresis loops in the thin section of the specimen. Within the observed timeframe, the hysteresis loops do not stabilize but instead translate along the strain axis with increasing cycles, indicating progressive ratcheting behaviour.

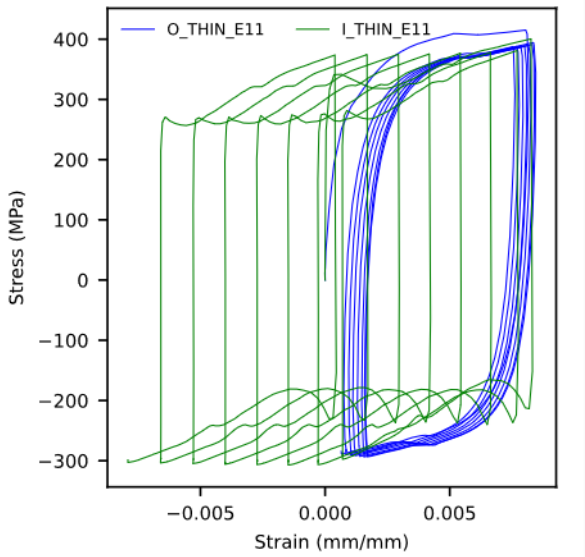

Figure 7.110. Stress–strain hysteresis loops.

7.5.4 CONCLUSIONS

A finite element–based computational model was employed to predict the stress, strain, and temperature time histories under thermo-mechanical cyclic loading. The research presented in this study confirms that the combined kinematic–isotropic formulation enables the proposed model to successfully capture the experimentally observed ratcheting behaviour. Furthermore, the obtained stress–strain and strain–time responses capture key fatigue–relevant features, including non-zero mean stress, plastic strain accumulation, and ratcheting, which can be used to estimate fatigue life under cyclic thermomechanical loading.

As future work, calibration of the constitutive model is required to improve the fidelity of the ratcheting prediction. In particular, the parameters of the Chaboche kinematic hardening model must be calibrated using cyclic and thermomechanical test data to ensure realistic backstress evolution and dynamic recovery. In addition, the isotropic hardening parameters should be refined to correctly capture cyclic hardening or softening and potential shakedown behaviour.

7.6 CONCLUSIONS

The purpose of this Chapter was to describe the advanced numerical and analytical methodologies used in the INCEFA-SCALE Project to reproduce material cyclic behaviour and predict fatigue damage. Numerical analyses are generally in agreement with experimental data, but the cyclic behaviour of the 316L austenitic stainless steel used in the project remains difficult to model. Let us note that peridynamics and critical distances theories have been successfully employed to estimate the fatigue life of various configurations.

REFERENCES

[7.1] S. Bhalchandra Pate, G. Dundulis, S. Kilikevičius, A. Grybenas, Experimental and numerical examination of low cycle fatigue behaviour on AISI304L steel, Nucl. Eng. Des. 429 (2024) 113599. doi:10.1016/j.nucengdes.2024.113599.

[7.2] S.B. Pate, G. Dundulis, P. Griskevicius, Modeling of LCF Behaviour on AISI316L Steel Applying the Armstrong–Frederick Kinematic Hardening Model, Materials (Basel). 17 (2024) 3395. doi:10.3390/ma17143395.

[7.3] S.B. Pate, G. Dundulis, S. Courtin, J.-C. Le Roux, The effects of strain amplitude and temperature on kinematic hardening parameters for low cycle fatigue of AISI316L stainless steel, Nucl. Eng. Des. 442 (2025) 114221. doi:10.1016/j.nucengdes.2025.114221.

[7.4] O. Ancelet, S. Chapuliot, G. Henaff, S. Marie, Development of a test for the analysis of the harmfulness of a 3D thermal fatigue loading in tubes, Int. J. Fatigue. 29 (2007) 549–564. doi:10.1016/j.ijfatigue.2006.04.002.

[7.5] W. Zhang, Fissuration par fatigue en plasticité généralisée sous chargement thermo-mécanique, Université Paris-Saclay, 2016.

[7.6] B. Nečemer, F. Zupanič, D. Gabriel, E.A. Tarquino, M. Šraml, S. Glodež, Low cycle fatigue behaviour of ductile aluminium alloys using the inelastic energy approach, Mater. Sci. Eng. A. 800 (2021) 140385. doi:10.1016/j.msea.2020.140385.

[7.7] S. Sajith, S.S. Shukla, K.S.R.K. Murthy, P.S. Robi, Mixed mode fatigue crack growth studies in AISI 316 stainless steel, Eur. J. Mech. - A/Solids. 80 (2020) 103898. doi:10.1016/j.euromechsol.2019.103898.

[7.8] A.M. Alshoaibi, A.H. Bashiri, Fatigue Crack Growth Studies under Mixed-Mode Loading in AISI 316 Stainless Steel, Appl. Sci. 13 (2023) 9446. doi:10.3390/app13169446.

[7.9] ANSYS 2025R1. Theory Reference, (2025).

[7.10] T. Vaitkunas, P. Griskevicius, G. Dundulis, S. Courtin, Peridynamic numerical investigation of asymmetric strain-controlled fatigue behaviour using the kinetic theory of fracture, Adv. Model. Simul. Eng. Sci. 11 (2024) 12. doi:10.1186/s40323-024-00264-4.

[7.11] E. Madenci, E. Oterkus, Peridynamic Theory and Its Applications, Springer New York, New York, NY, 2014. doi:10.1007/978-1-4614-8465-3.

[7.12] A. Javili, R. Morasata, E. Oterkus, S. Oterkus, Peridynamics review, Math. Mech. Solids. 24 (2019) 3714–3739. doi:10.1177/1081286518803411.

[7.13] E. Madenci, P. Roy, D. Behera, Bond-Based Peridynamics Including Rotation, in: Adv. Peridynamics, Springer International Publishing, Cham, 2022: pp. 283–325. doi:10.1007/978-3-030-97858-7_13.

[7.14] Y. Zhang, E. Madenci, A Coupled Peridynamic and Finite Element Approach in ANSYS Framework for Fatigue Life Prediction Based on the Kinetic Theory of Fracture, J. Peridynamics Nonlocal Model. 4 (2022) 51–87. doi:10.1007/s42102-021-00055-0.

[7.15] E. Madenci, A. Barut, M. Dorduncu, Peridynamic Differential Operator for Numerical Analysis, Springer International Publishing, Cham, 2019. doi:10.1007/978-3-030-02647-9.

[7.16] S. Silling, M. Epton, O. Weckner, J. Xu, E. Askari, Peridynamic States and Constitutive Modeling, J. Elast. 88 (2007) 151–184. doi:10.1007/s10659-007-9125-1.

[7.17] A.F. Queiruga, G. Moridis, Numerical experiments on the convergence properties of state-based peridynamic laws and influence functions in two-dimensional problems,

Comput. Methods Appl. Mech. Eng. 322 (2017) 97–122. doi:10.1016/j.cma.2017.04.016.

[7.18] P. Seleson, D.J. Littlewood, Convergence studies in meshfree peridynamic simulations, Comput. Math. with Appl. 71 (2016) 2432–2448. doi:10.1016/j.camwa.2015.12.021.

[7.19] E. Oterkus, I. Guven, E. Madenci, Fatigue failure model with peridynamic theory, in: 2010 12th IEEE Intersoc. Conf. Therm. Thermomechanical Phenom. Electron. Syst., IEEE, 2010: pp. 1–6. doi:10.1109/ITHERM.2010.5501273.

[7.20] S.A. Silling, A. Askari, Peridynamic model for fatigue cracking., (2014). doi:10.2172/1160289.

[7.21] E. Madenci, A. Barut, A. Yaghoobi, N. Phan, R.S. Fertig, Combined peridynamics and kinetic theory of fracture for fatigue failure of composites under constant and variable amplitude loading, Theor. Appl. Fract. Mech. 112 (2021) 102824. doi:10.1016/j.tafmec.2020.102824.

[7.22] A.C. Hansen, J. Baker-Jarvis, A rate dependent kinetic theory of fracture for polymers, Int. J. Fract. 44 (1990) 221–231. doi:10.1007/BF00035518.

[7.23] S.N. Zhurkov, Kinetic Concept of the Strength of Solids, Int. J. Fract. Mech. 1 (1965) 311–323. doi:10.1007/BF03545562.

[7.24] P.C. Paris, F. Erdogan, A critical analysis of crack propagation laws, J. Basic Eng. Trans. Am. Soc. Mech. Eng. (1963) 528–534.

[7.25] R.S. Fertig, D.J. Kenik, Predicting composite fatigue life using constituent-level physics, Collect. Tech. Pap. - AIAA/ASME/ASCE/AHS/ASC Struct. Struct. Dyn. Mater. Conf. (2011) 1–11. doi:10.2514/6.2011-1991.

[7.26] R.S. Fertig III, D.J. Kenik, Physics-Based Fatigue Life Prediction of Composite Structures, Nafems 2011. (2011) 1–12.

[7.27] M. Speronello, Study of computational peridynamics, explicit and implicit time integration, viscoelastic material, University of Padua, 2015.

[7.28] MATLAB peridynamics open source code, (n.d.).

[7.29] ASTM, Standard Test Method for Strain-Controlled Fatigue Testing, E606/E606M-12. (2004). doi:10.1520/E0606-04E01.Copyright.

[7.30] H. Neuber, Therory of notch stresses: principles for exact calculation of strength with reference to structural form and material, Springer Verlag, Berlin, 1958.

[7.31] R.E. Peterson, Notch sensitivity, in: G. Sines, J.L. Waisman (Eds.), Met. Fatigue, McGraw Hill, New York, 1959: pp. 293–306.

[7.32] D. Taylor, The Theory of Critical Distances, Elsevier, 2007. doi:10.1016/B978-0-08-044478-9.X5000-5.

[7.33] S. Bentachfine, G. Pluvinage, J. Gilgert, Z. Azari, D. Bouami, Notch effect in low cycle fatigue, Int. J. Fatigue. 21 (1999) 421–430. doi:10.1016/S0142-1123(99)00004-3.

[7.34] L. Susmel, The theory of critical distances: Applications in fatigue, in: Fract. Nano Eng. Mater. Struct. - Proc. 16th Eur. Conf. Fract., Springer Netherlands, Dordrecht, 2006: pp. 1101–1102. doi:10.1007/1-4020-4972-2_546.

[7.35] L. Susmel, D. Taylor, A novel formulation of the theory of critical distances to estimate lifetime of notched components in the medium-cycle fatigue regime, Fatigue Fract. Eng. Mater. Struct. 30 (2007) 567–581. doi:10.1111/j.1460-2695.2007.01122.x.

[7.36] S.S. Manson, Behavior Of Materials Under Conditions Of Thermal Stress, NACA Rep. 1170. (1953) 317–350.

[7.37] L.F. Coffin, A Study of the Effects of Cyclic Thermal Stresses on a Ductile Metal, J. Fluids Eng. 76 (1954) 931–949. doi:10.1115/1.4015020.

[7.38] M.N. James, C. Dimitriou, H.D. Chandler, Low Cycle Fatigue Lives of Notched Components, Fatigue Fract. Eng. Mater. Struct. 12 (1989) 213–225. doi:10.1111/j.1460-2695.1989.tb00528.x.

[7.39] G. Shatil, E.G. Ellison, D.J. Smith, Elastic-Plastic Behaviour and Uniaxial Low Cycle Fatigue Life of Notched Specimens, Fatigue Fract. Eng. Mater. Struct. 18 (1995) 235–245. doi:10.1111/j.1460-2695.1995.tb00158.x.

[7.40] L. Susmel, D. Taylor, An elasto-plastic reformulation of the Theory of Critical Distances to estimate lifetime of notched components failing in the low/medium-cycle fatigue regime, J. Eng. Mater. Technol. 132 (2010) 0210021–0210028. doi:10.1115/1.4000667.

[7.41] L. Susmel, The theory of critical distances: a review of its applications in fatigue, Eng. Fract. Mech. 75 (2008) 1706–1724. doi:10.1016/j.engfracmech.2006.12.004.

[7.42] Basquin OH, The experimental law of endurance tests, Proc ASTM. (1910) 625–630.

[7.43] Joint Research Center - European Commission, ODIN Portal - MatDB, (2025). https://odin.jrc.ec.europa.eu/alcor/.

[7.44] L. Susmel, D. Taylor, On the use of the Theory of Critical Distances to predict static failures in ductile metallic materials containing different geometrical features, Eng. Fract. Mech. 75 (2008) 4410–4421. doi:10.1016/j.engfracmech.2008.04.018.

[7.45] L. Susmel, B. Atzori, G. Meneghetti, D. Taylor, Notch and mean stress effect in fatigue as phenomena of elasto-plastic inherent multiaxiality, Eng. Fract. Mech. 78 (2011) 1628–1643. doi:10.1016/j.engfracmech.2011.02.011.

[7.46] Z.H. Li, K. Han, T. Chen, H.S. Yang, P. Liu, Y.H. Lu, Fatigue life prediction of nuclear reactor main bolt based on temperature effect and size effect, Int. J. Fatigue. 152 (2021) 106443. doi:10.1016/j.ijfatigue.2021.106443.

[7.47] S. Courtin, O. Ancelet, J. Beswick, O. Blakesley, R. Cicero, INCEFA-SCALE Project – Overview of the Modelling Plans, in: Vol. 1 Codes Stand., American Society of Mechanical Engineers, 2023. doi:10.1115/PVP2023-101351.

[7.48] W. Zhang, Fatigue crack growth in large scale yielding condition, Université Paris Saclay (COmUE), 2016.

[7.49] L. Doremus, O. Ancelet, L. Casulli, L. De Baglion, R. Kallout, M. Grimm, S. Courtin, J.-C. Le Roux, C. Jacquemoud, S. Arrieta, A. Fernandez Vina, T. Seppanen, Z. Que, G. Dundulis, R. Novotny, J. Beswick, Influence of Axisymmetric Notches on the Low Cycle Fatigue Life of a 316L Stainless Steel in the Frame of INCEFA-SCALE Project, in: Vol. 1 Codes Stand., American Society of Mechanical Engineers, Montreal, 2025. doi:10.1115/PVP2025-155088.

[7.50] D.A. Steininger, K. Wright, M. Twite, A. Morley, T. Métais, G. Léopold, J.C. Le Roux, Component Testing Proposal to Quantify Margins in Existing Environmentally Assisted Fatigue (EAF) Requirements, in: Vol. 3B Des. Anal., American Society of Mechanical Engineers, 2017. doi:10.1115/PVP2017-65995.

[7.51] T.M. Damiani, A.I. Morley, S. Cuvilliez, Environmentally Assisted Fatigue Component Test: Test Program Overview and Transient Benchmark Evaluation, in: Vol. 1 Codes Stand., American Society of Mechanical Engineers, 2025. doi:10.1115/PVP2025-154809.

This page intentionally left blank.

CHAPTER 8 CONCLUSIONS

The INCEFA-SCALE Project (2020–2026) has reduced the "knowledge gap" between small-scale laboratory fatigue data and the real-world performance of nuclear power plant components. By integrating experimental testing, advanced mechanistic modelling, and digital data curation, the project provides a modernized framework for environmentally assisted fatigue assessment that moves beyond the inherent conservatisms of existing design codes.

8.1 SYNTHESIS OF EXPERIMENTAL AND ANALYTICAL FINDINGS

The multi-scale approach of the project has yielded several transformative insights for the nuclear industry:

- Standardization and Baseline Behaviour: Testing on solid cylindrical specimens (Chapter 2) provided a high-quality baseline for 316L stainless steel, demonstrating showing how mean stress, hardening, surface finish and environment are handled in current and newly developed design curves.
- Geometry and Scale Effects: Investigations into hollow specimens (Chapter 3) and notched "component-like" features (Chapter 4) demonstrated that specimen geometry and stress concentrations significantly influence crack initiation and growth rates. Specifically, the project identified that hollow specimen designs can be a source of conservatism in fatigue design curves when thickness-to-volume ratios are not properly accounted for.
- Multiaxial Loading: The biaxial fatigue program (Chapter 5) addressed the complex loading states found in real components, confirming that Variable Amplitude loading under equi-biaxial conditions does not deviate significantly from uniaxial predictions, thereby supporting the simplification of multiaxial safety assessments.
- Data-Driven Robustness: The creation of the International Fatigue Database (Chapter 6) represents a major digital milestone. By harmonizing vast datasets from NUREG/CR-6909, Rev.1 and INCEFA-PLUS, the project identified temperature, strain waveform, and surface roughness as the dominant variables dictating fatigue life in PWR environments. This repository enables more statistically robust and environment-specific assessment criteria.
- Mechanistic Modelling: Advanced modelling actions (Chapter 7), including Peridynamics and the Theory of Critical Distances, have successfully reproduced experimental crack propagation paths. These tools provide the physical foundation necessary to transfer laboratory findings to large-scale component simulations, directly addressing high-priority gaps identified by the global research community and EPRI.

8.2 IMPACT ON CODES AND STANDARDS

The primary legacy of INCEFA-SCALE is the potential for reducing undue conservatism in nuclear safety cases. By demonstrating that actual field performance often exceeds laboratory-based predictions, the project provides a technical justification for refining the "sub-factors" used in ASME and other international design curves. Furthermore, the project has produced an exceptionally valuable dataset capable of forming the basis of further refinements to these

design curves. This advancement supports the safe long-term operation of the existing LWR fleet and informs the design requirements for the next generation of reactors.

8.3 FUTURE ROADMAP

While INCEFA-SCALE has significantly closed the laboratory-to-component scale gap, future research should continue to investigate more realistic conditions such as loading that produces less severe mean stresses through alternate loading patterns or stress relaxation. To support these kinds of efforts future projects should incorporate the development of laboratory capability to keep up with the demands of industry which requires more complex testing that is substantially more difficult to perform. For mechanistic understanding consideration should be given to refining the role of hydrogen-plasticity interactions and the transition from short to long crack growth in complex geometries. The framework established here, combining digital database infrastructures with mechanistic simulations, remains the recommended roadmap for the continued evolution of nuclear structural integrity standards.

ANNEX A INCEFA-SCALE SCIENTIFIC CONTRIBUTIONS

This annex summarizes the main international publications by INCEFA-SCALE Consortium during the development of this project.

2021

ASME 2021 Pressure Vessels and Piping Conference, PVP2021 (Virtual Conference):

- K. Mottershead, R. Cicero, A. McLennan, S. Courtin, C. Huotilainen, and S. Cicero, "INCEFA-SCALE: Increasing Safety in Nuclear Power Plants by Covering Gaps in Environmental Fatigue Assessment – Focusing on Gaps between Laboratory Data and Component-Scale", PVP2021-61793, Proceedings of the ASME 2021 Pressure Vessels and Piping Conference. Online, July 2021. 10.1115/PVP2021-61793

Data (MDPI):

- T. Austin, K. Bei, T. Efthymiadis, and E. Koumoulos, "Lessons Learnt from Engineering Science Projects Participating in the Horizon 2020 Open Research Data Pilot". Data, 6(9), 96, 2021. 10.3390/data6090096

2022

Metals (MDPI):

- S. Arrieta, F.J. Perosanz, J.M. Barcala, M.L. Ruiz, and S. Cicero, "Using Direct Current Potential Drop Technique to Estimate Fatigue Crack Growth Rates in Solid Bar Specimens under Environmental Assisted Fatigue in Simulated Pressurized Water Reactor Conditions". Metals, 12(12), 2091, 2022. 10.3390/met12122091

23rd European Conference on Fracture, ECF23 (Funchal, Madeira, Portugal):

- S. Arrieta, S. Cicero, K. Mottershead, R. Cicero, A. McLennan, S. Courtin, and Z. Que, "Environmentally Fatigue Analysis of nuclear components within the framework of INCEFA-SCALE project", Procedia Structural Integrity, 42, 2022. 10.1016/j.prostr.2022.12.002

ASME 2022 Pressure Vessels and Piping Conference, PVP2022 (Las Vegas, Nevada, USA):

- McLennan, R. Cicero, K. Mottershead, S. Courtin, Z. Que, and S. Cicero, "INCEFA-SCALE (Increasing Safety in Nuclear Power Plants by Covering Gaps in Environmental Fatigue Assessment – Focusing on Gaps between Laboratory Data and Component-Scale)", PVP2022-84625, Proceedings of the ASME 2022 Pressure Vessels and Piping Conference. Las Vegas, Nevada, USA, July 2022. 10.1115/PVP2022-84625
- B. Howe, J. Mann, Z. Que, C. Huotilainen, F. Scenini, and G. Burke, "Development of a robust Procedure for the Evaluation of Striation Spacings in Low Cycle Fatigue Specimens tested in simulated PWR environment", PVP2022-84027, Proceedings of the ASME 2022 Pressure Vessels and Piping Conference. Las Vegas, Nevada, USA, July 2022. 10.1115/PVP2022-84027

EPJ Nuclear Sciences & Technologies (EDP Sciences):

- T. Brynk, F.J. Perosanz, and A. McLennan, "Increase of nuclear installations safety by better understanding of materials performance and new testing techniques development (MEACTOS, INCEFA-SCALE and FRACTESUS H2020 Projects)", EPJ Nuclear Sciences & Technologies, 8, 42, 2022. 10.1051/epjn/2022033

2023

ASME 2023 Pressure Vessels and Piping Conference, PVP2023. INCEFA-SCALE Special Session (Atlanta, Georgia, USA):

- McLennan, R. Cicero, J. Beswick, S. Courtin, Z. Que, and S. Cicero, "INCEFA-SCALE (Increasing Safety in Nuclear Power Plants by Covering Gaps in Environmental Fatigue Assessment – Focusing on Gaps between Laboratory Data and Component-Scale)", PVP2023-105357, Proceedings of the ASME 2023 Pressure Vessels and Piping Conference. Atlanta, Georgia, USA, July 2023. 10.1115/PVP2023-105357
- R. Cicero, A. McLennan, J. Mann, J. Beswick, L. Doremus, and S. Cuvilliez, "INCEFA-SCALE Project – Data Mining and Lessons Learning", PVP2023-106618, Proceedings of the ASME 2023 Pressure Vessels and Piping Conference. Atlanta, Georgia, USA, July 2023. 10.1115/PVP2023-106618
- J. Beswick, M. Oliver, J.C. Le Roux, and L. Doremus, "INCEFA-SCALE Project – Phase 1 and 2 of Testing Programme", PVP2023-106243, Proceedings of the ASME 2023 Pressure Vessels and Piping Conference. Atlanta, Georgia, USA, July 2023. 10.1115/PVP2023-106243
- S. Courtin, O. Ancelet, J. Beswick, O. Blakesley, and R. Cicero, "INCEFA-SCALE Project – Overview of the Modelling Plans", PVP2023-101351, Proceedings of the ASME 2023 Pressure Vessels and Piping Conference. Atlanta, Georgia, USA, July 2023. 10.1115/PVP2023-101351
- A. Vainionpää, J. Spadotto, Z. Que, B. Connolly, A. McLennan, S. Arrieta, J. Huret, and T. Damiani, "Microstructure Characterization of EU INCEFA-SCALE 316L Stainless Steel Fatigue Specimens - Mechanistic Understanding", PVP2023-105888, Proceedings of the ASME 2023 Pressure Vessels and Piping Conference. Atlanta, Georgia, USA, July 2023. 10.1115/PVP2023-105888

2024

International Journal of Fatigue (Elsevier):

- A. Vainionpää, T. Seppänen, and Z. Que, "Effects of pressurized water reactor environment and cyclic loading parameters on the low cycle fatigue behavior of 304L stainless steel". International Journal of Fatigue, 182, 108231, 2024. 10.1016/j.ijfatigue.2024.108231

Advanced Modeling and Simulation in Engineering Sciences (Springer):

- T. Vaitkunas, P. Griskevicius, G. Dundulis, and S. Courtin, "Peridynamic numerical investigation of asymmetric strain-controlled fatigue behaviour using the kinetic theory of fracture". Advanced Modeling and Simulation in Engineering Sciences, 11, 12, 2024. 10.1186/s40323-024-00264-4

Materials (MDPI):

- S.B. Pate, G. Dundulis, and P. Griskevicius, "Modeling of LCF Behaviour on AISI316L Steel Applying the Armstrong–Frederick Kinematic Hardening Model". Materials, 17(14), 3395, 2024. 10.3390/ma17143395

2025

24th European Conference on Fracture, ECF24 (Zagreb, Croatia):

- A. Vainionpää, Z. Que, and T. Seppänen, "Effects of Pressurized Water Reactor Environment and Cyclic Loading Parameters on the Low Cycle Fatigue Behavior of 316L Stainless Steel", Procedia Structural Integrity, 68, 2025. 10.1016/j.prostr.2025.06.054

12th Annual Conference of Society for Structural Integrity and Life, DIVK12 (Belgrade, Serbia):

- S. Arrieta, S. Cicero, A. McLennan, R. Cicero, J. Beswick, S. Courtin, and Z. Que, "Review of INCEFA-SCALE Project Advances in Environmentally Assisted Fatigue in Pressurized Water Reactor", Procedia Structural Integrity, 72, 2025. 10.1016/j.prostr.2025.08.115

EPJ Nuclear Sciences & Technologies (EDP Sciences):

- V. Pištora, A. McLennan, and G. Bonny, "Link between material properties and integrity assessment of NPP components within EU funded projects APAL, INCEFA-SCALE and FRACTESUS", EPJ Nuclear Sciences & Technologies, 11, 16, 2025. https://doi.org/10.1051/epjn/2025015

International Journal of Fatigue (Elsevier):

- Vainionpää, P.A. Ferreirós, T. Seppänen, and Z. Que, "Microstructural insights into effects of pressurized water reactor environment and cyclic loading parameters on the low cycle fatigue behavior of 316L stainless steel". International Journal of Fatigue, 198, 109016, 2025. 10.1016/j.ijfatigue.2025.109016.

Nuclear Engineering and Design (Elsevier):

- S.B. Pate, G. Dundulis, S. Courtin, and J.C. Le Roux, "The effects of strain amplitude and temperature on kinematic hardening parameters for low cycle fatigue of AISI316L stainless steel". Nuclear Engineering and Design, 442, 114221, 2025. 10.1016/j.nucengdes.2025.114221

ASME 2025 Pressure Vessels and Piping Conference, PVP2025. INCEFA-SCALE Special Session (Montreal, Quebec, Canada):

- A. McLennan, R. Cicero, J. Beswick, S. Courtin, Z. Que, and S. Cicero, "INCEFA-SCALE (Increasing Safety in Nuclear Power Plants by Covering Gaps in Environmental Fatigue Assessment – Focusing on Gaps between Laboratory Data and Component-Scale)", PVP2025-155583, Proceedings of the ASME 2025 Pressure Vessels and Piping Conference. Montreal, Quebec, Canada, July 2025. 10.1115/PVP2025-155583
- A. Mclennan, R. Tregoning, and K. Mottershead, "International Fatigue Database in Support of Nuclear Energy Safety", PVP2025-155276, Proceedings of the ASME 2025 Pressure Vessels and Piping Conference. Montreal, Quebec, Canada, July 2025. 10.1115/PVP2025-155276
- C. Jacquemoud, C. Gourdin, G. Perez, and L. Doremus, "Biaxial Fatigue Tests in PWR Environment", PVP2025-151549, Proceedings of the ASME 2025 Pressure Vessels and Piping Conference. Montreal, Quebec, Canada, July 2025. 10.1115/PVP2025-151549
- Z. Que, A. Vainionpää, A. Anders, W. Beavan, B. Connolly, Z. Veselka, S. Arrieta, J. Huret, J.C. Le Roux, J. Spadotto, K. Arstila, T. Seppänen, and J. Beswick, "Mechanistic Understanding Based on Microstructure Characterization of 316L Stainless Steel Fatigue Specimens Tested in Eu Incefa-Scale Project", PVP2025-153678, Proceedings of the ASME 2025 Pressure Vessels and Piping Conference. Montreal, Quebec, Canada, July 2025. 10.1115/PVP2025-153678
- S. Arrieta, S. Cicero, L. Doremus, O. Ancelet, and S. Courtin, "Estimation of the Fatigue Life in LCF Regime of 316L Notched Specimens Using the Theory of Critical Distances", PVP2025-155730, Proceedings of the ASME 2025 Pressure Vessels and Piping Conference. Montreal, Quebec, Canada, July 2025. 10.1115/PVP2025-155730
- L. Doremus, O. Ancelet, L. Casulli, L. De Baglion, J.C. Le Roux, P. Spätig, J. Huret, Z. Que, and J. Beswick, "Evaluation of the Differences on Fatigue Life Between Hollow and Solid Specimens on a 316L Stainless Steel in the Frame of Incefa-Scale Project", PVP2025-154525, Proceedings of the ASME 2025 Pressure Vessels and Piping Conference. Montreal, Quebec, Canada, July 2025. 10.1115/PVP2025-154525

- L. Doremus, O. Ancelet, L. Casulli, L. De Baglion, R. Kallout, M. Grimm, S. Courtin, J.C. Le Roux, C. Jacquemoud, S. Arrieta, A. Fernandez Vina, T. Seppanen, Z. Que, G. Dundulis, R. Novotny, and J. Beswick, "Influence of Axisymmetric Notches on the Low Cycle Fatigue Life of a 316L Stainless Steel in the Frame of Incefa-Scale Project", PVP2025-155088, Proceedings of the ASME 2025 Pressure Vessels and Piping Conference. Montreal, Quebec, Canada, July 2025. 10.1115/PVP2025-155088
- J. Beswick, A. Mclennan, C. Currie, and S. Courtin, "Incefa-Scale Test Data Compared to Environmental Fatigue Design Curve Methodologies", PVP2025-154594, Proceedings of the ASME 2025 Pressure Vessels and Piping Conference. Montreal, Quebec, Canada, July 2025. 10.1115/PVP2025-154594
- P. Gee, R. Cicero, A. McLennan, and J. Beswick, "Incefa-Scale Project and International Fatigue Database: Reliable and Robust Fatigue Life Predictive Models", PVP2025-155700, Proceedings of the ASME 2025 Pressure Vessels and Piping Conference. Montreal, Quebec, Canada, July 2025. 10.1115/PVP2025-155700

2026

ASME 2026 Pressure Vessels and Piping Conference, PVP2026 (Anaheim, California, USA):

- S. Arrieta, S. Cicero, A. McLennan, and J. Beswick, "INCEFA-PLUS and INCEFA-SCALE: A Decade of European Research on Environmentally Assisted Fatigue in PWR Environments", PVP2026-176119, Proceedings of the ASME 2026 Pressure Vessels and Piping Conference. Anaheim, California, USA, July 2026. 10.1115/PVP2026-176119. *In press*.

THE INCEFA-SCALE COMPENDIUM: ADVANCED RESEARCH AND INTEGRATED FINDINGS ON ENVIRONMENTALLY ASSISTED FATIGUE

INCEFA-SCALE: Increasing Safety in NPPs by Covering Gaps in Environmental Fatigue Assessment – focusing on gaps between laboratory data and component scale

DOI: 10.5281/zenodo.18799092

https://incefascale.unican.es/

This project has received funding from the Euratom Research & Training Programme 2019-2020 under grant agreement nº 945300.